Gas permeation in two-dimensional membranes

Daniil Naberezhnyi

Dissertation

Faculty of Physics

Bielefeld University

Committee

Prof. Dr. Armin Gölzhäuser

Prof. Dr. Dario Anselmetti

Bielefeld, November 2021

Abstract

The separation of gases and vapors plays an important technological role, for instance, to produce medical oxygen from air. One of the separation technologies applied are membranes that act as selective barriers allowing the permeation for one component of a mixture while preventing the passage of others. Given Fick's law of diffusion, membranes have to be as thin as possible to obtain a maximum throughput, but their selectivity as a rule declines with a decreasing thickness. Two-dimensional (2D) materials promise atomically thin membranes whose separation performance is determined only by the size and the number of nanoscopic pores. However, perforating graphene and related structures has been proven challenging in terms of both controlling the size distribution and maintaining their integrity. Moreover, gas-surface interactions have been predicted to affect the transport in 2D membranes suggesting deviations from the size exclusion principle. The present work aims at exploring the mechanisms of molecular permeation in 2D membranes depending on the pore morphology and the physicochemical properties of the gases. To this end, three types of porous planar nanomaterials with distinct pore architectures are addressed with the help of advanced mass transfer measurements spanning a wide range of gaseous substances.

In the first part of the study, carbon nanomembranes (CNMs) with the tortuous pore geometry are demonstrated to enable an efficient isolation of water vapor mixed with atmospheric gases and organic solvents. The results are rationalized by the water condensation on CNMs that promotes its surface-mediated diffusion. This effect can be observed for other vaporous species as well. In contrast, non-condensable gases are believed to encounter steric hindrance at the pore entrance which gives rise to their immediate backscatter despite smaller molecular dimensions. To increase the residence time of the particles at the membrane surface, CNMs are covered with a layer of a CO_2-philic ionic liquid that is able to dissolve gases as described by Henry's law. Compared to bare CNMs, the permeation rate is found to increase manifold for carbon dioxide whereas the passage of helium is suppressed in accordance with the solubility constants.

The second 2D membranes of interest represent 2D covalent organic frameworks (COFs) featuring straight monodisperse pores of less than 2 nm in diameter. For the first time, individual single crystals of 2D COFs are subjected to quantitative gas permeation experiments. The open structure is illustrated to enable the free molecular flow while its areal porosity is measured to be as high as 40 % consistent with the material topography. On the other hand, the permeation rate for acetone, benzene, toluene, and p-xylene is found to be higher than anticipated from Graham’s law of diffusion. The heavier the molecules, the greater the deviation from the kinetic theory. The change in permeance observed is correlated with the saturation vapor pressure indicating the impact of adsorption. It is shown that the surface-mediated flow of condensable species can contribute much to the total molecular flux through a 2D COF.

Further efforts are devoted to the molecular transport across 2D silicon dioxide, or bilayer silica (BS), consisting of corner-sharing [SiO_4] tetrahedra. Large-area BS films are grown with atomic layer deposition (ALD) followed by a detailed spectroscopic and microscopic characterization. The study presents first-ever experiments with free-standing BS of vitreous morphology marked by four- to nine-membered pores. The network is found to pass helium atoms exhibiting far lower transport rates for other gases. However, BS membranes are shown to allow for a facile permeation of vaporous substances which reveals the high areal pore density. The data confirm the narrow pore size distribution and also point to the role of gas-solid interactions. In agreement with DFT calculations, the surface-mediated permeation appears to be faster for methyl isobutyl ketone than for 1-propanol and water in spite of the reverse order of the molecular dimensions.

This thesis pioneers the vapor permeation measurements with free-standing 2D membranes and goes beyond artificially perforated materials. The methodology used is capable of functional tests with microscopic samples and provides valuable mechanistic insights. The diversity of the synthetic approaches taken makes it possible to pursue different pore configurations, and the results obtained shed light on the significance of the molecular adsorption for permeation in 2D membranes. CNMs, 2D COFs, BS all display the surface-mediated transport of condensable species that can be a dominating mechanism if the pores are as small as the gas particles. Thus, molecular effusion takes no place in CNMs and BS, albeit it is prominent for 2D COFs. Regardless of the material, the size exclusion is hardly seen for inert gases whereas vaporous compounds can be clearly discriminated by narrow pores. The chemical affinity is additionally important in facilitating the surface-mediated flow as the number of adsorbates depends on the energetics of the fluid bonding to the membranes. Eventually, the concept of molecular sieving with 2D membranes seems to be oversimplified, especially in gas separation processes where the size of both the molecules and the pores is hidden by their quantum mechanical nature.

Table of contents

1 Introduction

The COVID-19 pandemic has embraced the world since the beginning of 2020. The new coronavirus infection can be severe leading to pneumonia and death. Presently, the number of infections and deaths worldwide exceed 242.3 million and 4.9 million respectively.[1] Artificial ventilation is essential for the survival of people with severe pneumonia caused by the COVID-19, so that the availability of equipment and the supply of medical oxygen are a matter of life and death. The pandemic has increased the demand for medical oxygen several times, and the oxygen shortage in low- and middle-income countries results in a high mortality.[2] The need for oxygen in such countries exceeded 28 million m^3 in May 2021,[3] and the challenge is to increase the supply of medical oxygen and reduce the cost of production making it available where it is needed most urgently. Beyond the medical use, around a half of the produced oxygen is consumed by metallurgy. Industrial oxygen is used for welding metals and the production of basic chemicals, and this liquefied gas acts as an oxidizer in rocket fuel. Oxygen (O_2), which is 21 % in the atmosphere, is being produced by air separation.[4,5] In addition to oxygen, there are other important products: nitrogen (N_2) and argon (Ar) which are 78 % and 0.93 % of the air correspondingly. These substances are widely applied as flushing or inert gases in the production of special metals and semiconductors. Food preservation is carried out by creating an inert atmosphere with nitrogen or argon. Liquid nitrogen is utilized in the cold-trapping of carbon dioxide and volatile organic compounds from gas streams. It is also known as a cooling agent for electronic equipment and biological samples.[4,5] Only in 2019, 6.28×10^9 m^3 of nitrogen, 5.61×10^9 m^3 of oxygen and 2.25×10^9 m^3 of argon were produced in Germany.[6]

The production of the pure gases from air is done by three methods: cryogenic distillation, adsorption processes and membrane separation.[4,5] When gigantic volumes of clean gases are required, very expensive cryogenic separation units are applied. The high energy consumption for large production volumes is an integral part of cryogenic technology.[5,7] The adsorptive separation technique having nearly the same energy cost is more efficient for producing gases of worse purity with less demand due to significantly lower capital costs of the setup.[8] In opposition, membrane separation being a fairly simple technology seems promising as the most energy efficient method with relatively lower capital costs. Membranes are currently used in the production of hydrogen, nitrogen, helium and natural gas.[7,9] The membrane allows the target molecules to pass through while it is difficult for other species to cross the membrane. However, industrial polymeric membranes do not possess great selectivity, and their performance is conditioned by distinct permeation rates of gases. The main disadvantage of membranes cutting their performance is the difficulty to have both a high permeation rate and a great selectivity.[9] A dense polymer can be nearly impermeable for large molecules while the compact polymer chains slow down small molecules leading to low permeation rate. Contrariwise, a low-density polymer has a sufficient free volume to provide a high throughput for small species as well as a noticeable permeation of large molecules. Decreasing the thickness of the membrane could gain the permeation rate, but linear polymers are not strong enough and cannot be defect-free at the nanoscale. Although membrane-based gas separation could reduce the energy consumption by up to three times, the disadvantages severely put bounds to the applicability of the membrane technology resulting in significant energy losses at the large scale. As a result, membranes remain efficient only for smaller volumes of production than adsorption processes.[10] The theory of gas separation and the problems of membranes are presented in the Chapter 2.

The existing limitations of polymeric membranes could be overcome by the application of two-dimensional (2D) materials with size-selective pores instead of the conventional polymers. While the industrial membranes have a thickness of an active layer of ~ 100 nm, the 2D membranes can be less than 1 nm thick providing the shortest path for permeation.[10,11] In this way, 2D membranes are offered as the thinnest separator for gas molecules where only the pore structure determines the selectivity. The fundamentals of the transport mechanisms in porous 2D materials are still poorly understood. According to predictions, the great performance in a 2D membrane with straight nanopores would be achieved at molecular sieving: one type of molecules is smaller than the pore and permeates in the steric regime, but other type of molecules has slightly larger size than the pore and could rarely pass in the activated regime.[12] Since the gaseous molecules have quite close sizes (0.26 – 0.5 nm), the creation of pores with precise diameters to cut off larger molecules is challenging. The most popular 2D membrane is nanoporous graphene which is being studied since 2012.[13] Intact graphene is impermeable for gases and has to either be etched or irradiated with an ion beam to form pores. Various methods of perforation for 2D material led to different pore sizes and distributions of these sizes. Direct permeation measurements with mass spectrometers in 2D membranes as well as imaging by electron microscopy were performed for the graphene with a mean pore size of 5.5 ± 1.3 nm, 7.6 ± 2.5 nm and for tungsten disulfide with sub-nanometer pores from ~ 0.3 to ~ 0.5 nm.[14–16] In other studies, permeation measurements were carried out indirectly, and the pores in graphene were not visualized that makes results uncertain. Thus, the graphene membrane after oxidative etching demonstrated ten times greater selectivity than graphene after ion irradiation followed by plasma treatment, but the pores size was estimated to be ~ 0.34 nm in the first case and ~ 0.29 nm for the last one.[13,17] In fact, the molecular sieving with an exponential dependence of the permeation rate on the kinetic diameter of gas was fundamentally studied by an indirect method only in the case of a single pore made by an electron beam.[18] Ongoing to the centimeter scale, graphene-based membranes have a larger scatter of pore sizes which leads to mediocre selectivity compared to polymeric membranes.[19–23] Despite the absence of ruptures after careful transfer procedures, the pore size distribution ensured the growth of nonselective pores with an increasing total pore density as the pore fabrication was scaled up.[21–23] The state-of-the-Art for 2D membranes is reviewed in the Chapter 2.

In contrast to single-layer materials, there exist other planar structures that have intrinsic pores and need no perforation. The inherently porous 2D materials can be often prepared on a centimeter scale, and their pore size distribution is usually narrow or even monodisperse in some cases. Unlike nanoporous graphene, whose strength correlates with the number of pores made, the 2D membranes with a high pore density demonstrate constant mechanical stability. The scope of this dissertation is to study the molecular transport in intrinsically porous 2D membranes with a distinct surface morphology and to explore how the permeation is affected by the nature gaseous species. There are three types of planar nanomaterials with a different pore geometry addressed, namely: carbon nanomembranes (CNMs), 2D covalent organic frameworks (COFs) and bilayer oxides (BOs). The synthesis and properties of these materials are discussed in the Chapter 3. The work relies on a new experimental methodology that is described in the Chapter 4. The permeating species studied span monatomic and polyatomic gases (He, Ne, N_2, O_2, Ar, CO_2, Kr, Xe, SF_6), vapors of heavy water (D_2O) and organic solvents (chloroform, hexane, acetonitrile, tetrahydrofuran, acetone, benzene, toluene, p-xylene, 1-propanol, methyl isobutyl ketone, 1-octene), and the results obtained are presented in the Chapters 4 – 6. The conclusions are drawn in the Chapter 7.

2 Theory

2.1 Cryogenic distillation

The first industrial-scale machine designed by Carl von Linde was run in 1902 for air separation. Contemporary cryogenic separation units are based on the same principles allowing to separate gases from a mixture according to their boiling points. Firstly, the filtered air is compressed and passed through adsorbents to exclude water, carbon dioxide and hydrocarbons. Secondly, the process air is cooled by a heat exchanger and undergoes Joule-Thomson expansion resulting finally in a liquefaction after several cycles. Further, the liquid air with a temperature of about 79 K (- 194 °C) is directed to a fractionation tower. The fractional distillation provides the separation of the components with close boiling points by the sequential cascading of condensation and evaporation. This concentration process is known as low-temperature rectification. The cryogenic air separation allows the production of pure gases (> 99.5%) but consumes a lot of energy due to many cycles of rectification.[7] Currently, the cryogenic air separation units demonstrate a capacity from 1000 to 150,000 m^3 of oxygen per hour.[5] The economies of scale lead to the fact that the specific energy consumption varies from 0.6 to 0.4 kWh/m^3, but capital cost of a cryogenic separation unit is quite high and might be estimated at over $110 million.[24,25] Large-scale cryogenic air separation units allow the extraction of helium, neon, krypton and xenon known as rare gases from atmosphere. Besides air, the cryogenic distillation is used to purify natural gas (mainly methane CH_4) and hydrogen (H_2) from impurities, as well as to recover helium (He) and carbon dioxide (CO_2) from natural gas.[4,26]

2.2 Adsorptive separation

The second most popular way to separate air is a non-cryogenic adsorption process. This method is based on the selective adsorption of the gas on the adsorbent removing that component from a mixture. The choice of adsorbents depends on the nature of gases because the adsorption strength is conditioned by the boiling point of the substance as well as its polarizability, dipole and quadrupole moments. The adsorption processes are identified by their regeneration method. Zeolites selectively adsorb nitrogen from compressed air in pressure swing adsorption (PSA) systems operating at ambient temperature. Different other adsorbents in layers are used to capture water, carbon dioxide and hydrocarbons in PSA processes. Upon reaching the saturation in zeolites with nitrogen, the chamber with oxygen-enriched gas is vented resulting in a pressure drop to the atmospheric. Reducing the pressure below the atmospheric increases the productivity of a cycle that is applied in a vacuum pressure swing adsorption (VPSA) process. Under a low partial pressure, nitrogen is released back from the zeolites and eluted from the chamber by dry waste nitrogen before the next cycle. Frequent PSA cycles of ~ 30 minutes result in a blowdown loss during depressurization and a faster valve wear. Unlike PSA, the temperature swing adsorption (TSA) processes operate with a much smaller quantity of adsorbents but the latter have a higher adsorption capacity that requires a higher temperature of 120 °C for the regeneration resulting in a large energy consumption and a time of the cycle to be of ~ 130 minutes.[7,27] The system of adsorptive air separation produces oxygen up to 90 – 95 % and nitrogen up to 99.99 %, therefore it is suitable for processes where high purity oxygen is not required.[5] The capital cost of the gas separation adsorber is significantly lower compared to the cryogenic separation unit, but at the same time, the PSA or TSA technologies remain profitable only at relatively low production volumes. Economies of scale in large optimized systems of adsorptive separation allow to extract oxygen with a specific energy consumption of about 0.5 kWh/m^3. These systems remain effective up to a capacity of 6000 – 8700 m^3 of oxygen per hour, since for a larger capacity it is more expedient to use cryogenic distillation.[8] Also pure helium (> 99.99 %) is recovered from natural gas by a PSA process, but it might be not efficient for its liquefaction due to the relatively small volumes.[26]

2.3 Membrane separation

2.3.1 Membrane technology

Membrane technologies emerged on the market in the 1980s as the third way to separate gas mixtures. The membrane system consists of a compressor for pressurizing, a coalescing filter and membrane modules. The advantages of the membrane separation are its simple operation, the absence of moving parts, low capital costs and energy consumption compared to other methods. The membranes play the role of a barrier that is much more permeable to one substance in contrast to others. Therefore, the membrane separation allows to recover the component with the highest permeation rate from a mixture. The molecules passed through the membrane are always enriched with the fastest gas and the enrichment level depends on the selectivity of the membrane. Non-target components may pass through the membrane at slower rates or not at all. The difference in concentrations (pressures) on the opposite sides of the membrane is the necessary driving force of the permeation. The transmembrane flux F ($\mathrm{mol \cdot s^{-1} \cdot m^{-2}}$) for single component is governed by Fick's law of diffusion:

$$F = -D \times \frac{dC}{dx}, \tag{2.1}$$

where D is the diffusion coefficient ($\mathrm{m^2 \cdot s^{-1}}$), dC is the concentration differential ($\mathrm{mol \cdot m^{-3}}$), dx is the differential coordinate on an axis perpendicular to the membrane surface (m). The flux is linearly dependent on the concentration gradient dC / dx through the membrane, so that a high pressure of a gas mixture up to 110 bar is applied to the membrane. The diffusivity depends on the properties of the gas and the membrane material. In this way, there are two parameters that can be increased for a gain in the membrane performance: diffusivity and concentration gradient.[9,28,29]

2.3.2 Transport models in membranes

Depending on the porosity of membranes, different transport mechanisms determining the diffusion coefficient can realize. Sometimes the membrane has such a morphology that the passage of a gas can be described by two or more transport models. The simplest transport model is a viscous flow shown in Figure 2.1a. It occurs in relatively large pores when their sizes exceed the mean free path of the gas molecules (around 100 nm at atmospheric pressure). In this case, the diffusivity is inversely proportional to the viscosity of the gas mixture. Since the molecules pass through the pores together, this mechanism does not imply any selectivity. When the characteristic sizes of pores are around 2 – 50 nm, i.e. larger than the molecules and less than the mean free path, Knudsen diffusion (effusion) takes place. It is demonstrated in Figure 2.1b how gas species move independently of each other. Collisions of the molecules with the walls are supposed to be elastic, and the permeation rate depends on only the

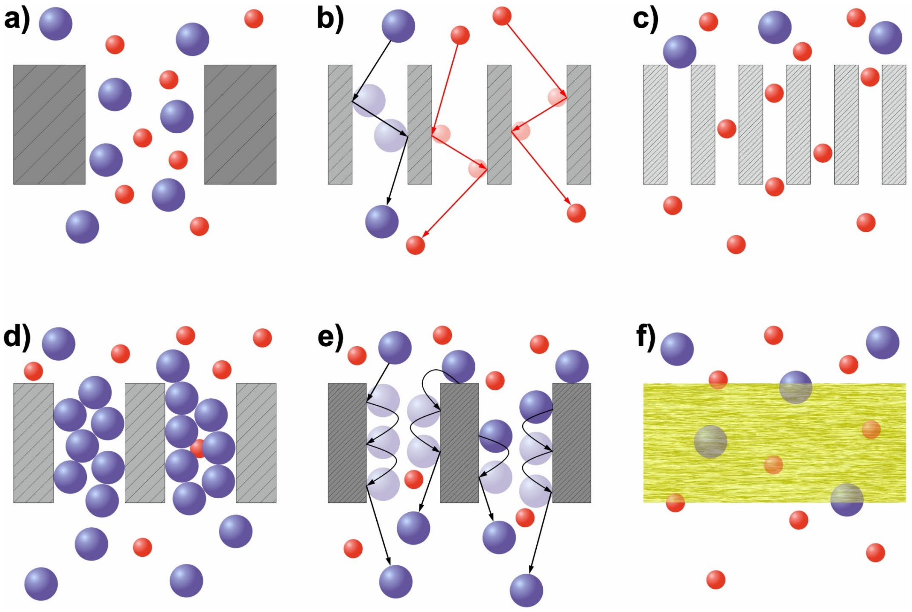

Figure 2.1 – Schemes of gas transport mechanisms through the porous membranes: **a)** Viscous flow; **b)** Knudsen diffusion; **c)** Molecular sieving; **d)** Capillary condensation; **e)** Surface diffusion; **f)** Solution-diffusion.

molecular velocity which is the higher the lighter the molecule is. The diffusion coefficient for the component is inversely proportional to square root of its molecular mass as a result of which the selectivity is quite low. If the pores are close to molecules in sizes, size exclusion known as molecular sieving might occur. This most desirable transport mechanism is presented in Figure 2.1c where the membrane is absolutely selective towards the smallest molecules being a hindrance for the larger molecules. The practical realization of such a transport is complicated because the pores usually have a size distribution. If the partial pressure of the gas on the feed side is close to its critical pressure, the gas condenses in the pores as displayed in Figure 2.1d. The capillary condensation provides a high selectivity as the liquefied substance fills the entire pore space. Such capillary transport usually takes place in mesopores larger than 3 nm, while the performance is restricted by the partial pressure of the condensed component that must be maintained on the feed side.[10,30] Adsorption and surface diffusion shown in Figure 2.1e make a significant contribution to the permeation of condensable gases. Unlike the capillary condensation, filling the pores with one component is not achieved. Nevertheless, the condensable molecules are more easily adsorbed on the pore walls and move along them with an advantage over non-condensable molecules.[28,30]

The solution-diffusion transport mechanism presented in Figure 2.1f is more conventional for describing the gas permeation in non-porous polymeric membranes. Since the permeation in most industrial membranes might be described by the dissolution-diffusion model, it is considered in more detail. The mechanism can be represented in three stages: dissolving in the membrane material from the upstream side (feed), diffusion through the membrane and desorption on the downstream (opposite) side.[9,10,28,29] The first stage may be defined by Henry's law:

$$C = S \times f = S \times \gamma \times p, \tag{2.2}$$

where C is the concentration of dissolved species in the material ($\mathrm{mol \cdot m^{-3}}$), S is the solubility coefficient ($\mathrm{mol \cdot m^{-3} \cdot Pa^{-1}}$), f is the fugacity (Pa), p is the partial pressure (Pa), γ is the activity coefficient. The solubility coefficient S depends mainly on the physical properties of the gas – the sorption is inversely proportional to the saturated vapor pressure of a substance and varies little for the same gas in chemically different polymers. The fugacity f acting as an effective gas pressure is a correction for real gases whose behavior deviates from an ideal gas at high pressures.[31] Equation (2.2) describes well the equilibrium concentration for rubbery polymers, while the concentration in glassy polymers is higher due to Langmuir adsorption in microvoids. Every polymer remains in a glassy state when the temperature is below the characteristic glass transition temperature T_g. The dual sorption model is acceptable at temperatures lower than T_g, and assumes that Henry's law sorption and Langmuir sorption occur simultaneously.[9,28,29] The transmembrane flux F ($\mathrm{mol \cdot s^{-1} \cdot m^{-2}}$) for the solution-diffusion model can be described as:

$$F = D \times S \times \frac{p_1 - p_2}{\Delta \ell} = \mathcal{P} \times \frac{\Delta p}{\Delta \ell}, \tag{2.3}$$

where p_1 is the applied pressure on the upstream side (Pa), p_2 is the pressure on the downstream side (Pa), $\Delta \ell$ is the thickness of the membrane (m), Δp is the pressure difference (Pa), $\mathcal{P}$ is the permeability coefficient ($\mathrm{mol \cdot m \cdot s^{-1} \cdot m^{-2} \cdot Pa^{-1}}$). The diffusivity D being a proportional coefficient depends on the molecular weight of the permeating gas and the type of the polymer. Heavier and larger molecules interacting with more segments of the polymer chains pass the membrane slower than small and light species. Rubbery polymers have a more flexible matrix – segments of the polymer backbone are able to rotate along their axes resulting in a larger diffusion coefficient compared to rigid glassy polymers. Moreover, the concentration of dissolved permeating molecules can influence on the rate of diffusion.[28,29] The permeability coefficient $\mathcal{P}$ determines the ability of the considered membrane for the gas permeation. It can be seen from equation (2.3) that the highest flux at a constant permeability would be achieved at the maximum possible pressure difference with the smallest membrane thickness. The ability of a membrane to separate two gases, *A* and *B*, is called the selectivity α(A/B) being the ratio of their permeabilities $\mathcal{P}_A$ and $\mathcal{P}_B$:

$$\alpha(A,B) = \frac{\mathcal{P}_A}{\mathcal{P}_B} = \frac{D_A}{D_B} \times \frac{S_A}{S_B}, \tag{2.4}$$

where D_A and S_A are the diffusivity and the solubility for gas *A*, D_B and S_B are the diffusivity and the solubility for gas *B.* The ratio D_A / D_B known as the mobility selectivity demonstrates the difference in sizes of the two permeating molecules. The ratio S_A / S_B is the solubility selectivity that reflects the difference in the relative condensabilities of these gases. In turn, larger molecules experiencing diffuse hindrances are more condensable, in other words, more soluble in the polymer.[28] Moreover, competitive sorption between gases results in their lower concentrations compared to the values for individual gases.[9]

2.3.3 Disadvantages of membranes

It was noticed that membranes cannot achieve high selectivity and high permeability simultaneously. The trade-off between selectivity and permeability is known as the Robeson limit – a gain in selectivity leads to a loss in permeability and vice versa.[32,33] The characteristics of membranes expressed in a logarithmic graph of the permeability-selectivity are located below a certain line, Robeson upper bound, that was determined empirically. The slope of this line depends on the difference in the kinetic diameters of the gas molecules. When the size of molecules changes by an order of magnitude, the diffusion coefficient changes by ten orders of magnitude. In this way, the mobility selectivity makes the largest contribution to the membrane performance, while the contribution of the solubility selectivity is minor. The mobility selectivity D_A / D_B is very sensitive to the molecular size especially in glassy polymers where the chain backbones are fixed and cannot rotate.[28,32] 17 years later, the upper

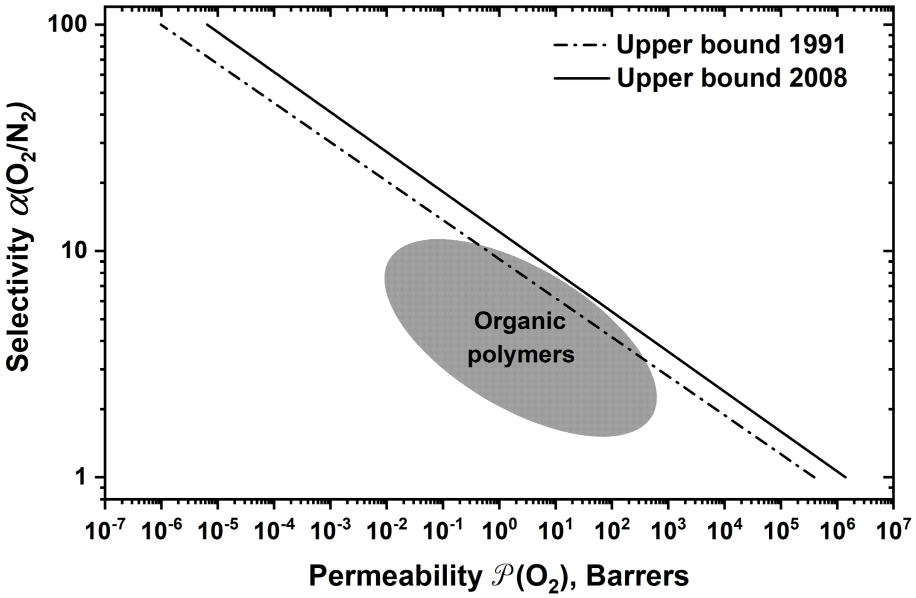

Figure 2.2 – Robeson upper bound correlation for membranes in O_2/N_2 separation in 1991 and 2008. Grey oval is the region of performances of polymeric membranes.

bound was revised and the progress found was not so significant. Rigid ladder-type polymers and fluorinated polymers provided the shift. It was suggested that changing the permeation mechanism from solution-diffusion to molecular sieving could give an outstanding performance, but in reality an increase of the pore size leads to Knudsen diffusion with low selectivity.[33] The Robeson upper bounds in 1991 and 2008 for O_2/N_2 separation are shown in Figure 2.2. The region of most polymeric membranes is schematically represented as a grey oval. The region of the desired performance is above the lines towards the upper right corner of the plot.

In addition to the Robeson trade-off, glassy polymers possessing good characteristics undergo physical aging – a slow change towards the thermodynamically equilibrium state. Physical aging results in the reduction of the free volume and an increase of the density. This process becomes more pronounced at a thickness below 1 μm, but the thickness of the active layer in industrial membranes is usually about 0.1 μm, therefore, the physical aging of the polymer membrane reduces the separation efficiency and a replacement of membranes is required after a certain service life.[10] As it can be seen from equation (2.3), the thinner the membrane, the greater the transmembrane flux is. But linear polymers possess a low mechanical stability, and it is hard to fabricate a polymer membrane with a defect-free active layer thinner than 100 nm. Another unfavorable phenomenon called plasticization is observed at high gas pressures, when the polymer swells due to gases dissolved in it. The chain movement becomes easier and the free volume increases, which leads to a rise in the diffusivities and hence to a decrease in the selectivity of the membrane. In addition, the chemical instability at high gas pressures and poisoning by impurities result in a degradation of the membrane and a decrease in its service life.[10]

2.3.4 State-of-the-Art for industrial membranes

Typically, industrial membranes are polymeric while the choice of the material depends on the preferred selectivity and the target gas mixtures: polyimide for O_2/N_2, polysulfone for H_2/N_2, cellulose acetate for CO_2/CH_4, etc.[7,28] Conventional membranes demonstrate a satisfactory performance, but each membrane is permeable to other components of the mixture more or less due to the trade-off. In this way, membranes are competitive to purify gas mixtures with a high concentration of the target component producing pure gases. It is known that achieved capacities are 1000 – 4000 m^3 of nitrogen per hour and 14,000 m^3 of hydrogen per hour.[7] Currently, a membrane cascade even with a low nitrogen selectivity N_2/O_2 is capable to separate pure nitrogen from air, and oxygen-enriched air with 50 % of O_2 is obtained at the outlet after passing two oxygen-selective membranes (O_2/N_2). The low molecular weight facilitates easy diffusion of hydrogen in the polymer and the membranes are widely used to recover hydrogen in syngas (H_2/CO), natural gas (H_2/CH_4) and in the production of ammonia (H_2/NH_3). Besides the air separation and hydrogen recovery, membranes accounted for one tenth of the natural gas purification technologies.[10] The membrane separation produces biomethane with content of carbon dioxide less than 3 % from biogas which contains 50 – 70 % of CH_4 and 30 – 50 % of CO_2. This method consumes 0.21 – 0.3 kWh/m^3 making it twice as economical as the pressure swing adsorption. Now highly selective membranes are critically required in industry for carbon dioxide capture from flue gases (CO_2/N_2 separation) and for the purification of natural gas from nitrogen (CH_4/N_2 separation).[9] The use of efficient membranes in a hybrid technology with cryogenic distillation in olefin/paraffin separation (ethylene/ethane, propylene/propane, butadiene/butane) is able to reduce the energy consumption by 2 – 3 times.[34] The membrane-based recovery of vapors from gas mixtures is not widespread. Although membrane technology appears to be attractive for capturing volatile organic compounds (VOCs) from polluted air, a suitable membrane has to be chemically stable, selective and high permeable. In view of the complexity of manufacturing such a membrane, this technology is considered potential.[35] However, water-selective membranes unlike adsorbents do not require regeneration, and membrane dryers are applied for dehydration of compressed air and natural gas.[10,36]

Eventually, the Robeson limit in polymeric membranes being a major drawback among other ones leads to a lower recovery and a lost money for the separation plants. The trade-off between selectivity and permeability severely restricts application of the membranes in the gas separation field. It seems the approaches for improving polymer membrane materials have exhausted themselves that encourages researchers to new ways. A use of two-dimensional (2D) membranes is a promising way for the ultimate membrane separation due to the absence of diffusion hindrances and other mechanisms of permeation.[30]

2.4 Two-dimensional membranes

2.4.1 Origin of 2D membranes

The interest towards 2D materials has been growing after the isolation of a graphene monolayer from graphite crystals in 2004 that proved the existence of stable materials of one atom in thickness. The possibility to produce such materials of a large area prompted the idea of using them as membranes for gas separation.[11,37] A nanoporous 2D membrane is a material with a thickness of several atoms which has many distributed pores.[11,38] Generally, nanopores are understood as pores with a size of 1 – 100 nm. According to the IUPAC, the pores can be classified by the size into macropores (larger than 50 nm), mesopores (from 2 to 50 nm) and micropores (less than 2 nm).[37] In fact, micropores are in scope of a 2D membrane because the size exclusion known as molecular sieving is the most desirable case for 2D membranes. Two-dimensional membranes can be said to have no thickness that provides a large concentration gradient dC/dx which in turn gives a higher transmembrane flux according to equation (2.1). Since the thickness-independent permeability coefficient $\mathcal{P}$ for the bulk material is not suitable to characterize membranes several atoms in thick, the performance of 2D membranes should be assessed by another value. The appropriate parameter called permeance Π ($\mathrm{mol \cdot s^{-1} \cdot m^{-2} \cdot Pa^{-1}}$) can be presented as follows:

$$\Pi = \frac{Q}{\Delta p \times A} = \frac{F}{\Delta p} = \frac{Q_L}{A}, \tag{2.5}$$

where Q is the flow rate through the membrane ($\mathrm{mol \cdot s^{-1}}$), Δp is the pressure difference (Pa), A is the area of the membrane ($\mathrm{m^2}$), F is the transmembrane flux ($\mathrm{mol \cdot s^{-1} \cdot m^{-2}}$), Q_L is the leak rate ($\mathrm{mol \cdot s^{-1} \cdot Pa^{-2}}$). In turn, the selectivity of two-dimensional membranes is calculated as a ratio of permeances:

$$\alpha_{A,B} = \frac{\Pi_A}{\Pi_B}, \tag{2.6}$$

where Π_A is the permeance for gas A, Π_B is the permeance for gas B.[11,12] Besides the permeance Π, a 2D membrane can be characterized with an effective porosity Φ – fraction (in percent) of the open area A_{open} available for the gas passage:

$$\Phi = 100\% \times \frac{A_{open}}{A_{total}} = 100\% \times \Pi \times \sqrt{2\pi RTM} = 100\% \times \frac{Q_L}{A_{total}} \times \sqrt{2\pi RTM}, \tag{2.7}$$

where A_{total} is the total membrane area, R is the universal gas constant ($\mathrm{J \cdot K^{-1} \cdot mol^{-1}}$), T is the absolute temperature of gas (K), M is the molar mass ($\mathrm{kg \cdot mol^{-1}}$). The molecular transport through atomically thin nanoporous membranes is predicted to be influenced by the size difference between the pores and the gas molecules as well as the adsorption and the surface diffusion. In theory, if the gas molecules were smaller than the pore diameter by 5 % or more, it would easily pass through the 2D membrane according to steric transport model. High permeances and low selectivity for gas mixtures are prescribed for the steric regime. If the gas molecules were equal or slightly larger than the pore diameter, the pore would present a barrier itself, and the gas molecules need an additional energy to overcome it and pass through the pores. Low permeances and high selectivity are expected for activated regimes. The ideal case for gas separation is the implementation of a steric regime for smaller molecules and an activated regime for larger molecules. For this purpose, the pores should have a size between the smaller and the larger molecules.[12] Thus, 2D membranes can theoretically exhibit high selectivity and permeability overcoming the Robeson trade-off that would promote membranes as an energy-efficient technology into new fields. The practical application of 2D membranes implies their placement on a macroporous substrate that provides the integrity for thin films and minor obstructions to the gas flow.[39]

2.4.2 State-of-the-Art for 2D membranes

Graphene is a 2D material composed of sp^2-hybridized carbon atoms in a hexagonal crystal lattice which has a Young's modulus of 1 TPa. High mechanical strength, chemical stability and thickness of one atom make graphene an excellent candidate as a 2D membrane. The central hexagonal “pore” being around 6.4 pm is too small for passage through it.[11,37,40] Lennard-Jones diameters of gaseous molecules calculated by gas viscosity are presented for clarity in Table 2.1.[41] Although some ripples, wrinkles and local curvatures are catalytically active and allow hydrogen to permeate through single-layer graphene, the defect-free material is completely impermeable to all gases and liquids.[42] For more than ten years, graphene is explored as an atomically thin membrane. The fabrication of sub-nanometer pores in such a rigid structure forms a prototype of an atomic-thick molecular sieve. In 2009 Jiang et al. did density functional theory (DFT) calculations which predicted the outstanding selectivity of a nanoporous graphene membrane. Thus, the removal of ten carbon atoms (two jointed hexagons) from the graphene structure followed by a passivation with hydrogen might lead to an exceptional selectivity of ~ 10^{23} for H_2/CH_4 mixture.[43] Hydrogen-passivated pores after removal of six atoms (one hexagon) could provide a selectivity of ~ 10^{10} for O_2/N_2 and ~ 10^6 for CO_2/N_2 mixtures according to DFT calculations done by Blankenburg et al. in 2010.[44] These predictions inspired further experimental research.

Koenig et al. showed the possibility of a size-selective permeation in nanoporous graphene for the first time in 2012. The graphene was exfoliated from graphite using Scotch tape followed by a transfer onto an oxidized silicon wafer with cylindrical microcavities of 5 μm in diameter. Ultraviolet-induced oxidative etching was applied to produce sub-nanometer pores in the free-standing bilayer graphene. The pressurized blister test and a mechanical resonance test were used to evaluate the permeation rate through the nanopores. In the first method, the samples were pressurized in different gases at high pressure until reaching the equilibrium. Then the membrane

Table 2.1 – Lennard-Jones diameters of some gaseous molecules estimated from viscosity in ascending order.[41] Lennard-Jones diameters can be considered equivalent or close to kinetic diameters.

Substance	Formula	Lennard-Jones diameter, pm
Helium	He	255
Water	H_2O	264
Neon	Ne	282
Hydrogen	H_2	283
Ammonia	NH_3	290
Oxygen	O_2	347
Argon	Ar	354
Hydrogen sulfide	H_2S	362
Krypton	Kr	365
Carbon monoxide	CO	369
Methane	CH_4	376
Nitrogen	N_2	380
Carbon dioxide	CO_2	394
Xenon	Xe	405
Ethylene	$CH_2=CH_2$	416
Ethane	CH_3-CH_3	444
Acetone	$CH_3-C(O)-CH_3$	460
Propylene	$CH_2=CH-CH_3$	468
Propane	$CH_3-CH_2-CH_3$	512
Sulfur hexafluoride	SF_6	513
Benzene	C_6H_6	535
Chloroform	$CHCl_3$	539
n-Hexane	$CH_3-(CH_2)_4-CH_3$	595

deflating over time was measured by atomic force microscopy (AFM) after removal the sample from the pressure chamber as shown in Figure 2.3a. The opposite happened

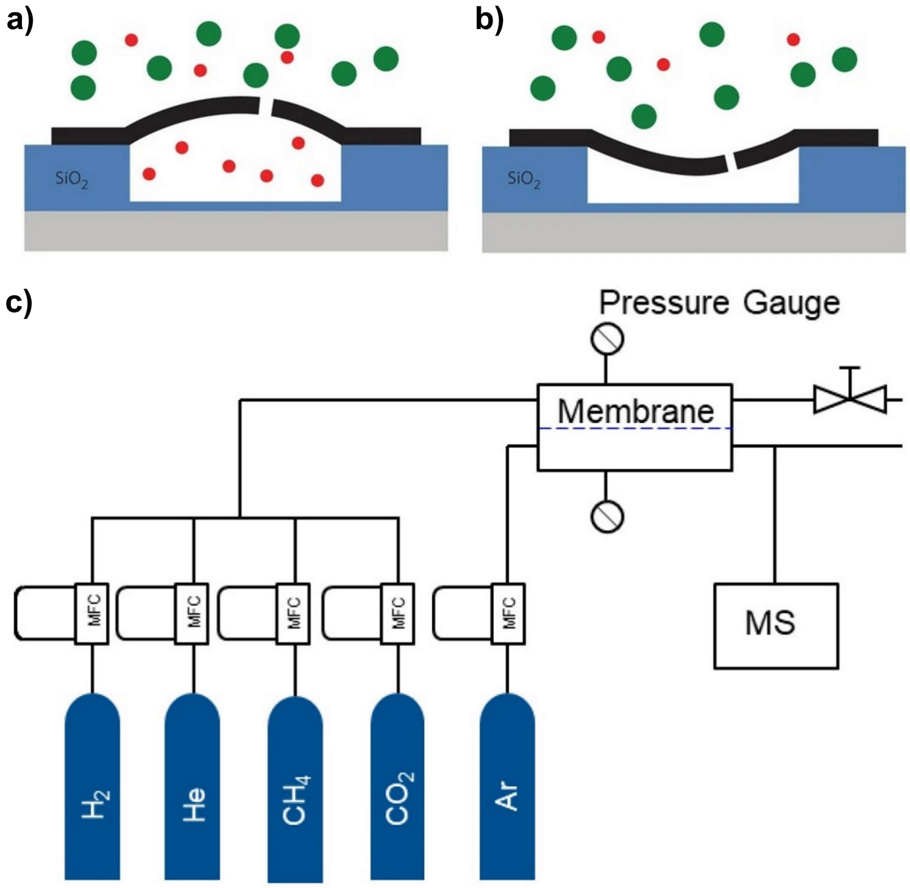

Figure 2.3 – Schemes of gas permeation measurements in 2D membranes. **a)** Pressurized blister test. A graphene membrane with hole(s) lay down on a substrate with a cavity. The membrane bulges upwards after removing it from a pressure chamber. Bulge changes over time is measured by AFM. **b)** Mechanical resonance test. The evacuated device was put into a pressure chamber. The mechanical resonance of the membrane changed as the cavity was filled with gas. An intensity-modulated blue laser was applied to drive the membrane while a red laser was utilized to detect the motion. **c)** Setup for direct gas permeation measurements. The feed gas is provided from gas cylinder and regulated by a mass flow controller (MFC). An argon flow sweeps the permeated molecules towards the mass spectrometer (MS). Parts **a)** and **b)** are reprinted and adapted with permission from Koenig et al.[13], Copyright 2012 Springer Nature. Part **c)** is reprinted and adapted with permission from Schlichting et al.[15], Copyright 2020 American Chemical Society.

in the second method – the evacuated sample was displaced into a pressure chamber, and the microcavity was filled with gas that led to a decrease in tension of the graphene as shown in Figure 2.3b. The resonant frequency of the membrane depends on the mechanical tension and can be detected with a laser beam. In the issue, hydrogen and carbon dioxide permeated noticeably through sub-nanometer pores whose mean size was declared to be close to the kinetic diameter of argon (~ 340 pm). The estimated H_2/CH_4 selectivity was 1.5×10^4 while the leak rate Q_L for hydrogen turned out to be a thousand times lower than predicted by calculations of Jiang et al. Instead, the hydrogen leak rate was comparable to the values calculated by Blankenburg et al. for pores consisting of a missing carbon hexagon, although the predicted H_2/CO_2 selectivity of ~ 10^{17} was very far from the obtained result (the measured selectivity for this pair was only 1.7). Furthermore, a small number of pores confirmed by Raman spectroscopy could not give a higher leak rate for this nanoporous graphene.[13] The effective porosity of this graphene can be estimated by the hydrogen leak rate as ~ 10^{-9} %. Indirect measurements, contribution from leakages, the unknown number of pores and their actual sizes had left some gaps, but the noticeable selectivity encouraged researchers to further study graphene membranes towards a size-exclusion separation.

In 2014, the gas transport in graphene membranes was investigated by Celebi et al. in great detail. Bilayer graphene synthesized on copper substrate was transferred with a poly(methyl methacrylate) (PMMA) coating onto a silicon nitride substrate with 49 orifices of 4 μm in diameter. Then the free-standing graphene was perforated by a focused ion beam (FIB) resulting in the pores with a narrow size distribution which was visualized by scanning electron microscopy (SEM) and transmission electron microscopy (TEM). Treatments with gallium ions allowed to make pores from 16 to 1000 nm in diameter. The smallest pores with dimensions of 7.6 ± 2.5 nm were produced by helium FIB. The transmembrane flow was investigated in a custom-made apparatus. The feeding gas in the upstream compartment was regulated with a mass flow controller. The permeating gas in the downstream compartment was detected by a mass flowmeter and a calibrated mass spectrometer. These direct measurements allowed to observe the permeation of different gases in nanopores. Although the effective porosity of graphene was 4 %, the 2D membrane showed a selectivity of 4.7 for H_2/CO_2 mixture and very high permeance of ~ 7.2×10^{-3} $mol \cdot s^{-1} \cdot m^{-2} \cdot Pa^{-1}$. On the one hand, Knudsen diffusion in an atomically thin membrane was enough to overcome the Robeson upper bound for polymeric membranes towards a greater permeation rate.[14] On the other hand, Knudsen selectivity cannot be high, so the performance of such membrane is far from desired.

In 2020 gas permeation in free-standing graphene was studied by Schlichting et al. in a similar experimental setup which is schematically presented in Figure 2.3c. Bilayer graphene was coated with poly(phthalaldehyde) (PPA) and displaced on a silicon nitride substrate with 64 orifices of 4 µm in diameter. The irradiation with an unfocused gallium ion beam followed by the exposure to 1 mbar O_2 at a high temperature led to formation of nanopores that were investigated with Raman spectroscopy, SEM and TEM. The mean pore diameter over all samples was estimated to be 5.5 ± 1.3 nm. Besides nanometer-sized pores, atomically small defects were found in the graphene after the ion and oxidative treatments. The pore density of 5×10^{10} cm^{-2} was achieved as the limit before the beginning of membrane rupture. Gas permeation experiments were carried out at a custom-made setup where the feed gases were regulated by mass flow controllers. Passed gas was carried with an argon sweep flow to a calibrated mass spectrometer. Gas molecules with hydrogen atoms (H_2 and CH_4) permeated faster than He and CO_2 with smaller kinetic diameters because of a probable affinity between the hydrogens and the oxygen-functionalized pore. The two-dimensional membrane with the highest hydrogen permeance of 3.7×10^{-3} $mol \cdot s^{-1} \cdot m^{-2} \cdot Pa^{-1}$ showed a H_2/CH_4 selectivity of 4.7. Intrinsic defects in pristine graphene exhibited a H_2/CH_4 selectivity of ~ 9 while the ion irradiation and a short exposure to O_2 resulted in the membrane with the same selectivity and tenfold larger permeance of hydrogen (1.0×10^{-5} $mol \cdot s^{-1} \cdot m^{-2} \cdot Pa^{-1}$).[15] Six years after the study of Celebi et al., it was shown that a graphene membrane with a less effective porosity (1.6 ± 0.6 %) may have the selectivity slightly better than Knudsen one due to smaller pores.

Significant selectivity in free-standing nanoporous graphene was achieved by Liu et al. in 2021. The study used a similar transfer procedure and the pressurized blister test as described in the paper of Koenig et al., but the nanopore fabrication was done by another method. More specifically, the free-standing bilayer graphene over microcavities was irradiated with helium ions followed by a treatment with hydrogen plasma. The graphene etched in the H_2 plasma without an ion irradiation showed a noticeable permeation only for helium and its pores were supposed to be ~ 260 pm. The membrane with the best characteristics was made after a low dose of ion irradiation and a short etching in hydrogen plasma. Again, the H_2 leak rate was comparable to that predicted by Blankenburg et al. Remarkably, the hydrogen-terminated pores were easily permeable to hydrogen than to helium with a smaller kinetic diameter. The mean diameter of the pores was said to be close to 289 pm. As a result, the selectivities were 495 and 877 for H_2/N_2 and H_2/CH_4 mixtures, respectively.[17] Although the defect density in graphene was high (~ 1.7 × 10^{11} cm^{-2}), the effective porosity turned out to be extremely low and amounted to ~ 3 × 10^{-10} %. Tenfold difference in H_2/CH_4 selectivity compared to the results of Koenig et al. as well as an inability to reliably estimate the pore sizes raises new questions, the answers to which have not yet been obtained.

The investigation of the molecular sieving effect in a single pore was reported by Sun et al. recently. Arrays of microwells 1 – 3 μm in diameter and ~ 0.1 μm in depth were created on the single crystal of graphite using e-beam lithography and dry etching. Single-layer graphene (0.34 nm-thick) was transferred onto these microwells making an atomically tight sealing. The impermeability of the samples was proved by pressurizing in a helium atmosphere followed by AFM scanning. Then the samples were treated with a low-energy electron beam until a leakage was detected by an AFM after a pressure chamber with helium. The number of pores was indirectly estimated by thermal evaporation of gold onto graphene. Since the leak was eliminated after covering < 1 % of the membrane area in most samples (38 of 40), it was concluded that only one pore was there. The atomically tight sealing allowed to measure leak rates with a high sensitivity. The effective porosity of such a membrane with a single pore was estimated at around 8 × 10^{-11} – 7 × 10^{-10} % depending on the membrane area. AFM scanning was used to measure the deflation of a graphene blister after removing the sample from the pressure chamber. Three types of pores showing a distinct selectivity were noted. Exponential dependences of the permeation rate on the kinetic diameters were demonstrated for all pores – gaseous molecules were passing in the activated transport regime. Temperature-dependent measurements were performed to find the activation energies for the gas passage. The experimental results were compared with DFT calculations which correspond to the data for a flexible hepta-vacancy (missing of 7 atoms), a fixed deca-vacancy and a flexible deca-vacancy (missing of 10 atoms). The smallest pore was supposed to have an effective diameter of ~ 200 pm resulting in missing of seven carbon atoms. This type of pores was shown to be completely impermeable for the larger molecules of methane and xenon while smaller species of helium and hydrogen demonstrated a leak rate of ~ 10^{-24} $mol \cdot s^{-1} \cdot Pa^{-1}$. Although the He/H_2 selectivity was very low, the selectivities for

H_2/CH_4 and He/Xe mixtures exceeded 10^7. Moreover, the measured number of molecules interacting with a pore is found out to be higher than the number of species bombing the pore from the gas phase because of the surface diffusion. The contribution of adsorbates diffusing on the surface provided a faster permeation for larger polyatomic gases compared to noble gases. For instance, oxygen (346 pm) having larger kinetic diameter permeated faster than argon (340 pm): $Q_L(O_2) \sim 2 \times 10^{-27}$ mol·s^{-1}·Pa^{-1} and $Q_L(\mathrm{Ar}) \sim 7 \times 10^{-28}$ mol·s^{-1}·Pa^{-1}, as well as nitrogen (364 pm) showed a higher leak rate then krypton (360 pm): $Q_L(N_2) \sim 2 \times 10^{-28}$ mol·s^{-1}·Pa^{-1} and $Q_L(\mathrm{Kr}) \sim 1 \times 10^{-28}$ mol·s^{-1}·Pa^{-1}. The experiments of Sun et al. proved the possibility of the size exclusion with a great selectivity in case of one pore, but 2D membranes should have a density of such pore at least of $10^{10} – 10^{12}$ cm^{-2} to be effective and it is a hard challenge.[18]

Besides graphene, other 2D materials are considered as atomic thin membranes for ultimate separation. Although nanopores were successfully produced in gas-impermeable molybdenum disulfide MoS_2 and hexagonal boron nitride h-BN, there have been no published papers specifically on gas permeation in them.[45–48] In 2020, a 0.7 nm-thick single-layer transition metal dichalcogenide was perforated and studied as a 2D membrane for gas separation by Thiruraman et al. Single crystals of tungsten disulfide WS_2 were transferred with a PMMA layer onto a silicon nitride substrate with nine orifices ~ 0.25 μm in diameter followed by annealing to seal. Then a gallium FIB was applied to fabricate nanopores in a free-standing flake of WS_2. Mainly three types of defects were produced as a result of the removal of one (1W+6S), two (2W+6S) or three (3W+12S) tungsten atoms together with the surrounding sulfur atoms. These pores having effective diameters from ~ 315 to ~ 525 pm were visualized by scanning transmission electron microscopy (STEM). The STEM images were found to be concerned with DFT calculations for the defects in the crystal: 1W+6S (320 × 320 pm), 2W+6S (210 × 620 pm), 3W+12S (580 × 620 pm). The silicon nitride substrate with a nanoporous WS_2 crystal was tightened between two vacuum compartments, and the passed helium was directly detected using a mass spectrometer. Permeation measurements at various temperatures showed that there were no energy barriers for helium to cross the defects. The gas transport occurred in the Knudsen diffusion regime as the pores were larger than the kinetic diameter of the permeating gas

(260 pm). The contribution from the surface diffusion was found to be negligible as the helium molecules do not tend to be adsorbed. Despite the declared defect density (~ 9 × 10^{11} cm^{-2}) in nanoporous tungsten disulfide, the effective porosity calculated from the helium permeance was only 8 × 10^{-3} – 8 × 10^{-2} %. Furthermore, tears were found in spoiled samples even in a sub-micron free-standing area that implies a low mechanical stability of WS_2 on a large scale. The irradiation with focused beam of Ga^+ ions gave rise to the following pore size distribution: ~ 69 % of 1W, ~ 22 % of 2W and ~ 9 % of 3W vacancies.[16] Despite the fact that the selectivity of the 2D WS_2 membrane was not studied towards other gases, it can be assumed that the defects 2W and especially 3W at such a high concentration will reduce the overall selectivity bringing it closer to the values of the Knudsen diffusion.

In addition to the fundamental studies on the gas transport in free-standing 2D membranes, attempts have been done to prepare membranes for practical applications. Since 2D membranes on a micron scale are not suitable for an industrial use, graphene-based membranes were produced on a large scale. For the first time such centimeter-sized membrane was made by Boutilier et al. in 2017. Single-layer graphene was situated on an anodic aluminum oxide (AAO) with pores of 20 nm in diameter. Then graphene was perforated with gallium ions and treated with an oxygen plasma that leads to sub-nanometer-sized pores. The pore density and the pore size distribution were investigated on similarly processed graphene suspended on TEM grids. The STEM analysis showed that most of the “nanopores” were smaller than a helium atom, so the defect density of ~ 10^{11} cm^{-2} did not mean a high efficiency. Indeed, the effective porosity of a supported graphene membrane varied from 3 × 10^{-4} % to 1 × 10^{-3} %. The membrane performance for a H_2/CH_4 mixture was comparable to those of polymeric membranes because large defects and tears reduced the selectivity while the mesoporous substrate further impeded the gas flow.[19] On the one hand, the problem of a 2D membrane rupture on a centimeter scale can be solved with a size-selective interfacial polymerization. Recently Cheng et al. showed how a reaction between octa-ammonium polyhedral-oligomeric-silsesquioxane with trimesoyl chloride resulted in the sealing of defects and pores up to 0.5 nm in nanoporous graphene. On the other hand, most gas molecules have characteristic sizes below 500 pm and the problem of making selective pores remains.[49]

In 2018 Choi et al. presented a bottom-up method for producing perforated single-layer graphene on a centimeter scale. The growth of graphene during chemical vapor deposition (CVD) was locally inhibited by tungsten islands on the catalytic copper substrate which led to the formation of pores in the place of the islands. The mean pore size estimated by SEM varied from 19.4 ± 7.7 to 54.1 ± 20.3 nm depending on the preparation conditions in both methods. Three layers of perforated graphene were sequentially transferred to silicon nitride wafer with 64 orifices of 4 μm in diameter for gas permeation measurements. In addition to effusion, a viscous flow took place that was expressed in a selectivity below Knudsen one.[20] Despite large pores, the effective porosity estimated by the hydrogen permeance was ~ 0.2 %.

Graphene-based membranes with an area of 1 mm^2 were developed by Huang et al. in 2018. Since large scale 2D membranes require special transfer procedure to prevent tearing and cracking, graphene was reinforced with a mesoporous carbon film. Single-layer graphene was spin coated with a block copolymer followed by an annealing in a reducing atmosphere. The carbon film with pores of 20 – 30 nm in diameter was 100 nm-thick and should expose around half of the graphene surface. This membrane was transferred onto a tungsten foil with multiple orifices of 5 μm in diameter. The good adhesion between graphene and carbon scaffolds resulted in mainly intact 2D membranes that was confirmed by SEM – no tears and cracks were found. Sub-nanometer intrinsic defects in graphene were visualized by high resolution TEM (HRTEM), and the gas transport in such membranes was studied. Although the leak rates were low and close to the results reported by Koenig et al., the selectivity was significantly lower because of a wider pore size distribution. The permeance and the selectivity increased with the temperature rise in the measurements as an activated transport regime played a role. The effective porosity being about $3 \times 10^{-6} – 4 \times 10^{-5}$ % at room temperature became ~ $2 \times 10^{-5} – 3 \times 10^{-4}$ % at 150 °C while the H_2/CH_4 selectivity changed from 4.8 – 13.0 to 7.1 – 23.5 in graphene-based membranes.[21] Further, Zhao et al. continued the study of these graphene-based membranes in 2019. The etching with O_2 plasma led to a rise in the number of nonselective pores: the permeance increased while the selectivity decreased. In contrast, an ozone treatment tended to increase the number of selective pores. The graphene-based membranes after two cycles of ozone treatment showed somehow a better performance than the conventional membranes: $\Pi(H_2) \sim 1.0 \times 10^{-6} - 1.2 \times 10^{-6}$ mol·s^{-1}·m^{-2}·Pa^{-1} and $\alpha(H_2/CH_4) \sim 25 - 29$ at 150 °C. But the third cycle led to a drop in the selectivity to 7.5 – 12 with a slight increase in the permeance. The effective porosity calculated from the permeance was around $6 \times 10^{-4} - 8 \times 10^{-4}$ % despite the fact that the declared pore density was very high (~ 10^{12} cm^{-2}).[22] Approaching to the practical use, Lee et al. prepared a centimeter-sized graphene-based membrane in 2021. A mesoporous carbon film with graphene was additionally spin coated with 0.5 µm-thick multi-walled carbon nanotubes film. This intermediate layer allowed the composite membrane to be placed on a low-cost steel wire mesh for permeation measurements. The membrane with graphene after a short treatment with ozone showed a H_2 permeance equivalent to the porosity of 7×10^{-5} % and a H_2/CH_4 selectivity of 11.[23]

2.4.3 Intrinsically porous 2D materials

Aforementioned 2D membranes demonstrate a wide pore size distribution that prevents outstanding selectivity and does not appear to be monodisperse. The fabrication of nanopores in 2D materials is carried out using expensive equipment, and this process is complicated by the need to have pores in a very narrow range of sizes. In addition, a great permeation rate can be achieved only with high pore density, but perforated two-dimensional materials lose in mechanical stability compared to pristine ones. There are though other 2D materials that are intrinsically nanoporous. Inherently porous two-dimensional materials are of interest for studying the gas transport for a number of reasons. Firstly, there is no need to perforate them by complex approaches like the ultraviolet-induced oxidative etching, a plasma treatment, FIB or electron irradiation. Secondly, such materials represent a 2D membrane with a constant mechanical stability and physical properties because they do not undergo an additional processing. Thirdly, their pore size distributions tend to be narrow or even monodisperse that implies their characterization. Fourthly, inherently porous 2D materials tend to have a high areal pore density and integral porosity. Fifthly, some of these 2D membranes can be prepared on a large scale like graphene making them easier to work with. The next chapter is devoted to a detailed examination of the intrinsically porous 2D materials studied in this dissertation.

3 Materials

3.1 Carbon nanomembranes

3.1.1 Synthesis of carbon nanomembranes

The carbon nanomembrane (CNM) is an amorphous 2D material which is usually formed after the electron irradiation of a self-assembled monolayer (SAM). This carbon material with a thickness of the order of a nanometer can be obtained free-standing on a centimeter scale. CNM's properties can be customized by the precursor selection and synthesis conditions which allows one to obtain a functional 2D material. The reparation of CNMs can be presented in three steps: (i) formation of the SAMs, (ii) cross-linking via electron irradiation and (iii) transfer for a followed use.[50]

Self-assembly being the autonomous organization of components into ordered structures allows to obtain a monolayer of oriented molecules on the substrate.[51] A clean surface tends to physically adsorb various organic molecules from the environment decreasing the free energy of the interface that is not self-assembly. The formation of SAMs involves the chemical adsorption of the molecules with a special group which has an affinity for the substrate of interest. The amphiphilic molecules coming from the liquid or the gas phase anchor to the surface by a head group filling the monolayer. The surface of the solid should be flat and have a minimal roughness as well as a low concentration of defects for the best monolayer quality, although the self-assembly on nanoparticles is also possible. Self-assembly is completed when an equilibrium is established between the adsorbates and rest species – almost the entire surface is covered with oriented molecules in a dense packing. Several self-assembly systems are known: thiols (R-SH) on metals, silanes ($R\text{-}Si(O\text{-}C_nH_{2n+1})_3$ or $R\text{-}SiCl_3$) on silicon dioxide, thiols on III-V semiconductors, alkenes ($R\text{-}CH{=}CH_2$) on silicon. The thiolate ($R\text{-}S^{\delta-}$) monolayers can be assembled on gold (Au), silver (Ag), palladium (Pd), platinum (Pt), nickel (Ni), copper (Cu) and even mercury (Hg) surfaces.[52–54]

Thiolates on gold is the most studied system thanks to the ease of preparation in the liquid phase. Despite the high cost of gold, the substrate can be obtained in the form of thin films, and the inertness of the metal allows operation under atmospheric

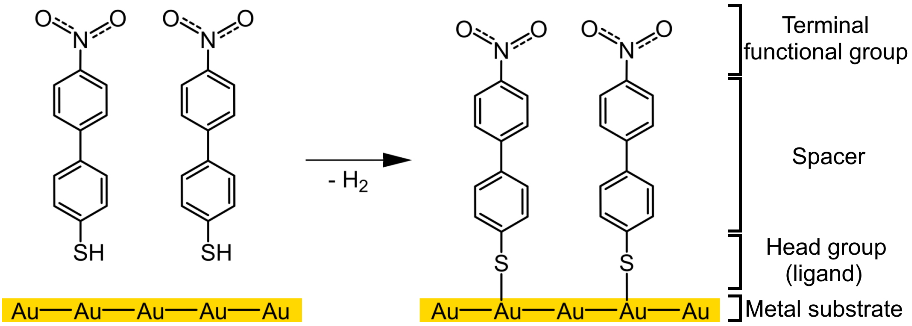

Figure 3.1 – Scheme for the formation of thiolate SAM on the gold surface in the form of chemical structures. 4'-nitro-1,1'-biphenyl-4-thiol (NBPT) is taken as an example of an amphiphilic molecule.

conditions. The S-H bond in thiols is able to dissociate and bind to the Au surface atom by a quite strong covalent Au-S bond with energy ~ 200 $kJ\cdot mol^{-1}$ while hydrogen leaves the interface irreversibly.[52,55] The formation of a thiolate SAM from thiols is shown schematically in Figure 3.1. The use of molecules with different terminal functional groups allows the preparation of a monolayer with adjustable properties of its surface. The thickness of the SAM can be defined by the length of the molecule and the angle to the surface. Like units of a solid, thiolates tend to form two-dimensional crystal phases on gold depending on the dimensions of the molecules. In addition to the covalent bonding with a substrate, chemisorbed molecules adopt conformations corresponding to maximum van der Waals interactions between each other that provides a secondary level of organization stabilizing the assembly. In this way, mainly the spacer defines the intrinsic properties of the SAM.[52] The study with X-ray photoelectron spectroscopy (XPS) and near edge X-ray absorption fine structure (NEXAFS) methods made clear that aromatic thiolates on gold demonstrate a smaller tilt angle of ~ 22° comparing to long-chain alkane thiolates (~ 30°). The increase of the number of phenyl rings in a row thiophenol (C_6H_5-SH) — 1,1'-biphenyl-4-thiol (C_6H_5-C_6H_4-SH, BPT) — 1,1',4'1''-terphenyl-4-thiol (C_6H_5-$(C_6H_4)_2$-SH, TPT) gains intermolecular interactions that leads to more rigid structure and less incline. Thiophenol molecules were poor oriented in monolayer because the only one phenyl ring was not enough for the lateral stabilization.[56] Typically, alkanethiolates in SAMs form a dense $(\sqrt{3} \times \sqrt{3})$ structure and one adsorbate is bonded with every third gold atom as known from a scanning tunneling microscopy (STM) study.[57,58] BPT molecules possess larger van der Waals dimensions that results in a less dense (2 × 2) structure of the SAM where one thiolate occupies 28.7 $Å^2$. The study of the SAMs using STM and low-energy electron diffraction (LEED) found that TPT having one more phenyl ring exhibits two equally dense phases with (√3 × √3) and (2√3 × √3) structures where one adsorbate occupies 21.6 Å^2 due to the larger intermolecular interactions.[58,59]

A dense coverage with thiolates is assembled on gold in seconds or minutes from millimolar solutions with thiols, but the reorganization process takes hours to reach the highest density of the SAM and minimize the defects. An elevated temperature is preferable for self-assembly because it promotes the reorganization and accelerates the desorption of non-target adsorbates. The suitable solvent should have weak solvent-adsorbate interactions to facilitate the diffusion of thiols from the liquid phase to the substrate. In addition, the solvent-substrate interactions should not be strong so that the solvent molecules do not interfere with the adsorption of the thiols on the substrate. Degassing the solvent with an inert gas improves the quality of the monolayer as it prevents the oxidation of thiol groups (-SH). Notably, thiol-based SAMs on gold demonstrate a better chemical stability towards oxygen comparing to other metals such as silver, copper and palladium. Oxidized molecules (organodisulfides, sulfonates, etc.) cannot be chemically adsorbed on gold, but these molecules take place on the metal surface by physisorption. The cleanness of the substrate, the purity of the reagent and the solvent are extrinsic factors for a defect formation and they can be mitigated. Moreover, the metal surface is replete with various structural defects even for a highly ordered (111) texture that becomes defects of SAMs after assembly. The intrinsic causes of defects include a complex phase behavior of dynamic SAMs as well as the relaxation of the gold surface due to the impact of thiolates resulting in areas with single-atom vacancies.[52]

Before free-standing carbon nanomembranes were obtained, there were researches about the irradiation of SAMs with low-energy electrons in the late 1990s. Predominantly, the phenomenon of cross-linked SAMs was studied as a negative resist in scope of nanolithography. The XPS method revealed a small decrease in the carbon and sulfur signals, while the NEXAFS spectroscopy confirmed the preservation of the aromatic structure in a BPT SAM after the irradiation with 50 eV energy electrons in dose of 10 mC·cm^{-2}. But infrared (IR) spectroscopy showed the disappearance of the vibrations along the phenyl rings and in hydrogens that witnessed an electron-induced C-H cleavage. The decrease in the etch rate of gold under irradiated SAM was associated with the cross-linking of the phenyl rings in different molecules with each other.[60] It was revealed that the exposure of NBPT SAMs to electrons leads not only to the formation of cross-linked and dehydrogenated structures on gold, but also to the reduction of a nitro group ($-NO_2$) to an amino group ($-NH_2$) by released hydrogen. As a result, irradiated areas became functionalized thin films that are suitable for further chemical immobilization.[61–63] Further, [1,1':4',1''-terphenyl]-4,4''-dimethanethiol ($HS-CH_2-(C_6H_4)_3-CH_2-SH$, TPDMT) was assembled on gold and exposed to 10 eV electrons in doses of 20 and 40 $mC\cdot cm^{-2}$. It was found by the NEXAFS spectroscopy that cross-linking occurred inhomogeneously and mainly the top of the SAM was affected by the low-energy electrons due to the dense packing.[64] Unlike aromatic thiolate monolayers, alkanethiolate SAMs after cross-linking exhibit a less dense material.[65,66] Electron-induced dissociations of C-H, C-C, C-S and Au-S bonds in molecules of hexadecanethiolate ($CH_3-(CH_2)_{15}-S^{\delta-}$, HDT) were found using the NEXAFS spectroscopy and XPS. Even irradiation with dose of 1 $mC\cdot cm^{-2}$ (~ 13 electrons per molecule) resulted in cleavage of ~ 40 % of Au-S bonds, formation of C=C bonds and decrease in thickness by a quarter.[65]

While graphene was discovered in 2004, ~ 1 nm-thick free-standing CNMs were first isolated in 2005 by Gölzhäuser and co-workers.[40,67] The monolayer was formed at room temperature for 5 days on 30 nm-thick silicon nitride (SiN_x) films after its hydroxylation by piranha solution (H_2SO_4/H_2O_2). The SiN_x film covered the silicon wafer with the windows of tens microns in dimensions. The assembly was carried out in a dry toluene solution with 10 mmol of the precursor shown in Figure 3.2a. The SAM was rinsed and subsequently irradiated with electrons using a flood gun with an acceleration voltage of 100 V. The irradiation dose by electrons with an energy of 100 eV was over 40 $mC\cdot cm^{-2}$. The underneath SiN_x film was etched with hydrofluoric acid (HF) for one hour and carefully rinsed by dipping it into water several times as shown schematically in Figure 3.2b. Since capillary forces could destroy such a thin membrane, only 30 – 50 % of the windows had a free-standing cross-linked SAM. Although considering the thickness of about 1 nm, the carbon membrane showed chemical and mechanical stability. The energy dispersive X-ray analysis (EDX) in the free-standing film (Figure 3.2c) revealed carbon, silicon and oxygen.[67]

The term “carbon nanomembrane” was introduced in 2010 when it was suggested as a support for biological specimens in the cryogenic TEM and AFM analysis. A CNM

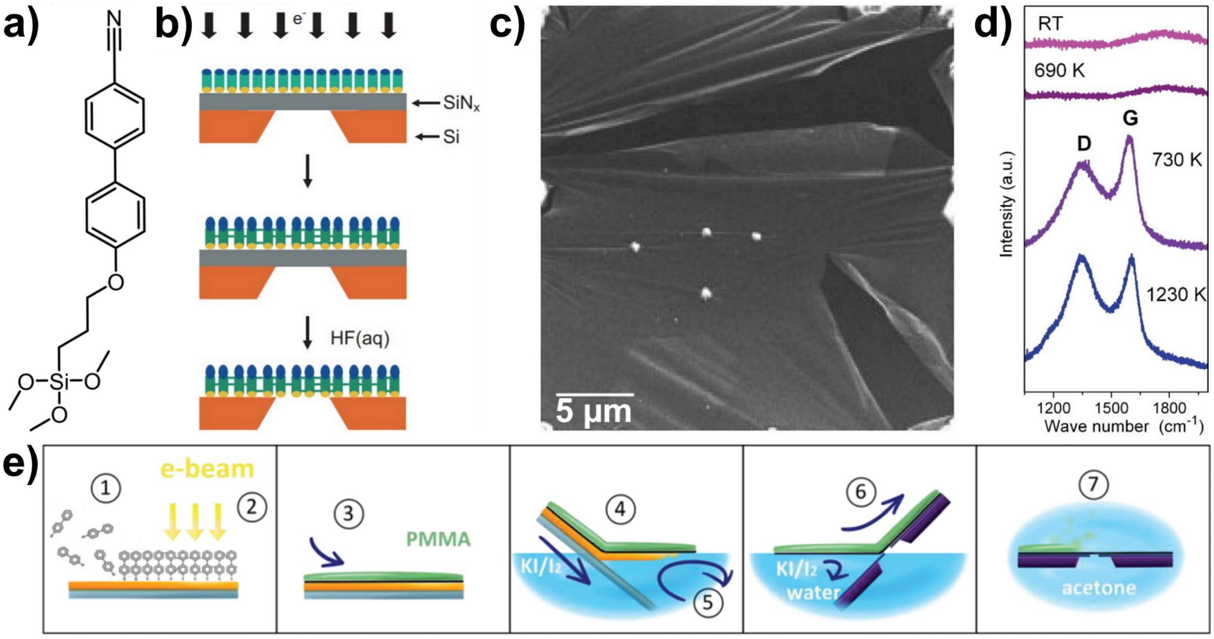

Figure 3.2 – Nature of the CNM and operation with it. **a)** Chemical structure of the precursor 4'-(3-(trimethoxysilyl)propoxy)-[1,1'-biphenyl]-4-carbonitrile. **b)** Scheme of the preparation process for the first CNM. **c)** SEM image of the first free-standing CNM with ruptures. **d)** Raman spectra of CNMs annealed in vacuum at various temperatures: room temperature, 690 K, 730 K and 1230 K. CNMs were transferred onto a silicon dioxide support. **e)** Schematic transfer procedure for BPT CNM. (1) Self-assembly on gold; (2) Electron irradiation; (3) Spin coating with protective PMMA layer; (4) Exfoliation of PMMA/CNM/Au sandwich from mica; (5) Etching of gold layer in I_2/KI solution followed by rinsing in pure water; (6) Fishing of PMMA/CNM film with substrate of interest. A Si_3N_4/Si chip is shown in the figure; (7) Dissolving of PMMA in acetone. The sample can be either pulled out from acetone or the acetone can be removed in a critical point dryer using CO_2. Parts **b)** and **c)** are reprinted and adapted with permission from Eck et al.[67],Copyright 2005 John Wiley and Sons. Part **d)** is reprinted and adapted with permission from Turchanin et al.[68], Copyright 2009 John Wiley and Sons. Part **e)** is reprinted and adapted with permission from Van Deursen et al.[69], Copyright 2019 Royal Society of Chemistry.

was declared to have no phase contrast in transmission electron microscopy.[70] The manufacturing of carbon nanomembranes based on BPT molecules is carried out according to the proven method shown schematically in Figure 3.2e.[59,68–70] The 300 nm-thick gold layer grown on mica is preliminarily cleaned in the UV/ozone cleaner. Polycrystalline gold films on quartz substrates can also be used instead of Au/mica substrates.[71] The gold surface is rinsed with ethanol, dried under a nitrogen flow and immersed into a millimolar solution of BPT molecules in anhydrous N,N-dimethylformamide (DMF). Self-assembly shown in the step (1) takes place at room temperature in an inert atmosphere for 3 days. The prepared SAM is rinsed with DMF, ethanol and dried under a nitrogen flow. In the case of other precursors for self-assembly, the method may vary. For instance, the best conditions for the self-assembly of a TPT monolayer in degassed DMF are the preparation time of 1 day and the temperature of 70 °C.[59] The cross-linking for a SAM depicted in the step (2) is implemented in high vacuum by an electron irradiation using a flood gun with an electron energy of 50 or 100 eV. The irradiation dose is calibrated and usually amounts to 50 $mC \cdot cm^{-2}$. To transfer a carbon nanomembrane to another substrate (TEM grids, oxidized silicon wafer, Si_3N_4 chip with an orifice, etc.), the CNM displayed in step (3) is spin coated with a solution of PMMA and backed on heat plate at 90 °C for the formation of a stabilizing layer hundreds of nanometers thick. The upper PMMA/CNM/Au sandwich was cleaved from the bulk mica substrate by etching in HF in the early papers.[68,70,72] Later, this toxic and inconvenient acid was excluded from the transfer procedure, and the edges of the gold layer were slightly etched in an I_2/KI aqueous solution for cleavage.[73] The upper PMMA/CNM/Au sandwich is detached from mica as shown in step (4), and the gold layer is completely dissolved in an iodine solution. Then the PMMA/CNM film is transferred onto a surface of pure water to rinse it from iodine and other ions in step (5). The transfer of the PMMA/CNM from the water surface onto the substrate of interest shown in step (6). The protective PMMA layer is removed by the immersion in acetone as depicted in step (7).[69]

It is known that the annealing of aromatic polymers in an inert atmosphere leads to their graphitization at temperatures above 1000 K.[74] In the view of this, the transformations of CNMs at high temperatures have been investigated. BPT CNMs were successfully transferred onto TEM grids with 130 × 130 μm square holes and onto a silicon dioxide substrate. The analysis via scanning Auger microscopy confirmed the presence of only carbon in the free-standing films. Raman spectroscopy revealed no vibrational modes in CNMs even after annealing at 690 K as can be seen in Figure 3.2d. Annealing at 730 K resulted in the appearance of D- and G-peaks (1350 cm^{-1}, 1592 cm^{-1}) in the Raman spectra which are characteristic for sp^2 carbon in its allotrope. Selected area electron diffraction (SAED) in the free-standing CNM after annealing at 1300 K revealed a crystal structure while the unannealed CNMs turned out to be amorphous. It was noted that the higher the annealing temperature, the more intense the D- and G-peaks in Raman spectrum and the higher the electrical conductivity of the samples are.[68] Unlike untreated CNMs, a local charging in the TEM images was not found for CNMs that were annealed at 1200 K.[70] Then, HR-TEM, Raman spectroscopy and electrical measurements confirmed the transformation of a BPT CNM into in-plane oriented nanocrystalline graphene on the catalytically inert substrates (gold, silicon dioxide) at high temperatures. No difference was found between the annealing in vacuum and in an inert atmosphere (Ar/H_2). Predominantly single-layer graphene domains with a lateral size of 2 – 5 nm alternated with less ordered regions of amorphous carbon.[72,73]

To study the conversion of carbon nanomembranes on a catalytically active substrate, CNMs were prepared in an ultra-high vacuum (UHV) chamber on a copper surface by Matei et al. A Cu(111) single crystal and a Cu polycrystalline foil were annealed and sputtered with Ar^+ ions 5 – 6 times. Then BPT molecules were evaporated into the chamber at 50 – 60 °C for 1 – 2 hours giving a pressure of ~ 10^{-7} mbar. Assembled at room temperature the BPT SAM on a copper substrate was cross-linked by 50 eV electrons with dose of 50 $mC \cdot cm^{-2}$. Afterwards, the CNMs were annealed in vacuum at 970 – 1100 K that led to the formation of single-layer microcrystalline graphene with mean domain sizes of ~ 300 nm. According to the Raman spectra, the conversion was completed at the highest annealing temperature.[75]

The cross-linking process for a BPT SAM was studied in details by Turchanin et al. An XPS study confirmed a little decrease (~ 10 %) in the quantity of carbon (C1s) and a significant decrease in the sulfur signal (S2p) after the electron irradiation. Besides thiolates, another oxidation state for sulfur was found according in CNMs. The new component can be associated with organosulfides (R-S-R) or organodisulfides (R-S-S-R) as well as with thiolate-dimers (R-S-Au-S-R) on a gold ad-atom. An oxygen signal (O1s) was not detected. The effective thickness of CNMs was estimated from the XP spectra assuming an exponential attenuation of the gold photoelectron signal ($Au4f_{7/2}$) under the carbon nanomembrane. A thickness of ~ 1 nm for the BPT CNM was in agreement with AFM measurements.[71,76] The NEXAFS spectra showed intensity changes after cross-linking: a reduction for π^* resonance and a rise for σ^* resonance that indicates a loss of aromaticity and growth the number of aliphatic bonds C-C. It was ascribed either to the binding of adjacent molecules to each other or to a partial decomposition of the molecules. The formation of double bonds C=C was excluded because of an absence of a new resonance. Angular measurements of the resonance intensities revealed an increase of the mean molecular tilt from 31° for the SAM to 41° for the CNM. UV photoelectron spectroscopy (UPS) was applied to study the molecular orbital energies in SAMs and CNMs compared to quantum-chemical calculations for the supposed cross-linked species. The photoelectron spectrum after cross-linking was comparable to the electronic excitations in BPT dimers where the molecules are linked to each other by four C-C bonds. Thermal desorption spectroscopy (TDS) revealed the desorption of entire BPT molecules and biphenyl fragments at ~ 400 K for the SAM. In general, the thermal desorption in the CNM released much fewer species that is consistent with the low carbon loss according to XPS. The desorption of non-crosslinked BPT molecules and biphenyl fragments was observed at a lower temperature (330 K) due to absence of an intermolecular stabilization. At higher temperatures (400 – 700 K) the CNM released phenyl, biphenyl and partially cross-linked biphenylene units. The sulfide on gold was desorbed at temperatures above 700 K. An irradiation dose around 50 $mC\cdot cm^{-2}$ (~ 3000 electrons per 1 nm^2) was enough for a maximum degree of cross-linking where 90 % of the BPT molecules are involved. A full cross-linking was found to be unachieved due to the dense molecular packing in SAM. A high irradiation dose (100 $mC\cdot cm^{-2}$) did not improve the thermal stability of CNM. The dissociative electron attachment (DEA) was supposed to be main process in the cross-linking of a SAM. Briefly, a molecule (AB) captures a low-energy electron (e^-) forming a transition negative ion (AB^-). Time evolution leads to bond splitting in the transition negative ion resulting in two particles: a neutral fragment (A) and an anion (B^-). The DEA process can be presented in the followed scheme:

$$AB + e^- \rightarrow AB^- \rightarrow A + B^-. \tag{3.1}$$

Moreover, it was noted that secondary electrons emitted from the gold also contribute in the cross-linking as well as primary electrons from the flood gun.[71,77] Schnietz et al. showed that a NBPT SAM could be crosslinked under extreme ultraviolet light (13.5 nm, 92.5 eV) primarily due to secondary electrons excited from the metal rather than photons. In turn, the cross-linking process led to similar mechanically stable NBPT CNMs. UV nanolithography allowed the bottom-up preparation of a mesoporous CNM with adjusted pore diameters from 31 to 138 nm. A dark-field TEM image of a free-standing NBPT CNM with pores of 31 ± 6 nm in size is presented in Figure 3.4a.[71,78,79]

Later, Zhang et al. reported about the successful formation of CNMs after irradiation with 35 keV helium ions. Although helium ions can result in a bond cleavage, the total scattering cross-section in SAMs is very small compared to low-energy electrons. The secondary electron yields for a gold surface were calculated for 100 eV electrons and for 35 keV He^+ ions that amounted to 0.85 and 2.7, correspondingly. Besides the larger number of emitted electrons for a helium ion, the secondary electrons have an average energy of ~ 2 eV while the primary 100 eV electrons excite the secondary electrons with an average energy of ~ 5 eV. Since the DEA process occurs more frequently with electrons of lower energies, cross-linking is more efficient for 2 eV secondary electrons. The DEA process is supposed to be endothermic because the electron affinity of BPT (0.03 – 0.07 eV) is significantly lower than the C-H bond energy (~ 4.46 eV). It was shown that the cross-linking process can be presented in three stages. At the first stage, the formation of nuclei takes place that corresponds to 6 – 10 % of the cross-linked area. At the second stage, an 1D growth begins at the ion dose of ~ 0.2 $mC\cdot cm^{-2}$ where the fraction of the crosslinked surface grows weakly and the phenyl rings are mainly crosslinked perpendicular to the gold surface. At the third stage over 35 % of the area is crosslinked at a dose of ~ 0.48 $mC\cdot cm^{-2}$ and a 2D growth of the crosslinked regions along the surface begins. The complete cross-linking of a NBPT SAM was reached at the ion dose of ~ 0.85 $mC\cdot cm^{-2}$ that is sixty times lower than the standard dose for low-energy electrons. The irradiation dose of He^+ over 4 $mC\cdot cm^{-2}$ led to swelling of the gold substrate and damage for the CNMs due to ions implantations in a solid phase.[80]

Afterwards, the structural changes in aromatic SAMs after electron cross-linking were monitored by surface-enhanced Raman spectroscopy (SERS). The 80 nm-sized gold nanoparticles were deposited by drop casting of the suspension on the surface of a SAM or a CNM for the enhancement of signal via plasmons. The fraction of Raman-inactive region increased drastically with an increase of the irradiation dose from 5 to 60 $mC\cdot cm^{-2}$ while ~ 90 % of the area was cross-linked at 20 $mC\cdot cm^{-2}$. It was shown that carbon nanomembranes do not appear to have Raman modes with the exception of a very broad D-peak at 1360 cm^{-1}. The D-peak was attributed to vibrations of carbon rings where sp^2-hybridized carbon is preserved. The modes from sp^3 carbon are most likely below the detection limit because their Raman scattering cross sections are several times lower than for the sp^2 hybridization.[81]

Although the formation of “graphene-like” nanoflakes after the electron irradiation of a BPT SAM on gold was predicted by DFT calculations, there was no experimental confirmation for this hypothesis.[82] Classical molecular dynamics investigations showed that a metastable irregular structure could be formed upon the electron irradiation of a BPT SAM reaching a local energy minimum.[83] Carbon nanomembranes could be compared rather with monolayer amorphous carbon (MAC) as both materials are amorphous and demonstrate low electrical conductivities, but an analysis via Raman spectroscopy reveals a dissimilarity. On the one hand, MAC consisting of five-, six-, seven- and eight-member carbon rings in plane has no Raman vibrational mode at ~ 2680 cm^{-1} which corresponds to the long-range order in microcrystalline graphene. On the other hand, the Raman spectrum of MAC has pronounced D- and G-peaks that, in the case of CNMs, appear only after the transformation into nanocrystalline graphene upon annealing above 730 K.[68,84] Eventually, the inner structure of carbon nanomembranes remains poorly understood.

Free-standing CNMs were prepared from various thiol precursors on a gold surface by Angelova et al. The synthesis schemes are presented in Figure 3.3a – 3.3c for different groups of precursors displayed in Figure 3.3d. The first group consisted of linear oligophenyl thiols such as BPT, BP3 (3-(biphenyl-4-yl)propane-1-thiol) and TPT. Their structures provided a better lateral stabilization in SAMs. The second group contained more rigid mercapto derivatives of naphthalene (NPTH), anthracene (ANTH) and pyrene (1MP, MP1, MP3, MP5) that ensured a higher carbon density in the monolayers. The third group was consisted of bulky molecules: a hexaphenylbenzene derivative (HPB) and two derivatives of disc-type hexa-peri-hexabenzocoronene (HBC). All monolayers were assembled in degassed solvents on a clean Au(111)/mica substrate under an inert atmosphere. The immersion time (1 or 3 days), temperature (without heating or 70 °C), concentration of the thiol and solvent (DMF, ethanol or dichloromethane) were selected individually for each compound. Thiols groups in the pyrene derivatives as well as in the compounds from the third group were previously protected by the formation of ethanethioate ($R\text{-}S\text{-}C(O)\text{-}CH_3$) that required the addition of a small amount of $NH_3{\cdot}H_2O$ before the self-assembly began. After the completion of the SAM formation in stage (i), the samples were rinsed with suitable solvents and dried in a nitrogen flow. Cross-linking of SAMs was performed with 50 eV and 100 eV electrons in a dose of ~ 60 $mC{\cdot}cm^{-2}$ in stage (ii). Afterwards, each CNM was spin

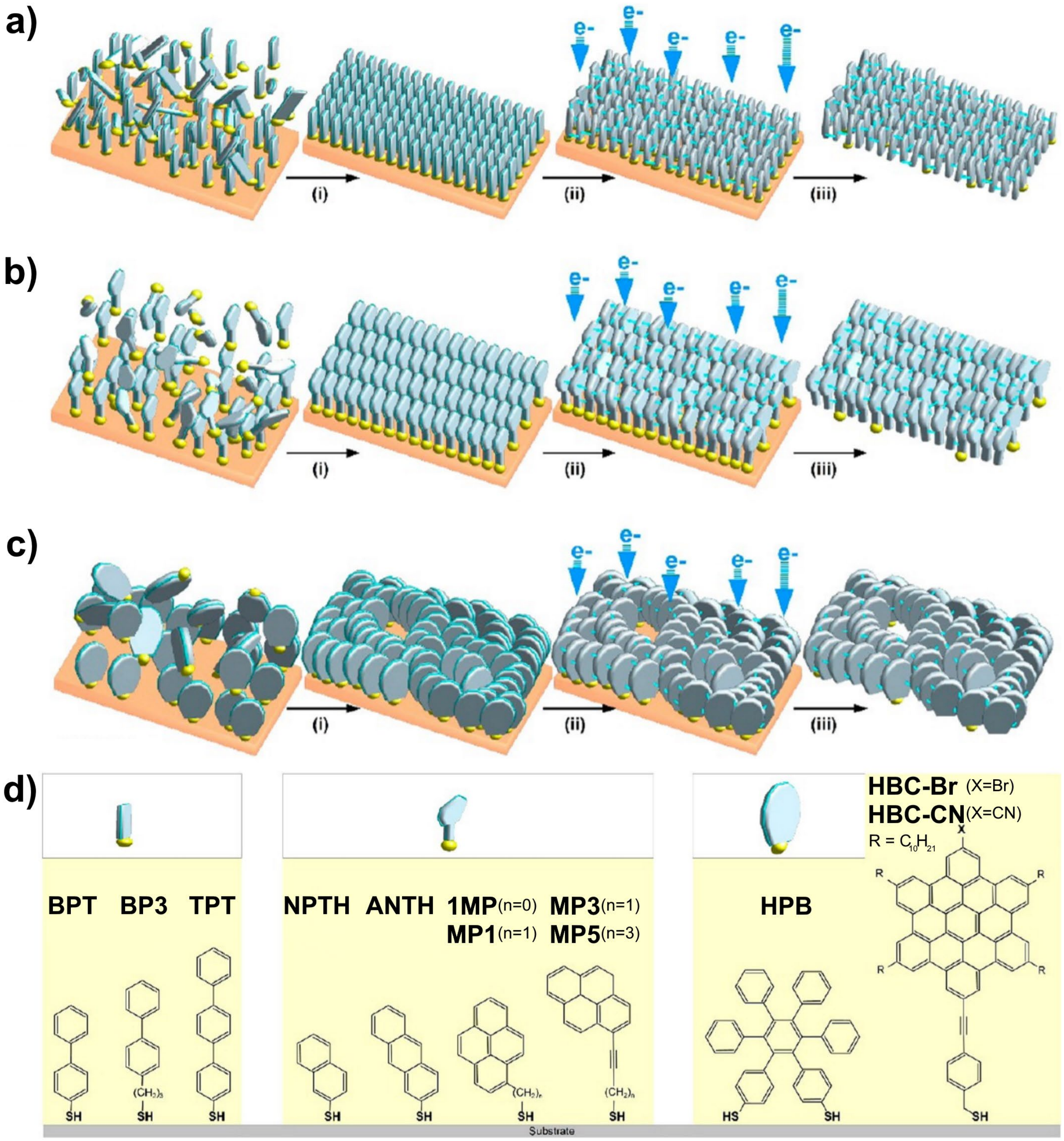

Figure 3.3 – Scheme of CNM preparation on gold from various precursors: (i) self-assembly of a monolayer; (ii) cross-linking by low-energy electrons; (iii) transfer to an arbitrary support. **a)** Fabrication of thin CNMs from linear oligophenyl precursors: BPT, BP3, TPT. **b)** Fabrication of thicker CNMs from condensed polycyclic precursors: NPTH, ANTH, 1MP, MP1, MP3, MP5. **c)** Fabrication of thick CNMs from bulky precursors: HPB, HBC-Br, HBC-CN. **d)** Chemical structures of the mentioned precursors. **Figure 3.3** is reprinted and adapted with permission from Angelova et al.[59], Copyright 2013 American Chemical Society.

coated with a PMMA layer, then the gold was etched in an I_2/KI aqueous solution and the PMMA/CNM film was transferred onto TEM grids. The protective PMMA film was dissolved in acetone which was removed in a critical point dryer with carbon dioxide leaving the free-standing CNM intact in stage (iii). Besides the mentioned compounds, self-assembly on gold was performed with pyridine-4-thiol molecules in an alkaline aqueous solution.[59]

The XPS study proved that all compounds formed SAMs with Au-S bonds, but for the HBC derivatives there was found unbounded with surface sulfur groups which witnessed about physisorbed molecules on thiolate adsorbates and low ordering. The STM and LEED methods showed that the SAMs prepared from BP3, NPTH, ANTH, 1MP and MP3 molecules form two phases with ($\sqrt{3} \times \sqrt{3}$) and ($2\sqrt{3} \times \sqrt{3}$) structures similar to a TPT SAM. The polycyclic bulky molecules from the third group (HPB, HBC-Br, HBC-CN) as well as MP1, MP5 and pyridine-4-thiol did not form any ordered structures on the gold surface. Moreover, the SAM based on pyridine-4-thiol was not converted into a carbon nanomembrane. The loss of carbon after the electron irradiation was proved by the XPS analysis and amounted to 2 – 16 %. The largest decrease in the carbon signal was observed for compounds with aliphatic backbones that is concerned with the behavior of alkanethiols under electron irradiation. Micrographs with free-standing CNMs taken by helium ion microscopy (HIM) in the secondary electron mode are presented in Figure 3.4b – 3.4j. All CNMs appearing as translucent films exhibited impressive mechanical stability on a large scale as shown in Figure 3.4d with a field of view of 300 × 300 μm. The effective thicknesses of CNMs were calculated from the XPS measurements. These values are shown in the lower insets in Figures 3.4b – 3.4h. It was found that the thickness of a CNM is determined by the length of the precursor and the packing density of its SAMs. Thus, the self-assembly and cross-linking with short NPTH molecules resulted in a 0.6 nm-thick CNM, while the bulky molecule (HBC-CN) led to a 2.2 nm-thick carbon nanomembrane. High magnification HIM revealed the CNMs based on densely packed SAMs to be defect-free and homogeneous (Figure 3.4h). On the contrary, the CNMs prepared from low-ordered SAMs from the third group were nanoporous. Dense arrangements of defects that look like black stains can be seen in Figures 3.4i and 3.4j. The mean pore size of ~ 6.0 nm and the pore density of 9.1×10^{10} cm^{-2} were estimated for HBC-based CNMs while for HPB CNMs the values were ~ 2.4 nm and 1.3×10^{11} cm^{-2}, correspondingly. It was proved that SAMs need to be stable scaffolds for the successful conversion into CNMs, and their structures should be rigid enough to withstand the electron irradiation. The density of carbon atoms in the original monolayer must be high enough to form a

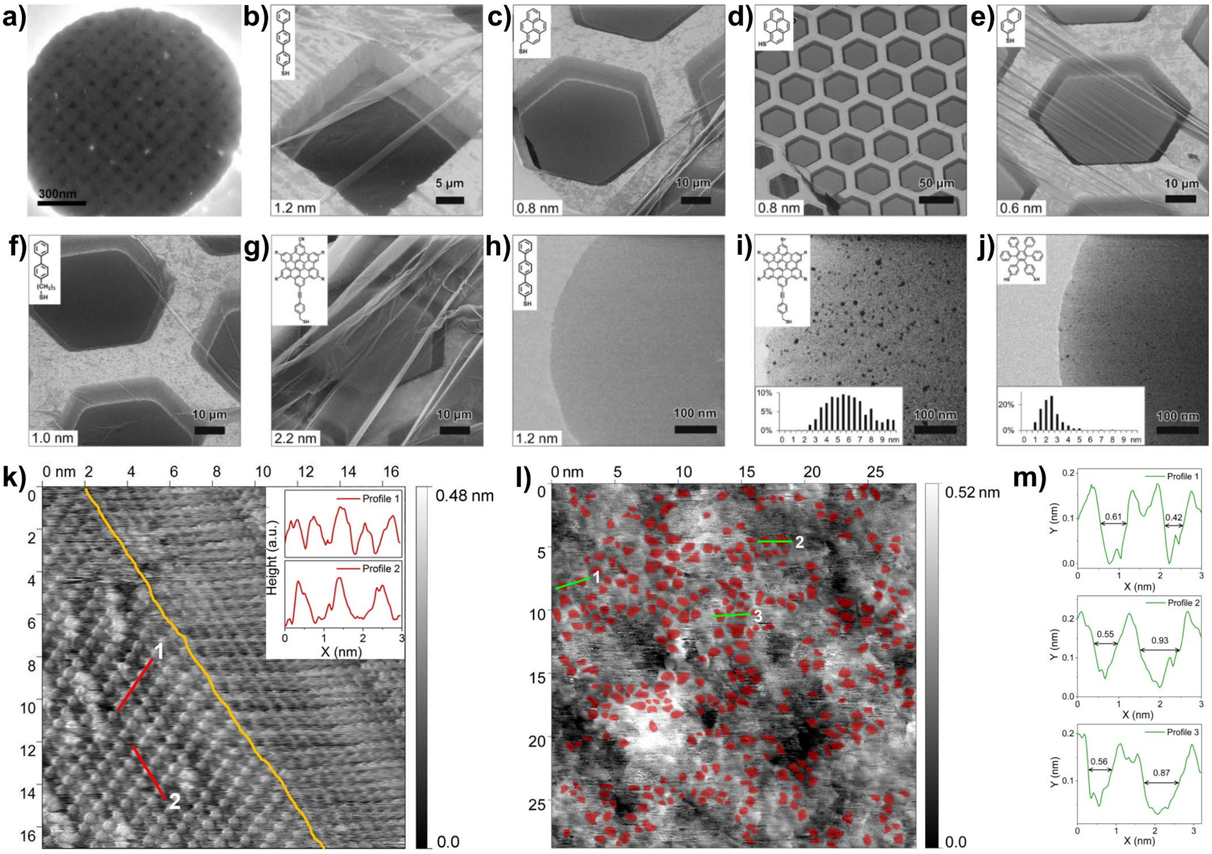

Figure 3.4 – Microscopic images of the free-standing CNMs (TEM, HIM) as well as a SAM and a CNM on gold (STM, AFM). **a)** Dark-field TEM image of a nanoporous NBPT CNM with pores of 31 ± 6 nm in size. **b)** HIM image of a TPT CNM. **c)** HIM image of a MP1 CNM. **d)** HIM image of a 1MP CNM. **e)** HIM image of a NPTH CNM. **f)** HIM image of a BP3 CNM. **g)** HIM image of an HBC-CN CNM. **h)** HIM image of a TPT CNM (higher magnification). **i)** HIM image of an HBC-Br CNM (higher magnification). The pore size distribution is presented as lower inset. **j)** HIM image of an HPB CNM (higher magnification). The pore size distribution is presented as lower inset. **k)** STM image of a TPT SAM on gold measured at room temperature in UHV. The yellow line indicates domain boundary. The line profiles are presented in insets. **l)** AFM image of a TPT CNM measured at 93 K in UHV. Expected pores of sub-nanometer size are marked in red. **m)** The line profiles of marked green lines in AFM image. All HIM images represented in parts **b)** – **j)** have insets with the chemical structures of the precursors. Thicknesses of the CNMs determined by the XPS method are presented as insets in parts **b)** – **h)**. Part **a)** is reprinted and adapted with permission from Schnietz et al.[78], Copyright 2009 John Wiley and Sons. Parts **b)** – **j)** are reprinted and adapted with permission from Angelova et al.[59], Copyright 2013 American Chemical Society. Parts **k)** – **m)** are reprinted and adapted with permission from Yang et al.[85], Copyright 2018 American Chemical Society.

crosslinked network, and the molecules in SAMs should have at least two phenyl rings in a direction perpendicular to the substrate for the conversion to a carbon nanomembrane. All prepared CNMs were annealed in an UHV chamber at 1170 K for 30 minutes to convert them into graphene. The second group having a higher density of carbon atoms gave thicker nanocrystalline graphene sheets than the first group with oligophenyls. In the case of pyrolyzed CNMs based on a bulky molecule (HPB), half of the area was single-layer graphene the rest was represented by double-layer graphene, amorphous carbon and defects.[59]

The morphology of a carbon nanomembrane was explored with STM and AFM methods by Yang et al. Two domains of a highly-oriented TPT SAM on gold can be distinguished in the STM image in Figure 3.4k where the yellow line marks domain boundary. The line profiles presented in the inset in Figure 3.4k demonstrate the distinct periodicity along the two crystallographic directions of the adsorbate structure: 0.58 ± 0.01 nm for line 1 and 1.03 ± 0.02 nm for line 2. The molecules in the monolayer underwent a serious reorganization losing their order after the irradiation with 50 eV electrons at a dose of 50 $mC \cdot cm^{-2}$ as can be seen from the AFM image in Figure 3.4l. Densely located depressions of varying width can be observed from the line profiles in Figure 3.4m. The depressions were addressed to pores and marked with red in the AFM image (Figure 3.4l). The mean pore density was estimated to be $\sim 6 \times 10^{13}$ cm^{-2}. The width of the expected pores in a TPT CNM varied from 0.4 to 1.1 nm (~ 0.7 nm on the average).[85]

Neumann et al. reported about new inert all-carbonaceous CNMs prepared on the silver substrate, while conventional thiolate-based CNMs have sulfide/disulfide groups after the transfer procedure. The two precursors with the same backbones but with distinct head groups were chosen for comparison: 2-(4'-methyl-[1,1'-biphenyl]-4-yl)ethane-1-thiol (CH_3-$(C_6H_4)_2$-$(CH_2)_2$-SH) marked as BP2SH and 3-(4'-methyl-[1,1'-biphenyl]-4-yl)propanoic acid (CH_3-$(C_6H_4)_2$-$(CH_2)_2$-COOH) marked as BP2COOH. Both molecules form identical structures on the Ag(111) surface but with a thiolate-metal bond (R-S-Ag) and with a bidentate carboxylate-metal bond (R-CO_2Ag), correspondingly. The SAMs were prepared on freshly evaporated 100 nm-thick Ag(111) on mica in a millimolar absolute ethanol solution with the compound. The self-assembly took 5 minutes for the carboxylate monolayer and 1 day for the thiolate SAM. Then the SAMs were rinsed with ethanol and dried in a nitrogen flow. The cross-linking was done with 50 eV electrons at various doses in the UHV. The CNMs were transferred via the PMMA-assisted protocol, but the detachment of the CNMs from the silver surface was performed by the electrochemical delamination in a NaOH aqueous solution. Then the PMMA/CNM films were transferred onto TEM grids or a silicon dioxide substrate followed by the dissolving of the PMMA in acetone and rinsing with isopropanol. The XPS analysis of BP2COO/Ag SAM revealed the partial elimination of the carboxylate group and formation of intermediate oxygen groups C-O/C=O in the structure at a low irradiation dose. The high electron dose of 150 mC·cm^{-2} led to complete vanishing of the oxygen groups for carboxylate-based SAMs, but the thiolate-based CNMs still had sulfur groups. The electron irradiation resulted in a carbon loss of ~ 5 % for the BP2S/Ag SAM and ~ 28 % for the BP2COO/Ag SAM. In turn, such large carbon loss led to a nanoporous CNM with pores below 50 nm in size that was confirmed by a SEM analysis. It was shown that the use of a precursor with a longer alkyl spacer compensates for carbon losses and better stabilizes the monolayer laterally. The SAM of 6-(4'-methyl-[1,1'-biphenyl]-4-yl)hexane-1-thiol (CH_3-$(C_6H_4)_2$-$(CH_2)_6$-SH, BP6COOH) being irradiated resulted in non-porous CNMs, as for the thiolate precursor BP2SH.[86]

Dalpke prepared carbon nanomembranes from alkanethiols. The followed substances were used as precursors: 1-dodecanethiol (CH_3-$(CH_2)_{10}$-CH_2-SH, DDT), 1-tetradecanethiol (CH_3-$(CH_2)_{12}$-CH_2-SH, TDT), 1-hexadecanethiol (CH_3-$(CH_2)_{14}$-CH_2-SH, HDT), 1-octadecanethiol (CH_3-$(CH_2)_{16}$-CH_2-SH, ODT) and 1-docosanethiol (CH_3-$(CH_2)_{20}$-CH_2-SH, DST). The alkanethiolate monolayers were assembled on clean Au/mica substrates in 1 mM ethanol solutions with the precursors followed by electron irradiation with a dose of 50 mC·cm^{-2}. Most of the sp^3 carbon in the SAMs was partially converted to sp^2 carbon after the electron cross-linking. The loss of carbon was more pronounced for the shorter adsorbates (DDT, TDT) compared to the longer molecules (HDT, ODT, DST) that lost about half of their carbon. DDT CNMs were shown to be unstable for the transfer procedure, while the fragile and porous CNMs based on TDT and HDT precursors were found to be free-standing on TEM grids. The sufficiently stable CNMs were obtained on the basis of ODT and DST molecules.[66]

3.1.2 Properties of carbon nanomembranes

Since CNMs demonstrated a good mechanical stability, their mechanical properties were studied using the bulge test on a pressure cell.[68,87,88] The nanomembranes were suspended over holes in a silicon wafer. The silicon wafer was mounted in a sealed pressure cell as shown in Figure 3.5a. Polydimethylsiloxane (PDMS) was used for the gas-tight sealing. The position of a nanomembrane was identified by the AFM tip. Figure 3.5b presents an AFM image with the profile of a free-standing CNM without an applied pressure difference. The AFM image of a CNM with the profile at an applied pressure difference of 750 Pa is displayed in Figure 3.5c. The Young's modulus E (Pa) and the residual stress σ_0 (Pa) for 2D materials were extracted from the experimental data using the equation:

$$p = \frac{c_1 \times \sigma_0 \times t}{a^2} \times h + \frac{c_2 \times E \times t}{(1 - \nu) \times a^4} \times h^3, \tag{3.2}$$

where p is the applied pressure (Pa), c_1 is the coefficient dependent on the aspect ratio for the nanomembrane, t is the nanomembrane thickness (m), a is the half-width of the short edge in nanomembrane (m), h is the deflection of a nanomembrane center (m), c_2 is the coefficient dependent on the Poisson ratio, ν is the Poisson's ratio. It was shown that the Young's moduli values grew with an increase in the irradiation dose from 30 to 50 $\text{mC}\cdot\text{cm}^{-2}$ that corresponded to an increase in the degree of cross-linking. In turn, the stiffness remained nearly constant for fully crosslinked CNMs at the irradiation dose of 50 – 80 $\text{mC}\cdot\text{cm}^{-2}$.[87] The mechanical properties of CNMs depending on their precursors were estimated by Zhang et al.[88] The compounds such as BPT, TPT, NPTH, HPB, HBC-Br as well as pyrene-2-thiol (2MP) were considered in the experiments. Bulge tests were performed with a positive pressure difference (deflection up) of ~ 100 kPa and a negative pressure difference (deflection down) of ~ 125 kPa to minimize the possible influence from detachment. The deflection-pressure curves as well as stress-strain curves demonstrated a hysteresis that could be assigned to the

viscoelastic deformation.[88] Creep deformations in the CNMs were found to partially recover after each test cycle.[87] It was noted that the increase in molecules rigidity leads to the gain in the macroscopic stiffness. The condensed aromatic molecules (NPTH, 2MP) are more rigid than the oligophenyl ones (BPT, TPT) that affects the mechanical properties of a nanomembrane. The NPTH CNM had the largest Young's modulus as can be seen from Figure 3.5d because of the dense ordered structures in the SAMs, the high molecular rigidity and the highest density of carbon atoms in monolayer. The poor structural order in the 2MP SAM and the lower carbon density resulted in a lower

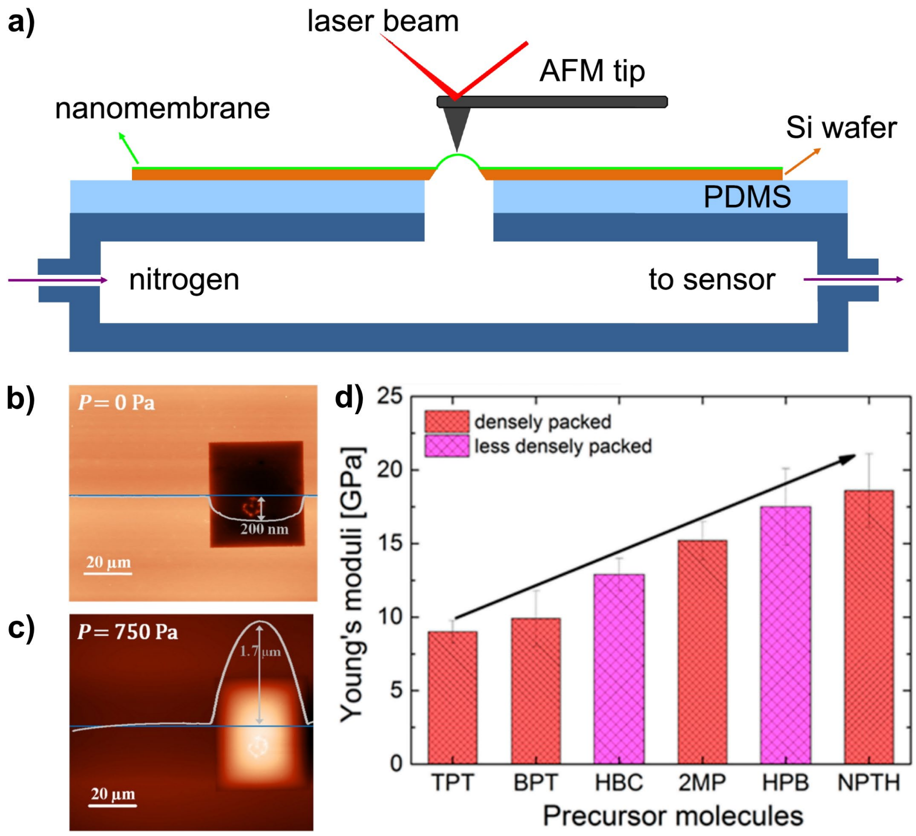

Figure 3.5 – Investigation of the mechanical properties in CNMs. **a)** Schematic diagram of a bulge test in a nanomembrane. **b)** AFM image with the profile of a free-standing CNM sagging down by ~ 0.2 µm without an applied pressure difference. **c)** AFM image with the profile at an applied pressure difference of 750 Pa that induced bulging up at ~ 1.7 µm. **d)** The Young's moduli of CNMs made from different precursors. Parts **a)** – **c)** are reprinted and adapted from the open access article[87], Copyright 2011 Creative Commons Attribution License. Part **d)** is reprinted and adapted with permission from Zhang et al.[88], Copyright 2014 American Chemical Society.

Young's modulus for the 2MP CNM compared to the NPTH CNMs. The smallest Young's modulus for a TPT CNM was explained by the lower degree of cross-linking due to dense packing of the TPT SAM. The bulky molecules (HPB, HBC-Br) formed low-ordered SAMs and become a nanoporous CNM after cross-linking. The HPB CNM being less porous exhibited a higher stiffness than the HBC-Br CNM with a larger porosity.[88] The Young's modulus of an ODT CNM was found to be around 0.6 GPa because the alkanethiolate SAMs has a lower density of carbon atoms than aromatic monolayer.[66] Turchanin et al. reported that the free-standing BPT CNM being annealed at ~1000 K exhibited the Young's modulus of 48 GPa which was consisted with the high stiffness of nanocrystalline graphene.[68]

The first gas permeation study in CNMs was performed by Ai et al. in 2014. The CNMs based on CBPS, BPT and NBPT molecules were transferred onto porous PDMS supports and then inserted into the constant volume experimental setup. The measurements were carried out four times in the one-layer CNMs and three-layer stacked CNMs in a millimeter scale at a feed pressure of 108 – 280 mbar. The AFM analysis confirmed a good adhesion between the CNM and the polymeric support and revealed a decrease in the surface roughness for the three-layer CNMs (3.1 nm) compared to one layer (5.5 nm) of a carbon nanomembrane. One-layer CNMs placed on PDMS led to a 20 – 60 % permeance reduction compared to bare PDMS. Three-layer CNMs exhibited permeation rates approximately three-fold lower than the one-layer CNM because the stacking of CNMs overlaid large defects in the nanomembranes. The He/N_2 selectivity was 4.1 for one CNM/PDMS and 11.4 for three CNMs/PDMS. The permeation rate in an ideal composite membrane was considered similar to the electrical conductance in a series circuit:

$$\Pi_{composite} = \frac{1}{\Pi_{2D}} + \frac{1}{\Pi_{support}}, \tag{3.3}$$

where $\Pi_{composite}$ is the total permeance for the composite membrane, Π_{2D} is the permeance for the 2D membrane, $\Pi_{support.}$ is the permeance for the bulk porous support. In fact, HIM analysis revealed micron-sized defects in the CNMs laying on PDMS. The areal fraction of defects (bare support) was estimated by microscopy to extract the permeation rates Π_{2D} in CNMs from the total permeance in the composite membrane. The gas permeation rates in isolated CNMs are presented in Figure 3.6a. The processes of permeation were found to be identical in BPT CNMs and in NBPT CNMs. Three-layer stacked CNMs demonstrated low permeances for all gases except small helium and hydrogen molecules that was attributed to a molecular sieve-like behavior. Carbon dioxide passed through a one-layer CNM at a rate comparable to the permeances of He and H_2. It was explained by the existence of channels with dimensions close to the sizes of He, H_2 and CO_2 species. These channels cannot spatially match for three stacked carbon nanomembranes that led to the substantially lower permeation rates for CO_2 in three-layer CNMs.[89]

Yang et al. studied the permeation of water vapor in the free-standing TPT CNMs using two measurement methods in 2018. Carbon nanomembranes were transferred onto the Si_3N_4/Si chip with a single orifice 18 µm in diameter (500 nm-thick silicon nitride film grown on a 200 µm-thick silicon wafer with a window). The CNM/Si_3N_4/Si was glued onto a stainless-steel container with water in the mass-loss method as schematically presented in the left inset in Figure 3.6b. The HIM image of the free-standing CNMs is demonstrated in Figure 3.6c. The vessel was put on the high-precision microbalance in a low-humid environment, and the permeance Π ($mol \cdot m^{-2} \cdot s^{-1} \cdot Pa^{-1}$) of the vapor was determined by changing its mass Δm (g):

$$\Pi = \frac{\Delta m}{M \times A \times t \times \Delta p}, \tag{3.4}$$

where M is the molecular mass of the studied compound ($g \cdot mol^{-1}$), t is the time interval for experiment (s), A is the area of a free-standing nanomembrane (m^2), Δp is the vapor pressure difference (Pa). The permeation rate found by the mass-loss method was 1.1×10^{-4} $mol \cdot m^{-2} \cdot s^{-1} \cdot Pa^{-1}$ (a red square in Figure 3.6b) that is hundreds to thousands of times greater than the water permeance in commercial membranes. The experiments with the inverted container gave the same permeance value that could mean water transport from a liquid film on the CNM surface. Mass-loss experiments with various volatile solvents such as ethanol, 2-propanol, acetonitrile and n-hexane did not reveal permeation through CNMs. In the second method, the permeation was measured directly in a vacuum setup. The CNM was exposed to water vapor at a set pressure on the one side and the passed species were detected with a mass spectrometer on the other side as schematically shown in the right inset in Figure 3.6b. The permeation rate Π was evaluated by comparing the CNM signal I_{sample} with the reference signal I_{ref} through a nanoaperture from another channel of the setup according to equation:

$$\Pi = \frac{p_{ref} \times I_{sample} \times A_{ref}}{p_{sample} \times I_{ref} \times A_{sample}} \times \frac{1}{\sqrt{2\pi m_0 k_B T} \times N_A}, \tag{3.5}$$

where p_{ref} is the pressure applied to nanoaperture (Pa), A_{ref} is the area of the nanoaperture (m^2), p_{sample} is the pressure applied to nanomembrane (Pa), A_{sample} is the area of the nanomembrane (m^2), m_0 is the molecular mass of the gaseous species (kg), k_B is the Boltzmann constant ($m^2 \cdot kg \cdot s^{-2} \cdot K^{-1}$), T is the absolute temperature (K), N_A is Avogadro's constant (mol^{-1}). The water permeance rose with increasing humidity

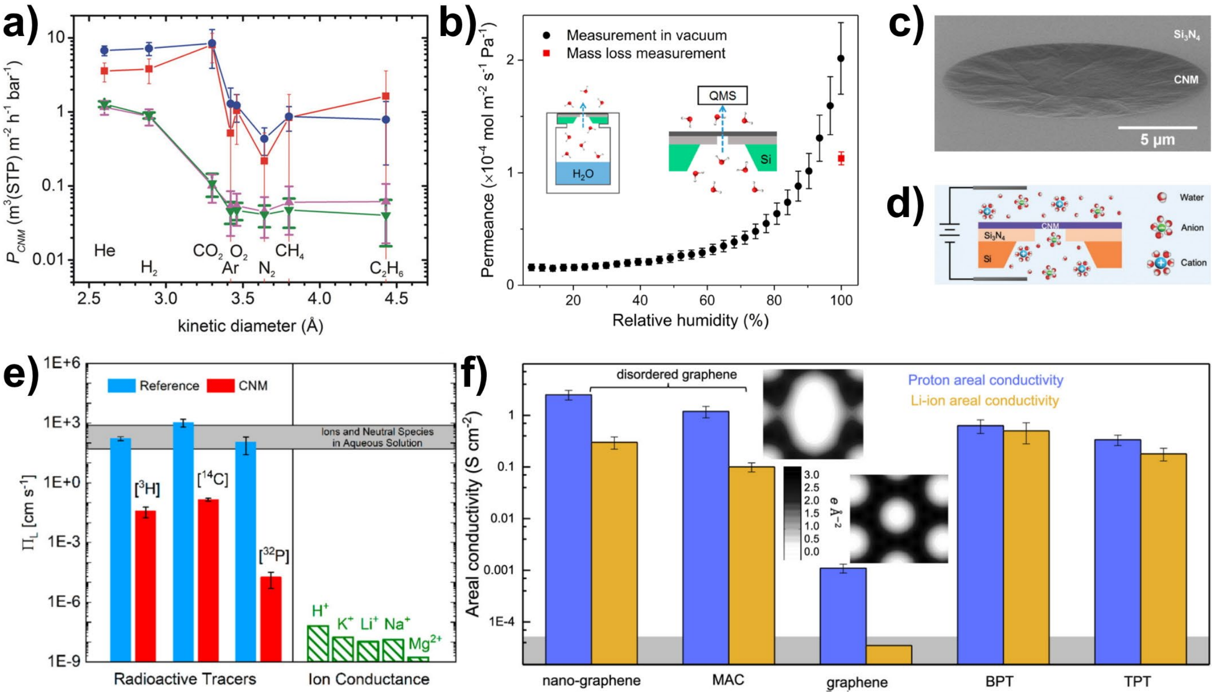

Figure 3.6 – Permeation in CNMs. **a)** Gas permeances in isolated CNMs depending on the kinetic diameter of species. The permeation rates were extracted from the total permeance in the composite membranes. A one-layer BPT CNM and NBPT CNM are marked with red squares and with blue dots, correspondingly. A three-layer BPT CNM and NBPT CNM are marked with purple triangles and with green inverted triangles, correspondingly. **b)** Permeation of water vapor in a TPT CNM depending on the relative humidity. The left inset indicates a mass-loss method. The right inset indicates a scheme of direct measurement in a vacuum setup with a quadrupole mass spectrometer. **c)** HIM image of a free-standing TPT CNM over an orifice in Si_3N_4/Si chip. **d)** Scheme of ion permeation measurements in free-standing CNM with aqueous electrolyte solutions. **e)** Liquid phase permeance for radioactive traces (H_2O with ^3H, $NaHCO_3$ with ^{14}C, H_3PO_4 with ^{32}P) through an uncovered orifice in Si_3N_4/Si chip (blue bars) and through a free-standing TPT CNM (red bars). Green dashed bars show the estimated liquid phase permeances for cations. Grey area indicates the liquid phase permeances for unobstructed movement in water. **f)** Proton (blue bars) and Li-ion (orange bars) areal conductivities for 2D carbonaceous materials. The grey area indicates the detection limit. The insets show the charge density for eight-membered ring (top) and for six-membered ring (bottom) in graphene. Part **a)** is reprinted and adapted with permission from Ai et al.[89], Copyright 2014 John Wiley and Sons. Parts **b)** – **c)** are reprinted and adapted with permission from Yang et al.[85], Copyright 2018 American Chemical Society. Part **d)** is reprinted and adapted from the open access article[90], Copyright 2020 Creative Commons License. Part **e)** is reprinted and adapted with permission from Dalpke et al.[91], Copyright 2020 American Chemical Society. Part **f)** is reprinted and adapted with permission from Griffin et al.[92], Copyright 2020 American Chemical Society.

that was explained by probable higher adsorbate numbers on the CNMs surface with an increasing vapor pressure as displayed in Figure 3.6b. The permeance values found for the saturated water vapor from two the methods were quite close. The inert helium atoms crossed CNMs in 2500 times slower than the water molecules. Moreover, the permeation of other gases was not detected despite quite large nanochannels of ~ 0.7 nm estimated by AFM. Firstly, it was supposed that liquid water has a higher chance to reach a nanochannel due to a higher density number compared to the gaseous helium. Secondly, the single-channel permeation coefficient for water was estimated to be ~ 66 $s^{-1} \cdot Pa^{-1}$ that was attributed to the cooperative transport of molecules through the nanochannel as a single-file due to hydrogen-bonding.[85] As it was shown later by mass-loss experiments, two-layer TPT CNMs exhibited nearly the same permeation rate for water as one-layer CNM that confirmed the single-file transport behavior.[90]

Ion permeation through CNMs in aqueous electrolyte solutions was studied in a similar way. The CNM was transferred onto a Si_3N_4 film with a single orifice, and the device was mounted into a custom fabricated permeation cell as schematically shown in Figure 3.6d. The permeation cell was filled with an aqueous electrolyte solution of interest. Since pure water is poorly conductive, the measured current was addressed to ion movements between the electrodes in the cell. Van Deursen et al. estimated the pore density in BPT CNM from ionic conductance measurements in 2019. CNMs were suspended over an orifice 20 – 80 nm in diameter. No visible pores in the free-standing CNM were found by HR-TEM, but the resolution was limited to prevent the rupture of the nanomembrane under the intensive electron flow. In this way, the pores were supposed to be below 1 nm. The ionic conductance was extracted from current-voltage curves measured in the cell, and CNMs resulted in a 30 % drop in the conductance compared to an uncovered orifice in the Si_3N_4/SiO_2 chip. The average areal conductance in a CNM was found to be 4.8×10^{-2} $nS \cdot nm^{-2}$. Since the electrolyte solution had the largest K^+ ion which hydrated diameter is 0.56 nm, the pores smaller than this size were excluded from the estimation according to the model. As a result, the effective pore density was only 1 – 2.7 pores per 100 nm^2 considering pores from 0.56 to 1.00 nm in diameters. Moreover, the BPT CNM was found to be selective for ions according to the Nernst-Plank membrane theory. The Nernst membrane potential corresponding to the complete rejection of one ion type and passage for another ion type was calculated. The experimental value for CNMs was 32 % of the theoretical value for a 3D membrane that was attributed to an easier ion transport in 2D membranes. The membrane potential changed sign for the $MgCl_2$ electrolyte where the Cl^- ion with a higher diffusivity became the main charge carrier in contradistinction to KCl and CsCl solutions with K^+ and Cs^+ as the main charge carriers, correspondingly.[69] Yang et al. reported about an ion exclusion behavior for TPT CNMs in 2020. The ionic current was not found after the orifice (0.15, 3.4 or 15 µm in diameter) in Si_3N_4/Si chip was covered by a TPT CNM. Electrochemical impedance spectroscopy (EIS) revealed the highest resistance for the $MgCl_2$ solution compared to LiCl, NaCl, KCl and HCl electrolytes. It was exhibited that the high electrical resistance of the CNM is comparable to the sealed Si_3N_4/Si chip. The estimated liquid phase permeances for cations are presented as green dashed columns in Figure 3.6e. Farther, forward osmosis experiments were carried out for two-layer CNMs supported on porous polymeric substrates. The estimated water permeance for isolated CNMs was two orders of magnitude lower than the value obtained from mass-loss experiments that was explained by concentration polarization.[90] Then Dalpke et al. investigated the diffusion of the radioactive neutral molecules in an aqueous solution through TPT CNMs. It was used a similar cell where a free-standing CNM on a Si_3N_4/Si chip with a ~ 7 µm orifice was a separator between the donor and the acceptor compartments. The followed radioactive tracers were added to the donor compartment: H_2O with ^3H, H_3PO_4 with ^{32}P and $NaHCO_3$ with ^{14}C. The radioactivity was measured by liquid scintillation counting (LSC) in both compartments after certain time intervals. The liquid phase permeances for the tracers in CNMs as well as in an uncovered orifice of Si_3N_4/Si chip (reference) were evaluated and compared with the ion conductivity. The results are presented in Figure 3.6e. The TPT CNMs hindered the diffusion of H_2O and $NaHCO_3$ species by 3 – 4 orders of magnitude, while the liquid phase permeance for the phosphoric acid was equal to the detection limit. In this way, CNMs were considered to be almost impermeable for H_3PO_4 species.[91]

The permeation of helium, protons and Li ions in nanocrystalline graphene, monolayer amorphous carbon, carbon nanomembranes and defect-free graphene was investigated by Griffin et al. in 2020. The 2D materials were transferred onto a Si_3N_4/Si chip with an orifice ~ 1 µm in diameter. The gas permeation measurements were performed in the vacuum setup where the free-standing 2D material separated the feed and the permeate chamber. A feed pressure was controlled by an electric dosing valve, and the permeate chamber was connected with a mass spectrometer. Helium permeation was not detected at a pressure of tens mbar for all 2D carbon materials. To measure H^+ transport, free-standing materials were covered with a proton-conducting polymer (Nafion) on both sides and then electrically connected with porous carbon electrodes with a platinum catalyst followed by backing in a humid Ar/H_2 atmosphere. Nanocrystalline graphene and MAC exhibited close proton conductivities in thousand times higher than for the defect-free graphene as presented in Figure 3.6f. The CNMs showed lower proton conductivity than MAC. Moreover, the protons crossed BPT CNMs more often than TPT CNMs that was explained by the greater thickness of the latter nanomembrane. For the Li^+ transport measurement, the free-standing materials were covered with a lithium-conducting polymer (poly(ethylene oxide) with LiTFSI salt) and connected to lithium metal electrodes in an inert atmosphere. The Li-ion permeation was not detected in defect-free graphene. Eight-membered carbon rings give a lower electron density than six-membered rings in crystalline graphene, as shown in the insets in Figure 3.6f, that make possible the lithium transport through nanocrystalline graphene and MAC. In turn, CNMs having relatively larger pores were found to be more permeable for Li^+ ions than other 2D materials. Notably, their Li-ion conductivities correlated with the thickness of the CNM, and the H^+/Li^+ selectivity was less pronounced than for MAC and nanocrystalline graphene due to wider sub-nanometer channels.[92]

The lithium transport through TPT CNMs in a non-aqueous electrolyte inside a lithium electrochemical cell was reported by Rajendran et al. in 2021. The CNM was transferred onto a commercial macroporous Celgard separator which was mounted into the electrochemical cells in an inert atmosphere. The electrolyte was consisted of $LiPF_6$, ethylene carbonate and dimethyl carbonate. SEM analysis revealed lithium dendritic structures on the electrode after long-term cycling in the case of the Celgard separator, but a presence of the CNM on the separator resulted in a uniform Li coverage. The CNM was found to suppress the formation of dendrites providing a uniform flux of Li^+ ions through the sub-nanometer channels.[93]

3.2 2D covalent organic frameworks

3.2.1 Synthesis of 2D covalent organic frameworks

Covalent organic frameworks (COFs) are a class of crystalline extended materials that are assembled from organic precursors (linkers) in a chemical condensation reaction. Although COFs with 3D lattices are known, most COFs have two-dimensional lattices where the building blocks are connected by a strong covalent bond, and these layers are stacked together by weaker interactions like van der Vaals forces, aromatic stacking or hydrogen bonding.[94,95] A 2D lattice (layer) of COFs is composed of linkers located in the same plane. Geometries of linkers determine the symmetry of frameworks as shown in Figure 3.7a.[96] In view of the presence of long-range order and molecular-sized building blocks, COFs are intrinsically porous. Actually, a COF is an array of regular pores with ultra-narrow size distributions and isthmuses between them.[97] Layered structures of COFs are presented in different types of stacking. The most common cases are eclipsed AA-stacking and staggered AB-stacking, but other intermediate positions are also possible as shown in Figure 3.7b. The type of stacking determines the pore geometry in the frameworks in addition to the symmetry of a 2D lattice.[98] The COFs resemble metal organic frameworks (MOFs) which were discovered in 1998.[95] The covalent bonds in COFs are stronger than coordination bonds with metals in MOFs resulting in greater strength of organic frameworks that is compared with graphene.[99] By modifying the linkers, one can design the pore geometry as well as other properties that make COFs eminent among other 2D materials.[94,95]

The first COFs were synthesized via a condensation reaction under solvothermal conditions in 2005. The synthesis was carried out in a sealed glass tube under heating for 3 days using mixture of mesitylene and 1,4-dioxane as the solvent. COF-1 was synthesized by dehydration of 1,4-benzenediboronic acid (BDBA). COF-5 was prepared by condensation of BDBA with 2,3,6,7,10,11-hexahydroxytriphenylene (HHTP). Both compounds were obtained in powder form consisted of microcrystals that was confirmed by SEM analysis. The new crystal structures were defined by powder X-ray diffraction (XRD), Fourier transform infrared spectroscopy (FTIR) and nuclear magnetic resonance (NMR) methods. The structure of COF-1 was found to consist of AB staggered layers of hexagonal lattice similar to graphite as shown in

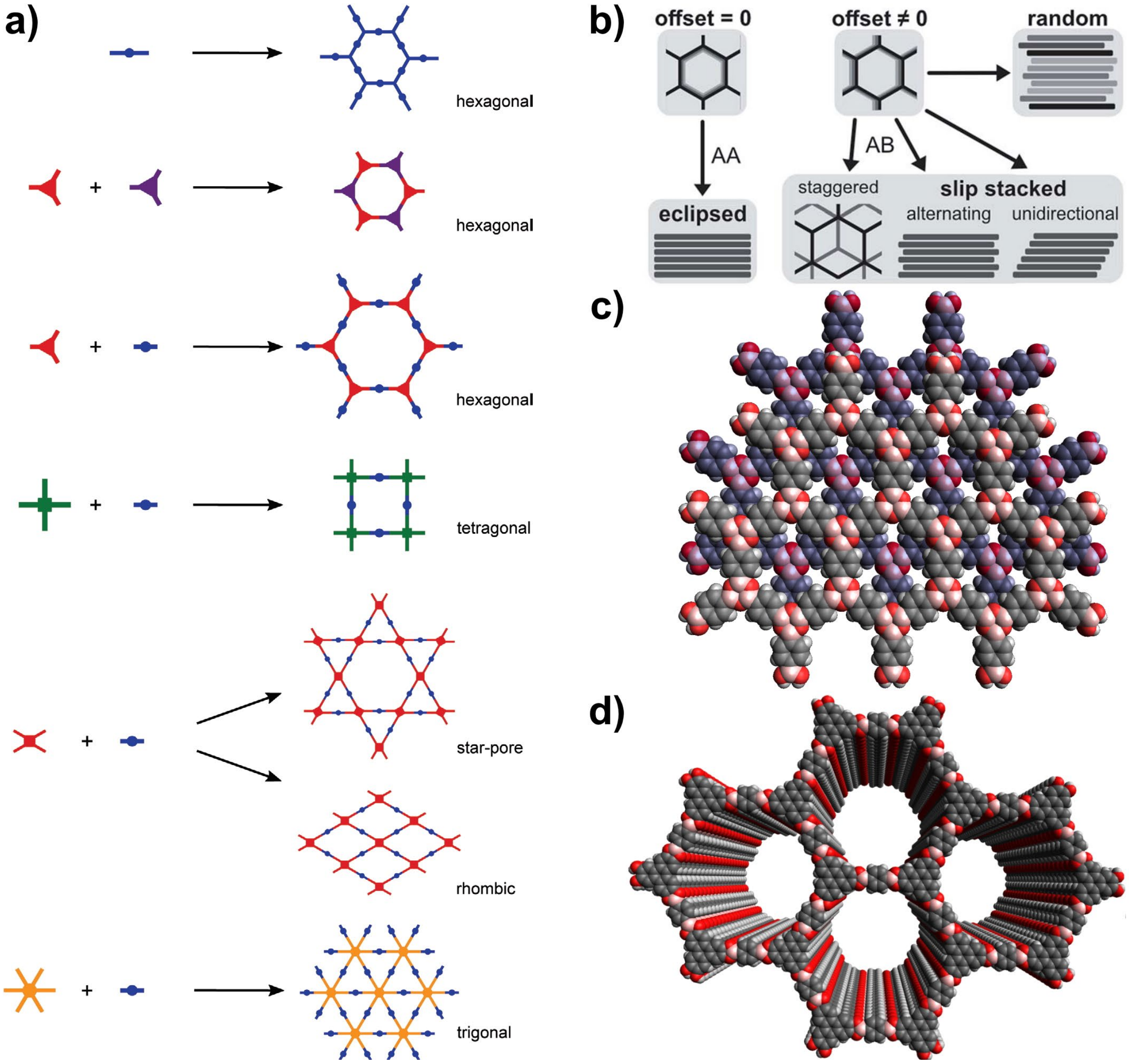

Figure 3.7 – Structure of covalent organic frameworks. **a)** Common linker geometries and resulting 2D lattice. **b)** Types of stacking for layered COF. **c)** Structure of COF-1 with staggered AB-stacking. **d)** Structure of COF-5 with eclipsed AA-stacking. Part **a)** is reprinted and adapted with permission from Lohse et al.[96], Copyright 2018 John Wiley and Sons. Part **b)** is reprinted and adapted from open access article[98], Copyright 2020 Creative Commons Attribution 3.0 Unported Licence. Parts **c)** and **d)** are made in Avogadro free software.

Figure 3.7c. The diameter of the hexagonal micropore was ~ 1.5 nm, but a staggered stacking led to ~ 0.7 nm-width channels considering van der Waals radii in COF-1. COF-5 with a structure similar to boron nitride consists of eclipsed AA layers with mesopores of ~ 2.7 nm in diameter as can be seen in Figure 3.7d. Distinct stacking was attributed to preferable π-π interactions in HHTP units in COF-5, while van der Waals interactions between B_3O_3 cycles in adjacent layers dominated in COF-1. The first representatives of a new class of materials exhibited high thermal stability up to

500 – 600 °C. Moreover, the surface areas estimated from nitrogen adsorption isotherm according to the Brunauer-Emmett-Teller (BET) theory were record high: 711 $m^2 \cdot g^{-1}$ for COF-1 and 1590 $m^2 \cdot g^{-1}$ for COF-5. This was consistent with the nature of the new materials, which were solid with an array of 1D nanochannels.[100]

Despite two-dimensional lattices, most layered COFs are synthesized by solvothermal approach and represent bulk polycrystalline materials in powder form.[94] The discovery of graphene through mechanical exfoliation of graphite inspired the development of 2D COFs which consisted of one or few layers. All preparation methods of 2D COFs can be classified in two ways: top-down and bottom-up approaches. The top-down approach includes mechanical, ultrasonic, chemical, intercalate-assisted exfoliations and self-exfoliation, while the bottom-up approach implies the formation of 2D COF at interfaces.[95] Both approaches have been evolving in parallel. First assembly of covalent organic structures on metal surfaces was found via STM by Grill et al. in 2007. The precursor tetra(4-bromophenyl)porphyrin (Br_4TPP) was deposited onto Au(111) surface in UHV. Thermal activation of the molecules occurred if the evaporator temperature reached 590 K that led to removal of bromine atoms. As a result, the activated Br_4TPP molecules diffused over the gold surface and formed nanosized covalently bound structures.[101] Also it was reported about assembly of thermally-activated 5,10,15,20-(tetramesityl)porphyrin molecules on Cu(110) surface.[102] Monolayers of covalent organic frameworks were assembled at room temperature on the metal surface by Zwaneveld et al. in 2008. BDBA molecules were evaporated form the monolayer of COF-1 onto a clean Ag(111) surface. To prepare COF-5, HHTP molecules were sublimated to fill a HHTP monolayer on the silver surface followed by co-evaporation of BDBA and HHTP species. The excess of unbound HHTP molecules was removed by annealing. The STM analysis revealed the pore diameters of ~ 1.5 nm for COF-1 and ~ 2.9 nm for COF-5 on Ag(111) surface.[103] Colson et al. demonstrated the possibility of non-epitaxial growth of thin COF films on a supported graphene via solvothermal synthesis in 2011. The substrates (Cu, SiO_2, SiC) with a single-layer graphene were simply immersed into the reaction mixture followed by rinsing in toluene, sonication and vacuum drying. The thickness of COF films varied from 70 to 210 nm depending on the duration of the synthesis.[104] Although synthesis on a solid surface allowed to obtain sufficiently thin COF film or monolayer, the surface should be atomically flat for a high-quality coverage. Preparation at vacuum/solid interface requires expensive UHV technique, while the subsequent transfer seems to be challenging.[105] Only in 2020 thin COF films were prepared on a usable salt surface. Shi et al. synthesized 2D COFs on NaCl crystals in solvothermal conditions. Unlike other solid surfaces, this method provides easy release of 2D COFs nanosheets by dissolving salt in water. Three imine-based 2D COFs were grown on NaCl crystals in a mixture of mesitylene and 1,4-dioxane under solvothermal conditions for 3 days. The solution/salt interface reduced thermodynamic barrier for the condensation reactions that led to preferable growth on the NaCl surfaces. Imine-based frameworks demonstrated lateral size up to several microns according to SEM and AFM analysis. The 2D COFs grown on 12 µm-sized crystals had thicknesses of 3 – 5 nm, while the frameworks on 440 µm-sized NaCl particles were ~ 12 nm-thick.[106]

Eventually, free 2D COF layers were obtained for the first time using top-down approaches in 2011. Berlanga et al. reported about the first exfoliation of the layered COF-8 via ultrasonic treatment. COF-8 was synthesized from HHTP and 1,3,5-tris[4-phenylboronic acid]benzene (BTPB) precursors under heating and inert atmosphere in a mixture of mesitylene and 1,4-dioxane for 3 days. The portion of COF-8 was dissolved in dichloromethane CH_2Cl_2 and sonicated for 15 minutes resulting in exfoliation. The suspension was centrifuged at 9000 rpm for 5 minutes followed by dilution by 10^{12} times. The solution was drop-casted on mica and silicon dioxide surfaces. The scheme of the experiment is presented in Figure 3.8a. AFM analysis revealed sheets with micron lateral dimensions and with a thickness of 4 – 10 nm that corresponded to 10 – 25 layers of COF-8. Increasing the concentration of the suspension led to an increase in the height of the sheets rather than covering the entire surface of the substrate that is stacking on COF layers.[107,108] Das et al. applied sonification in water to exfoliate layered imine-based COFs that resulted in submicron nanosheets with thickness of 1.0 – 1.5 nm.[109]

The solvent-assisted exfoliation in mild condition was reported by Bunck et al. in 2013. Hydrazone-linked COF-43 synthesized via solvothermal method was found to lose its crystallinity according to XRD analysis after two-hour soaking in water, 1,4-dioxane or N,N-dimethylformamide. Other solvents such as toluene, chloroform, tetrahydrofuran and methanol did not affect the crystallinity. FTIR analysis confirmed stability of bonds in 2D layers, while formation of polycrystalline nanosheets that was proven by SAED.

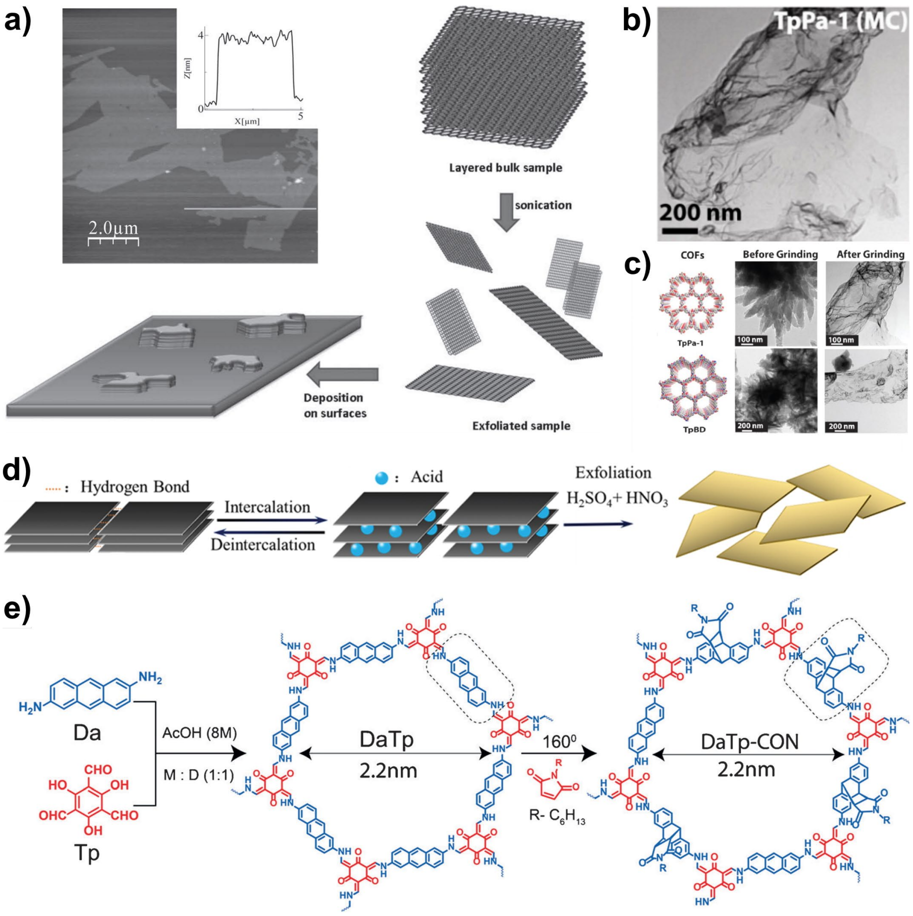

Figure 3.8 – Top-down approach for preparation of 2D COFs and the results. **a)** Ultrasonication in solvent medium. Inset: AFM image of exfoliated COF sheet on mica substrate. Common linker geometries and resulting 2D lattice. **b)** HR-TEM image of TpPa-1 COF after mechanochemical synthesis. **c)** HR-TEM images of two solvothermally synthesized COFs: before and after grinding in a mortar. **d)** Intercalate-assisted exfoliations with acids in nitrating mixture. **e)** Chemical exfoliation via Diels-Alder cycloaddition reaction in anthracene-based COF. Part **a)** is reprinted and adapted with permission from Berlanga et al.[107], Copyright 2011 Wiley VCH. Part **b)** is reprinted and adapted with permission from Biswal et al.[110], Copyright 2013 American Chemical Society. Part **c)** is reprinted and adapted with permission from Chandra et al.[111], Copyright 2013 American Chemical Society. Part **d)** is reprinted and adapted with permission from Zhu et al.[112], Copyright 2019 Royal Society of Chemistry. Part **e)** is reprinted and adapted with permission from Khayum et al.[113], Copyright 2016 John Wiley and Sons.

2D COF nanosheets has average lateral size of ~ 200 nm and thickness of 0.3 – 1.3 nm according to TEM and AFM methods.[114] Zhu et al. used a nitrating mixture to exfoliate triazine-based COF. The method is presented in Figure 3.8d. The layered COF was soaked in either oxidizing H_2SO_4 or non-oxidizing H_3PO_4 for 5 minutes to obtain the intercalation compounds. Then the COF with intercalated acids was exposed to a mixture of H_2SO_4 and HNO_3 for 10 minutes under heating and microwave irradiation. Nitronium ions NO_2^+ reacted with the intercalated compounds leading to exfoliation of the layered COF. The XPS analysis confirmed a formation of nitro ($-NO_2$) and carboxyl (-COOH) groups after nitrating. SEM and AFM methods revealed micron-sized 2D COF nanosheets with a thickness of 1.2 – 1.9 nm.[112]

In 2013, Biswal et al. applied a solvent-free mechanochemical synthesis that provides exfoliation in COF layers. The precursors were loaded into a mortar and grinded with a pestle for 45 minutes. The formation of exfoliated COF nanosheets was confirmed by HR-TEM as can be seen in Figure 3.8b that was consistent with lower surface areas found from N_2 adsorption isotherm as well as broader peaks in XRD pattern compared to the materials prepared via solvothermal synthesis.[110] Chandra et al. showed that COF powders synthesized by the solvothermal method can be delaminated in a mortar as well. The HR-TEM and AFM analyses revealed 3 – 10 nm-thick (10 – 30 layers) COF sheets with a lateral size of 0.1 – 1 µm. The TEM images before and after grinding are presented in Figure 3.8c.[111] Later, Wang et al. used a ball milling for mechanical exfoliation of solvothermally synthesized imine-based COFs. The time of milling varied from 30 minutes to 2 hours depending on COFs. As a result, 3 – 5 nm-thick 2D COF nanosheets with submicron lateral dimensions were obtained.[115] Lei et al. showed that a ball milling without solvent for 8 hours followed by ball milling with ethanol for 30 minutes produced submicron 2D COF nanosheets with a thickness below 2 nm.[116] Zhang et al. applied a ball milling for 10 hours to exfoliate perfluorinated triazine-based COF. 2D COF nanosheets with an average thickness of 4.2 nm had large lateral dimensions up to 1 – 3 µm.[117]

Khayum et al. reported about successful chemical exfoliation in anthracene-based COF in 2016. Da-Tfp COF was solvothermally synthesized from 2,6-diaminoanthracene (Da) and 2,4,6-triformylphloroglucinol (Tfp) as presented in Figure 3.8e. Then, as a result of the Diels-Alder cycloaddition reaction, N-hexylmaleimide was joined to the Da-Tfp COF structure that led to an exfoliation due to the new spatial arrangement. The electron microscopy confirmed the formation of nanosheets with lateral dimensions of ~ 500 nm and the average thickness of ~ 17 nm. Da-Tfp nanosheets were shown to form thin films by layer-by-layer (LbL) assembly. Suspension of nanosheets in CH_2Cl_2 was dropped onto a water surface. Fast evaporation of the solvent allowed formation of a floating thin COF film that could be transferred. It was demonstrated that varying the concentration resulted in Da-Tfp COF films with a thickness of 1.2 to 19 nm.[113] Later, Haldar et al. applied the same approach. The anthracene-based COFs were subjected to a Diels-Alder cycloaddition reaction with maleic anhydride. The formation of 2D COF nanosheets with a lateral size of 1 – 3 µm and a thickness of 1.0 – 1.5 nm was confirmed by the AFM analysis.[118] The chemical exfoliation via Diels-Alder cycloaddition is applicable only for anthracene-based COFs. Using strong oxidants for the chemical exfoliation breaks covalent bonds rather than exfoliating them. Zhu et al. applied ionothermal approach to synthesize chemically stable triazine-based COFs. Then the COF was exposed to piranha solution (H_2SO_4/H_2O_2) for 5 minutes under heating. As a result, 0.7 nm-thick nanosheets with a lateral size of only 15 – 35 nm was obtained which belong rather to 1D materials than the 2D ones.[119]

The use of linkers with an ionic group in the synthesis of COFs can lead to the repulsion of layers in the aqueous medium. Self-exfoliation of ionic covalent organic framework (iCOF) in water was found out by Mal et al. The imine-based EB-TFPs were solvothermally synthesized from 2,4,6-triformylphloroglucinol (Tfp), ethidium bromide (EBr) in the mixture of mesitylene, 1,4-dioxane and aqueous acetic acids. Ionic nature of EBr-Tfp iCOF was determined by ethidium bromide-based fragments. As a result, layered EBr-Tfp immersed in pure water for 2 days turned into 1.5 nm-thick submicron nanosheets.[120] A similar water-assisted exfoliation was later observed in the propidium iodide-based iCOF. The prepared micron-sized 2D COF nanosheets had an uniform thickness of 1.6 nm according to the AFM analysis.[121]

Although exfoliated planar COF particles can be assembled from colloidal solutions into laminated thin films,[122,123] it is impossible to control the position of an individual nanosheet which floats randomly in suspension. In turn, large integral thin COF films made by bottom-up approaches are preferable for membrane application as it is easier to operate with them, but the nature of COF results in large amorphous regions due to a strong covalent bonding. The crystallinity and stability compete with each other – reversible reaction between linkers leads to higher crystallinity in the structure tending to thermodynamic minimum, while non-dynamic bonds provide stiff framework with low ordering. So far, the obtained COF single crystals do not exceed the micron scale.[95,124] The liquid interface-assisted synthesis remains attractive for the preparation of 2D covalent organic frameworks due to the atomic smoothness and the ability to control the film thickness by adjusting the concentration of monomers in solution.[125] The common methods are presented in Figure 3.9.

In 2016 Dai et al. synthesized imine-based 2D COFs at the air-water interface using Langmuir-Blodgett trough as shown in Figure 3.9a. The two monomers were pre-mixed in chloroform and spread using a microsyringe on water surface in the trough. After evaporation of $CHCl_3$, the surface was compressed until the surface pressure reached 3 $mN \cdot m^{-1}$. Then the trifluoroacetic acid was added into the solution as a catalyst. The polymerization took 12 hours. The thin COF film was transferred for subsequent analyses using Schäfer method: the pre-submersed horizontally oriented silicon wafer was lifted up at rate of 0.5 $mm \cdot min^{-1}$. Lateral dimensions of the film were in the range of hundreds micron, while thickness amount to 0.7 nm corresponding to a monolayer. The mechanical stability of the 2D COF allowed the film to be free-standing over a 100 × 100 μm window in TEM grids.[126] Sahabudeen et al. prepared 0.7 nm-thick 2D COFs with lateral sizes of several centimeter using similar methods in 2016. The organization of the first precursor at the air-water interface was achieved in the Langmuir-Blodgett trough. The chloroform solution with the first monomer was spread over the water surface followed by a compression until the surface pressure became 10 $mN \cdot m^{-1}$. Then the second precursor was injected into the water phase. The polymerization took 16 hours resulting in a highly crystalline monolayer COF which was horizontally transferred.[99] The Langmuir-Blodgett vertical transfer can also be applied to 2D COF, as was reported later for 3 nm-thick films.[127]

A liquid-liquid interface-assisted synthesis was carried out for 2D COFs preparation by Dey et al. in 2017. This method is presented in Figure 3.9b. The dichloromethane solution with the first monomer (1,3,5-triformylphloroglucinol, Tp) was poured into a glass beaker. Then water was added on the top of CH_2Cl_2 solution as a spacer layer. The aqueous solution with the second monomer was slowly dropped on top of the spacer solution during 30 minutes. The compounds marked as Bpy, Azo, Tta, Ttba were taken as the second monomer. The synthesis took 3 days in undisturbed condition at room temperature. The upper aqueous layer was removed with a pipette followed by transfer of COF films. The minimal average thicknesses of COF films were found to be 75 nm for Tp-Bpy, 90 nm for Tp-Azo, 45 nm for Tp-Ttba and 90 nm for Tp-

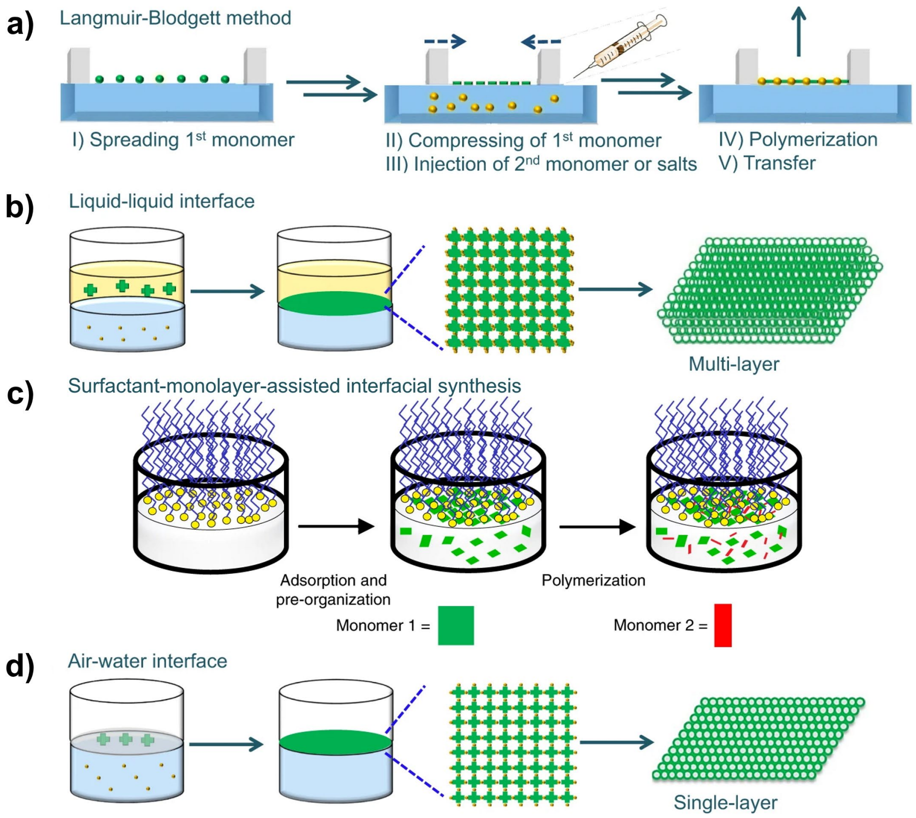

Figure 3.9 – Synthesis of 2D COF on liquid interfaces. **a)** Langmuir-Blodgett method at air-water interface: compressing the liquid surface. **b)** Liquid-liquid interface-assisted synthesis: two immiscible solvents in a vessel. **c)** Surfactant-monolayer-assisted interfacial synthesis (SMAIS): surfactant arranges the monomer molecules. **d)** Air-liquid interface-assisted synthesis: monomer spreads over the liquid surface. Parts **a)**, **b)**, **d)** are reprinted and adapted from open access article[125], Copyright 2018 Springer Nature. Part **c)** is reprinted and adapted with permission from Liu et al.[128], Copyright 2019 Springer Nature.

Tta. The crystallinity was confirmed by XRD. The surfaces of the films were heterogeneous, and the films with sheet-like morphology consisted of layers with lateral size above 100 µm, according to SEM images.[129] The thickness of the COF films can be controlled by varying the concentration of monomers, while the area is determined by cross-section of the beaker. Later, it was reported about a thickness of 2.5 – 5 nm in the 2D COF films obtained via the liquid-liquid interface-assisted synthesis.[130,131] Li et al. presented a buffering interlayer interface (BII) method to grow large area 2D COF films. Since both precursors were soluble in miscible solvents, the synthesis in liquid-liquid interface was modified. The bottom solution of 1,3,5-triformylphloroglucinol (Tp) in CH_2Cl_2 was covered with a buffer liquid layer – the acetic acid solution. The upper solution of 3,3'-dihydroxybenzidine (DHBD) in a mixture of dichloromethane and dimethylformamide was dropped on the acetic acid-based buffer.

The DHBD molecules diffused and reacted with Tp molecules on an interface of the bottom solution giving a two-dimensional COF. The crystals of 2D COF with a thickness of about 0.35 nm and an area of more than 200 µm^2 were examined by SEM, TEM and AFM methods.[132]

In 2019, Liu et al. applied surfactant-monolayer-assisted interfacial synthesis (SMAIS) to improve crystallinity in 2D COFs as an alternative to Langmuir-Blodgett trough. The chloroform solution with sodium oleyl sulfate (SOS) was dropped on water surface and a surfactant monolayer was formed after the evaporation of $CHCl_3$. The first monomer with porphyrin fragment was injected into the liquid phase and left for 30 minutes. Since the amphiphilic SOS molecules were oriented perpendicular to air-water interface, their hydrophilic sulfate groups preorganized the porphyrin-based molecules parallel to the water surface as shown in Figure 3.9c. Then alkaline solution with the second monomer was injected into aqueous phase. The synthesis lasted 7 days. The resulting imine-based 2D COF exhibited crystallinity of 69 % according to the TEM analysis. The average crystal domain had an area of 3.5 µm^2 and the thickness amounted to be ~ 2 nm, while these monomers formed only amorphous films without surfactant.[128] Later, Park et al. synthesized boronate-based 2D COFs with large crystal domains of 60 µm^2 using the SMAIS method. The thickness was tuned from 6 to 16 nm by varying the concentration of precursors.[133] Qi et al. synthesized highly crystalline imine-based 2D COFs with a thickness of ~ 40 nm by applying surfactant assistance. A detailed examination using transmission electron microscopy did not reveal any amorphous regions for the COF film, which consisted of micron-sized crystalline domains.[134]

Ying et al. synthesized two iCOFs at the air-water interface in 2020. The syntheses scheme is depicted in Figure 3.9d. To prepare cationic 2D Tp-EBr COF, the aqueous solution with ethidium bromide (EBr) and trifluoroacetic acid was poured into a dish with diameter of 6 cm. The toluene solution with 1,3,5-triformylphloroglucinol (Tp) was spread over the liquid surface using a microsyringe. The synthesis lasted 2 days at room temperature without disturbance. The anionic 2D Tp-Pa-SO_3Na COF was prepared similarly using the aqueous solution with sodium 2,5-diaminobenzene sulfate (Pa-SO_3Na) and p-toluenesulfonic acid. Polycrystalline 2D iCOF films were 2.5 – 3 nm in thickness, and the lateral size of sheets exceeded 80 µm according to the AFM and TEM analysis.[135]

3.2.2 Properties of 2D covalent organic frameworks

Researches about gas transport in 2D COF-based membranes have been carried out rarely, and a thickness of frameworks exceeds 100 nm in most studies.[136] Li et al. studied gas permeation in exfoliated COF-1 nanosheets supported on macroporous alumina in 2017. AB-stacked COF-1 was synthesized under solvothermal conditions followed by dispersion in CH_2Cl_2 and sonification to produce 2D COF nanosheets. The AFM method revealed the thickness of a single nanosheet to be ~ 0.5 nm that corresponded to one layer. The suspension with COF-1 nanosheets was dropped onto macroporous Al_2O_3 substrates with smooth SiO_2-ZrO_2 intermediate layer followed by drying to form the layer as presented in Figure 3.10a. According to SEM analysis, the thickness of a homogeneous layer of stacked COF-1 nanosheets was about 100 nm. The average pore size was estimated to be 0.39 nm from nitrogen adsorption isotherm. Single-gas permeation experiments with He, H_2, N_2 and SF_6 were performed at 30 – 400 °C by applying pressure difference of ~ 100 kPa. The feed gas was regulated with a pressure controller and the permeate gas was detected with a bubble flow meter. The gas permeation rates decreased with rising temperature that indicated the predominance of Knudsen diffusion, and estimated H_2/N_2 selectivity amounted to be 3.3. Despite larger kinetic diameter, H_2 permeance (1.68×10^{-6} $mol \cdot s^{-1} \cdot m^{-2} \cdot Pa^{-1}$) was higher than the permeation rate of helium (1×10^{-6} $mol \cdot s^{-1} \cdot m^{-2} \cdot Pa^{-1}$). Such gas behavior was ascribed to the presence of relatively large pores and dominant gas flow through them. As the pore size in COF-1 lattice is 1.5 nm, these pores could contribute to permeation due to random stacking.[122]

Ying et al. prepared a hybrid 2D COF nanosheet-based membrane using the LbL approach in 2020. 2D iCOFs were transferred on 1 mm-thick macroporous Al_2O_3 supports (pores of ~ 70 nm in diameter) by the Langmuir-Schäfer method: the horizontally oriented support was brought into contact with the liquid surface where the 2D iCOFs nanosheets were located and then lifted up. Firstly, cationic 2D Tp-EBr COFs were transferred onto support of 2.5 cm in diameter followed by drying in air flow and in vacuum. Secondly, anionic 2D TpPa-SO_3Na COFs were transferred over the cationic framework using the same method followed by rinsing with an aqueous ethanol solution. Electrostatic interactions between two oppositely charged iCOFs resulted in the thin ordered structure with staggered stacking which is depicted in

Figure 3.10b. The overlaying of cationic Tp-EBr with 1.6 nm-sized pores and anionic Tp-Pa-SO_3Na with 1.4 nm-sized pores gave smaller pores. This membrane structure agreed with zeta potential measurements and molecular dynamic simulations. Gas permeation experiments were performed at pressure difference of 20 kPa using a custom-made apparatus with mass flow controllers. The gases on a permeate side were swept by argon to a chromatograph for analysis. Heating in a sealed membrane cell was carried out using a furnace. The feed gas was passed through a vessel with water for measurements under humidified conditions. Three hybrid 2D COF membranes supported on alumina with thickness of 21, 41 and 63 nm were prepared via LbL assembly. Gain in the thickness led to rise in selectivity and reduction in permeance as presented in Figure 3.10c. Hybrid 2D COF membranes with a thickness of 41 nm exhibited pronounced molecular sieve effects with the high H_2/CO_2 selectivity of 26.2 and the H_2 permeance of 8.6×10^{-7} $mol \cdot s^{-1} \cdot m^{-2} \cdot Pa^{-1}$ exceeding the Robeson upper bound. The highest H_2/CO_2 selectivity was only 8.1 for 40 nm-thick 2D membranes based on anionic Tp-Pa-SO_3Na, so the high performance of the hybrid 2D membrane was attributed to the staggered structure with reduced pores. Hydrogen permeance increased with increasing temperature from 25 to 150 °C, while CO_2 permeance remained almost the same. This behavior was considered to be an activation diffusion transport for H_2 molecules. Gas permeation rates at relative humidity of 85 % were found to be lower than in dry conditions due to competitive adsorption of water species on the 2D COF membrane. Moreover, the presence of water vapor affected stronger on CO_2 permeation rate than on the permeance of inert hydrogen.[135]

Wang et al. revealed selectivity towards CO_2 in three distinct 2D COF membranes in 2021. Three covalent organic frameworks based on 1,3,5-triformylphloroglucinol (Tp) were prepared via the solvothermal synthesis using benzene-1,4-diamine (Pa-1), 2,5-dimethylbenzene-1,4-diamine (Pa-2) and hydrazine (Hz) precursors. TpPa-1 was exfoliated by shaking in ethyl acetate. Ball milling with ethyl acetate was applied to TpPa-2 and TpHz. The colloidal solutions were kept for two weeks for sedimentation of large particles. The 2D COF nanosheets characterized by SEM, TEM, AFM methods were 1.7 – 2.5 nm in thickness and several microns in lateral dimensions. The pore sizes were predicted to be 1.6 nm for TpPa-1, 1.2 nm for TpPa-2 and 0.8 nm for TpHz

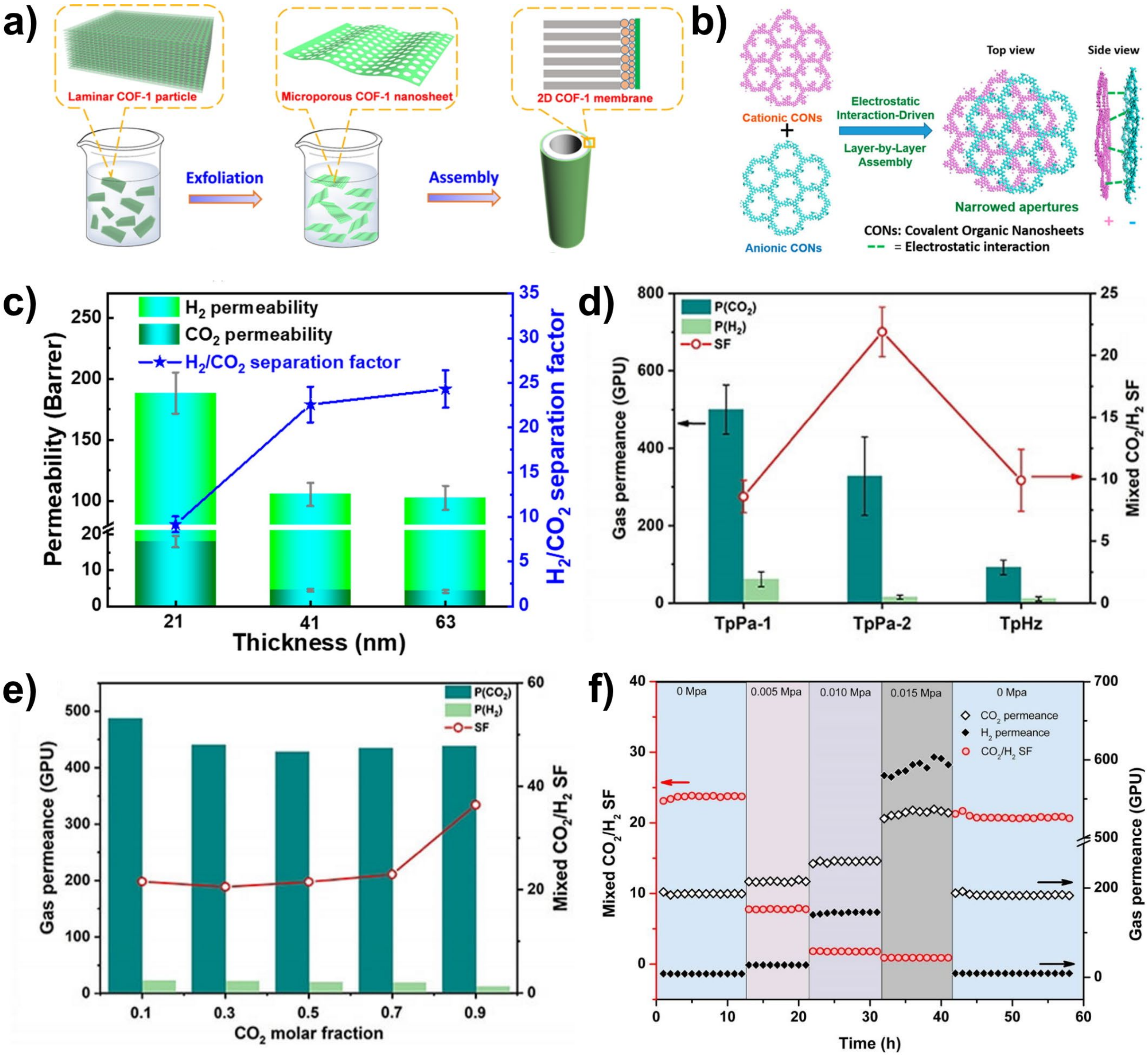

Figure 3.10 – Gas permeation in 2D COFs. **a)** Preparation of 2D COF-based membrane assembled from nanosheets. **b)** Compact staggered stacking between the anionic and cationic COF nanosheets. **c)** Permeability and H_2/CO_2 selectivity in hybrid 2D iCOF-based membranes depending on their thickness at 150 °C. **d)** Permeance and CO_2/H_2 selectivity in ultrathin 2D COF-based membranes: TpPa-1 (1.6 nm pore), Tp-Pa-2 (~ 1.2 nm pore), TpHz (~ 0.8 nm pore). **e)** Permeance for H_2/CO_2 mixture at the different molar fraction of carbon dioxide in the 2D TpPa-2 nanosheet-based membrane. The total feed pressure was 100 kPa. **e)** Performance of the 2D TpPa-2 nanosheet-based membrane depending on the pressure difference. Part **a)** is reprinted and adapted with permission from Li et al.[122], Copyright 2017 American Chemical Society. Parts **b)** and **c)** are reprinted and adapted with permission from Ying et al.[135], Copyright 2020 American Chemical Society. Parts **d)**, **e)** and **f)** are reprinted and adapted with permission from Wang et al.[123], Copyright 2021 John Wiley and Sons.

according to DFT calculations. Alumina substrates with a diameter of 1.8 cm and a thickness of 1 mm were used as macroporous supports (~ 70 nm pores) for 2D COFs.

A hot-drop coating method was applied for membrane making: the suspension was slowly dropped onto heated at 120 °C Al_2O_3 support. The thicknesses of COF films were estimated to be ~ 10 nm. Although eclipsed AA-stacking was confirmed by XRD analysis for bulk TpPa-1, TpPa-2 and TpHz COFs, staggered AB-stacking of 2D COF nanosheets on alumina support was found. Gas permeation experiments were carried out in a Wicke-Kallenbach cell at room temperature and a feed pressure was regulated with mass flow controllers. The gases on a permeate side were swept by helium to a chromatograph. All 2D COF membranes showed CO_2-selective permeation in mixtures of CO_2 and H_2 as presented in Figure 3.10d. The highest CO_2/H_2 selectivity of 22 was observed for 2D TpPa-2 nanosheet-based membranes while CO_2 permeance amounted to be 1.1×10^{-7} $mol \cdot s^{-1} \cdot m^{-2} \cdot Pa^{-1}$. To study this phenomenon, TpPa-2 thick films were grown by the liquid-liquid interfacial synthesis and transferred onto alumina supports. As a result, H_2 permeance in 1D channels of eclipsed TpPa-2 COF exceeded CO_2 permeance by 2.5 times. The selectivity towards carbon dioxide in 2D TpPa-2 nanosheet-based membranes was explained by reduced pore size and high affinity of TpPa-2 framework to CO_2 that was confirmed by adsorption studies. Staggered TpPa-2 nanosheets were supposed to form pores of ~ 0.6 nm in diameter that was optimal for preferable transport of CO_2 species via surface diffusion but it could obstruct a passage of H_2 molecules. CO_2-philic nature of TpPa-2 was confirmed at higher partial pressures. An increase in molar fraction of carbon dioxide led to noticeable blocking effects on the H_2 transport due to probable capillary condensation at CO_2 partial pressure of 90 kPa as shown in Figure 3.10e. Since water molecules are more condensable than carbon dioxide, their adsorption can hinder the gas transport. Gas permeation rates were slightly lowered by water vapor in experiments with humidified gas mixtures. Temperature-dependent experiments revealed distinct transport mechanisms for carbon dioxide and hydrogen. CO_2 permeance exhibited little decrease under heating until 100 °C, while H_2 permeance slightly rose. The permeation rates recovered after cooling back to room temperature that was attributed to prevailing surface diffusion for CO_2 and activated diffusion for H_2. In addition, the pressure difference was found to distort TpPa-2 nanosheets that was expressed in a decrease in CO_2/H_2 selectivity up to the predominance of hydrogen transport over carbon dioxide at 15 kPa as shown in Figure 3.10f. It was suggested that the pressure exerted on staggered frameworks led to the changes in interlayer distances and the expansion of slit-like pores between nanosheets. These distortions were reversible due to flexibility of 2D COF nanosheets.[123]

3.3 Bilayer oxides

3.3.1 Synthesis of bilayer oxides

Bilayer oxides represent a class of two-dimensional materials synthesized on metal surfaces. These structures are bound with the metal interface only via weak van der Waals interactions, while planar metal supports play guiding roles for the growth of two-dimensional structures. Similar to bulk oxides, in particular silicates, bilayer oxides exist in various phases of crystalline and vitreous structures. Being self-containing materials with thickness below 1 nm and known short-range order, bilayer structures act as an open object for surface science researches as well as prospective 2D materials for electronic, catalytic and membrane technologies.[137–140] Before the bilayer structure of oxides was discovered, the pseudohexagonal structure of monolayer SiO_2 on molybdenum surface was studied in details.[141] In 2000, physical vapor deposition (PVD) of silicon onto clean Mo(112) single crystals was performed in UHV conditions followed by oxidation in 5×10^{-5} mbar of O_2 at 800 K by Schroeder et al. After four cycles of exposition and oxidation, the sample was annealed in 5×10^{-6} mbar of O_2 at 1100 – 1150 K. The hexagonal-like crystal structure with a lattice parameter of ~ 5.2 Å was commensurately grown on Mo(112) structure according to LEED studies, and fully oxidized silicon state was confirmed by XPS and Auger electron spectroscopy (AES). The ultrathin film of SiO_2 was found to protect the molybdenum support from oxidation, while the uncovered metal was oxidized to MoO_2 after annealing in an oxygen-containing atmosphere.[142] Later, the structure of the film was defined using a multi-technique approach with STM, infrared reflection absorption spectroscopy (IRRAS), electron energy loss spectroscopy (EELS) and DFT calculations. The monolayer silica was revealed to be a 2D network of corner-sharing [SiO_4] tetrahedra forming (2 × 2) structure on (112)Mo as shown in Figure 3.11a. One corner is based on molybdenum atom that provides stabilization and results in an intensive vibrational mode at ~ 1060 cm^{-1} assigned to the asymmetric stretching of Si-O-Mo bonds. The resulting stoichiometry of one monolayer (1 ML) is $SiO_{2.5}$. Deposition of silicon in a larger amount, for example 2 or 3 ML, led to reconstructed cristobalite structures.[143,144]

Annealing at high temperatures led to the removal of an excess material leaving only a monolayer $SiO_{2.5}$ that was referred to self-limiting growth on Mo(112).[139,145] Stacchiola et al. proved the possibility of preparing an aluminosilicate monolayer on molybdenum surface. Aluminum (Al) and silicon were co-deposited on the preoxidized Mo(112) in 5×10^{-8} mbar of O_2 at 900 K followed by annealing at 1100 K in UHV. As a result, the aluminosilicate monolayer exhibited a structure similar to $SiO_{2.5}$/Mo(112) with partially substituted Si atoms on Al, but the aluminum atoms were coordinated by three oxygen atoms [AlO_3] that were not bonded to the molybdenum support.[146]

The history of bilayer oxides began with the discovery of bilayer silica (BS) by Löffler et al. in 2010. The Ru(0001) surface was exposed to 1×10^{-7} mbar of O_2 at 373 K for 5 minutes to form O(2 × 1) structure of chemisorbed oxygen to prevent intermixing of silicon and metal. The substrate was covered with 1.3 ML of silicon at 630 K applying the same oxygen pressure in the chamber. The resulting film was amorphous and silicon was not fully oxidized according to LEED and XPS study. The sample was annealed in 2×10^{-6} mbar of O_2 at 1140 K for 15 minutes to form an ordered film. After annealing, most of the chemisorbed oxygen atoms became part of the new structure according to XP spectra. AFT, STM and LEED methods revealed hexagonal structure with a lattice parameter of 5.42 Å. DFT calculations of vibrational spectra for bilayer structure was consistent with IRRAS results. Both monolayers are mirror-symmetrical with respect to the plane passing through the oxygen atoms in the middle of the structure as shown in Figure 3.11b. IRRAS spectrum exhibited two sharp peaks at ~ 1300 cm^{-1} and 692 cm^{-1} corresponding to asymmetric and symmetric stretching vibrations perpendicular to the substrate plane in Si-O-Si bonds, respectively. Silicon was fully oxidized giving stoichiometry SiO_2 for the first bilayer oxide structure.[147]

Yang et al. revealed different silica structures on ruthenium (Ru) support depending on coverage.[148] Clean Ru(0001) single crystals were exposed to 3×10^{-6} mbar of O_2 at 1200 K for 5 minutes to prepare denser coverage of chemisorbed oxygen 3O(2 × 2) followed by cooling until 500 K in the same atmosphere. The same potential was applied to the substrate as for the silicon rod to prevent ions acceleration during electron beam-assisted PVD. The substrate was cooled down to ~ 100 K to improve adhesion, and different silicon coverages were deposited in 2×10^{-7} mbar of O_2 using

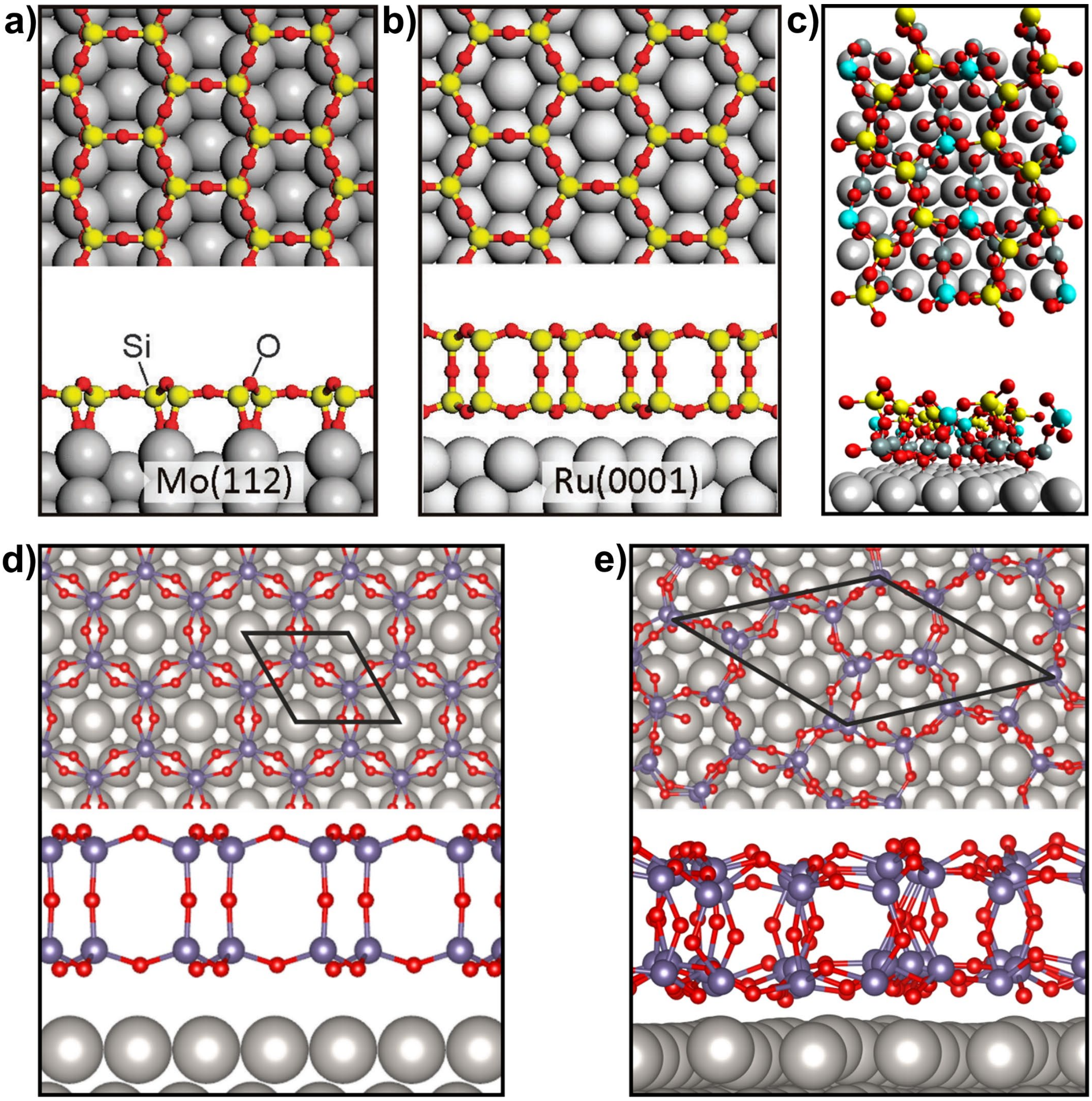

Figure 3.11 – Structures of two-dimensional oxides. **a)** Monolayer silica on Mo(112). **b)** Bilayer silica on Ru(0001). Si atoms are yellow, O atoms are red. **c)** Zigzag structure of silica on Ru(0001). O atoms are red, top Si atoms in zigzag lines are yellow, top Si atoms between the zigzag lines are cyan, bottom Si atoms are dark grey. The structure was imported from Kuhness et al.[149] and visualized in Avogadro free software **d)** Hexagonal bilayer germania on Pt(111). Ge atoms are blue, O atoms are red. **e)** 558 bilayer germania on Pt(111). Ge atoms are blue, O atoms are red. Parts **a)** and **b)** are reprinted and adapted with permission from Yang et al.[148], Copyright 2012 Royal Society of Chemistry. Parts **d)** and **e)** are reprinted and adapted with permission from Lewandowski et al.[150], Copyright 2019 John Wiley and Sons.

a $SiO_{2.5}$/Mo(112) system as a reference under XPS control. Finally, the films were annealed at 1200 K in 3×10^{-6} mbar of O_2. The coverage with 1 ML resulted in a hexagonal monolayer structure (2 × 2) with lattice parameter of 5.42 Å on Ru(0001) similar to the structure on Mo(112). The IRRAS spectra had intense peaks at 1134 cm^{-1} corresponding to Si-O-Ru vibrations instead of ~ 1300 cm^{-1} for bilayer structures. Both vibration modes at 1134 cm^{-1} and 1300 cm^{-1} coexisted after deposition of 1.5 ML that indicated a thermodynamically preferred bilayer structure on ruthenium surface, while coverage with 2 ML resulted in only bilayer structure. The cooling rate after last oxidative annealing at 1200 K was found to influence the ordering of BS. Bilayer silica exhibited regular honeycomb-like structures in STM upon slow cooling (below 1 $K \cdot s^{-1}$). Fast cooling (below ~ 5 $K \cdot s^{-1}$) led to the coexistence of a hexagonal regular structure and disordered vitreous phase. XPS and IRRAS measurements showed no substantial differences for BS cooled at distinct rates. In addition, higher crystallinity in BS was observed at lower deposition temperatures. The deposition of 4 ML led to a loss of atomic smoothness and a three-fold decrease in the area of the two-layer structures. It was associated with the formation of 3D networks due to pronounced vibrational modes at 1257 cm^{-1} and 1164 cm^{-1} that are typical for quartz-like SiO_2 structures.[148] Self-limiting growth of bilayer silica on ruthenium was not observed due to the self-sufficiency of the 2D structure which is bound with the metal support by weak van der Waals interactions.[139,145]

Besides monolayer and bilayer silica on Ru(0001), Kuhness et al. discovered new crystalline “zigzag” polymorph of 2D silicon dioxide in 2018. The PVD of 1.8 – 2.2 ML of silicon was carried out on pretreated 3O(2 × 2)-Ru(0001) surface in oxygen-containing atmosphere at room temperature. Final annealing was performed in 2×10^{-6} mbar of O_2 at 1130 – 1180 K for 15 minutes. Rectangular unit cell 9.4 Å × 7.6 Å was found by LEED. The complex structure was simulated using DFT and shown in Figure 3.11c. The yellow Si atoms in sharing-corner [SiO_4] tetrahedra form parallel zigzag lines which were observed in STM. The [SiO_4] tetrahedra with cyan Si atoms are located lower than the yellow ones forming distorted eight-membered rings. Zigzag structure can be considered as an intermediate one between monolayer where some fragments resemble a bilayer SiO_2 without a chemical bond with the support, and some fragments resemble a monolayer $SiO_{2.5}$ with Si-O-Ru bonds that gives the stoichiometry of $SiO_{2.17}$. The silica zigzag polymorph being metastable phase can be transformed into crystalline bilayer silica upon annealing at 1260 K for 10 minutes in oxygen-containing atmosphere.[149]

In 2012, Huang et al. reported about formation of bilayer silica on supported graphene by accident in a CVD setup. A polycrystalline copper foil on a quartz substrate was placed into a quartz tube followed by heating at 950 °C in the flow of forming gas (Ar/H_2) at a pressure of ~ 5 mbar. The flow was interrupted and the Cu sample was fed with 0.5 mbar of hexane vapor for 1 minute followed by cooling under the forming gas flow. Probable air leaks could oxidize copper and resulted in silica formation. The Cu support was etched in nitric acid and graphene/silica film was transferred onto TEM grids without polymer coating. As a result, the first TEM images of bilayer silica with atomic resolution were obtained. Mostly vitreous BS with crystalline inclusions was observed due to the large lattice mismatch of 7 % between graphene and silica lattices. The lattice parameter for crystalline BS was 5.3 Å according to diffractograms. Vitreous BS consisted of tetrahedra that were disordered in two dimensions but oriented in the third direction perpendicular to the graphene plane. The rings in amorphous regions were formed from three to ten corner-sharing tetrahedra units.[151]

The atomic structure of vitreous and crystalline phases of BS was studied by Lichtenstein et al. using STM and non-contact AFM at 5 K in UHV. A bilayer silica on Ru(0001) was prepared according to an original procedure and cooled after final annealing at different rates to govern the crystallinity.[152–155] The STM images of crystalline and vitreous BS showing the positions of oxygen atoms are presented in Figure 3.12a and Figure 3.12b, respectively. Crystalline BS with long-range order was found to consist of six-membered rings where corner-sharing [SiO_4] units are consistent with the (2 × 2) structure on Ru(0001) and characteristic Si-Si-Si angle amounts to 120.2 ± 6.3°. The distance between the closest silicon atoms was 3.12 ± 0.08 Å in hexagonal bilayer structure.[153,154] Later, Björkman et al. revealed point defects in crystalline BS on a graphene support using aberration corrected high resolution transmission electron microscopy (AC-HRTEM). The defects were found to be similar to those in graphene and represented combination of five- and seven-membered rings: Stone-Wales (Figure 3.12c), flower (Figure 3.12d), divacancy (Figure 3.12e) and cross-shaped (Figure 3.12f) defects.[156] Burson et al. using STM showed that crystalline BS on ruthenium has domain boundaries consisted of alternating five- and seven-member rings but four- and eight-membered rings were also found.[157]

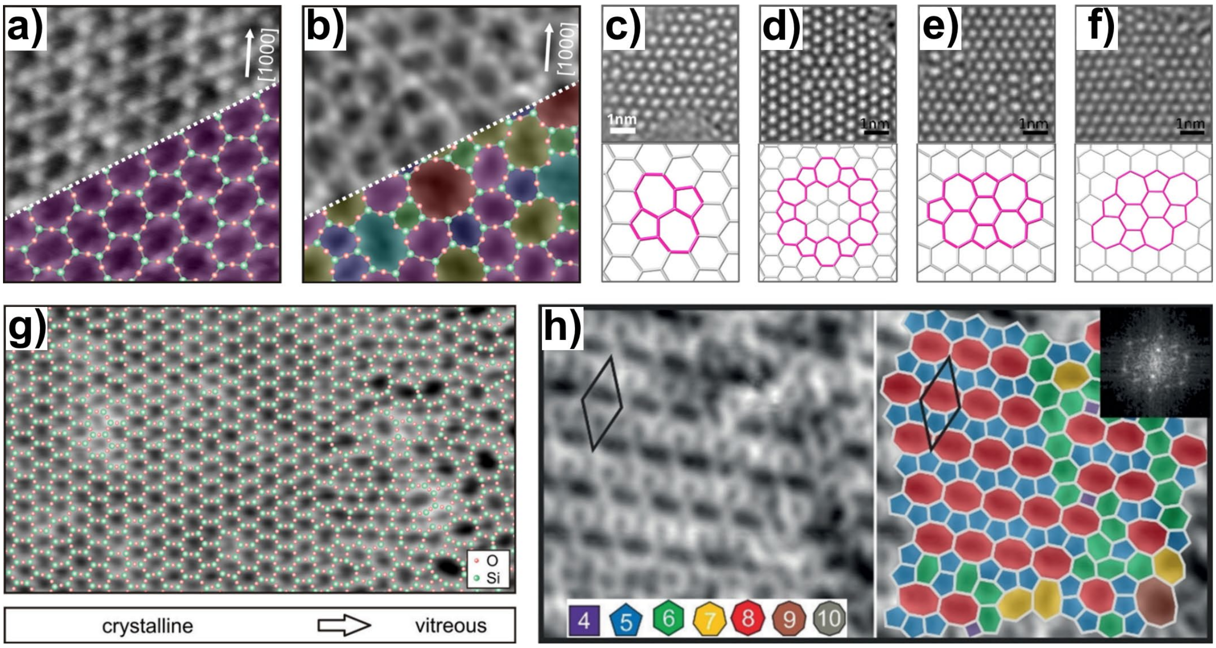

Figure 3.12 – Microscopy images of bilayer oxides. **a)** STM image of crystalline BS showing the arrangement of oxygen atoms with superimposed structure. **b)** STM image of vitreous BS showing the arrangement of oxygen atoms with superimposed structure. **c)** AC-HRTEM image of Stone-Wales defect in BS and its scheme. **d)** AC-HRTEM image of flower defect in BS and its scheme. e) AC-HRTEM image of divacancy defect in BS and its scheme. **f)** AC-HRTEM image of cross-shaped defect in BS and its scheme. **g)** STM image of crystalline-vitreous interface in BS with superimposed structure. Si atoms are green, O atoms are orange in the superimposed structures on bilayer silica. **h)** STM image of crystalline bilayer germania and STM image with superimposed color-coded rings. Inset is a fast Fourier transform representation of the STM image. Parts **a)** and **b)** are reprinted and adapted with permission from Lichtenstein et al.[154], Copyright 2012 American Chemical Society. Parts **c)** – **f)** are reprinted and adapted from open access article[156], Copyright 2013 Creative Commons CC BY license. Part **g)** is reprinted and adapted with permission from Lichtenstein et al.[153], Copyright 2012 American Physical Society. Part **h)** is reprinted and adapted with permission from Lewandowski et al.[150], Copyright 2019 John Wiley and Sons.

In oppose to crystalline phase, vitreous BS exhibited complex network with four-, five-, six-, seven-, eight-, nine-membered rings. Six-membered rings are more common than others leading to characteristic Si-Si-Si angle of 120.2 ± 14.7° and the average distance between silicon atoms of 3.01 ± 0.12 Å.[152,154] The STM image with atomic model of crystalline-vitreous interface is shown in Figure 3.12g. The 1.6 nm-length buffer region was consisting of five- and seven-member rings.[153] According to DFT calculations, six-membered rings were revealed to be the most stable. In this way, vitreous bilayer silica was suggested to be a metastable phase.[152] The phase transformation in perfectly crystalline BS on Ru(0001) was observed by Klemm. The

DFT calculations with temperature-dependent measurements were carried out in oxygen-containing atmosphere and UHV applying LEED and XPS methods. The ruthenium support facilitated crystalline-to-vitreous transformation in BS, while a reverse transformation vitreous-to-crystalline was supposed to be impossible.[158]

The first bilayer aluminosilicate was synthesized by Boscoboinik et al. in 2012. Sequential deposition of Si and Al on 3O(2 × 2)-Ru(0001) surface was carried out in 2×10^{-7} mbar of oxygen followed by oxidative annealing in 3×10^{-6} mbar at 1200 K for 10 minutes and slow cooling. The sum of the molar amounts of Si and Al was equivalent to 2 ML. The maximum molar fraction of aluminum was declared to be 0.5 ($Al_{0.5}Si_{0.5}O_2$) because the Al-O-Al linkage in zeolitic frameworks is forbidden. Thus, the Al molar concentration above 25 % was considered as high concentration of aluminum in structure. According to STM analysis consistent with DFT calculations, Al atoms substituted silicon atoms in the bottom tetrahedra at small concentrations resulting in flat hexagonal networks with domain boundaries similar to bilayer silica. In oppose to zeolites, Al atoms in [AlO_4^-] tetrahedra were segregated in regions, but a new phase of pure Al_2O_3 was not found. The charge imbalance in bilayer aluminosilicate was compensated by the metal support, and protonation could also stabilize the structure. High Al concentration led to coexistence of crystalline and vitreous aluminosilicate bilayer where aluminum occupied top tetrahedra as well. The intensity of the characteristic peak in IRRA spectra did not decrease with increasing Al content but there was a slight red shift.[159] For instance, bilayer aluminosilicate $Al_{0.36}Si_{0.64}O_2$ exhibited intense peak at1277 cm^{-1} in vibrational spectrum. The vitreous phase contained of four- to eleven-membered rings, but five- and six-membered rings were the majority.[160]

Besides the surfaces of ruthenium and graphene-covered copper, bilayer silica was prepared on other metals. Yu et al. reported about preparation of BS on Pt(111) single crystals.[161] Silicon was deposited on platinum surface with chemisorbed oxygen O(2 × 2) at ~ 100 K in oxygen-containing atmosphere via electron beam PVD. Final oxidation was carried out in 1×10^{-5} mbar of O_2 at ~ 1200 K. According to LEED and STM analyses, only vitreous bilayer silica was formed on platinum due to larger mismatches in surface structures compared to ruthenium. While the lattice constant in unsupported bilayer silica was predicted to be 5.3 Å,[162] the surface structures (2 × 2) have parameters of 5.42 Å for Ru(0001) and 5.54 Å for Pt(111). Deposition of 1 ML resulted in partial coverage of BS because inert platinum having less affinity towards oxygen and bilayer oxides is more preferable than monolayer silica with Si-O-Pt bonds.[161] Altman et al. prepared crystalline BS on Pd(100) where square (2 × 2) structure had a period of 5.50 Å. Silicon was deposited on the pretreated palladium single crystal at 550 – 600 K in ~ 10^{-6} mbar of O_2. The deposited thick films exhibited no diffraction pattern, but the annealing at 975 – 1075 K in oxygen-containing atmosphere resulted in crystallization of hexagonal bilayer structure. The self-limitation on palladium surface was observed even for coverage with 5.1 ML due to probable decomposition and diffusion into the metal crystal. As a result, the bilayer silica was strained and commensurately grown along the Pd[011] direction. The bilayer silica did not match the substrate in the perpendicular Pd$[0\bar{1}1]$direction but remained crystalline. The tensile stress of the epitaxial structure was relieved by periodic domain boundaries which were located much more often along the Pd[011] direction making domain elongated in the Pd$[0\bar{1}1]$ direction.[163] Using Pd(111) surface with hexagonal symmetry, Jhang et al. reported about incommensurate growth of crystalline BS applying molecular beam epitaxy (MBE). In the study, no differences were noted between an expensive palladium single crystal Pd(111) and a cheaper epitaxial thin film Pd(111). 2ML of SiO_2 were deposited on clean Pd(111) surface using an effusion cell with SiO in ~ 2 × 10^{-6} mbar of O_2 followed by annealing in the same atmosphere. Moiré patterns were observed in LEED and STM as superposition of mismatched lattices of palladium and bilayer silica. In oppose, the bilayer aluminosilicate $Al_{0.25}Si_{0.75}O_2$ was epitaxially grown by co-deposition of SiO_2 and Al on Pd(111) using the same procedure. According to DFT calculations, Al-O bonds were predicted to be longer that reduced strain and allowed the commensurate growth of strained aluminosilicate structure.[164] Hutchings et al. prepared crystalline BS on the surface of $Ni_{0.48}Pd_{0.52}$ alloy. The alloy thin film (50 nm) was deposited on Cr_2O_3(0001)/Al_2O_3(0001) substrate via MBE followed by annealing. The palladium content was chosen to be 52 % to have best match with lattice of crystalline bilayer silica. The distance between atoms on (111) plane was 2.63 Å that is 5.26 Å for (2 × 2) structure. This parameter was very close to the lattice constant of 5.30 Å in unstrained crystalline BS. After MBE process and annealing, the epitaxially grown bilayer silica was confirmed by LEED and STM methods.[165] However, a prolonged annealing at high temperature in ~ 10^{-6} mbar of O_2

led to migration of Ni atoms into bilayer structure forming 2D Ni silicate which was chemically bound with Ni_xPd_{1-x} support. Despite perfect matches between lattices, the crystalline BS was shown to become vitreous silica after annealing at low oxygen pressure (~ 10^{-8} mbar) due decomposition into volatile SiO and O_2.[166,167]

A solid state growth of silica bilayers on iron (Fe), cobalt (Co) and Ru nanoparticles was directly observed in transmission electron microscope by Ben Romdhane et al.[168,169] The metals were sputtered on 10 nm-thick SiO_2 films followed by annealing at 973 K that led to formation of plate particles with a thickness about 10 nm. The growth of honeycomb-like structures began in few minutes after cooling until 723 K at pressure of ~ 10^{-7} mbar. The growth occurred at temperatures above 623 K. It was supposed that Si atoms diffused through nanoparticles and formed 2D SiO_2 on the clean metal surface. A bilayer silica with a thickness of 7.2 Å was formed on Ru and Co surfaces, while a monolayer silica with a thickness of 3.4 Å was found on Fe surface.[168] If surface steps prevailed on the metal substrates, the growth of 1D chains of monolayer $SiO_{2.5}$ was favorable in all metals.[169]

Recently, new two-dimensional structures based on germanium dioxide (germania) were synthesized on various supports by Lewandowski et al. using PVD of Ge in 2×10^{-6} mbar of oxygen followed by annealing in the same atmosphere.[170] Firstly, a germania monolayer was obtained on pretreated 3O(2 × 2)-Ru(0001) surface in 2018. A monolayer $GeO_{2.5}$ was found to be similar to the silica monolayer $SiO_{2.5}$ on Mo(112) and Ru(001) being hexagonal network of corner-sharing [GeO_4] tetrahedra which is chemically bound with metal support via Ge-O-Ru bonds. Since Ge-O-Ge bonds is longer than in silica, the germania structure was compressed that led to smaller angles in Ge-O-Ge bonds.[171] The DFT calculation predicted stronger interaction of bilayer germania with metal substrates compared to bilayer silica. The adhesion energies were supposed to be -1.76 eV·nm^{-2} for SiO_2/Ru(0001) and -6.78 eV·nm^{-2} for GeO_2/Ru(0001). In this way, the covalently bound monolayer germania was more preferable for the ruthenium substrate. A very distorted structure of bilayer germania coexisting with the monolayer $GeO_{2.5}$ was observed by STM on Ru(0001).[172] The smaller adhesion energy (~ -2.4 eV·nm^{-2}) was predicted for bilayer GeO_2/Pt(111) system. The platinum surface for germanium dioxide behaved like the ruthenium surface for silicon dioxide. A low coverage with germanium led to the monolayer

$GeO_{2.5}$/Pt(111) with prevailing six-membered rings. DFT calculations predicted two stable bilayer phase of GeO_2 on platinum surface: hexagonal lattice with parameter of 5.47 Å and 558 monoclinic lattice which are presented in Figure 3.11d and Figure 3.11e, respectively. The germania bilayer exhibited more distorted [GeO_4] tetrahedra and lower symmetry compared to BS. Bilayer GeO_2 structures had no mirror plane of symmetry between its layers due to the rotation of the top and bottom [GeO_4] tetrahedra. Indeed, higher coverage of Ge resulted in bilayer phases on Pt(111). It was concluded that a higher temperature (900 K) in the final oxidative annealing led to higher crystallinities while lower temperature (800 K) resulted in low order despite slow cooling (~ 1 $K \cdot s^{-1}$). By varying the annealing temperature, three phases of bilayer germania, with prevailing five-membered rings, designated as crystalline, intermediate and amorphous were obtained on Pt(111). The crystalline phase was consisted of nanodomains with five- and eight-membered rings (588 structure) and rows of six-membered rings as can be seen from STM image with superimposed color-coded rings in Figure 3.12h. The intermediate phase exhibited some arrangements of rings where eight-membered rings had orientation and was surrounded with five-membered rings. The amorphous phase was fully disordered and the rings did not follow any distribution and orientation.[150] In addition, the complex zigzag phase of GeO_2 with a rectangular unit cell 9.6 Å × 8.3 Å was also revealed on Pt(111) by STM analysis.[170] The minimal adhesion energy (~ - 1.6 $eV \cdot nm^{-2}$) was predicted for bilayer GeO_2/Au(111) interface. Another amorphous phase of bilayer germania was revealed on reconstructed Au(111) surfaces by STM. The formation of monolayer germania was not confirmed. Amorphous bilayer germanium dioxide with prevailing six-membered rings was formed after oxidative annealing at temperatures as low as ~ 580 K.[173]

In summary, the structure of bilayer oxides is influenced by many factors. The inert substrate without affinity to oxygen is preferable for bilayer formation.[148,150,159,161,163,164] For the best quality, the clean surface should be as flat as possible with a minimum of atomic steps.[169] The lattice mismatch between the oxide and the support determines the phase composition of the film: the smaller mismatch, the greater crystallinity.[151,161,164,165] The coverage below 2 ML can result in loose vitreous structure[139] or monolayer oxide, while the coverage above 2 ML is able to blur bilayer structure forming 3D network.[148] A low deposition temperature can improve the crystallinity of 2D oxide.[148] Atmospheres with low oxygen content during the final annealing may provide decomposition of bilayer oxide.[166] High annealing temperatures could facilitate transformation from crystalline state into vitreous state. A low cooling rate after final oxidative annealing favors the crystallinity.[148]

3.3.2 Properties of bilayer oxides

At present, mechanical properties of bilayer oxides were measured only in theory. A bilayer silica should be quite a stable and stiff structure according to DFT calculations.[174] The Young's moduli were estimated by molecular dynamics simulations to be 416.2 GPa for crystalline BS and 270.2 GPa for vitreous BS that makes them comparable in strength to graphene. Brittle ruptures were predicted for crystalline phase, while vitreous bilayer silica was supposed to be a ductile 2D material.[175] The high mechanical stability of bilayer silica was demonstrated by Büchner et al. through transferring the millimeter-sized 2D material. The BS grown on Ru(0001) was spin coated with PMMA solution in acetone. The 300 µm-thick polymer layer was mechanically cleaved from ruthenium support and transferred onto clean a Pt(111) crystal. The mechanical exfoliation with adhesive tape instead of PMMA was not successful due to a high adhesion of silica on ruthenium. The polymer layer was fully evaporated at 573 K for 3 hours. Intact vitreous bilayer silica on platinum and empty surface of ruthenium was confirmed using LEED and STM methods.[176]

Concerning permeability, the adsorption of various molecules on supported 2D oxides was studied. The epitaxial monolayer silica on Mo(112) was shown to be impermeable for D_2 using TDS methods. The film was exposed to ~ 2.7×10^{-5} mbar·s of D_2 at 200 K, and the following desorption was measured by mass spectrometer. The clean Mo(112) substrate exhibited a high desorption rate after 300 K, while deuterium does not adsorb on silicon dioxide at temperatures above 100 K. A full coverage with crystalline silica monolayer provided complete blocking of D_2 adsorption implying that hexagonal pores were too small for deuterium molecules.[142] Wendt et al. studied water adsorption in 2D silica on Mo(112) via multi-technique approaches using TDS, UPS, EELS and metastable impact electron spectroscopy (MIES). The samples were annealed at temperatures above 1000 K in oxygen-containing atmosphere, and the presence of hydroxyl (silanol) groups was not clear. The fraction of hydroxyl group was estimated at most 9 %. The TDS analysis revealed water desorption at 160 – 180 K. It was concluded that the hydrogen bonding between H_2O molecules was stronger than the

H_2O-SiO_2 interaction, and clustering of water began at very low coverages on silica surfaces.[177]

The adsorption of labeled carbon monoxide ^{13}CO on bilayer silica on Ru(0001) was studied by Yang et al. using the TDS analysis. The samples were exposed to ~ 6.7 × 10^{-6} mbar·s of ^{13}CO at ~ 180 K. Vitreous BS demonstrated ten-fold higher adsorption capacity than the crystalline phase. Carbon monoxide desorbed from crystalline BS at temperatures about 200 K. The desorption peaks at 320 K and 450 K for the vitreous phase were at the same temperature as for the 3O(2 × 2)-Ru(0001) surface.[148]

Büchner et al. researched adsorption of Au and Pd atoms on bilayer silica supported on Ru(0001). The metals were deposited at 150 K using PVD and studied with the AFM and STM methods at 5 K. As a result, single atoms and clusters below 0.9 nm were observed. Palladium ad-atoms were uniformly distributed over crystalline and vitreous regions, while gold ad-atoms were found only on vitreous BS and on domain boundaries with eight-membered rings. A decrease in the binding energy in ad-atoms in comparison with larger clusters on the silica surface was observed in the photoelectron spectra, and it was explained by the lower coordination of ad-atoms in the silica pores and charge transfer to the ruthenium surface. DFT calculations predicted the preferred interaction of ad-atoms with the ruthenium surface rather than with the silica surface. The energy barriers to pass through six-membered ring were negligible for Pd (< 0.1 eV) and significant for Au (~ 0.82 eV). It was assumed that the gold atoms pass the seven-membered rings with a negligible barrier (< 0.1 eV), while the eight-membered ring contains no barrier at all.[178] Later, Akter et al. reported that Pd atoms from 2 nm-thick palladium film on crystalline 2D $Al_{0.35}Si_{0.65}O_2$ were able to migrate though this bilayer aluminosilicate structure upon heating at 530 K.[179]

Emmez et al. researched adsorption of CO and D_2 on supported BS using TDS and IRRAS methods. The bilayer SiO_2/Ru(0001) was exposed to ~ 10^{-9} mbar of CO and ~ 10^{-6} mbar D_2 at 150 K. Desorption in bilayer silica occurred at higher temperatures compared to bare Ru(0001) surface. The presence of silica on ruthenium reduced the adsorption capacity by only 35 % concluded from integral desorption signals. The gases were supposed to permeate through pores and adsorb on Ru(0001) surface. Deuterium molecules dissociated on metal surface and quickly diffused underneath the bilayer silica. In contrast, the surface diffusivity of CO was low. The bilayer SiO_2 at room temperature was subjected to short-term exposure to 10^{-6} mbar of CO and then to 10^{-6} mbar of D_2 that led to an increase in D_2 desorption temperature. This phenomenon was explained by the limited surface diffusion for deuterium due to adsorbed CO molecules on ruthenium, while D_2 desorption was possible only through certain pores. It was concluded that six-membered rings in crystalline bilayer silica are impermeable for D_2 and CO molecules, but eight-membered rings in vitreous BS were supposed to be suitable for gas passage.[180] Similar adsorption behaviors of D_2 and CO on vitreous bilayer silica on Pd(111) were reported later.[181] Schlexer et al. estimated the energy barrier for CO passage through six-membered rings in free-standing silica as 0.5 eV that makes permeation rather unfavorable than impossible.[182] The investigation of metal oxidation beneath bilayer oxides revealed passivation feature. The bare Ru(0001) single crystal and bilayer silica on Ru(0001) were exposed to 10^{-5} – 15 mbar of O_2 at 700 K for 45 minutes for metal oxidation. Then the ruthenium oxide was decaying during TDS measurements. In comparison with bare metal, SiO_2/Ru(0001) system exhibited significantly lower desorption peaks at higher temperatures. It was assumed that oxygen atoms take time to recombine into O_2 molecule and find a suitable pore in BS structure to leave the interface. Moreover, bilayer silica was prepared with labeled oxygen ^{18}O, and there was no decomposition or substitution in the silicon dioxide structure under oxidative annealing. The bilayer aluminosilicate $Al_{0.25}Si_{0.75}O_2$ on Ru(0001) was revealed to protect ruthenium from oxidation to a greater extent.[183]

Boscoboinik et al. modified the bilayer aluminosilicate on Ru(0001) with hydroxyl groups by exposition to water vapor at ~ 100 K followed by heating until 300 K. IRRAS revealed only small amount of silanol groups (Si-OH) in pure bilayer silicon dioxide. Bridging hydroxyl groups (Si-OH_{br}-Al) were found in bilayer aluminosilicate with high Al content (more than 25 %). These OH_{br} groups were strongly acidic and formed adduct $[OH_{br}]^{\delta+}[CO]^{\delta-}$ in 2×10^{-5} mbar of CO under IRRAS study. Also, a hydrogen-to-deuterium exchange was found when D_2O molecules were adsorbed by OH_{br} at 100 K, and deuterium-containing bridging hydroxyls OD_{br} remained after water desorption at 300 K. Bridging hydroxyl groups in bilayer aluminosilicate showed thermal stability up to 650 K.[159]

Jhang et al. investigated water adsorption in bilayer SiO_2 and on Pd(111). The films were annealed after deposition at 1000 K. Then the samples were immersed in water or treated with deuterium plasma to form hydroxyl groups on the surface. The TDS experiments found that desorption behavior on supported bilayer silica was similar to desorption on bare Pd(111) surface. Since DFT calculations predicted very weak interactions between water and bilayer silica, water molecules were supposed to permeate pores and adsorbed on the metal. The barrier for water permeation through six-membered rings was estimated to be 0.303 eV. Surface modifications of 2D aluminosilicate led to stronger H_2O bonding expressed in higher desorption temperatures. The acidic groups Al-OH_{br}-Si were predicted to be more stable up to 1100 K. The attenuation in IRRAS signal at temperatures above 550 K was attributed rather to the IR-inactive geometry than to the removal of hydrogens from the aluminosilicate structure.[184] Later, hydrogen was demonstrated to permeate through supported bilayer silica and interact with chemisorbed oxygen at SiO_2/Pd(111) interface giving water. Ambient-pressure XPS (AP-XPS) analysis confirmed vanishing of the signal from chemisorbed oxygen (~ 529 eV) on platinum and appearance of molecular water (~ 533 eV) in 0.27 mbar of H_2. The same reaction was observed for 2D aluminosilicate.[185]

Yao et al. estimated gas transport though various pores in bilayer silica using density functional theory. The DFT calculations were performed for optimized free-standing crystalline structures and defective structures with 585 divacancy, Stone-Wales defect, 555777 divacancy and tetravacancy. The five-membered rings in such defects could be occupied by spheres with diameters of 0.58 – 0.88 Å. The six-membered rings were supposed to accommodate a sphere with the diameter of 1.92 Å. Spheres with diameters of 2.32 – 2.56 Å could fit into the seven- and eight-membered rings. The largest pore consisted of nine corner-sharing [SiO_4] tetrahedra was spacious for a sphere with a diameter of 4.56 Å. The local minima (red) and local maxima (black) in the potential energy surfaces for gases over the pores are presented with the considered geometries (insets) in Figures 3.13a – 3.13e. The barriers for passage through six-membered rings in crystalline BS (Figure 3.13a) were lower for He, Ne and H_2 predicting possible permeation only for these gases. Carbon monoxide had a lower activation barrier in the oxygen forward orientation marked as “OC”. Seven- and eight-membered rings were predicted to be easier permeable for gases, but the energy

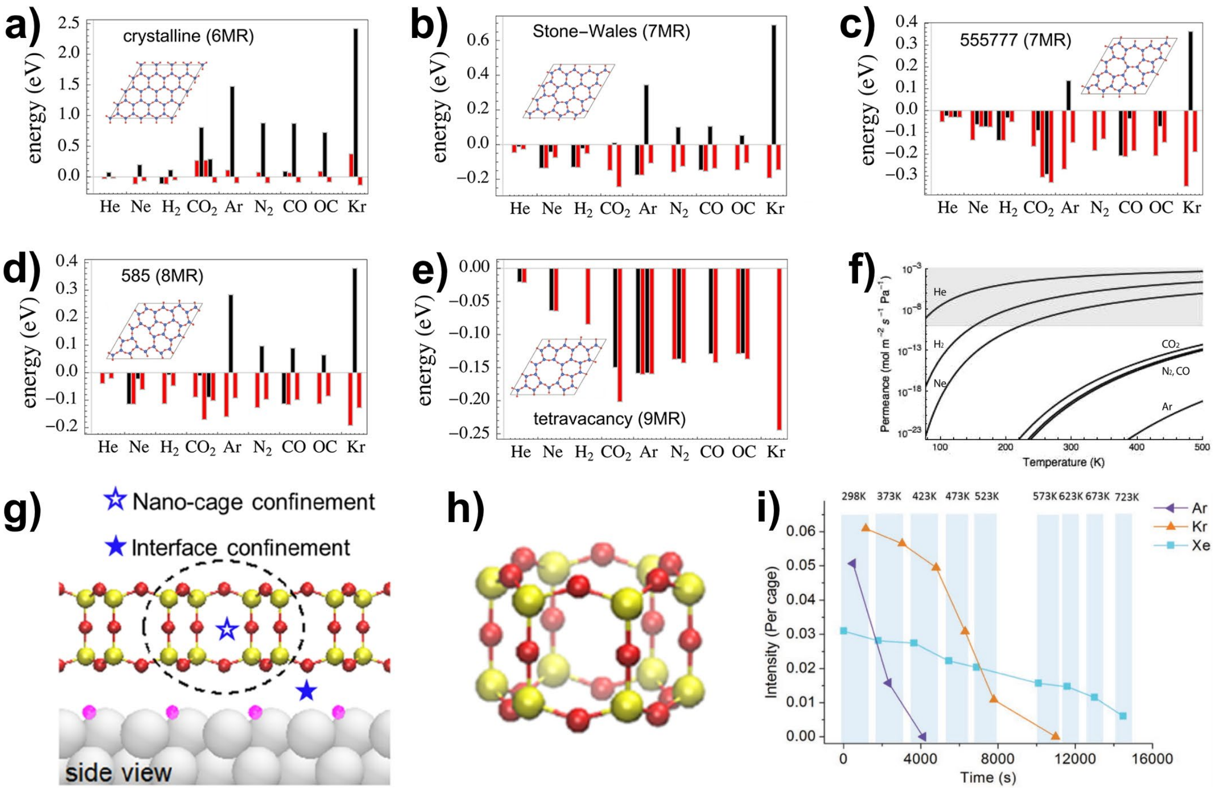

Figure 3.13 – Permeation in bilayer oxides. **a)** Potential energy local minima (red) and maxima (black) for gas transmission in six-membered ring of crystalline BS. Inset is a structure of crystalline BS. **b)** Potential energy local minima (red) and maxima (black) for gas transmission in seven-membered ring of Stone-Wales defect. Inset is a structure of Stone-Wales defect in BS. **c)** Potential energy local minima (red) and maxima (black) for gas transmission in seven-membered ring of 555777 divacancy in BS. Inset is a structure of 555777 divacancy defect in BS. **d)** Potential energy local minima (red) and maxima (black) for gas transmission in eight-membered ring of 585 divacancy in BS. Inset is a structure of 585 divacancy defect in BS. **e)** Potential energy local minima (red) and maxima (black) for gas transmission in nine-membered ring of tetravacancy in BS. Inset is a structure of tetravacancy defect in BS. **f)** Calculated gas permeation rates for crystalline BS depending on temperatures. **g)** Confined spaces in crystalline BS structure with chemisorbed oxygen O(2 × 1) on Ru(0001). Chemisorbed O are pink, Si atoms are yellow, O atoms are red. **h)** Nano-cage in the BS structure (hexagonal pore). Si atoms are yellow, O atoms are red. **i)** XPS signals of noble gases trapped in bilayer aluminosilicate on Ru(0001) depending on time and temperature. Parts **a)** – **f)** are reprinted and adapted with permission from Yao et al.[186], Copyright 2017 American Chemical Society. Parts **g)** and **h)** are reprinted and adapted with permission from Zhong et al.[187], Copyright 2019 American Chemical Society. Part **i)** is reprinted and adapted with permission from Zhong et al.[188], Copyright 2019 John Wiley and Sons.

barriers for argon and krypton seemed to be higher than for other species (Figures 3.13b – 3.13d). The barrierless transmission was predicted for all gases in nine-membered rings as shown in Figure 3.13e. Considering activated transport through pores in bilayer silica, the H_2/CO_2 selectivity was predicted to be ~ 10^{11} for crystalline phase and ~ 20 for vitreous phase. In general, the low selectivity was attributed to vitreous phase compared to crystalline BS. The permeation rates were estimated on the assumption that permeation occurs only if a molecule with sufficient energy collides within a region of the largest fitted sphere in a pore. In this way, 12 % of incident collisions could result in transmission through crystalline BS. The predicted permeances in crystalline BS depending on temperature are presented in Figure 3.13f. The region of industrially acceptable values above 10^{-10} $mol \cdot s^{-1} \cdot m^{-2} \cdot Pa^{-1}$ was marked in grey, and helium, hydrogen and neon were predicted to permeate fast enough for separation process from other gases.[186]

Zhong et al. studied trapping of noble gases in bilayer oxide structures applying AP-XPS.[187–189] The capture of argon atoms was observed in the photoelectron spectra of SiO_2/Ru(0001) at room temperature after exposure to at least 0.2 mbar of Ar, but the IRRAS method revealed Ar capturing at pressures above 2 mbar. Angle dependent XPS measurements distinguished two positions of Ar atoms: inside the structure and under the structure as shown in Figure 3.13g. Most captured atoms were in the silica nano-cage that is presented in Figure 3.13h. The amount of trapped Ar atoms at the interface confinement could be adjusted by the coverage of chemisorbed oxygen on Ru(0001). Thus, the maximum coverage 3O(2 × 2)-Ru(0001) corresponds to the maximum distance of 3.85 Å between BS and metal which allowed to trap more atoms than the interface without chemisorbed oxygen (2.75 Å). In addition, the trapped argon atoms interfered with the CO adsorption that was expressed in a weaker signal of chemisorbed CO in IRRA spectrum compared to bilayer silica without captured argon.[189] Subsequently, capturing of other noble gases were studied. The bilayer silica and aluminosilicate on Ru(0001) were exposed to 2 mbar of individual He, Ne, Ar, Kr and Xe at room temperatures under AP-XPS measurements. Atoms of helium and neon were too small for capturing by the bilayer oxide structure or their interfaces after evacuation. 2D aluminosilicate could capture noble gases only in nano-cages due to stronger electrostatic interaction with ruthenium support and smaller interfacial space. The DFT calculations predicted favorable capturing rather by nano-cages than by interfaces. The energy barriers for trapping were quite high for room temperatures. Since krypton atoms were not trapped without X-ray irradiation, it was concluded that ionized atoms under intense synchrotron X-rays easily pass into the pore due to the smaller size of ions and the polarization between the bilayer oxide and the metal. The trapped ion being neutralized remained stable in the nanocage. For instance, the apparent trapping energy barrier for neutral Ar was + 0.91 eV, while for Ar^+ ion the barrier was - 0.19 eV. The desorption temperatures in bilayer silica were consistent with DFT calculations and correlated with the sizes of noble gases: 373 K for Ar, 473 K for Kr and 623 K for Xe. The bilayer $Al_{0.35}Si_{0.66}O_2$/Ru(0001) was exposed to equimolar gas mixture during AP-XPS measurements followed by heating. The change in concentration depending on time and temperature is shown in the Figure 3.13i. Distinct energies of desorption allowed to release gases at different temperatures.[188]

4 Gas and vapor permeation in carbon nanomembranes

4.1 Introduction

Since membrane technology exhibits the lowest energy costs for an industrial separation, 2D membranes were predicted to be an ideal solution ensuring the shortest path for transmembrane flows. The transport of gases and vapors across ultrathin nanoporous materials is of interest for fundamental investigations and practical problems of membrane separation. Unlike bulk, planar materials allow one to highlight surface phenomena of a transmembrane passage. In this way, intrinsically porous carbon nanomembranes (CNMs) with a high density of channels represent an intriguing platform for the study of mass transfer in nanometer-thick films.

The CNMs were prepared by electron irradiation of aromatic self-assembled monolayers (SAMs). Initially, thiolate SAMs were prepared from 1,1',4'1''-terphenyl-4-thiol molecules on gold substrates. Next, carboxylate monolayers were assembled from p-(terphenyl)-4-carboxylic acid and biphenyl-4-carboxylic acid on the gold substrates pre-covered with silver bilayers by an underpotential deposition resulting in similar carbon nanomembranes after electron cross-linking.

A new methodology was used for the permeation measurements *in situ*. The CNMs were transferred onto Si_3N_4/Si chips with single micron-sized orifices resulting in free-standing films. The samples were mounted in a leak-tight cell of the vacuum setup, and a feed pressure was applied in the upstream compartment. The UHV downstream compartment of the experimental equipment had a quadrupole mass spectrometer (QMS) for the direct detection of permeating species. The transmembrane flow rates were evaluated by comparison with the reference signals through a nanoscale aperture.

The permeation experiments were performed with non-condensable atmospheric gases and different vapors applying single components and binary mixtures to the CNMs. The roles of the molecular size and relative pressure of the permeating substances were considered in the following papers. As a result, it was suggested the phenomenological model for gas and vapor permeation across the CNMs. In addition, coating the CNMs with an ionic liquid (IL) was shown to control the selectivity of the nanomembrane depending on the affinity of the liquid layer.

4.2 Experimental

4.2.1 Preparation of the nanomembranes

Epitaxial 300 nm-thick gold substrates on mica were cleaned with ozone and rinsed with ethanol. To prepare thiolate SAM, an outgassed Au/mica substrate was poured with anhydrous DMF, and 1,1',4'1''-terphenyl-4-thiol (TPT) was added to make a nanomolar solution. The self-assembly took 24 hours at 75 °C in an inert atmosphere. The TPT SAMs were rinsed with DMF, ethanol and blown with dry nitrogen.

For underpotential deposition, the Au/mica substrates were exposed in an aqueous solution with 10 mM $AgNO_3$ and 100 mM HNO_3 at - 10 mV for 2 minutes. The substrates with the silver bilayers were rinsed with ethanol, dried and immersed into solutions with the precursors: either for 20 hours at 65 °C in a water-ethanol mixture with p-(terphenyl)-4-carboxylic acid (TPC) to make TPC SAMs or for 5 minutes at 65 °C in water with biphenyl-4-carboxylic acid (BPC) to produce BPC SAMs.

Electron cross-linking of the SAMs was performed with a dose of 50 $mC{\cdot}cm^{-2}$ in a vacuum chamber using a flood gun. Two layers of 50K and 950K PMMA were applied onto CNMs by spin-coating at 4000 rpm. Then the protected samples were placed onto aqueous iodine solution and metal layers were etched. The PMMA/CNMs films were transferred onto either Si_3N_4/Si chips with single orifices of 4 – 15 μm in diameter or onto TEM grids. The PMMA layers were dissolved in acetone.

To make composite membranes, the acetonitrile solution with the ionic liquid [bmim][Tf_2N] was dropped onto the CNM/Si_3N_4/Si either during rotation or in a static state. The amount of [bmim][Tf_2N] on the samples for permeation measurements was estimated from the IRRAS data. The fluorescence microscope BX51 (Olympus) was applied for a visual control of the droplets of [bmim][Tf_2N].

4.2.2 Characterization of the nanomembranes

The infrared spectrometer VERTEX 70 (Bruker) was connected with a polarization-modulation module PMA 50 (Bruker) to measure the PM-IRRAS spectra for the SAMs, CNMs and IL/CNMs. The spectra were recorded in dry nitrogen flow at a resolution of 4 cm^{-1}. A solution of the ionic liquid in acetonitrile was applied dropwise onto the CNM/Au/mica for a quantitative analysis via PM-IRRAS. The spectra were recorded after drop casting and spin coating of the acetonitrile solution, and the concentrations of [bmim][Tf_2N] on the CNM surface were estimated from the calibration plots. The sample was rinsed with acetonitrile and checked by spectroscopy before each deposition.

The XPS analysis of the SAMs and CNMs was done in the UHV Multiprobe system (Omicron) with a monochromatic X-ray source (AlK_α, 1486.7 eV) and a hemispherical electron analyzer (SPHERA) with a pass energy of 25 eV and step of 0.05 eV. The XP spectra were fitted in CasaXPS software.

4.2.3 Permeation measurements

The vacuum setup for permeation measurements is depicted in Figure 4.1. The Si_3N_4 chip with a CNM was glued onto a copper ring. Then the sample was inserted in the membrane cell of the vacuum setup, i.e. clamped between two conflat flanges. The free-standing nanomembrane divides the inner space of the permeation apparatus into the downstream compartment (the UHV detection chamber with a quadrupole mass spectrometer) and the upstream compartment (a sample channel and mixing chamber). Besides the sample channel, the vacuum setup has a reference channel with the mounted Si_3N_4 chip (the reference cell) with an aperture of ~ 110 nm in diameter. The flow though this nanoaperture was quantified applying the Hertz-Knudsen equation:

$$Z_W = \frac{p_u}{\sqrt{2\pi m k_B T}} , \tag{4.1}$$

where Z_W is the number of gas molecules impinging on an unit area per second ($s^{-1} \cdot m^{-2}$), p_u is the pressure in the upstream compartment (Pa), m is the mass of the gas molecule (kg), k_B is the Boltzmann constant ($m^2 \cdot kg \cdot s^{-2} \cdot K^{-1}$), T is the absolute

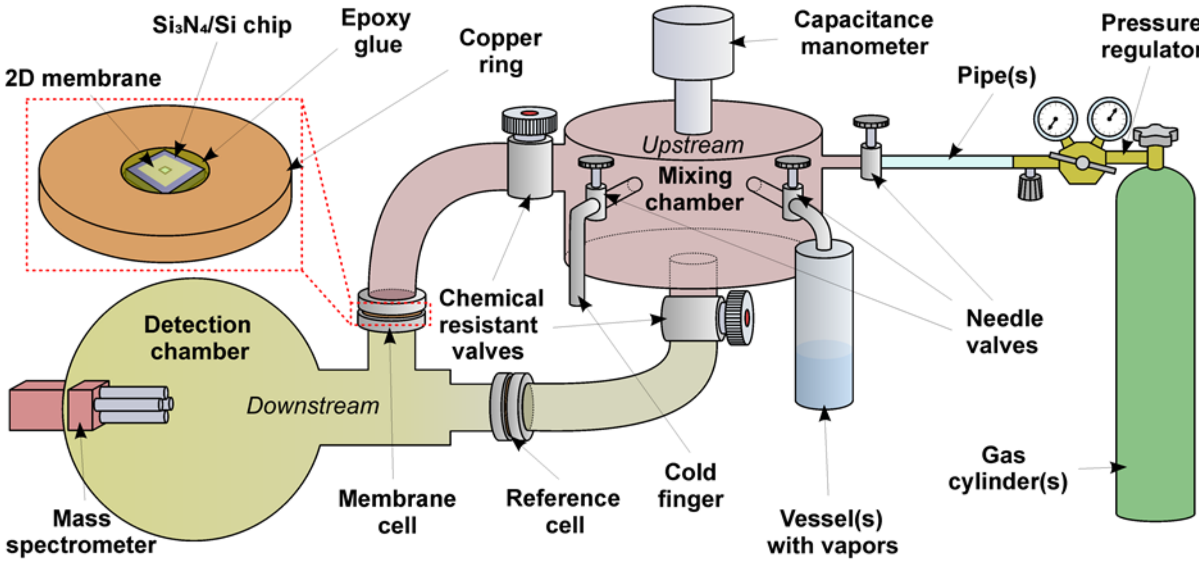

Figure 4.1 – Schematic diagram of the permeation apparatus. The pumps are not shown for simplicity. Figure 4.1 is reprinted with permission from Naberezhnyi et al.[190], Copyright 2021 John Wiley and Sons.

temperature (K). The QMS reference signal I_{ref} (counts·s^{-1}) is recorded in each permeation experiment, while the sample channel is closed by a chemical resistant valve. In this way, the permeance Π (mol·s^{-1}·m^{-2}·Pa^{-1}) in the nanomembrane can be determined as follows:

$$\Pi = \frac{J_{sample}}{A \times (p_u - p_d)} \cong \frac{J_{ref} \times I_{sample}}{A \times p_u \times I_{ref}}, \tag{4.2}$$

where J_{sample} and J_{ref} are the molar flows (mol·s^{-1}) through the membrane and the reference orifice, I_{sample} is the intensity of the QMS signal (counts·s^{-1}) with open sample channel and closed reference channel, p_d is the pressure in the downstream compartment (Pa) that is significantly lower than p_u, A is the nanomembrane area (m^2). To determine the limit of detection for the substance, the calibration slope J_{ref}/I_{ref} was multiplied by 10 times the standard error of the background signal.

The mixing chamber is connected to a roughing pump through a chemically resistant valve (the pumps are not shown in Figure 4.1 for simplicity) and is pumped out between experiments. The sample and reference channels are connected to a turbomolecular pump through chemically resistant valves, and the ultra-high vacuum (~ 2 × 10^{-9} mbar) in the detection chamber is maintained by another turbomolecular pump.

The mixing chamber is connected to pressurized gas cylinders, a cold finger and stainless-steel vessels with liquid substances as shown in Figure 4.1. The gaseous substances are dosed by needle valves, while the feed pressure is controlled by a capacitance manometer. Heavy water D_2O was used instead of regular water H_2O because of lower signal noise for m/z = 20. The vessels with liquids were degasses prior to use.

The cold finger was cooled with a liquid nitrogen to trap a vapor in the experiments with binary mixtures (gas-vapor, vapor-vapor). Then the closed cold finger was heated to the ambient temperature and the vapor was released in the mixing chamber to intermix with another component. The chemical resistant valve on the sample channel was opened after mixing and the QMS signal for both components was recorded simultaneously.

4.3 Results

As previously reported, the CNMs were shown to be highly permeable for water.[85] To compare water permeance with other components, the permeation experiments with binary mixtures at ~ 20 % of relative humidity were carried out. The partial pressure of D_2O was set to be 5 mbar, while the partial pressures of N_2 and $CHCl_3$ were varied from 0 to 45 mbar. In this way, the molar fraction of heavy water was decreasing with an increase in the total pressure. These experiments revealed the constant water permeance, but the permeation rates of nitrogen and chloroform were below the limits of detection.

Further, binary mixtures with other substances were studied at a constant total pressure of 20 mbar and relative humidity of ~ 40 %. Again, the water passage at 10 mbar was shown to be independent of the presence of other components such as helium, nitrogen, oxygen, carbon dioxide, chloroform, toluene and hexane. The permeation rates of these substances at their partial pressure of 10 mbar were not detected and the CNM selectivity towards water was supposed to be at least 100.

Only helium permeation was detectable with a rate of $\sim 2 \times 10^{-8}$ $mol \cdot s^{-1} \cdot m^{-2} \cdot Pa^{-1}$ among other atmospheric gases (Ne, N_2, O_2, Ar, CO_2) in the dry CNMs under a feed pressure of 150 – 250 mbar. Poorly condensable particles weakly interacted with the CNM

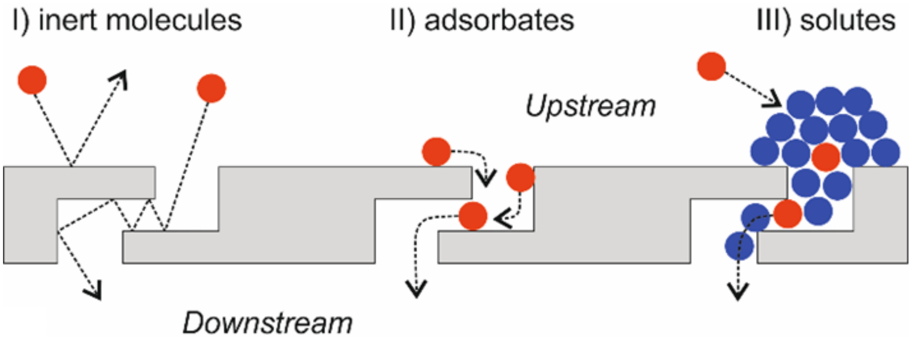

Figure 4.2 – The phenomenological model for molecular permeation in carbon nanomembranes: I) direct impact transfer for non-condensable species; II) surface diffusion for vapor molecules; III) water-assisted permeation. Figure 4.2 is reprinted and adapted with permission from Naberezhnyi et al.[191], Copyright 2019 American Chemical Society.

surface and desorbed back into the gas phase inside the upstream compartment as shown in Figure 4.2, case I. Steric hindrances prevent most gases from permeating, while the smallest helium atoms seem to pass through the CNM with a higher probability.

The transport of condensable water in carbon nanomembranes differs from the transport of inert gases and can be presented in two steps:

$$D_2O^{u}_{gas} \overset{K}{\leftrightarrow} D_2O^{u}_{ads} \overset{k}{\rightarrow} D_2O^{d}_{gas}\ , \tag{4.3}$$

where $D_2O^{u}_{gas}$ is the molecule in a gas phase on the upstream side, $D_2O^{u}_{ads}$ is the adsorbed molecule on the membrane (on the upstream side), K is the adsorption-desorption equilibrium constant, $D_2O^{d}_{gas}$ is the desorbed molecule on the downstream side, k is the effective first-order rate constant (s^{-1}) accounting for the surface and the transmembrane diffusion together. The adsorption-mediated transport for condensable molecules is schematically presented in Figure 4.2, case II). Although it is assumed that a gas permeance is a value independent of pressure, the water permeation rate was found to be strongly dependent on its partial pressure that was consistent with monolayer and multilayer adsorption model. The transmembrane flow rate J (s^{-1}) for condensable species can be described as:

$$J = k_{mono} \times \theta_{mono} \times n_0 + k_{multi} \times \theta_{multi} \times n_0\ , \tag{4.4}$$

where k_{mono} and k_{multi} are the effective rate constants (s^{-1}) for individual and collective motion, θ_{mono} and θ_{multi} are the fractions of the membrane area containing single adsorbates and their agglomerates respectively, n_0 is the total number of adsorption sites. At low relative pressures, individual adsorbates diffuse over the CNMs until they find a pore and pass through it. High relative pressure is supposed to result in formation of water clusters that provide collective flow through the pores enhancing the permeation rate up to 1×10^{-4} mol·s^{-1}·m^{-2}·Pa^{-1}.

Despite the fact that the packing density in TPC SAMs is 8 % higher than in TPT SAMs, electron cross-linking of the TPC SAMs with a dose of 50 mC·cm^{-2} led to carbon nanomembranes with identical properties. The PM-IRRAS and the XPS studies confirmed partial loss of aromaticity and elimination of the carboxylate groups after the electron irradiation resulting in the formation of mechanically stable carbon nanomembranes similar to TPT CNMs. No essential differences were noted between CNMs derived from the thiolate and carboxylate SAMs judging by the permeation rates across them. Similar to water, acetonitrile passed the CNMs with a rate of $\sim 1 \times 10^{-7}$ mol·s^{-1}·m^{-2}·Pa^{-1}, while larger species of chloroform, toluene and tetrahydrofuran exhibited the permeances of about 10^{-8} mol·s^{-1}·m^{-2}·Pa^{-1} in their saturated vapors. Notable, the size cut-off in the CNMs was found for elongated molecules of hexane which could not pass the nanomembrane at all. Therefore, the nanochannels in the CNMs are supposed to be tortuous and narrower inside, which has a significant effect on the transport of molecules larger than water species.

In addition, the collective transmembrane flow at high relative humidity was capable to carry gaseous substances from the mixture through the CNMs as shown in Figure 4.2, case III). Since gases can be dissolved in water in accordance with Henry's Law, water-assisted transport of them with detectable permeances was found. Acetonitrile with a higher solubility in water exhibited the transmembrane flux which was linearly growing with an increase of its fraction in the mixtures at 100 % of relative humidity. These observations were consisted with the linearity of Henry's law. On the contrary, the water-assisted permeation of the larger molecules (chloroform) was not detected. The formation of water clusters on the CNM surface at high relative pressures of D_2O is supposed to be responsible for these phenomena, and the resulting transmembrane flux of solutes is determined by their solubility in water and the molecular sizes of substances.

The hydrophobic IL did not wet CNMs according to optical microscopy, but higher coverages with [bmim][Tf_2N] were able to suppress the water permeation compared to bare nanomembranes. In this way, ten-fold reducing in the water flux was noted if the CNM was completely covered with an IL droplet of tens of microns in size. It was assumed that the entry of the ionic liquid into the pores of the CNM is impossible due to the large size of the cations and anions. The CO_2-philic IL covering the CNM surface resulted in an enhancement of the carbon dioxide transport because of an increase in its number density by a factor of 2.5 in the near-surface layer as compared to uncovered CNMs. While the tortuous nanochannels in the bare carbon nanomembranes hindered the passage of inert molecules, the CO_2 species from the IL layer impinging the CNM surface more frequent led to the higher gas flow through the carbon nanomembranes. The CO_2 permeance of ~ 2×10^{-9} $mol \cdot s^{-1} \cdot m^{-2} \cdot Pa^{-1}$ was an order of magnitude higher than the limit of detection. Despite progress in the mass transfer of carbon dioxide, the permeation rates of nitrogen, oxygen and argon remained undetected. The helium permeance through the composite membranes IL/CNM was reduced. These results were consisted with the solubility coefficients of the substances in the ionic liquid in accordance with Henry's law.

4.4 Conclusion

To summarize the above, carbon nanomembranes being prepared from the thiolate and carboxylate aromatic SAMs appear to have pores with tortuous and narrow interiors at the sub-nanometer scale. The molecular transport across the CNMs can be realized in three ways depending on the size of molecules and condensability of the substances.

In the first case, non-condensable atmospheric gases behave as an ideal gas and permeate the CNMs poorly at a pressure difference about 200 mbar due to steric hindrances. The probability for an inert particle to pass the tortuous nanochannel is assumed to depend on the molecular size, and helium atoms seem small enough for a noticeable direct impact transfer unlike other atmospheric gases. The ionic liquid on the nanomembrane results in an increase in the number density of CO_2 in the near-surface layer that leads to the detectable passage of carbon dioxide, while the He permeance in the IL/CNMs becomes lower in accordance with its solubility in the IL.

In the second case, the adsorption plays a key role in the transport through the CNMs for condensable substances providing a longer residence time on the surface to find a pore. At low relative pressures, vapor molecules cross the nanomembrane as single adsorbates, but the collective flows are supposed to occur in the saturated vapors leading to the highest possible permeation rates for the substances. D_2O molecules as the smallest condensable particles exhibit the highest permeance among the vapors giving the selectivity of the CNMs towards water of $10^3 – 10^4$. The transport of organic solvents through such narrow pores could be slowed down due to their molecular dimensions, and the size exclusion effect was revealed for hexane.

In the third case, poorly condensable species being dissolved in water can pass the CNMs in the collective flow at high relative humidity. While water permeance remained stable and unaffected, the permeation rates of the solutes appear to depend on their solubilities and the molecular sizes.

4.5 Publication: Vapour permeation measurements with free-standing nanomembranes

This article is reprinted with permission from Royal Society of Chemistry. The original paper appeared as:

P. Dementyev, T. Wilke, D. Naberezhnyi, D. Emmrich and A. Gölzhäuser, *Vapour permeation measurements with free-standing nanomembranes*. ***Phys. Chem. Chem. Phys.***, 2019, **21**, 15471–15477.

Contribution:

Preparation of SAMs, electron cross-linking of the SAMs, transfer of the CNMs, permeation experiments and data evaluation were performed by the author.

PCCP

PAPER

View Article Online
View Journal

Cite this: DOI: 10.1039/c9cp03038g

Vapour permeation measurements with free-standing nanomembranes†

Petr Dementyev, * Timo Wilke, Daniil Naberezhnyi, Daniel Emmrich and Armin Gölzhäuser

Received 29th May 2019,
Accepted 25th June 2019

DOI: 10.1039/c9cp03038g

rsc.li/pccp

Mass transfer across porous materials with nanoscale thickness is of great interest in terms of both fundamentals of fluid dynamics and practical challenges of membrane separation. In particular, few-atom thick sieves are viewed as attractive candidates to achieve ultimate permeability without compromising membrane selectivity. In this work, we introduce a vacuum system for studying vapour and gas permeation in micrometre-sized samples of suspended nanometre-thick films. Steady-state permeation rates are measured with a mass-spectrometer directly connected to the downstream side of a membrane cell. A built-in nanoaperture is used as a reference to calibrate the detector *in situ*. A feed compartment is designed in a way that allows for preparing gaseous mixtures of variable composition, including vapours of volatile liquids. Room-temperature measurements with carbon nanomembranes confirm that this material is selective to water vapour and can efficiently separate it from mixtures with a variety of gases and organic compounds. We demonstrate that a high permeance for water is maintained regardless of the molar fraction and discuss its strong pressure dependence by invoking adsorption-related formalism.

1 Introduction

There is a growing interest in exploiting two-dimensional (2D) materials as extremely thin separation membranes.[1] Theoretically, such membranes can yield utmost throughput with least energy costs while their angstrom-scale porosity is likely to result in great separation factors in accordance with molecular sieving principles.[2] The performance of the "nanomembranes" has been extensively explored in computational studies forecasting many interesting physicochemical effects.[3–7] Following the conventional membrane technologies, gas separation and water filtration appear to be the main scope of the experimental efforts in this emerging field of research.[8] However, pervaporation and vapour permeation seem to be somewhat overlooked in spite of the fact that these are closely related processes which have intriguing prospects in renewable energy applications. For example, recovery and dehydration of alcohols with membranes could significantly advance the biofuel production.[9]

In permeation measurements, a sample to be studied is placed between two regions of different chemical potential for a target substance, and the net movement of the respective particles across the sample is monitored by determining their amount on either or both of the membrane sides. Changes in concentration or partial pressure are the practical measures which are governed by the diffusion laws and scale linearly with the membrane area. Although planar nanomaterials are often fabricated on a centimetre-scale, the use of standard methods for studying mass transport properties of the free-standing layers is complicated. Indeed, single layer sheets exhibit outstanding mechanical characteristics, but their breaking strength in the self-supported state is reversely proportional to the lateral dimensions.[10] To be used in the macroscopic environment, these entities have to be carried by a holey support, and the smaller the size of its openings, the more stable the nanomembranes.[11]

The gas transport selectivity in 2D films was first demonstrated with the aid of an atomic force microscope upon measuring leak rates across individual graphene membranes of 5 μm in diameter.[12] Park and coworkers[13] later fabricated arrays of more than 1000 highly porous perforated graphene sieves and employed a conventional cross-flow apparatus for measuring gas permeance, but the size of the suspended sheets was always 4 μm. Frames with 5 μm large holes were also used for studying water pervaporation and ion rejection in graphene nanomembranes by means of weight loss and ion conductance measurements.[14] The same dimensions of the free-standing graphene were recently utilized by Yuan *et al.*[15] to address molecular separation in real gas mixtures by detecting the permeate in the accumulation mode. Despite the remarkable progress in scaling up the production of graphene membranes,[16,17] more fundamental studies on mass transfer in nanometre-thick sheets are still to come, especially for other materials such as molybdenum disulfide[18] and bilayer silica.[19] In this context, the size scale of a few μm seems to be

---

Physics of Supramolecular Systems and Surfaces, Faculty of Physics, Bielefeld University, Bielefeld, 33615, Germany. E-mail: dementyev@physik.uni-bielefeld.de

† Electronic supplementary information (ESI) available. See DOI: 10.1039/c9cp03038g

favourable for working with single nanomembranes as it provides enough mechanical stability to withstand high pressure gradients and mitigate formation of defects while enabling a sufficiently large sample area to observe permeating species.

Recently, we reported on a prototypical experiment where a vacuum scheme was implemented for sensitive detection of gases passing suspended nanomembranes of 5–18 μm in size.[20] The samples were fixed in a leak-tight cell coupled to a quadrupole mass-spectrometer (QMS), and the molecular fluxes were measured in real time with no sweep gas. Since then, we have completely upgraded the upstream compartment of our permeation facility to allow for operation with vaporous compounds and for preparation of arbitrary feed mixtures. This paper describes in detail the system configuration and presents the first measurements on test mixtures permeation through carbon nanomembranes (CNMs).

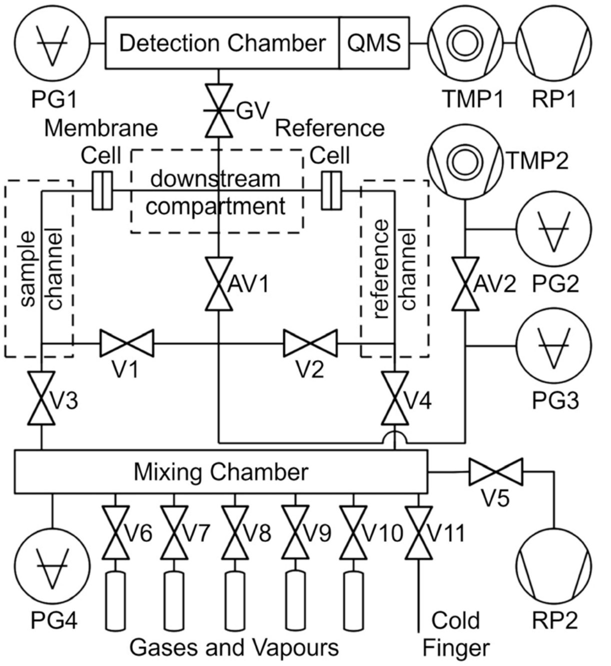

Fig. 1 System overview. The abbreviations designate standard equipment items: PG – pressure gauge, TMP – turbomolecular pump, RP – roughing pump, GV – gate valve, AV – angle valve, V – valve. The specific components are described in Table SM1 (ESI†).

2 Experimental

2.1 System design

Consider a gas permeation experiment with an arbitrary nanomembrane sample of 10 μm in diameter located between an upstream and a downstream compartment which are characterized by the pressure p_u and p_d respectively. Assume that the permeate compartment is well evacuated, *i.e.* $p_d \ll p_u$. The number of gas molecules impinging upon the membrane surface is given by the Hertz–Knudsen equation:[21]

$$Z_w = \frac{p_u}{\sqrt{2\pi m k_B T}} \tag{1}$$

where m is the mass of the gas particle, k_B is the Boltzmann constant, and T is the temperature. Imagine that the effective porosity of the nanomembrane φ is 1%. Given the ideal gas law, the relative change in the total number of molecules in the feed compartment N due to permeation can be estimated as following:

$$\frac{\Delta N}{N} = \frac{\varphi A}{V}\sqrt{\frac{k_B T}{2\pi m}}\Delta t \tag{2}$$

where A is the membrane area, V is the volume of the upstream compartment, and Δt is the time of observation. For experimentally reasonable parameters (T = 300 K, V = 100 cm^3, Δt = 100 s, nitrogen as permeating species), one obtains the value of 10^{-4} indicating that this decrease is hardly to be determined reliably by measuring p_u. On the other hand, this condition allows for straightforward calculation of steady-state permeation rates provided the number of the permeating particles is measured on the downstream side. The corresponding gas flow rate J through the membrane would be on the order of 10^{-12}–10^{-10} mol s^{-1} depending on the applied feed pressure (1–100 mbar) which matches the working range of high-vacuum sensors.[22]

Fig. 1 illustrates schematically the high-vacuum permeation apparatus developed in this study (see also Fig. SM1 in ESI†). It is built around a vacuum chamber with a base pressure of 2×10^{-9} mbar and utilizes a QMS to measure permeation rates in individual nanomembranes. Mass-spectrometry has been widely employed for studying transport of gases through barrier and composite films,[23–25] and the proposed methodology is based on the active pumping approach in which the membrane cell is brought into contact with the constantly pumped detection chamber. Since the incoming molecular flux is equilibrated by the vacuum pump, the steady-state permeation rate to be determined is associated with a partial pressure increase in the chamber:

$$p_d = \frac{JRT}{S_{\text{eff}}} \tag{3}$$

where R is the universal gas constant, S_{eff} is the effective pumping speed of the system, p_d is measured relative to its background level. In QMS, the detected ion current is linearly proportional to the partial pressure, so that accurate quantitative measurements are possible upon calibration. However, the corresponding sensitivity coefficients are known to alter with time, and also the effective pumping speed is always system-dependent.[22] In order to overcome these circumstances, we equip the upstream compartment with a physical leak element of defined conductance which is mounted parallel to the membrane cell and ensures the same geometry for penetrating molecules. In this way, the pressure rise caused by permeation through the sample can be compared on-line to that due to the reference channel, and hence neither the QMS settings nor the volumetric rate play longer a role in evaluation. Now, using eqn (3) and accounting for the linearity of the detector response, one can readily deduce the membrane permeance as follows:

$$\Pi = \frac{J_{\text{sample}}}{A(p_u - p_d)} \simeq \frac{J_{\text{ref}} I_{\text{sample}}}{A p_u I_{\text{ref}}} \tag{4}$$

where J_{sample} and J_{ref} are the molar flows through the membrane and the reference orifice, I_{sample} and I_{ref} are the intensities of the respective QMS signals, $p_d \ll p_u$. Our method allows the transport rates to be probed for a wide range of gaseous substances irrespective of their sensitivity factors, even if these are not known. As the reference, we deploy a nanoaperture proposed by Firpo *et al.*[26] This type of leak devices was proven to be much more resistant to clogging compared to μm-sized openings, and it operates in the free molecular flow regime up to 1 bar upstream pressure. The flow rate J_{ref} is calculated using eqn (1) and taking the geometry of the nanohole into account (Fig. SM2 in ESI†). The reliability of the system was confirmed with another nanoorifice placed in the sample position. Additionally, the reference aperture is used to verify that the mass-spectrometer behaves linearly with the leak rate (Fig. SM3 in ESI†).

2.2 Operating procedure

Unlike centimetre-large polymeric films, free-standing nanomembranes are not ordinary to integrate into high-vacuum apparatus as the layers are usually transferred onto micromachined devices of a few mm in size. Commercially available silicon nitride windows have been proven to be particularly convenient in this regard, and we introduced a special holder for typical 5 × 5 mm^2 chips. The membrane as well as the reference cells represent conflat flanges, and the sample assembly is detailed in Fig. SM4 (ESI†). The downstream compartment is a custom made 4-way cross hosting equivalent flanges for both cells whereas the corresponding upstream flanges are on flexible corrugated hoses (sample and reference channels). Upon inserting a sample, the valves GV, AV2, and V5 are closed, the valves AV1, V1–V4 are open, and the system is vented with nitrogen (Fig. 1). Once the sample is mounted, the upstream and the downstream sides are evacuated simultaneously in order to prevent the damage of the nanomembrane. This is done with the valve V5 and controlled by the gauge PG3 until the pressure is about 1×10^{-3} mbar. Then, the valves V3, V4 are closed, and the downstream compartment is pumped along with the sample and the reference channels by TMP2 through the valve AV2. As soon as the pressure indicated by the gauge PG2 reaches the 10^{-7} mbar range, the valve AV1 is closed, and the permeate compartment is connected to the detection chamber *via* the gate valve. Thanks to the small size of the downstream compartment ($\sim$150 cm^3), the system is left overnight without baking which enables the pressure in the vacuum chamber to approach the base level next day.

The custom-built mixing chamber and the two channels, which are altogether referred to as the feed compartment, are constructed out of all-metal parts in order to impart chemical resistance for dealing with organic solvents. The exception is the high-throughput valves V1–V5 which are fitted with a perfluoroelastomeric sealing and thus have a prolonged lifetime. The mixing chamber has a volume of about 110 cm^3 and carries five inlet ports (valves V6–V10) for admitting gases and vapours. The pressure is measured by means of a capacitance manometer PG4. While gases can be normally mixed by consecutive dosing from high-pressure cylinders, this procedure does not work with vapours because of their low saturation pressure and tendency to condense when overpressed. For this reason, we installed an additional volume of roughly 1 cm^3 (cold finger) which is used to isolate a portion of one vapour before another vapour or gas is let in. More specifically, if a mixture of vapours X and Y needs to be prepared, the target amount of X is first dosed into the mixing chamber and then collected in the cold finger by freezing it with liquid nitrogen. Afterwards, the valve V11 is closed, and Y is admitted to the mixing chamber. The cold finger is heated to the ambient temperature with a water bath, and X is subsequently allowed to intermix with Y. The mixing time depends on diffusion coefficients and changes drastically with the total pressure, therefore the whole process may take up to several hours. We empirically established appropriate time intervals for most frequent experiments.

The mass-spectrometer is warmed up for at least two hours prior to measurements in order to achieve stable background signals. For mixture permeation studies, it is run in the multiple-ion detection mode and set at the base *m*/*z* peaks of the species under investigation. Fig. 2 shows a representative QMS output with the key experimental steps depicted. At first, residual partial pressure is registered for all constituents of the mixture of interest as long as the sample and the reference channels are both pumped by TMP2 (valves V3 and V4 closed). Next, the valve V1 is closed, and a freshly prepared mixture is let to the membrane cell through the valve V3. The volume ratio between the sample channel and the mixing chamber is identified precisely, so that the target feed pressure can be defined in advance. After the steady-state permeation signals are recorded, the valve V5 is open to evacuate the upstream side. Then, the system is switched over to the reference channel as follows: V3 is closed, V1 is open, V2 is closed, V4 is open. Finally, the reference cell is successively fed with the pure ingredients to measure the calibration signals. It is worth noting that the devised vacuum scheme excludes any bypassing

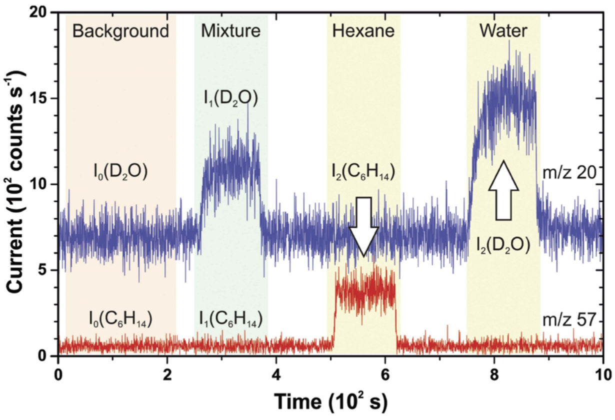

Fig. 2 QMS permeation experiment with a CNM. A 1 : 1 binary mixture of D_2O and C_6H_{14} at the total pressure of 10 mbar was used as the feed. The depicted signals are defined as the mean values of the detector current. The differences $I_1 - I_0$ and $I_2 - I_0$ correspond to the intensities I_{sample} and I_{ref} in eqn (4).

interference between the channels because if one is in operation, the other one is pumped out by the turbopump.

The shot noise in the secondary electron multiplier is known to increase with the absolute signal, as one can notice from Fig. 2. It is possible to improve the signal-to-noise ratio by degrading the time resolution, although we usually acquire the data at default QMS settings (100% dwell time in MASsoft Professional software). The signals of interest are then averaged over extended periods which results in similar standard errors as for longer dwell times. To quantify the limits of detection, we multiply the calibration slope $J_{\mathrm{ref}}/I_{\mathrm{ref}}$ for a given species by 10 times the standard error of the respective background signal. This leads to the minimum flow rate to be measured which is apparently molecule-specific.

2.3 Materials

CNMs were synthesized using gold substrates (Georg Albert PVD) as described elsewhere.[27] Terphenylthiol (Sigma-Aldrich, 97%) was purified by sublimation before use. The films were transferred onto silicon nitride windows with 6.5 μm large holes (Silson Ltd). Heavy water (Sigma-Aldrich, 99.9% atom D), hexane (Fisher Scientific, 95%), toluene (Fisher Scientific, >99.8%), and chloroform (VWR, 99.8%) were repeatedly outgassed prior to permeation measurements. The laboratory gases were supplied by Linde.

3 Results and discussion

As revealed by the previous study, CNMs enable rapid transport of water vapour, whereas the permeation of helium and small molecules is orders of magnitude slower.[20] This 1 nm thick material prepared out of arene molecules *via* electron-induced dehydrogenation appears to be microporous in nature.[20,28] In this study, we examine directly the permeation of water molecules through CNMs when accompanied by other species. Fig. 3 shows water permeance as a function of its molar fraction in binary mixtures with nitrogen and chloroform. Within the experimental error, the presence of the components has seemingly no effect on the transport rate of water that remains the same as in the net state. Heavy water was used instead of regular water for more accurate measurements since the background of *m*/*z* 20 in the detection chamber is significantly less than that of *m*/*z* 18. Apart from a lower saturation vapour pressure of D_2O, there was no much difference found between the isotopologues. The experiments with nitrogen and chloroform were performed at the constant partial pressure of water corresponding to approximately 20% of relative humidity. In turn, the composition was varied gradually by increasing the total pressure of the mixtures. Note that the indicated limit of detection is derived from the minimum flow rate described above, and it is a function of the sample area and the applied feed pressure. The shown permeance was calculated for the least detectable component (nitrogen) relative to its highest partial pressure in the mixtures. Our results confirm that CNMs act as a highly permeable water-selective membrane.

To further explore the separation performance of CNMs, we carried out permeation experiments with multiple one-to-one mixtures (Fig. 4). In this case, the total pressure was kept at 20 mbar, and the relative humidity was about 40%. Again, water permeance is independent of the mixture contents, while other ingredients are all blocked by the membrane. The permselectivity observed is as great as 100 relative to the highest detection limit among the species in question. Neon and argon were excluded from the investigation due to their cross sensitivity with D_2O in QMS, otherwise water vapour can be efficiently isolated from the atmospheric gases. This property might have a useful practical meaning, for instance, in gas sensing applications. Chloroform, toluene, and hexane all form heterogeneous azeotropes with water, and the data obtained point to the perspectives of their drying by CNMs.

The fast water transport observed resembles that in graphene oxide and carbon nanotubes and can be understood in terms of collective motion of hydrogen-bonded molecules.[29–31] Yet, the permeance of water vapour in CNMs changes much with the

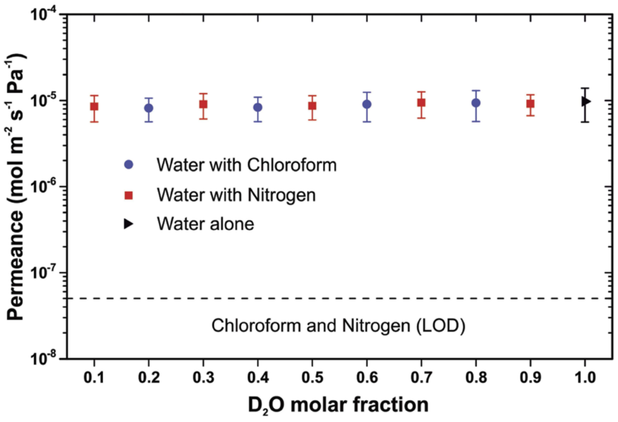

Fig. 3 Permeance of D_2O in mixtures with N_2 and $CHCl_3$. Partial pressure of D_2O was 5 mbar, partial pressure of N_2 and $CHCl_3$ was varied accordingly from 0 to 45 mbar. The experiments were done at 298 K. The data points represent mean values over 5 samples. The error bars indicate standard deviation. The dashed line is the limit of detection (LOD) for other components of the mixtures.

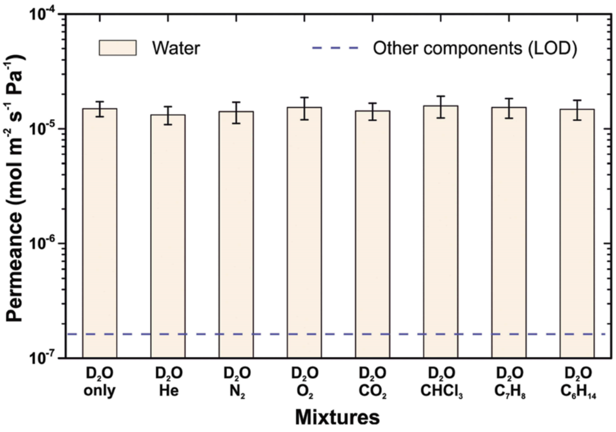

Fig. 4 Permeance of water in binary mixtures. The partial pressure of all components was 10 mbar. The data were averaged over 5 samples. The shown limit of detection (LOD) is the theoretical permeance for the least detectable substance (nitrogen).

partial pressure which is indicative of complex surface phenomena. As reported, the maximum of the permeation rate is reached under saturation conditions, and the value agrees with that obtained in pervaporation measurements, *i.e.* when the membrane is exposed to the liquid phase.[20] It is clear that the saturated vapour gives rise to water condensation on the membrane, but the humidity dependence found cannot be rationalized based on bulk water transport solely. The fact that the permeance stays very high even at relative pressure as low as 0.02 justifies that water molecules are able to penetrate the membrane individually. However, given the measured permeation rate for helium, there are presumably strong steric constraints in place which prevent inert particles from direct impact translocation. Therefore, water molecules are likely to interact with the membrane surface and have much longer residence times to pass the pores. The entire transport can be thus viewed as a two-step process:

$$\mathrm{D_2O^u_{gas}} \overset{\mathrm{K}}{\rightleftarrows} \mathrm{D_2O^u_{ads}} \xrightarrow{\mathrm{k}} \mathrm{D_2O^d_{gas}}$$

where the superscripts u and d denote molecules on the upstream and the downstream sides of the membrane, and the subscripts gas and ads stand for the gas-phase and the adsorbed species respectively. In fact, the number of vapour molecules striking the membrane (eqn (1)) greatly exceeds the number of particles permeating through CNMs, so that the constant K can be used to describe the adsorption–desorption equilibrium on the surface. Owing to high-vacuum ambience in the downstream compartment, we believe that the molecules crossing the pores leave the nanomembrane immediately and there is no reverse flux. Accordingly, k represents an effective first-order rate constant accounting for the surface and the transmembrane diffusion together. As a result, the molecular flux per unit area can be expressed as a function of surface coverage:

$$F = k\theta n_0 \tag{5}$$

where θ is the fraction of the membrane area occupied by adsorbates (coverage), and n_0 is the number of molecules needed to complete the monolayer (total number of adsorption sites). Providing the adsorption isotherm is known, *i.e.* the amount of adsorbed water *versus* pressure, this equation is correlated with the experimentally measured flow rate. Generally, there are six types of isotherms with very distinct shapes of the coverage–pressure curves,[32] and one can expect the adsorption-mediated permeation rates to be in line with those dependences. As follows from the data concerned, the cross-membrane flux of water molecules through CNMs appears to be convex over the whole range of the relative vapour pressure. Such a behaviour is similar to the isotherm Type III, and below we work out a simple kinetic model to describe the permeation results.

Two boundary conditions need to be taken into consideration when calculating the flow rate as a function of the relative pressure $x = p/p_0$. The first point is that at low humidity ($x \ll 1$) the permeation is most likely dominated by separate water molecules. The second one is prescribed by the fact that the permeation at saturated pressure ($x \approx 1$) is governed by the bulk-like phase. Our starting assumption consists in that water condensation on CNMs obeys an adsorption isotherm of Type III. This kind of isotherms is known to arise if adhesion is energetically not more favourable than cohesion, *i.e.* adsorbates start interacting with each other before the surface is fully covered. In other words, the molecules adsorbed as a multilayer coexist with those being in a sub-monolayer. This means the total permeation rate splits into two contributions:

$$F = k_\mathrm{mono}\theta_\mathrm{mono}n_0 + k_\mathrm{multi}\theta_\mathrm{multi}n_0 \tag{6}$$

where k_mono and k_multi designate the effective rate constants for individual and collective motion, θ_mono and θ_multi are the fractions of the membrane area containing single adsorbates and their agglomerates respectively. Given the boundary conditions, k_multi is greater than k_mono, and the interpretation of the eqn (6) is rather straightforward. At low vapour pressure, the adsorbed water molecules mainly cross the membrane as single entities. As condensation proceeds, the adsorbates get involved into intermolecular interactions, and cooperative passage starts playing a role. Eventually, a complete liquid layer is built up, and all the membrane channels become capable to transmit it in the single-file mode. This representation accounts only those molecules constituting agglomerates which are in close proximity to the membrane surface, *i.e.* the first molecular layer.

We assume that the adsorption energy of water molecules on CNMs is equal to the heat of liquefaction, so as to apply the simplified BET theory:[33]

$$n = n_0\frac{x}{1-x} \tag{7}$$

where n describes the total number of adsorbed molecules as a function of the relative pressure. Furthermore, the adsorbates are assumed to be evenly distributed between the two states as long as $\theta_\mathrm{mono} + \theta_\mathrm{multi} < 1$, *i.e.* $n_\mathrm{mono} = n_\mathrm{multi} = n/2$. In this regime, the coverage of the individually adsorbed molecules is given by the simple relation:

$$\theta_\mathrm{mono} = \frac{x}{2(1-x)}, \tag{8}$$

while otherwise $\theta_\mathrm{mono} = 1 - \theta_\mathrm{multi}$. In order to quantify θ_multi, the average height of the clusters L can be introduced which is defined as an apparent number of molecular layers (Fig. 5). Let us now imagine that the agglomerates are uniformly spread over the surface and have the same cubic shape with a volumetric size of L^3. When the multilayer islands coalesce, θ_multi approaches unity yielding the critical thickness L_0. At this limit, one obtains the areal density of the clusters as n_0/L_0^2 which is in this model extrapolated to the number of nucleation centres. Therefore, the coverage θ_multi can be always written *via* L as following:

$$\theta_\mathrm{multi} = \frac{L^2}{L_0^2} \tag{9}$$

Under the above approximations, the mass balance exactly relates the size of the agglomerates L to the relative pressure x. When $\theta_\mathrm{mono} + \theta_\mathrm{multi} < 1$, the number of molecules in clusters gives:

$$n_0\theta_\mathrm{multi}L = n_0\frac{L^3}{L_0^2} = n_0\frac{x}{2(1-x)} \tag{10}$$

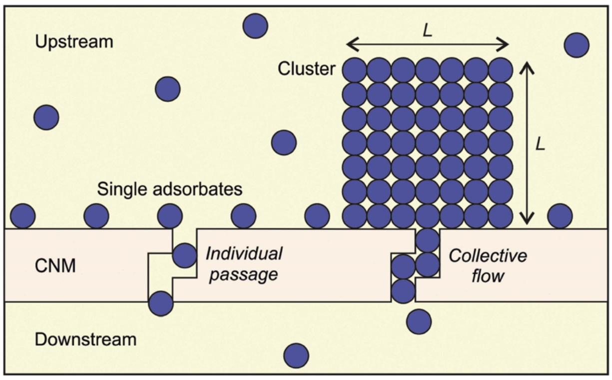

Fig. 5 Cross-sectional view of the adsorption model used for the kinetic simulations. The membrane channels are assumed to be tortuous to explain the observed transport rates of gases.

When $\theta_{\text{mono}} + \theta_{\text{multi}} = 1$, L is evaluated from the total number of adsorbates:

$$\begin{aligned} n_0(1-\theta_{\text{multi}}) + n_0\theta_{\text{multi}}L &= n_0 + n_0\frac{L^2}{{L_0}^2}(L-1) \\ &= n_0\frac{x}{(1-x)} \end{aligned} \tag{11}$$

Both equations are solved analytically (see ESI†), and we used the respective parametric formulae to determine the whole range of θ_{mono} and θ_{multi} (Fig. SM5, ESI†).

Fig. 6 compares the measured flux of D_2O molecules with the simulations done by eqn (6). The rate constants were established from the boundary conditions at x equal to 0.02 and 1, and n_0 was taken as 2×10^{-13} mol m^{-2} (a typical value for water physisorption on flat surfaces[34]). The calculations were carried out for different values of L_0 to find the closest correspondence with the experimental data set. The resulting transmembrane flux is limited by $\theta_{\text{multi}} = 1$, *i.e.* when the surface is entirely covered with a liquid film. Despite its crudeness, the model predicts a steep increase in the permeation rate at any L_0, but most agreement with the measured dependence is attained at $L_0 \gg 10$. The meaning of this parameter consists in the speed of the multilayer completion. Smaller L_0 imply that many agglomerates are formed at early stages of adsorption which rapidly evolve into a continuous layer. Conversely, larger L_0 indicate that multilayer clusters are rather rare and can grow considerably before encountering each other. As suggested by the modelling, adsorption of water on CNMs likely induces formation of nanodroplets that gradually increase with the relative humidity. Over a substantial part of the isotherm, the permeation is controlled by concurrent transport mechanisms involving isolated adsorbates and interconnected molecules.

In light of the developed model, one can likewise explain the above described permeation experiments with the binary mixtures. Indeed, the used D_2O pressures 5 and 10 mbar indicate that the coverage of nanodroplets was insignificant ($\theta_{\text{multi}} <$ 0.05), although the membrane was to a great extent covered by adsorbed water molecules (θ_{mono} = 0.1–0.3). These adsorbates are unlikely to affect much permeation of gas molecules which should behave as in the pure state, *i.e.* bounce back from the membrane surface. As to organic substances, vapour molecules can also adsorb and condense depending on the partial pressure. All three solvents probed are hydrophobic and do not dissolve in water, albeit they can compete with water for the available adsorption sites. However, the highest relative pressure achieved in our measurements was about 0.3 for toluene, and there is no information available on the affinity of these compounds to CNMs. It appears though that either water hinders adsorption of the other vapours or their isotherms allow only little coverage under the applied conditions. More complex phenomena are expected to occur when vapour pressure extends to saturation, and this is going to be the subject of future efforts.

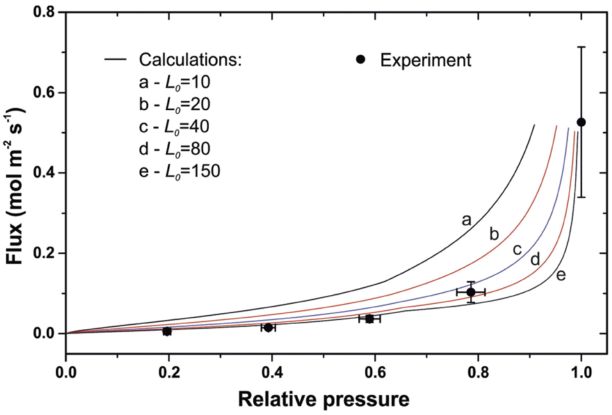

Fig. 6 Transmembrane flux of D_2O molecules as a function of relative pressure. The solid circles indicate the experimental data, while the lines show the simulation results. In calculations, k_{mono} and k_{multi} were taken as 2.0×10^{11} s^{-1} and 2.6×10^{12} s^{-1} respectively. The experimental data points are average over 14 measurements with 5 different samples. The large dispersion at $x \approx 1$ is likely due to temperature fluctuations in the laboratory.

4 Conclusions

We elaborated and successfully implemented the experimental methodology for examining permeation of gases and vapours in nanometre-thin membranes. As evidenced, steady-state flow rates can be reliably determined for single samples down to a few micrometres in size. The apparatus enables transport measurements with feed mixtures of arbitrary composition and also helps to identify membrane defects upon probing permeation rates of different net species. If the molar fluxes follow Graham's law, samples are supposed to have irregular openings whose apparent area can be quantified precisely. Further upgrade of the system is possible by bringing a temperature control to the membrane cell, and such an auxiliary is currently under design.

For the first time, free-standing CNMs were studied with respect to vapour mixtures permeation. We proved that this material is selectively permeable to water vapour by varying the molar fraction from 100 to 10%. Separation performance was verified in binary mixtures with helium, nitrogen, oxygen, carbon dioxide, chloroform, toluene, and hexane. At relative humidity as high as 40%, the membrane was found to readily pass water while rejecting all other components. The results might have straight implications in dehumidification of air and breaking aqueous azeotropes, if the membrane fabrication is scaled up. Future work will expand to more polar and water-miscible organic compounds such as alcohols.

In addition, the one-parameter kinetic model was devised to rationalize the pressure-dependent permeance of water vapour. The experimental flux–humidity curve is reproduced by accounting for adsorption processes. The calculations also predict formation of water nanodroplets which seem to contribute much into the fast cross-membrane passage. Our model is rather speculative and can be improved by investigating water adsorption isotherms on CNMs. This can be done, for example, with the aid of surface-sensitive vibrational spectroscopy. Conducting super-resolution imaging experiments in well-defined vaporous atmosphere would be highly valuable, but seems to be much more challenging.

Conflicts of interest

A. G. is a co-founder and shareholder of CNM Technologies GmbH, a company that specializes on the development of carbon nanomembranes. A. G. is a co-author of a patent for A Method for Separating Fluidic Water from Impure Fluids and a Filter, which is related to the published research.

Acknowledgements

P. D. thanks the "Fonds der Chemischen Industrie (FCI)" for a Liebig Fellowship. The authors cordially thank Dr Berthold Völkel for technical assistance.

References

1 Z. Zheng, R. Grünker and X. Feng, *Adv. Mater.*, 2016, **28**, 6529.
2 L. Wang, M. S. H. Boutilier, P. R. Kidambi, D. Jang, N. G. Hadjiconstantinou and R. Karnik, *Nat. Nanotechnol.*, 2017, **12**, 509.
3 L. W. Drahushuk and M. S. Strano, *Langmuir*, 2012, **28**, 16671.
4 K. Solvik, J. A. Weaver, A. M. Brockway and J. Schrier, *J. Phys. Chem. C*, 2013, **117**, 17050.
5 C. Sun, M. S. H. Boutilier, H. Au, P. Poesio, B. Bai, R. Karnik and N. G. Hadjiconstantinou, *Langmuir*, 2014, **30**, 675.
6 B. Wen, C. Sun and B. Bai, *Phys. Chem. Chem. Phys.*, 2015, **17**, 23619.
7 B. Jin, X. Zhang, F. Li, N. Zhang, Z. Zong, S. Cao, Z. Li and X. Chen, *Phys. Chem. Chem. Phys.*, 2019, **21**, 6126.
8 L. Prozorovska and P. R. Kidambi, *Adv. Mater.*, 2018, **30**, 1801179.
9 L. M. Vane, *Sep. Sci. Technol.*, 2013, **48**(3), 429.
10 D. Cohen-Tanugi and J. C. Grossman, *Nano Lett.*, 2014, **14**, 6171.
11 L. Wang, C. M. Williams, M. S. H. Boutilier, P. R. Kidambi and R. Karnik, *Nano Lett.*, 2017, **17**, 3081.
12 S. P. Koenig, L. Wang, J. Pellegrino and J. S. Bunch, *Nat. Nanotechnol.*, 2012, **7**, 728.
13 K. Celebi, J. Buchheim, R. M. Wyss, A. Droudian, P. Gasser, I. Shorubalko, J.-I. Kye, C. Lee and H. G. Park, *Science*, 2014, **344**, 289.
14 S. P. Surwade, S. N. Smirnov, I. V. Vlassiouk, R. R. Unocic, G. M. Veith, S. Dai and S. M. Mahurin, *Nat. Nanotechnol.*, 2015, **10**, 459.
15 Z. Yuan, J. D. Benck, Y. Eatmon, D. Blankschtein and M. S. Strano, *Nano Lett.*, 2018, **18**, 5057.
16 D. Jang, J.-C. Idrobo, T. Laoui and R. Karnik, *ACS Nano*, 2017, **11**, 10042.
17 J. Zhao, G. He, S. Huang, L. F. Villalobos, M. Dakhchoune, H. Bassas and K. V. Agrawal, *Sci. Adv.*, 2019, **5**, eaav1851.
18 P. M. Das, J. P. Thiruraman, Y.-C. Chou, G. Danda and M. Drndić, *Nano Lett.*, 2019, **19**, 392.
19 J.-H. Jhang, C. Zhou, O. E. Dagdeviren, G. S. Hutchings, U. D. Schwarz and E. I. Altman, *Phys. Chem. Chem. Phys.*, 2017, **19**, 14001.
20 Y. Yang, P. Dementyev, N. Biere, D. Emmrich, P. Stohmann, R. Korzetz, X. Zhang, A. Beyer, S. Koch, D. Anselmetti and A. Gölzhäuser, *ACS Nano*, 2018, **12**, 4695.
21 K. W. Kolasinski, *Surface Science: Foundations of Catalysis and Nanoscience*, John Wiley & Sons, Ltd, Chichester, 2012.
22 *Foundations of Vacuum Science and Technology*, ed. J. M. Lafferty, John Wiley & Sons, Inc., 1998.
23 A. Ranade, N. A. D'Souza, R. M. Wallace and B. E. Gnade, *Rev. Sci. Instrum.*, 2005, **76**, 013902.
24 X. D. Zhang, J. S. Lewis, S. D. Wolter, C. B. Parker and J. T. Glass, *J. Vac. Sci. Technol., A*, 2007, **25**, 1587.
25 R. Checchetto, P. Bettotti, R. S. Brusa, G. Carotenuto, W. Egger, C. Hugenschmidt and A. Miotello, *Phys. Chem. Chem. Phys.*, 2018, **20**, 24671.
26 G. Firpo, L. Repetto, F. Buatier de Mongeot and U. Valbusa, *J. Vac. Sci. Technol., B*, 2009, **27**, 2347.
27 P. Angelova, H. Vieker, N.-E. Weber, D. Matei, O. Reimer, I. Meier, S. Kurasch, J. Biskupek, D. Lorbach, K. Wunderlich, L. Chen, A. Terfort, M. Klapper, K. Müllen, U. Keiser, A. Gölzhäuser and A. Turchanin, *ACS Nano*, 2013, **7**, 6489.
28 A. Turchanin and A. Gölzhäuser, *Adv. Mater.*, 2016, **28**, 6075.
29 J. K. Holt, H. G. Park, Y. Wang, M. Stadermann, A. B. Artyukhin, C. P. Grigoropoulos, A. Noy and O. Bakajin, *Science*, 2006, **312**, 1034.
30 R. R. Nair, H. A. Wu, P. N. Jayaram, I. V. Grigorieva and A. K. Geim, *Science*, 2012, **335**, 442.
31 J. Hassan, G. Diamantopoulos, L. Gkoura, M. Karagianni, S. Alhassan, S. V. Kumar, M. S. Katsiotis, T. Karagiannis, M. Fardis, N. Panopoulos, H. J. Kim, M. Beazi-Katsioti and G. Papavassiliou, *J. Phys. Chem. C*, 2018, **122**, 10600.
32 K. S. W. Sing, *Pure Appl. Chem.*, 1982, **54**, 2201.
33 S. Brunauer, L. S. Deming, W. E. Deming and E. Teller, *J. Am. Chem. Soc.*, 1940, **62**, 1723.
34 P. Dementyev, K.-H. Dostert, F. Ivars-Barcelo, C. P. O'Brien, F. Mirabella, S. Schauermann, X. Li, J. Paier, J. Sauer and H.-J. Freund, *Angew. Chem., Int. Ed.*, 2015, **54**, 13942.

4.6 Publication: Water-Assisted Permeation of Gases in Carbon Nanomembranes

This article is reprinted with permission from American Chemical Society. The original paper appeared as:

D. Naberezhnyi, A. Gölzhäuser and P. Dementyev, *Water-Assisted Permeation of Gases in Carbon Nanomembranes.* ***J. Phys. Chem. Lett.***, 2019, **10**, 5598–5601.

Contribution:

Preparation of SAMs, electron cross-linking of the SAMs, transfer of the CNMs, permeation experiments and data evaluation were performed by the author.

THE JOURNAL OF PHYSICAL CHEMISTRY Letters

Letter

Cite This: J. Phys. Chem. Lett. 2019, 10, 5598−5601

pubs.acs.org/JPCL

Water-Assisted Permeation of Gases in Carbon Nanomembranes

Daniil Naberezhnyi, Armin Gölzhäuser, and Petr Dementyev*

Physics of Supramolecular Systems and Surfaces, Faculty of Physics, Bielefeld University, 33615 Bielefeld, Germany

ABSTRACT: Planar nanomaterials finished with transverse ducts represent an intriguing avenue for exploring interfacial phenomena. Due to their small thickness, the kinetics of molecular diffusion across the channels is likely to be dominated by entrance events. Therefore, measuring transport rates in freestanding films can yield valuable information on surface processes. In this work, we study permeation of gases in carbon nanomembranes (CNMs) when accompanied by saturated water vapor. The experimental data reveal a manifold increase in transmembrane fluxes compared to dry conditions. Gas molecules are found to be trapped in adsorbed water, which enhances their translocation likelihood. We demonstrate that the permeance correlates with the vapor relative pressure and discuss the observed crossing mechanism in terms of water condensation and Henry's law. Our findings provide guidance for designing gas separation membranes upon two-dimensional materials.

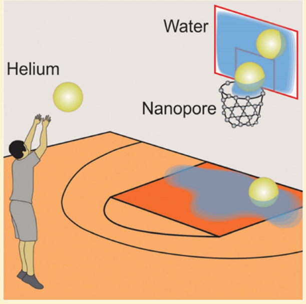

Energy-efficient chemical separation is one of the most promising applications of 2D materials as they can serve for high-throughput molecular sieving when equipped with uniform pores.[1,2] Gas transport in nanomembranes has been widely addressed by computations, and in addition to size exclusion, surface adsorption often appears to be an important factor in mixture separation.[3−8] In theory, particles accommodated on the membrane surface should have a greater chance of entering and passing the pores compared to their gas-phase counterparts. Although different types of gas−surface interactions have been proposed to affect molecular transport in single-layer materials, the area remains largely unexplored from an experimental perspective. Wang et al. studied gas permeation in porous graphene as a function of molecular size and observed a significant deviation from the geometrical trend for CO_2 and N_2O.[9] Graphene nanomembranes were also used to probe separation of multicomponent mixtures and exhibited appreciable permselectivity to CO_2 and CH_4 over He and H_2.[10] These scarce examples confirm that surface properties might be relevant for tailoring membrane performance, and it is even more evident in permeation of vapors whose adsorption is governed by relative pressure. Thus, intrinsically porous carbon nanomembranes (CNMs) with a high density of channels were found to pass water vapor much faster than any other substance, featuring a pronounced humidity dependence.[11] While condensed water is known to reveal spectacular dynamics in nanoconfinement,[12−14] at low relative pressure, water molecules are believed to diffuse through CNMs predominantly as separate adsorbates.[15] As supported by experiments with mixtures, the membrane selectivity toward water in this nanometer-thick material is due to the higher probability of adsorbed species to penetrate into the channels. This Letter reports on a significant increase in permeation rates of gases across CNMs upon combining with saturated water vapor.

The basics of the transport measurements employed are illustrated in Figure 1a, while the complete experimental system is detailed elsewhere.[15] A suspended CNM is secured between the three-section upstream compartment and the high-vacuum detection chamber with a quadrupole mass spectrometer (QMS). The mixing chamber and the small

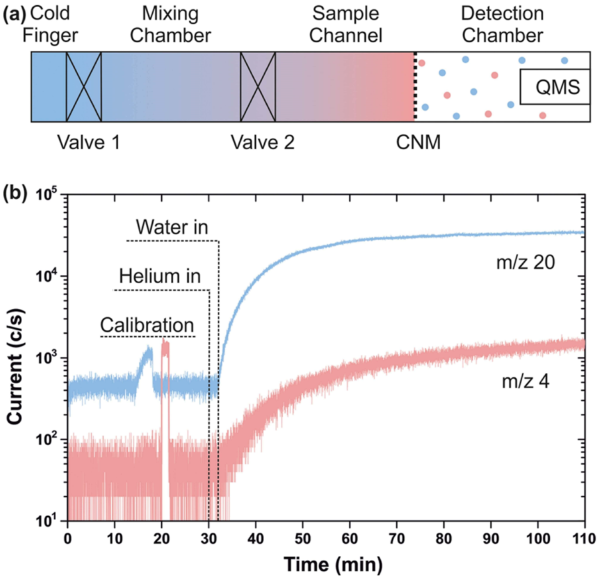

Figure 1. (a) Schematic of the permeation experiments with gas−vapor mixtures. The volume ratio among the coldfinger, the mixing chamber, and the sample channel is 1:80:100. (b) Representative QMS output for a binary feed mixture. First, calibration signals for D_2O and He were recorded; then, 25 mbar of He was dosed into the mixing chamber and the sample channel; finally, D_2O was released from the coldfinger at a saturation pressure of around 25 mbar.

Received: August 8, 2019
Accepted: September 3, 2019
Published: September 4, 2019

DOI: 10.1021/acs.jpclett.9b02321

coldfinger are designed for preparing gaseous and vaporous mixtures, but there is always a pressure drop upon connecting with the membrane cell. Therefore, feed mixtures with saturated vapor were prepared in a different way with valve 2 open. Specifically, an excess amount of water was first stored in the coldfinger followed by admitting a gas of interest into the total volume of the mixing chamber and the sample channel. Water vapor was then released through valve 1 to allow for intermixing with the gas and reaching the membrane. The equilibration took a few hours depending on the gaseous species, and Figure 1b shows how the process was monitored by the QMS. The signal of permeating water molecules grew rapidly as their concentration near the membrane increased, leveling off at a relative pressure close to unity. Surprisingly, one can also see simultaneous evolution of the signal corresponding to the gas particles, despite the fact that they were let into the sample long before and their partial pressure was constant. This observation strongly suggests that water vapor is able to promote permeation of molecular species through otherwise gas-tight CNMs.

Previously, helium was reported to be the only gas whose cross-membrane flux was determined reliably under a feed pressure of 130 mbar with a permeance in the range of 10^{-8} mol m^{-2} s^{-1} Pa^{-1}.[11] In order to facilitate the mixing, the above-described experiments with saturated vapor were carried out at partial pressures as low as 25 mbar, and the He signal was revealed to stay at the background level until water was let in. Yet, its QMS intensity associated with the water-induced transport gave rise to a steady-state permeance value as great as 3×10^{-6} mol m^{-2} s^{-1} Pa^{-1}, meaning a 2 orders of magnitude increase. To exclude diffusion anywhere else in the sample fixture, we checked permeation of the dry gas over the same time scale, and it was clear that the observed enhancement was caused by the presence of water. The measurements were conducted with multiple species, and the results obtained are shown in Figure 2a. In addition to helium, the effect of water vapor on permeation was found for nitrogen, oxygen, and carbon dioxide, whereas no flow rate was measured for chloroform. Regardless of the mixtures, the water permeation rate was proven to be the same as that in the net state ($\sim 10^{-4}$ mol m^{-2} s^{-1} Pa^{-1}), which is indicative of unimpeded condensation. At saturation pressure, water is expected to extensively cover the membrane surface, and its trans-membrane flow is considered to be liquid-like, in agreement with pervaporation measurements.[11] It appears that condensed water takes up the gas particles and carries them away through the membrane channels. In comparison to anhydrous conditions, the trapped molecules exhibit much greater access to the CNMs' interior, pointing to steric hindrance at the pore entrances. To understand how water alters the residence time of gaseous species at the surface, one can recall Henry's law, which describes the amount of gases dissolved in liquids[16]

$$c = Hp \tag{1}$$

where c is the molar concentration, H is the Henry's law solubility constant, and p is the partial pressure. According to this relation, the number of gas molecules absorbed by the water layer is in equilibrium with the gas phase, and hence, the permeation process can be modeled by two steps

$$A_g^u \overset{H}{\rightleftharpoons} A_{dis}^u \xrightarrow{k} A_g^d$$

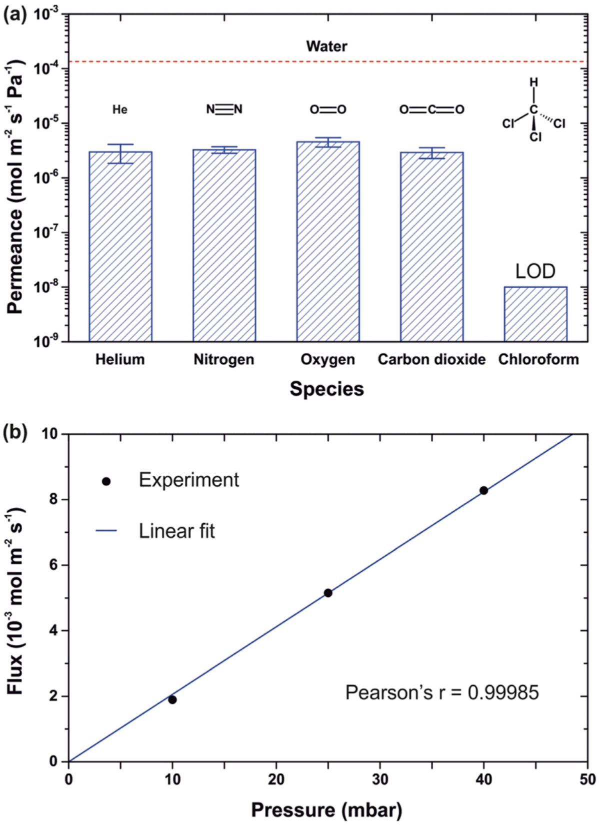

Figure 2. (a) Permeance of gaseous substances in CNMs upon mixing with saturated water vapor. The partial pressure of each component was 25 mbar (about 10% relative pressure for chloroform). The data represent mean values over five samples, and the error bars are standard deviations. LOD is the limit of detection as defined in ref 15. The dashed line indicates the average permeation rate for water. (b) Transmembrane flux of acetonitrile in CNMs as a function of its partial pressure in mixtures with saturated water vapor. The permeation measurements were done in the opposite order compared to that shown in Figure 1a, i.e., acetonitrile was frozen in the coldfinger while water was dosed into the mixing chamber and the sample channel. This arrangement enabled shorter intermixing times.

Here, the superscripts u and d denote particles on the upstream and the downstream, the subscripts g and dis are for the gas and the liquid phase, and k represents an effective rate constant. Under steady state, the flux of gas molecules crossing the membrane is expressed as follows

$$F = kc = kHp \tag{2}$$

It is interesting that the linear pressure dependence was established even for condensable species (Figure 2b). Although solubility constants in water are known to vary in a broad range (Table 1),[17] the measured transport rates for gases are very similar (Figure 2a), indicating a trade-off between k and H in eq 2. Indeed, the rate constant is likely to be size-dependent and should diminish for larger particles. For instance, carbon dioxide molecules are triatomic and can react with water, yielding bicarbonate anions, albeit it is much more soluble than helium. Because vaporous substances behave as gases at low relative pressure, acetonitrile and chloroform were used to widen the scope of molecular dimensions and solubility. Thus, the former compound is fully miscible with water, while its

Table 1. Henry's Law Solubility Constants in Water [mol m^{-3} Pa^{-1}][17]

helium	nitrogen	oxygen	carbon dioxide	chloroform	acetonitrile
3.8×10^{-6}	6.4×10^{-6}	1.3×10^{-5}	3.3×10^{-4}	2.5×10^{-3}	5.2×10^{-1}

molecules are bulkier than atmospheric gases. Similarly, the solubility of chloroform exceeds those for all the gases probed, but because of its size, no permeation was observed in the experiments with water. In contrast, organic vapors are supposed to adsorb themselves when their partial pressure approaches saturation. We studied permeation of pure toluene, hexane, chloroform, and acetonitrile, and measurable flow rates were witnessed for all of them except hexane (Figure 3a).

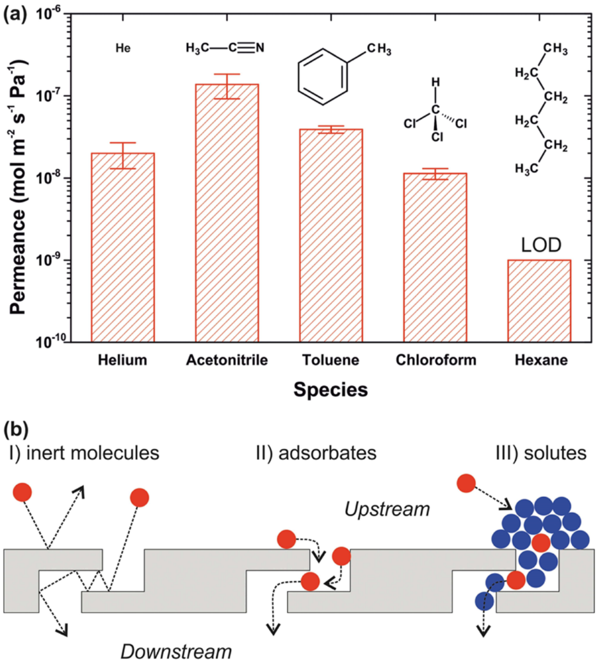

Figure 3. a) Permeance of net substances in CNMs under the following feed conditions: $p(\mathrm{He})$ = 150 mbar; $p(\mathrm{CH_3CN}) \approx 115$ mbar (sat.); $p(\mathrm{C_7H_8}) \approx 35$ mbar (sat.); $p(\mathrm{CHCl_3})$ = 150 mbar; $p(\mathrm{C_6H_{14}}) \approx 180$ mbar (sat.). The data are averaged over 3−4 measurements, and the error bars are standard deviations. (b) Phenomenological model for gas and vapor permeation across nanomembrane channels.

These data support the idea that transmembrane channels in CNMs are tortuous and preclude translocation of inert gas particles.[15] Moreover, it is clear that the ducts are narrower inside than their external appearance[11] because the length of hexane molecules does not exceed 1 nm. Figure 3b summarizes the mechanisms of molecular transport in nanomembranes that merge from this study: (i) direct impact transfer (seen only for He); (ii) surface diffusion (possible for vapor molecules); (iii) water-assisted permeation.

As evidenced from Figure 1b, the gas flux increases gradually with time and follows the signal of water molecules, implying a humidity-driven behavior. Given the experimental configuration, it is difficult to track the water relative pressure during mixing. However, if the amount of water vapor is initially set to a precise value other than saturation, the experiments can be done at specific relative pressure. We watched the changes in permeation rates for helium and oxygen as a function of humidity and obtained very steep curves (Figure 4). Because the transport of water vapor in CNMs is rationalized in terms of multilayer adsorption,[15] surface clustering seems to be responsible for the trends revealed. Moreover, the coverage of water agglomerates predicted by the kinetic model is well in line with the measured data points. It means that the solvent-assisted permeation occurs in water nanodroplets formed at the membrane surface in the course of vapor condensation. This environment might result in interesting confinement effects, such as oversolubility,[18,19] and requires further microscopic and theoretical investigation.

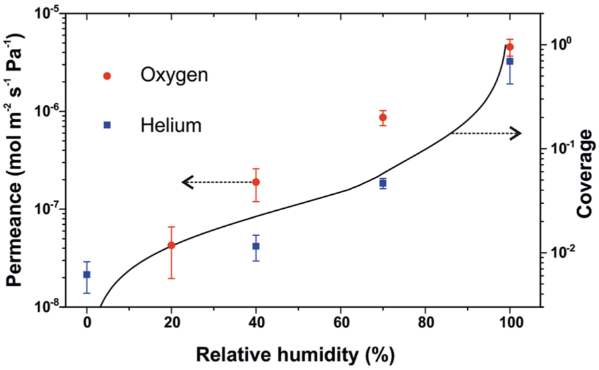

Figure 4. (a) Permeance of gases in binary mixtures with water vapor at different humidity. The total pressure was kept at 50−60 mbar. The measurements were done with 3−5 samples, and the errors bars indicate standard deviations. The solid line is the coverage of water clusters calculated by the kinetic model introduced in ref 15 with the parameter L_0 = 100.

In conclusion, we demonstrated a novel experimental approach to examine physicochemical events at solid−gas and liquid−gas interfaces. Upon exposing porous nanosheets to well-defined atmospheres and looking at the outside, we were able to get insights into complex adsorption, absorption, and diffusion processes taking place on the inner surface. The procedure is readily extendable to any 2D material provided that its perforation is properly fulfilled.[20] Surface modification by chemical means turns out to be an effective route with respect to controlling gas permeability in nanoscale membranes. For example, ionic liquids could be used to overlay the membranes and impart variable affinity for certain molecular species. CNMs were proven to be selective to water vapor under high humidity, and the data presented display a clear cutoff of their pore size distribution. Filtration experiments with liquid water would shed more light on their separation performance as hydrophilic, and especially ionic solutes can differ greatly in size due to hydration shells.

■ EXPERIMENTAL METHODS

CNMs were prepared out of terphenylthiol (Sigma-Aldrich, 97%) and suspended over holey substrates (4−7 μm openings in 500 nm S_3N_4 windows, Silson Ltd.), as specified formerly.[11] Seven defect-free samples were probed during this study. The experiments were performed at room temperature with a vacuum system described in ref 15. He, N_2, O_2, and CO_2 were used as delivered by Linde. Acetonitrile (Merck, 99.9%), toluene (Fisher Scientific, 99.8%), chloroform (VWR, 99.8%), hexane (Fisher Scientific, 95%), and deuterium oxide (Sigma-Aldrich, 99.9% atom D) were degassed before use.

■ AUTHOR INFORMATION

Corresponding Author

*E-mail: dementyev@physik.uni-bielefeld.de.

ORCID

Armin Gölzhäuser: 0000-0002-0838-9028

Petr Dementyev: 0000-0002-9957-2070

Notes

The authors declare the following competing financial interest(s): A. G. is a co-founder and shareholder of a company aimed at commercializing carbon nanomembranes (CNM Technologies GmbH).

■ ACKNOWLEDGMENTS

P.D. thanks the Fonds der Chemischen Industrie for financial support (Liebig fellowship).

■ REFERENCES

(1) Prozorovska, L.; Kidambi, P. R. State-of-the-Art and Future Prospects for Atomically Thin Membranes from 2D Materials. *Adv. Mater.* **2018**, *30*, 1801179.

(2) Moghadam, F.; Park, H. B. 2D Nanoporous Materials: Membrane Platform for Gas and Liquid Separations. *2D Mater.* **2019**, *6*, No. 042002.

(3) Du, H.; Li, J.; Zhang, J.; Su, G.; Li, X.; Zhao, Y. Separation of Hydrogen and Nitrogen Gases with Porous Graphene Membrane. *J. Phys. Chem. C* **2011**, *115*, 23261−23266.

(4) Schrier, J. Carbon Dioxide Separation with a Two-Dimensional Polymer Membrane. *ACS Appl. Mater. Interfaces* **2012**, *4*, 3745−3752.

(5) Drahushuk, L. W.; Strano, M. S. Mechanisms of Gas Permeation through Single Layer Graphene Membranes. *Langmuir* **2012**, *28*, 16671−16678.

(6) Sun, C.; Boutilier, M. S. H.; Au, H.; Poesio, P.; Bai, B.; Karnik, R.; Hadjiconstantinou, N. G. Mechanisms of Molecular Permeation through Nanoporous Graphene Membranes. *Langmuir* **2014**, *30*, 675−682.

(7) Tian, Z.; Mahurin, S. M.; Dai, S.; Jiang, D. Ion-Gated Gas Separation through Porous Graphene. *Nano Lett.* **2017**, *17*, 1802−1807.

(8) Sun, C.; Bai, B. Improved CO_2/CH_4 Separation Performance in Negatively Charged Nanoporous Graphene Membranes. *J. Phys. Chem. C* **2018**, *122*, 6178−6185.

(9) Wang, L.; Drahushuk, L. W.; Cantley, L.; Koenig, S. P.; Liu, X.; Pellegrino, J.; Strano, M. S.; Bunch, J. S. Molecular Valves for Controlling Gas Phase Transport Made from Discrete Ångström-Sized Pores in Graphene. *Nat. Nanotechnol.* **2015**, *10*, 785−790.

(10) Yuan, Z.; Benck, J. D.; Eatmon, Y.; Blankschtein, D.; Strano, M. S. Stable, Temperature-Dependent Gas Mixture Permeation and Separation through Suspended Nanoporous Single-Layer Graphene Membranes. *Nano Lett.* **2018**, *18*, 5057−5069.

(11) Yang, Y.; Dementyev, P.; Biere, N.; Emmrich, D.; Stohmann, P.; Korzetz, R.; Zhang, X.; Beyer, A.; Koch, S.; Anselmetti, D.; et al. Rapid Water Permeation through Carbon Nanomembranes with Sub-Nanometer Channels. *ACS Nano* **2018**, *12*, 4695−4701.

(12) Reiter, G. F.; Deb, A.; Sakurai, Y.; Itou, M.; Kolesnikov, A. I. Quantum Coherence and Temperature Dependence of the Anomalous State of Nanoconfined Water in Carbon Nanotubes. *J. Phys. Chem. Lett.* **2016**, *7*, 4433−4437.

(13) Hassan, J.; Diamantopoulos, G.; Gkoura, L.; Karagianni, M.; Alhassan, S.; Kumar, S. V.; Katsiotis, M. S.; Karagiannis, T.; Fardis, M.; Panopoulos, N.; et al. Ultrafast Stratified Diffusion of Water Inside Carbon Nanotubes; Direct Experimental Evidence with 2D $D-T_2$ NMR Spectroscopy. *J. Phys. Chem. C* **2018**, *122*, 10600−10606.

(14) Li, Q.-Y.; Matsushita, R.; Tomo, Y.; Ikuta, T.; Takahashi, K. Water Confined in Hydrophobic Cup-Stacked Carbon Nanotubes beyond Surface-Tension Dominance. *J. Phys. Chem. Lett.* **2019**, *10*, 3744−3749.

(15) Dementyev, P.; Wilke, T.; Naberezhnyi, D.; Emmrich, D.; Gölzhäuser, A. Vapour Permeation Measurements with Free-Standing Nanomembranes. *Phys. Chem. Chem. Phys.* **2019**, *21*, 15471−15477.

(16) Battino, R.; Clever, H. L. The Solubility of Gases in Liquids. *Chem. Rev.* **1966**, *66*, 395−463.

(17) Sander, R. Compilation of Henry's Law Constants (Version 4.0) for Water as Solvent. *Atmos. Chem. Phys.* **2015**, *15*, 4399−4981.

(18) Ho, L. N.; Clauzier, S.; Schuurman, Y.; Farrusseng, D.; Coasne, B. Gas Uptake in Solvents Confined in Mesopores: Adsorption versus Enhanced Solubility. *J. Phys. Chem. Lett.* **2013**, *4*, 2274−2278.

(19) Lidon, P.; Marker, S. C.; Wilson, J. J.; Williams, R. M.; Zipfel, W. R.; Stroock, A. D. Enhanced Oxygen Solubility in Metastable Water under Tension. *Langmuir* **2018**, *34*, 12017−12024.

(20) Kozubek, R.; Tripathi, M.; Ghorbani-Asl, M.; Kretschmer, S.; Madauß, L.; Pollmann, E.; O'Brien, M.; McEvoy, N.; Ludacka, U.; Susi, T.; et al. Perforating Freestanding Molybdenum Disulfide Monolayers with Highly Charged Ions. *J. Phys. Chem. Lett.* **2019**, *10*, 904−910.

4.7 Publication: Carbon Nanomembranes from Aromatic Carboxylate Precursors

This article is reprinted with permission from John Wiley and Sons. The original paper appeared as:

P. Dementyev, D. Naberezhnyi, M. Westphal, M. Buck and A. Gölzhäuser, *Carbon Nanomembranes from Aromatic Carboxylate Precursors.* ***ChemPhysChem***, 2020, **21**, 1006–1011.

Contribution:

The synthesis of thiolate SAMs, electron cross-linking of thiolate and carboxylate SAMs, transfer of the CNMs, characterization of the materials by XPS and PM-IRRAS, permeation experiments and data evaluation were performed by the author.

ChemPhysChem

Articles
doi.org/10.1002/cphc.202000150

Chemistry Europe
European Chemical Societies Publishing

Carbon Nanomembranes from Aromatic Carboxylate Precursors

Petr Dementyev,*[a] Daniil Naberezhnyi,[a] Michael Westphal,[a] Manfred Buck,*[b] and Armin Gölzhäuser[a]

Self-assembled monolayers (SAMs) serve as convenient platform for fabricating carbon nanomembranes (CNMs) of extended lateral dimensions. Highly porous CNMs are emerging as interesting materials for membrane technologies as they exhibit selectivity for water permeation and, owing to their reduced dimensionality, promise increased energy efficiency compared to established systems. In the present study terphenylcarboxylate SAMs, prepared on silver underpotential deposited on Au and irradiated by 100 eV electrons, were successfully converted into free-standing CNMs. Infrared and X-ray photoelectron spectroscopy reveal pronounced chemical changes both of the anchoring carboxylate moiety and the aromatic backbone upon electron irradiation. Permeation studies showed high specificity for water as demonstrated by the separation from tetrahydrofuran. Compared to thiols on gold, the standard CNM precursor system, the carboxylic acid based SAM exhibits equivalent characteristics. This suggests that electron-induced carbonization is insensitive to the particular choice of the anchor moiety and, therefore, the choice of precursor molecules can be extended to the versatile class of aromatic carboxylic acids.

1. Introduction

With membrane separation gaining increasing technological importance, designing well-defined pores and narrowing their size distribution as well as minimizing the thickness of active layers are among the main strategies to advance the respective processes.[1] In this regard, a few classes of nanostructured membranes, such as metal-organic frameworks (MOFs),[2] covalent-organic frameworks (COFs),[3] zeolites,[4] and carbonaceous materials,[5] have demonstrated an intriguing potential, even though industrial readiness has not yet been reached. Graphitic and amorphous carbon is particularly advantageous due to its thermal and chemical stability, ease of fabrication, and low costs. However, pyrolytic carbon often exhibits significant fragility when prepared on a thickness scale of several micrometers. In contrast, nanometer-thick carbon nanomembranes (CNMs) made from self-assembled monolayers (SAMs) via electron bombardment are flexible and have outstanding mechanical characteristics.[6] Since SAMs are formed upon adsorption of organic molecules on solid surfaces, there is no principal limitation on the size of CNMs produced, and continuous films have been studied under both supported and free-standing conditions.[6]

As a rule, SAMs represent highly ordered structures whose properties are prescribed by the nature of their molecular precursors and the underlying substrates.[7] The chemical interactions between the surface and the adsorbates are determined by the head groups, while the molecular backbones govern the macroscopic behavior of the layers, including electronic and optical phenomena. The electron-induced synthesis of CNMs has typically been done on gold substrates and cross-linking of the SAM molecules was proven to occur with different polyaromatic thiols.[8] The influence of the precursor molecules has been established for diverse extensive properties, such as mechanical strength and electrical conductivity.[9] However, the microstructure of the final material remained rather elusive, despite numerous spectroscopic efforts to understand the mechanism of the radiation carbonization.[10] Recently, Neumann *et al.* have pioneered CNMs prepared from SAMs of aromatic carboxylic acids on silver substrates, suggesting that the scope of this nanofabrication method can be significantly widened by this type of compounds.[11] Indeed, compared to thiols which are prone to oxidation under ambient conditions and require delicate handling upon functionalization and use,[12] aromatic carboxylic acids are more benign from the synthesis point of view and the large variety of commercially available precursor molecules would be highly beneficial, provided material performance is not compromised.

Thus far, terphenylthiol (TPT) (Figure 1) has been mostly employed as a precursor in mass transfer experiments with free-standing CNMs.[13,14] In particular, TPT CNMs were found to enable selective permeation of water molecules in mixtures with a range of gases and organic vapors.[15–17] The topography of the material was probed with atomic force microscopy (AFM), and densely packed arrays of ordered TPT molecules were revealed to be transformed completely to a new sponge-

---

[a] *Dr. P. Dementyev, D. Naberezhnyi, M. Westphal, Prof. Dr. A. Gölzhäuser*
Physics of Supramolecular Systems and Surfaces
Bielefeld University
Universitätsstr. 25, 33615 Bielefeld (Germany)
E-mail: dementyev@physik.uni-bielefeld.de
[b] *Prof. Dr. M. Buck*
EaStCHEM School of Chemistry
University of St Andrews
North Haugh, St Andrews KY16 9ST (U.K.)
E-mail: mb45@st-andrews.ac.uk

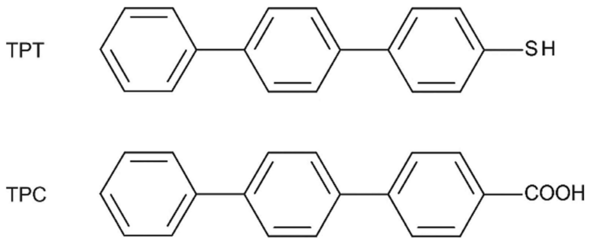

Figure 1. Molecular structures of TPT and TPC precursors.

like morphology. In this study, we advance CNM preparation using gold substrates modified by underpotential deposition (UPD) of a bilayer of silver, in order to impart affinity for carboxylic acids. The UPD-Ag substrates were exposed to terphenyl carboxylic acid (TPC) (Figure 1) to form SAMs, followed by electron irradiation to produce CNMs. The synthesis process was characterized by scanning tunneling microscopy (STM), helium ion microscopy (HIM), infrared reflection absorption spectroscopy (IRRAS), and X-ray photoelectron spectroscopy (XPS). Finally, comparative experiments on molecular permeation were carried out to explore whether the microporous structure of CNMs is affected by the change of the head group.

2. Results and Discussion

2.1. Structural Characterization

Self-assembly of TPC molecules on electrodeposited silver was studied previously.[18] Anchored to the substrate by coordination bonding of the carboxylate moiety, the molecules stand upright and form a highly crystalline single-phase overlayer (Figure 2a,b). The lattice is described by a rectangular $(5\times\sqrt{3})$ unit cell, and the packing density corresponds to 4.17 molecules/nm^2. It is noticed that the appearance of the structure is sensitive to the tunneling conditions. Depending on the condition of the tip, not all molecules might be resolved as illustrated by the comparison of Figures 2a and 2b. In the image of Figure 2a, the protrusions reflect only a subset of the molecules which would suggest a much lower packing density. That this is not the true structure is evidenced by the image of Figure 2b where a change in contrast occurs during the scan. The structure in the central part of the image looks like the one in Figure 2a, as indicated by the yellow unit cell, whereas the top part shows additional protrusions and the unit cell as described previously.[18]

Different from TPC, TPT interacts with the gold surface through covalent Au–S bonds and exhibits polymorphous periodicity.[19] Despite the fact that the phases differ by 10–20° in the tilt angle, TPT SAMs are characterized by an average areal density of 3.82 molecules/nm^2, which is, within less than 10% difference, comparable to TPC SAMs. At the same irradiation dose employed for the thiol, TPC SAMs are readily converted into CNMs. Figure 2c shows a free-standing CNM made from TPC and transferred onto a holey microscopy grid (Quantifoil, Jena). The imaging contrast is highlighted by the two dark circular holes at the bottom of the micrograph which, resembling ∞, result from a rupture of the CNM. Otherwise, the material appears to preserve its mechanical integrity over the rest of the support, indicating a great fraction of laterally interconnected molecules. It is clear that individual molecules comprising the primary monolayer (Figure 2a,b) have undergone substantial chemical transformations to maintain a continuous two-dimensional character of the suspended sheet on such a large scale.

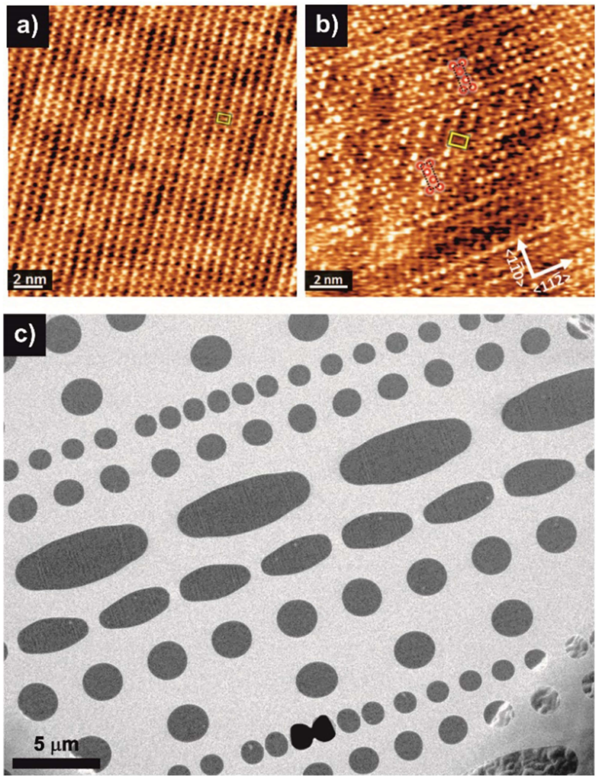

Figure 2. a,b) Molecularly resolved STM images of TPC SAM on Ag/Au/mica at different magnification. The $(5\times\sqrt{3})$ unit cell and the packing of the molecules are indicated in (b) by the black dotted rectangles and the red circles, respectively. The unit cell (yellow rectangle) seen in (a) is also indicated in (b) revealing that in (a) not all molecules are resolved. For details, see text. c) HIM image of a large area TPC CNM suspended over a TEM grid covered with a thin carbon film. Underlying Cu grid is seen on the right corners.

IRRAS and XPS were employed to follow changes in structure and chemical composition of the TPC SAM upon irradiation. The vibrational spectra displayed in Figure 3a reveal pronounced changes upon irradiation with the complete disappearance of the most intense band at 1406 cm^{-1} as the most striking difference. Attributed to the symmetric stretching of the bidentate COO$^-$ anchor group,[20] this suggests either a profound chemical change or a complete loss of the carboxylate moiety. Furthermore, the bands located in the region 1485 to 1605 cm^{-1} and around 3000 cm^{-1}, assigned to the skeletal and C–H stretching modes of the terphenyl moiety,

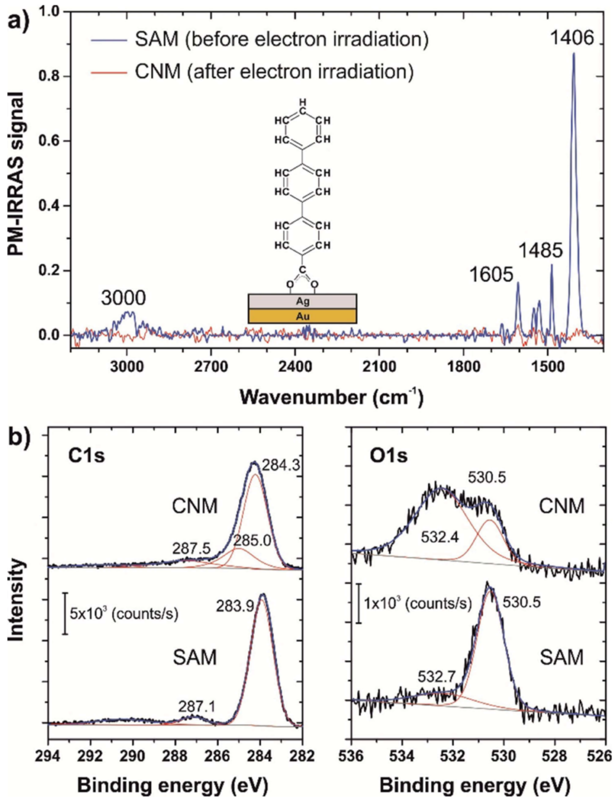

Figure 3. IRRAS (a) and XPS (b) spectra of pristine and cross-linked TPC SAM on Ag/Au/mica. The irradiated samples were exposed to air prior to taking spectra.

respectively, are similarly affected.[10] Their vanishing intensity after irradiation indicates fundamental changes in the geometrical arrangement of the molecular moieties and chemical nature of the layer as can be expected from cross-linking of the molecules.

Comparing the XP spectra before and after irradiation (Figure 3b), both the C1s and O1s regions show clear differences. The main peak in the C1s spectrum shifts to higher binding energy and is broadened, which, in agreement with the IRRAS data, reflects a chemical change of the terphenyl moieties. Chemical changes give also rise to intensity in the region between 285–287 eV and, as a consequence, it is not really possible to infer on changes of the carboxylate signal which is clearly visible in the native SAM at 287.1 eV. Even though there are significant changes in the C 1 s signal, its overall intensity is not altered substantially, which is in agreement with previous work on thiol based aromatic SAMs[10] and indicates that, despite pronounced chemical changes, not much material is lost.

In the O1s region electron irradiation causes major changes. The native layer is characterized by the carboxylate signal at 530.5 eV.[18] A minor signal at 532.7 eV indicates the presence of additional species which is ascribed to some oxygen containing carbon, observed when the SAMs are exposed to ambient atmosphere. Irradiation results in a significant reduction of the oxygen signal of surface-bound carboxylate groups whereas a large and broad signal at around 532.4 eV evolves. This feature is assigned to dangling carbonyl and/or carboxylate groups, i.e. with oxygen atoms not directly connected to the substrate.[21] . It is noted that the gain of this signal upon irradiation is significantly larger than the loss of the one at 530.5 eV which makes it difficult to explain this gain just by a conversion of the carboxylate moiety. Considering that the sample is exposed to atmosphere after irradiation, it is more likely that unstable species, generated by the electron bombardment under vacuum, react with oxygen and water vapor. This is in agreement with the C1s signal where the changes are too large to be explained by changes of the small carboxylate signal.

While the IRRAS and XPS data, in general, are consistent, there is one open point at this stage which has to be investigated further. The IRRAS data show a complete disappearance of the band at 1406 cm^{-1} and possible interpretations are a complete elimination of the carboxylate moiety, a distinct chemical change, reorientation, or a combination of all three. The XPS O1s signal seems to contradict the complete elimination as a significant carboxylate signal is still observed after irradiation. However, since oxygen species adsorbed on Ag also generate a signal in the 530.5 eV region,[22] the difference between the IRRAS and XPS data for the carboxylate remains elusive. In this context it is worth noting that the study of biphenyl SAMs on thick Ag films reported an essentially complete loss of the carboxylate O1s signal, even though the structure of the SAMs differs from the purely aromatic TPC SAM by a short aliphatic chain between the carboxylate and the aromatic moiety.[11]

2.2. Functional Characterization

Irrespective of the incomplete knowledge of the chemical composition and mechanistic details, the generation of the free-standing TPC membranes was reliable. Six intact micrometer-sized samples were studied with respect to gas and vapor permeation. Figure 4 illustrates transport rates of several pure substances. The permeance Π was measured with a mass-spectrometer as following:[15]

$$\Pi = \frac{J}{A \times p} \tag{1}$$

where J is the molar flow rate through the membrane, A is the membrane area, and p is the applied feed pressure.

Similar to TPT CNMs, the material exhibits high affinity to water vapor with a pronounced humidity dependence. This behavior was recently rationalized in terms of water condensation and collective motion of hydrogen-bonded molecules when the mass transfer is determined by surface species rather than gas-phase ones.[13,15] On the contrary, the passage of inert gas particles is significantly hindered, and only helium flow could be detected. The phenomenon is believed to be caused by a tortuous nature of the transmembrane channels, which imposes steric barriers for gaseous species.[16] Similar to water

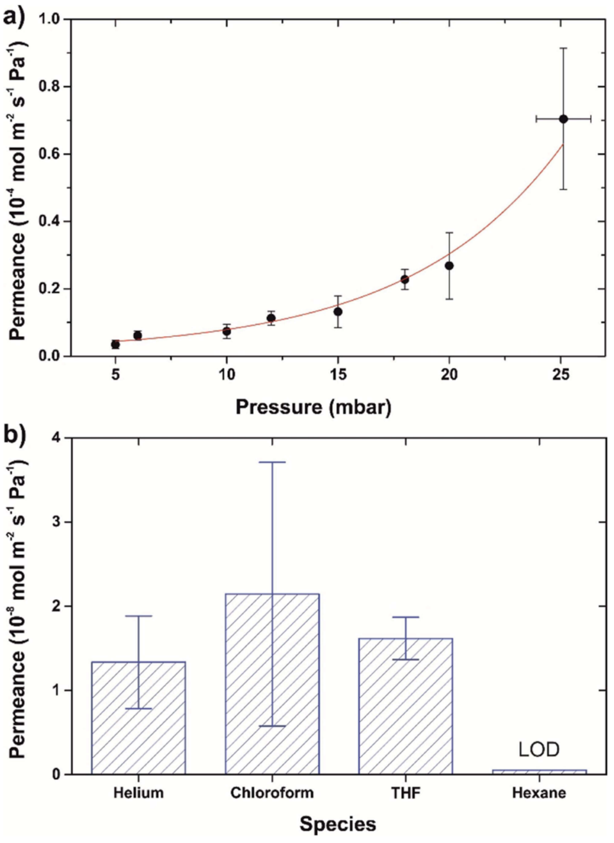

Figure 4. a) Permeance of D_2O vapor in TPC CNMs as a function of its pressure. The data represent mean values over 10 measurements with 6 different samples. Error bars are standard deviations. The last point at 25 mbar corresponds to the saturation vapor pressure, and it changed due to temperature fluctuations. The solid line is intended to guide the eye. b) Permeance of net species in TPC CNMs at the following feed pressures: p(He) = 250 mbar; p($CHCl_3$) ≈ 240 mbar (sat.); p(C_4H_8O) ≈ 200 mbar (sat.); p(C_6H_{14}) ≈ 180 mbar (sat.). The data were averaged over multiple room-temperature measurements with 6 samples. LOD is the limit of detection as specified in ref. 15.

though, saturated organic vapors are expected to adsorb and diffuse on the membrane surface, and indeed, small permeation rates were obtained for chloroform and tetrahydrofuran (THF). In fact, despite the difference in the molecular sizes, the fluxes measured are comparable to that of helium, and the explanation is the different transport mechanisms. While only direct impact translocation is possible for helium atoms, adsorption-mediated permeation is likely to take place for solvent molecules.[17] However, surface diffusion was not observed for bulkier hexane molecules which is very much analogous to TPT CNMs.[16] In general, our mass transfer measurements revealed no essential difference between TPC and TPT nanomembranes, suggesting their similar microstructure. The head groups seem to play no significant role in the carbonization process, as long as the molecular backbone and the packing density do not differ much.

Although the observed permselectivity (Figure 4) looks promising for separating water-organic mixtures, it is a so called ideal gas value and should be controlled in experiments with mixtures. THF is a versatile solvent which forms a minimum boiling homogenous azeotrope with water at 64 °C and atmospheric pressure.[23] To produce anhydrous THF, extractive distillation with various entrainers is usually employed, whereas dehydration with membranes is considered to be more energy-efficient.[24] In this work, we performed vapor permeation experiments with TPC CNMs exposed to water-THF mixtures. One-to-one feed composition was achieved by introducing saturated D_2O vapor into 25 mbar vaporous THF, as described in the earlier publication.[16] Under such model conditions, the membrane selectivity was found to amount to at least 500 (with respect to the mass-spectrometer detection limit). Very similar performance was noticed for TPT CNMs, confirming again the same microporous nature of the carbonized material.

CNMs are known to be converted to graphene upon heating to 800 °C.[25] This is the reason why their atomic structure is difficult to resolve with electron microscopy, because beam heating induces further transformations during imaging. There exist many types of amorphous carbon allotropes, but it is well accepted that they are all categorized into either graphitizable or non-graphitizable.[26] The former ones are more ordered and able to continuously rearrange into graphitic structures with temperature. Both classes consist of irregular sheets of sp^2-hybridized C atoms interconnected by sp^3 C atoms, and the difference is that the sp^2 regions in graphitizable materials are less cross-linked.

Indeed, the partial loss of aromaticity and appearance of aliphatic carbon in TPT SAMs was unambiguously revealed by high resolution electron energy loss spectroscopy (HREELS).[10c] The fact that CNMs readily yield graphene is indicative of the favorable orientation of their sp^2 constituents. Interestingly enough, the results of our gas and vapor permeation measurements evidenced a tortuous character for the membrane interior.[17] The only way to correlate these data with the earlier reported AFM images[13] is to assume that the interlaminar spacing in CNMs is the very bottleneck controlling their separation performance. Given the similarity between the nanomembranes made of TPC and TPT precursors, we propose that the radiation carbonization of aromatic SAMs obeys a generic mechanism. The surface mediation seems to facilitate the reorganization preferentially in the plane direction, giving rise to the laminar microstructure. Moreover, the length of the backbone of the SAM molecules is likely to determine the strength of the final material as the lateral integrity depends on the vertical cross-linking. Consequently, shorter components derived from biphenyl, such as biphenylthiol (BPT) and nitrobiphenylthiol (NBPT), were found to be much less suitable for producing defect-free micrometer-sized membranes, featuring irregular nanoscale holes.[27]

3. Conclusion

We showed that carboxylate SAMs on electrodeposited silver could be easily converted into functional nanomembranes. For the first time, the ultrasensitive permeation apparatus was applied to compare molecular transport in free-standing CNMs prepared from different head groups and on different substrates. The results obtained revealed very similar characteristics over TPC and TPT membranes, indicating common structural motifs of the carbonaceous materials. Electron irradiation of the densely packed adsorbates was proven to be an effective method for producing nanometer-thick microporous films. The chemical separation with CNMs displayed a narrow size distribution of their ducts, suggesting a somewhat higher degree of ordering in the transverse direction compared to the lateral one.

This study further establishes carbonized polyaromatic SAMs as generic systems for permeable nanomembranes and, by demonstrating the suitability of aromatic carboxylic acids in combination with UPD-Ag substrates, substantially broadens the basis of molecular precursors. Extension beyond the standard combination, thiolates on gold, opens the possibility of a more flexible design of precursor layers enabling new architectures as recently demonstrated with SAMs featuring nanotunnels and the option of intercalating additional species.[28] Albeit carboxylate SAMs have been shown to form also on Ag films,[11] the use of UPD-Ag substrates offer a convenient handling of substrates as regards control of oxidation and contaminations. Firstly, the electrodeposition of Ag bilayer on Au enables the use of freshly prepared substrates that outperform commercial thin films in terms of surface cleanliness. Secondly, these substrates can be easily handled in air and even in aqueous environments. It is noted that the range of substrates can be further extended to Cu-UPD by employing the analogous electrodeposition procedure.[29] We anticipate that future developments exploring the structural and functional variability of aromatic carboxylic acids, also in combination with widespread metals like copper and aluminum enables the development towards large-area ultrathin separation membranes, thus, reinforcing the application prospects of CNMs.

Experimental Section

SAMs and CNMs Preparation

Epitaxial gold substrates on mica (Georg Albert PVD) were used for both TPC and TPT systems. TPC SAMs were prepared with p-(terphenyl)-4-carboxylic acid (97% Aldrich) dissolved in 50/50 (vol.) water-ethanol mixture (saturated solution at room temperature). Prior to silver deposition, Au/mica was flame annealed and immersed into 10 mM $AgNO_3$ solution in 100 mM HNO_3. After a potential of 10 mV was applied for 2 min, the substrates were immediately placed into the preheated TPC solution and left overnight at 65 °C. The incubation time was around 20 hours. The substrates were then rinsed with ethanol and blown dry with N_2. The preparation of TPT SAMs was done with sublimated p-(terphenyl)-4-thiol (97%, Sigma-Aldrich) dissolved in anhydrous N,N-dimethylformamide (99.8%, Sigma-Aldrich). In this case Au/mica as delivered was first cleaned with ozone and subsequently outgassed in vacuum. Assembly was over 24 hours at 75 °C under argon atmosphere using a 100 nM TPT solution. The substrates were rinsed with DMF and ethanol and blown dry with N_2.

SAMs samples were loaded into a homemade radiation chamber and evacuated down to 5×10^{-8} mbar. An electron flood gun with beam energy of 100 eV was employed to irradiate the substrates for 12 min, and the total exposure corresponded to 50 mC/cm^2. CNMs on native substrates were covered with poly(methyl methacrylate) (PMMA) by means of a spin coater and dried on a hot plate at 90 °C. The benzene solutions of 50 and 950 kDa PMMA were used to deposit two protection layers respectively. Afterwards, mica was detached and gold was etched away in an aqueous I_2/KI solution. No additional etching step was undertaken for the Ag covered substrates. CNMs with PMMA were thoroughly rinsed in ultrapure water and transferred onto either Quantifoil Multi A TEM grids (Quantifoil Micro Tools GmbH) for helium ion microscopy or perforated Si_3N_4/Si windows (Silson Ltd) for permeation measurements. The size of the suspended CNMs samples varied between 2 and 7 micrometers.

STM and HIM Measurements

STM imaging was performed with a Molecular Imaging Pico IS microscope under ambient conditions. A Pt/Ir 80:20 wire (Advent Research Materials Ltd., 0.25 mm diameter) was used to cut tips mechanically. Tunneling parameters were typically between 0.010–0.070 nA, and $\pm$0.20–0.60 V.

Free-standing nanomembranes were imaged with a helium ion microscope (Zeiss Orion Plus) at a resolution limit below 1 nm. The images were scanned at 1 μs dwell time, beam energy of 35 keV, and a beam current of 0.3 pA.

IRRAS and XPS Measurements

IRRAS spectra were taken at a spectrometer VERTEX 70 (Bruker) equipped with a polarization-modulated reflectance module PMA 50 (Bruker). During measurements, the spectrometer was purged with a dry nitrogen flow of 3 L/min. The MCT detector was cooled with liquid nitrogen. Typically, 1024 scans were recorded at resolution of 4 cm^{-1}.

XPS spectra were obtained in an ultrahigh vacuum (10^{-11} mbar) Multiprobe system (Omicron) with a monochromatic X-ray source (Al K_α, 1486.7 eV) and a hemispherical electron analyzer (SPHERA) with pass energy of 25 eV. The binding energy scale was calibrated relative to Au $4f_{7/2}$ peak at 84.0 eV. The data were evaluated with CasaXPS software. The spectra were fitted by a sum of Gaussian/Lorentzian functions using linear backgrounds.

Permeation Measurements

Mass transfer measurements with free-standing CNMs were carried out at the custom-made system described in [15]. Briefly, a suspended CNM sample was secured between a high vacuum detection chamber with a quadrupole mass-spectrometer and a multi-section feed compartment. Steady-state permeation rates were determined upon exposing CNMs to defined amounts of gaseous and vaporous substances as measured with a capacitance manometer. Helium was supplied by Linde. Chloroform (VWR, 99.8%), tetrahydrofuran (Fisher Chemical, 99.99%), hexane (Fisher Scientific, 95%), and heavy water (Sigma-Aldrich, 99.9% atom D) were repeatedly degassed before use.

Acknowledgements

P. D. thanks the "Fonds der Chemischen Industrie" for a Liebig Fellowship, the Royal Society of Chemistry for a Researcher Mobility Grant, and the "Max-Buchner-Forschungsstiftung" for a Max-Buchner Fellowship. P. D. is also grateful to Kelly Turner and Zhen Yao for their kind assistance during his stay in St Andrews. This work was in part financed by the German Federal Ministry for Education and Research (BMBF) within the bilateral German-Greek Research and Innovation Cooperation, project Caerus 03XP0155 A.

Conflict of Interest

The authors declare no conflict of interest.

Keywords: amorphous materials · membranes · self-assembly · thin films · vapor permeation

[1] H. B. Park, J. Kamcev, L. M. Robeson, M. Elimelech, B. D. Freeman, *Science* **2017**, *356*, eaab0530.

[2] a) B. Zornoza, B. Seoane, J. M. Zamaro, C. Téllez, J. Coronas, *ChemPhysChem* **2011**, *12*, 2781–2785; b) T. M. Osborn Popp, A. Z. Plantz, O. M. Yaghi, J. A. Reimer, *ChemPhysChem* **2020**, *21*, 32–35; c) G. He, M. Dakhchoune, J. Zhao, S. Huang, K. V. Agrawal, *Adv. Funct. Mater.* **2018**, 1707427 ; d) A. Knebel, P. Wulfert-Holzmann, S. Friebe, J. Pavel, I. Strauß, A. Mundstock, F. Steinbach, J. Caro, *Chem. Eur. J.* **2018**, *24*, 5728–5733; e) R. L. Papurello, L. A. Lozano, E. V. Ramos-Fernández, J. L. Fernández, J. M. Zamaro, *ChemPhysChem* **2019**, *20*, 3201–3209; f) Y. Peng, Y. Li, Y. Ban, W. Yang, *Angew. Chem. Int. Ed.* **2017**, *56*, 9757–9761.

[3] a) B. P. Biswal, H. D. Chaudhari, R. Banerjee, U. K. Kharul, *Chem. Eur. J.* **2016**, *22*, 4695–4699; b) V. A. Kuehl, J. Yin, P. H. H. Duong, B. Mastorovich, B. Newell, K. D. Li-Oakey, B. A. Parkinson, J. O. Hoberg, *J. Am. Chem. Soc.* **2018**, *140*, 18200–18207; c) K. Dey, M. Pal, K. C. Rout, H. S. Kunjattu, A. Das, R. Mukherjee, U. K. Kharul, R. Banerjee, *J. Am. Chem. Soc.* **2017**, *139*, 13083–13091; d) M. Shan, B. Seoane, E. Rozhko, A. Dikhtiarenko, G. Clet, F. Kapteijn, J. Gascon, *Chem. Eur. J.* **2016**, *22*, 14467–14470.

[4] a) M. Y. Jeon, D. Kim, P. Kumar, P. S. Lee, N. Rangnekar, P. Bai, M. Shete, B. Elyassi, H. S. Lee, K. Narasimharao, S. N. Basahel, S. Al-Thabaiti, W. Xu, H. J. Cho, E. O. Fetisov, R. Thyagarajan, R. F. DeJaco, W. Fan, K. A. Mkhoyan, J. I. Siepmann, M. Tsapatsis, *Nature* **2017**, *543*, 690–694; b) D. Kim, M. Y. Jeon, B. L. Stottrup, M. Tsapatsis, *Angew. Chem. Int. Ed.* **2018**, *57*, 480–485; c) Z. Cao, S. Zeng, Z. Xu, A. Arvanitis, S. Yang, X. Gu, J. Dong, *Sci. Adv.* **2018**, *4*, eaau8634; d) T. H. Nguyen, H. Gong, S. S. Lee, T.-H. Bae, *ChemPhysChem* **2016**, *17*, 3165–3169.

[5] a) H. Richter, H. Voss, N. Kaltenborn, S. Kämnitz, A. Wollbrink, A. Feldhoff, J. Caro, S. Roitsch, I. Voigt, *Angew. Chem. Int. Ed.* **2017**, *56*, 7760–7763; b) C. Zhang, W. J. Koros, *Adv. Mater.* **2017**, *29*, 1701631; c) D. Bouša, K. Friess, K. Pilnáček, O. Vopička, M. Lanč, K. Fónod, M. Pumera, D. Sedmidubský, J. Luxa, Z. Sofer, *Chem. Eur. J.* **2017**, *23*, 11416–11422; d) P. Panigrahi, A. K. Dhinakaran, Y. Sekar, R. Ahuja, T. Hussain, *ChemPhysChem* **2018**, *19*, 2250–2257.

[6] A. Turchanin, A. Gölzhäuser, *Adv. Mater.* **2016**, *28*, 6075–6103.

[7] J. C. Love, L. A. Estroff, J. K. Kriebel, R. G. Nuzzo, G. M. Whitesides, *Chem. Rev.* **2005**, *105*, 1103–1170.

[8] P. Angelova, H. Vieker, N.-E. Weber, D. Matei, O. Reimer, I. Meier, S. Kurasch, J. Biskupek, D. Lorbach, K. Wunderlich, L. Chen, A. Terfort, M. Klapper, K. Müllen, U. Kaiser, A. Gölzhäuser, A. Turchanin, *ACS Nano* **2013**, *7*, 6489–6497.

[9] a) X. Zhang, C. Neumann, P. Angelova, A. Beyer, A. Gölzhäuser, *Langmuir* **2014**, *30*, 8221–8227; b) P. Penner, X. Zhang, E. Marschewski, F. Behler, P. Angelova, A. Beyer, J. Christoffers, A. Gölzhäuser, *J. Phys. Chem. C* **2014**, *118*, 21687–21694; c) C. Yildirim, E. Sauter, A. Terfort, M. Zharnikov, *J. Phys. Chem. C* **2017**, *121*, 7355–7364.

[10] a) W. Eck, A. Küller, M. Grunze, B. Völkel, A. Gölzhäuser, *Adv. Mater.* **2005**, *17*, 2583–2587; b) A. Turchanin, D. Käfer, M. El-Desawy, C. Wöll, G. Witte, A. Gölzhäuser, *Langmuir* **2009**, *25*, 7342–7352; c) L. Amiaud, J. Houplin, M. Bourdier, V. Humblot, R. Azria, C.-M. Pradier, A. Lafosse, *Phys. Chem. Chem. Phys.* **2014**, *16*, 1050–1059; d) J. Houplin, C. Dablemont, L. Sala, A. Lafosse, L. Amiaud, *Langmuir* **2015**, *31*, 13528–13534; e) C. Yildirim, M. Füser, A. Terfort, M. Zharnikov, *J. Phys. Chem. C* **2017**, *121*, 567–576.

[11] C. Neumann, M. Szwed, M. Frey, Z. Tang, K. Kozieł, P. Cyganik, A. Turchanin, *ACS Appl. Mater. Interfaces* **2019**, *11*, 31176–31181.

[12] G. Capozzi, G. Modena, in *The Chemistry of the Thiol Group, Part 2* (Ed.: S. Patai), John Wiley&Sons Ltd., **1974**, pp. 785–839.

[13] Y. Yang, P. Dementyev, N. Biere, D. Emmrich, P. Stohmann, R. Korzetz, X. Zhang, A. Beyer, S. Koch, D. Anselmetti, A. Gölzhäuser, *ACS Nano* **2018**, *12*, 4695–4701.

[14] Y. Yang, R. Hillmann, Y. Qi, R. Korzetz, N. Biere, D. Emmrich, M. Westphal, B. Büker, A. Hütten, A. Beyer, D. Anselmetti, A. Gölzhäuser, *Adv. Mater.* **2020**, 1907850.

[15] P. Dementyev, T. Wilke, D. Naberezhnyi, D. Emmrich, A. Gölzhäuser, *Phys. Chem. Chem. Phys.* **2019**, *21*, 15471–15477.

[16] D. Naberezhnyi, A. Gölzhäuser, P. Dementyev, *J. Phys. Chem. Lett.* **2019**, *10*, 5598–5601.

[17] P. Dementyev, Y. Yang, M. Rezvova, A. Gölzhäuser, *J. Phys. Chem. Lett.* **2020**, *11*, 238–242.

[18] H. Aitchison, H. Lu, S. W. L. Hogan, H. Früchtl, I. Cebula, M. Zharnikov, M. Buck, *Langmuir* **2016**, *32*, 9397–9409.

[19] a) V. V. Korolkov, S. Allen, C. J. Roberts, S. J. B. Tendler, *J. Phys. Chem. C* **2011**, *115*, 14899–14906; b) A. Bashir, W. Azzam, M. Rohwerder, A. Terfort, *Langmuir* **2013**, *29*, 13449–13456.

[20] a) N. E. Schlotter, M. D. Porter, T. B. Bright, D. L. Allara, *Chem. Phys. Lett.* **1986**, *132*, 93–98; b) E. L. Smith, M. D. Porter, *J. Phys. Chem.* **1993**, *97*, 8032–8038; c) A. Krzykawska, J. Ossowski, T. Żaba, P. Cyganik, *Chem. Commun.* **2017**, *53*, 5748–5751; d) M. H. Hsu, W. S. Hu, J. J. Lin, Y. J. Hsu, D. H. Wei, C. W. Yang, C. S. Chang, Y. T. Tao, *Langmuir* **2004**, *20*, 3641–3647.

[21] a) S. Stepanow, T. Strunskus, M. Lingenfelder, A. Dmitriev, H. Spillmann, N. Lin, J. V. Barth, Ch. Wöll, K. Kern, *J. Phys. Chem. B* **2004**, *108*, 19392–19397; b) W. Zhang, A. Nefedov, M. Naboka, L. Cao, Ch. Wöll, *Phys. Chem. Chem. Phys.* **2012**, *14*, 10125–10131.

[22] T. C. R. Rocha, A. Oestereich, D. V. Demidov, M. Hävecker, S. Zafeiratos, G. Weinberg, V. I. Bukhtiyarov, A. Knop-Gericke, R. Schlögl, *Phys. Chem. Chem. Phys.* **2012**, *14*, 4554–4564.

[23] Z. Zhang, D. Huang, M. Lv, P. Jia, D. Sun, W. Li, *Sep. Purif. Technol.* **2014**, *122*, 73–77.

[24] L. M. Vane, *J. Chem. Technol. Biotechnol.* **2019**, *94*, 343–365.

[25] D. G. Matei, N.-E. Weber, S. Kurasch, S. Wundrack, M. Woszczyna, M. Grothe, T. Weimann, F. Ahlers, R. Stosch, U. Kaiser, A. Turchanin, *Adv. Mater.* **2013**, *25*, 4146–4151.

[26] E. H. L. Falcao, F. Wudl, *J. Chem. Technol. Biotechnol.* **2007**,*82*, 524–531.

[27] Unpublished data.

[28] R. Ortiz de la Morena, A. Asyuda, H. Lu, H. Aitchison, K. Turner, S. M. Francis, M. Zharnikov, M. Buck, *Phys. Chem. Chem. Phys.* **2020**, *22*, 4205–4215.

[29] a) I. Cebula, C. Shen, M. Buck, *Angew. Chem. Int. Ed.* **2010**, *49*, 6220–6223; b) H. Aitchison, H. Lu, M. Zharnikov, M. Buck, *J. Phys. Chem. C* **2015**, *119*, 14114–14125; c) H. Aitchison, H. Lu, R. Ortiz de la Morena, I. Cebula, M. Zharnikov, M. Buck, *Phys. Chem. Chem. Phys.* **2018**, *20*, 2731–2740.

Manuscript received: February 25, 2020
Revised manuscript received: March 19, 2020
Accepted manuscript online: March 23, 2020
Version of record online: April 14, 2020

4.8 Publication: Molecular transport in ionic liquid/nanomembrane hybrids

This article is reprinted with permission from Royal Society of Chemistry. The original paper appeared as:

D. Naberezhnyi and P. Dementyev, *Molecular transport in ionic liquid/nanomembrane hybrids.* ***Phys. Chem. Chem. Phys.***, 2020, **22**, 9808–9814.

Contribution:

Preparation and transfer of the CNMs, characterization of the materials by XPS and PM-IRRAS, coating with ionic liquid and quantitative analysis of the ionic liquid by PM-IRRAS, optical microscopy and estimation of a thickness of the IL droplets, permeation experiments and data evaluation were performed by the author.

PCCP

ROYAL SOCIETY OF CHEMISTRY

PAPER

View Article Online
View Journal | View Issue

Cite this: *Phys. Chem. Chem. Phys.*, 2020, **22**, 9808

Molecular transport in ionic liquid/nanomembrane hybrids†

Daniil Naberezhnyi and Petr Dementyev *

Ionic liquids and nanoscale membranes are both considered as promising functional components to design next-generation gas separation technologies. Herein, we combine free-standing carbon nanomembranes (CNMs) with [bmim][Tf_2N] ionic liquid having affinity to carbon dioxide, and explore molecular permeation through such a composite membrane. Gas transport measurements reveal an increase in the transmembrane flux of carbon dioxide as compared to that of bare CNMs, whereas passage of helium is found to be suppressed in accordance with the solubility constants. Upon exposure to water vapor, the behavior of the hybrid membrane appears to differ strikingly as hydrophilic properties of CNMs are camouflaged by the hydrophobic nature of the ionic liquid. Kinetic simulations are conducted to account for the change in permeation mechanism, and the results agree with the experimental data obtained. Our study confirms that molecular transport in two-dimensional membranes can be tailored by imparting chemical functionalities, but at the same time highlights practical challenges in surface modification.

Received 4th March 2020,
Accepted 17th April 2020

DOI: 10.1039/d0cp01233e

rsc.li/pccp

Introduction

The global warming problem is continuously raising public awareness worldwide.[1] While net-zero emission of greenhouse gases appears to be an urgent necessity, pre- and post-combustion capture of carbon dioxide remains challenging both technologically and economically. Membrane processes are among the most energy-efficient approaches, which are virtually implementable in all concerned industries from hydrogen production to oxyfuels.[2–5] Notably, high-throughput membranes can be directly used at power plants to extract CO_2 from flue gases, provided there is good selectivity over nitrogen.[6–9] However, the combination of a high flux and a great separation factor is not easy to achieve due to material properties that dictate a selectivity–permeability trade-off.[10,11] In theory, two-dimensional membranes could provide ultimate transport performance as the diffusion rate is reversely proportional to the thickness.[12,13] Although size exclusion with nanomembranes seems to be a straightforward separation strategy, computational studies have found various affinity effects to be feasible as well.[14–22] In particular, ionic liquids (ILs) have been predicted as effective modifiers to tailor permselectivity in graphene membranes due to specific interactions with certain gas species.[23] Recently, He *et al.* used CO_2-philic polymers to functionalize plasma-treated graphene and obtained outstanding membrane characteristics.[24] The active layers in the hybrids were proven to be as thin as 20 nm displaying synergy between the chemical affinity of the modifier and mechanical stability of the single-layer material. The authors proposed their approach to be generally applicable in creating sorption functionalities upon nanomembranes, including surface immobilization of ILs.

Room-temperature ILs with melting points below 20 °C represent salts consisting of large asymmetric organic cations (imidazolium, pyridinium, quaternary ammonium, *etc.*) and inorganic anions (chloride, tetrafluoroborate, trifluoromethylsulfonate, *etc.*).[25,26] Physicochemical properties of ILs have been shown to depend on the cation–anion combinations and are typically characterized by negligible vapor pressure (10^{-8}–10^{-13} mbar), high viscosity, low electric conductivity, and remarkable thermal stability.[27–32] Thanks to their absorption capabilities, ILs have been widely pursued as impregnating agents in gas separation membranes.[33–36] 1-Butyl-3-methylimidazolium tetrafluoroborate [bmim][BF_4], 1-butyl-3-methylimidazolium hexafluorophosphate [bmim][PF_6], 1-hexyl-3-methylimidazolium bis(trifluormethylsulfonyl)imide [hmim][Tf_2N], 1-hexyl-3-methylimidazolium tetracyanoborate [hmim][$B(CN)_4$], and 1-butyl-3-methylimidazolium bis(trifluoromethylsulfonyl)imide [bmim][Tf_2N] are the most frequently used commercially available compounds, which exhibit appreciable CO_2/N_2 selectivity.[37–42] While the solubility of carbon dioxide in the ILs is similar (Henry's constants $\sim 10^{-3}$ mol m^{-3} Pa^{-1}), their viscosity is known to vary from around 50 to 300 mPa s.[43–48] Because spin coating is an appropriate method with respect to depositing ILs onto ultrathin

---

Physics of Supramolecular Systems and Surfaces, Faculty of Physics, Bielefeld University, Bielefeld 33615, Germany. E-mail: dementyev@physik.uni-bielefeld.de

† Electronic supplementary information (ESI) available. See DOI: 10.1039/d0cp01233e

membranes,[49] the least viscous [bmim][Tf_2N] with η = 45.6 ± 0.3 mPa s^{43} has been chosen for experiments on adjusting gas permeability in carbon nanomembranes (CNMs).

Previously, free-standing CNMs were found to pass water molecules much faster than helium and other gases.[50–52] The structure of the 1 nm thick material is intrinsically microporous, but the tortuous geometry of its channels is believed to sterically hinder the transmembrane passage of non-adsorbing particles.[53] In this work, we pioneer the use of ILs for controlling molecular transport in nanoscale membranes and explore practical ways for bringing together these delicate constituents. Drop casting and spin coating of both pure and diluted ILs were implemented to directly overlay micrometer-scale suspended samples. CNMs covered with a layer of [bmim][Tf_2N] were demonstrated to enhance the permeation rate of carbon dioxide, whereas the flux of water vapor was found to decrease manifold compared to bare nanomembranes.

Experimental

CNMs were prepared *via* electron-induced carbonization of self-assembled aromatic carboxylates.[54] Prior to use, 300 nm gold films on mica (Georg Albert PVD) were cleaned for 6 minutes using a UV-ozone cleaning system, UVOH 150 LAB (FHR Anlagenbau), and rinsed with ethanol (absolute, 99.8%, VWR Chemicals). The substrates were immersed into an aqueous electrolyte solution of 10 mM $AgNO_3$ (ACS reagent, 99.9999%, Sigma-Aldrich) and 100 mM HNO_3 (purified by redistillation, 99.999%, Sigma-Aldrich) to deposit a silver bilayer in underpotential mode at 10 mV during 2 minutes.[55] After deposition, substrates were rinsed with ethanol, dried with nitrogen flow and immersed directly into precursor solutions. BPC self-assembled monolayers (BPC-SAMs) were obtained during 5 minutes at 65 °C in a saturated solution of biphenyl-4-carboxylic acid (95%, TCI) in Milli-Q water. TPC-SAMs were synthesized during 20 hours at 65 °C in a saturated solution of *p*-(terphenyl)-4-carboxylic acid (97%, Sigma-Aldrich) in a 1 : 1 water–ethanol mixture.

Electron irradiation was carried out in a home-made flood gun chamber at a pressure of 5×10^{-8} mbar for 14 minutes, and the total dose to convert SAMs into CNMs was 50 mC cm^{-2}. The samples were coated with two layers of 50 K and 950 K poly(methyl methacrylate) (PMMA) using a SPIN150i spin coater (SPS Europe) at 4000 rpm. The protected CNMs on native substrates were placed in aqueous I_2/KI solution (mass ratio $I_2 : KI : H_2O = 1 : 4 : 40$) to etch away the underlying gold film in accordance with: $2Au + I_2 + 2KI \rightarrow 2K[AuI_2]$. Under these conditions, the silver layer is known to dissolve as follows: $AgI + 2KI \rightarrow K_2[AgI_3]$.[56] Floating CNM/PMMA films were transferred onto Si_3N_4/Si chips with orifices of 4 μm, 7 μm or 15 μm in diameter (Silson Ltd). The chips were submersed in acetone for 1 hour to dissolve PMMA layers yielding free-standing nanomembranes for permeation measurements.

The [bmim][Tf_2N] IL (for synthesis, 98%, Sigma-Aldrich) was dissolved in acetonitrile[57] (gradient grade for liquid chromatography, 99.9%, Merck) to gradually change the amount of deposited material. The following concentrations were prepared: C1 = 3.4×10^{-5} M (0.53 nmol cm^{-2}); C2 = 6.0×10^{-4} M (10 nmol cm^{-2}); C3 = 1.4×10^{-3} M (22 nmol cm^{-2}); C4 = 3.0×10^{-3} M (45 nmol cm^{-2}); C5 = 6.0×10^{-3} M (90 nmol cm^{-2}). Indicated in the brackets is the coverage of the IL on the surface upon drop-casting 56.8 μL of the solutions onto CNM/Au. This volume was defined to cover the sample area of 375 mm^2 with 2, 40, 85, 170, and 341 monolayers of IL in nominal thickness (with respect to [bmim][Tf_2N] molar volume).[58] The IL solutions were spin-coated at 6000 rpm onto the CNM/gold substrate for spectroscopic analysis. Before each deposition, the sample was rinsed with acetonitrile and checked by infrared spectroscopy. For transport measurements, free-standing CNMs on Si_3N_4/Si chips of 25 mm^2 in total area were first glued onto CF-compatible copper disks and then directly drop-cast with 2.5 μL of the solution C5. The samples were either spun or dried in air without spinning.

A VERTEX 70 (Bruker) FTIR spectrometer coupled with a PMA 50 (Bruker) polarization-modulation module was used to obtain the PMIRAS spectra of SAMs and CNMs on native substrates (ESI) and to analyze the [bmim][Tf_2N] covered samples.[59] During measurements, the spectrometer was purged with dry nitrogen at 3 L min^{-1}, and the MCT detector was cooled down with liquid nitrogen. 1024 scans were recorded at a resolution of 4 cm^{-1}. XPS spectra (ESI) were obtained in an ultrahigh vacuum (10^{-11} mbar) Multiprobe system (Omicron) with a monochromatic X-ray source (AlKα, 1486.7 eV) and a hemispherical electron analyzer (SPHERA) with a pass energy of 25 eV and step of 0.05 eV. Gaussian and Lorentzian functions were applied to fit C 1s and O 1s spectra, and an exponential asymmetric blend based on the sum of Gaussian/Lorentzian was used for Ag3d spectra. The fitting was done by means of CasaXPS software with a linear background for carbon, a Shirley background for metallic silver, and a Tougaard background from polymers for oxygen. A fluorescence microscope, BX51 (Olympus), with six objectives was employed to investigate the spatial distribution of [bmim][Tf_2N] deposits on both gold substrates and Si_3N_4/Si chips. A custom-made permeation system equipped with a quadrupole mass-spectrometer was used to study molecular transport in the hybrid membranes.[51] Helium, nitrogen, oxygen, argon, and carbon dioxide were supplied by Linde. Deuterium oxide was purchased from Sigma-Aldrich (99.9% atom D).

Results and discussion

Depositing nanoscopic layers of IL onto CNMs turned out to be difficult in spite of the fact that their mechanical stability allows for various manipulations, even with free-standing samples. When supported by the native substrates, drop casting of the net compound followed by spinning at 6000 rpm was found to yield a rather thick film of about 1 μm, as estimated from infrared spectra (see below). Therefore, we dissolved [bmim][Tf_2N] in acetonitrile at varied concentrations, and used

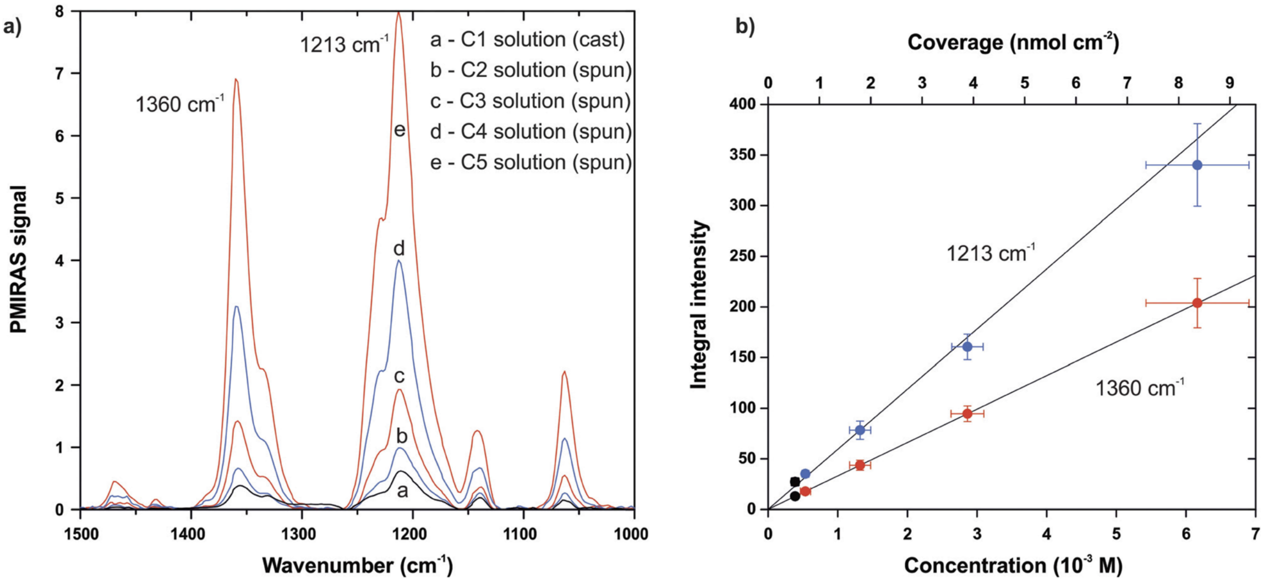

Fig. 1 (a) Infrared spectra of [bmim][Tf$_2$N] deposited onto CNMs on gold. The spectra (b–e) were obtained upon spin-coating CNMs with the solutions C2–C5, respectively. The spectrum a was obtained without spinning with the solution C1 and is referred to as a reference. (b) Calibration plots from the spectroscopic measurements. The integrated peak intensity for the absorption bands 1213 and 1360 cm^{-1} is plotted against the concentration of the solutions (blue and red dots). The data were averaged over three depositions, and the error bars correspond to standard deviation. The top scale relates the concentration to the deposited coverage as determined from the reference signals (black dots). The *x*-error bars indicate uncertainty in the calculated values of the coverage.

the solutions to cover nanomembrane samples. Fig. 1 illustrates the results of our spectroscopic measurements done with as-prepared CNMs on gold. The most pronounced bands at 1360 cm^{-1} and 1213 cm^{-1} are due to asymmetric stretching of the sulfonyl SO_2 and trifluoromethyl CF_3 moieties, respectively.[60] As evidenced, the spectra evolve gradually with concentration, and the integral peak intensities comply well with the linear law. To calibrate the plot, the solution C1 was cast without spinning, and the surface coverage was calculated as a function of concentration. One can see that the amount of IL left after spinning is considerably reduced compared to the nominal one expected from evaporation of the solvent. For instance, the solution C4 gives rise to only about 4 nmol cm^{-2} as opposed to 45 nmol cm^{-2} if the sample was not spun. Based on these findings, the most concentrated solution C5 was selected to deposit the IL onto suspended nanomembranes.

As CNMs are known to enable unimpeded water transport, we performed permeation measurements with water vapor in order to test the efficacy of IL deposition. Fig. 2a shows the comparison of four different samples, including a bare nanomembrane. The flux through the first modified sample (C5 fast) was found to remain almost unchanged, although the amount of IL deposited was expected to be as much as 5 nmol cm^{-2} corresponding to the nominal thickness of 19 monolayers. This observation was rationalized upon inspecting the sample with optical microscopy (Fig. 2c), which suggests that the IL does not wet CNMs. Indeed, one can clearly see micrometer-sized agglomerates, which are uniformly spread over the surface and not forming a continuous film. It is likely that the relative coverage of [bmim][Tf$_2$N] on the free-standing part is much less than 100%, consistent with the small decline in water permeation rate. The fact that adhesion of the IL on CNMs is not favorable becomes obvious in Fig. 2d and e, where large individual droplets are present. While the sample C5 (slow) was spun at 1000 rpm and the sample C5 (still) was not at all, in both cases, the nominal IL thickness was expected to be more than 200 monolayers. Instead, a considerable fraction of the surface was left uncovered, and the droplets formed appeared to be as thick as a few μm (estimated from interference minima).

The poor interaction energetics between [bmim][Tf$_2$N] and CNMs can be interpreted in terms of their different hydrophilicities. In fact, IL with the $N(SO_2CF_3)_2^-$ anion is known to be rather hydrophobic, and the surface tension of [bmim][Tf$_2$N] amounts to 37.5 dyn cm^{-1}.[61] The water contact angle on bare CNMs was found to equal 65 ± 4°, confirming their hydrophilic properties. As demonstrated in Fig. 2a, the IL significantly reduces water permeation rate when it covers CNMs (samples C5 slow and C5 still). The difference between these two samples stems from the fact that the former one contained an IL droplet only partially overlapping with a free-standing part. In contrast, the nanomembrane in the sample C5 (still) (Fig. 2e) was entirely under the IL and exhibited a ten-fold decrease in water flux. Interestingly, IL deposits were found to slowly reshape themselves after spinning, whereas circular droplets were formed immediately upon drop-casting. Therefore, the latter method was applied in the following experiments, and all the composite samples were checked with a microscope before and after permeation measurements.

Permeation of gases in the CNM/IL hybrids appeared to differ from that in ordinary membranes. As reported before,

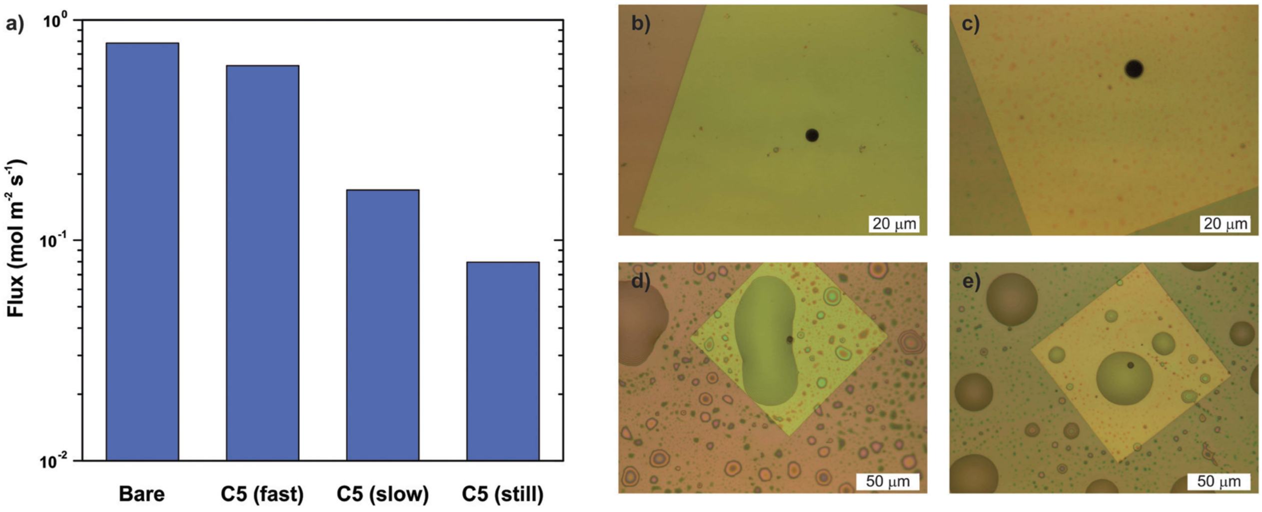

Fig. 2 (a) Transmembrane flux of D_2O molecules in BPC-CNMs. The following designation applies: bare – CNM without IL, C5 (fast) – CNM casted with 2.5 μL of the solution C5 and spun at 6000 rpm; C5 (slow) – CNM casted with 2.5 μL of the solution C5 and spun at 1000 rpm; C5 (still) – CNM casted with 5.0 μL of the solution C5 without spinning. The measurements were conducted at 20 mbar feed pressure. (b–e) Optical micrographs of the samples as ordered in (a). The orifice size is 4.61, 7.10, 4.12, and 4.49 μm, respectively.

only He was able to pass through the bare CNMs, while the transport rate for other gases was not detected.[50] First of all, CO_2-philic [bmim][Tf_2N] was found to promote permeation of carbon dioxide (Fig. 3a). It is evident that under identical conditions, the modified nanomembrane does allow carbon dioxide to permeate, as opposed to the case of bare CNMs. Measurements on four samples yield a permeance of $1.8 \pm 0.4 \times 10^{-9}$ mol m^{-2} s^{-1} Pa^{-1}, which is about an order of magnitude higher than the upper limit for the unmodified samples. While this enhancement is significant, no effect was observed for nitrogen, oxygen, and argon as their fluxes were below the detection limit similar to that of uncovered CNMs. Another striking observation was that the transmembrane passage of helium in the hybrids was suppressed compared to that of bare membranes (Fig. 3b). The resulting permeation rate was calculated to be $4.2 \pm 0.9 \times 10^{-9}$ mol m^{-2} s^{-1} Pa^{-1} (mean value over four samples) meaning almost a two-fold reduction. These findings are consistent with the different solubilities of the gases in the modifying layer. Indeed, Henry's constants in [bmim][Tf_2N] decrease significantly going from CO_2 (1.03×10^{-3} mol m^{-3} Pa^{-1})[43] to He (1.18×10^{-4} mol m^{-3} Pa^{-1}),[39] and O_2 and N_2 (8.16×10^{-5} and 4.28×10^{-5} mol m^{-3} Pa^{-1}, respectively).[62] Our interpretation is that preferential absorption of carbon dioxide in the IL facilitates its permeation due to the increased probability of entering the nanomembrane channels. The volume concentration of dissolved CO_2 molecules exceeds that in the gas phase, while the opposite effect takes place for helium. These findings confirm that chemical modification of nanomembranes enables tailored control over their separation performance.

It is also remarkable that despite their hydrophobicity, ILs are capable of rather intense water uptake.[61] As shown spectroscopically, absorbed water molecules form hydrogen bonds with anionic species whereas titration measurements indicate great solubility constants.[63] Clearly, the IL impedes permeation of water vapor in CNMs (Fig. 2a), but it does not block it completely. On the basis of the literature data for H_2O,[64] we estimated the Henry's constant for heavy water in [bmim][Tf_2N] to be 3.0×10^{-1} mol m^{-3} Pa^{-1}. This value is two orders of magnitude larger than that for CO_2 and makes it possible to explore molecular transport in the hybrid membranes in more detail. In bare CNMs, the flux of water is well rationalized by accounting for its adsorption and condensation on the membrane surface:[51]

$$F = k_{\text{mono}}\theta_{\text{mono}}n_0 + k_{\text{multi}}\theta_{\text{multi}}n_0 \qquad (1)$$

where θ_{mono} and θ_{multi} are the relative surface coverage of separate and clustered adsorbates, n_0 is the areal density of adsorption sites, and k_{mono} and k_{multi} stand for individual and cooperative transport mechanisms, respectively. Although the [bmim][Tf_2N] coating prevents direct gas–solid interactions in the hybrid membranes, the same kinetic formalism is still suitable to describe the passage of D_2O molecules as their amount at the IL/CNM interface is quantifiable. According to Henry's law, the volume concentration of water c in the IL is given by:

$$c = Hp \qquad (2)$$

where p is the upstream vapor pressure. Now, the amount of absorbed D_2O molecules (per unit area) in the vicinity of CNM is expressed as follows:

$$N = cl \qquad (3)$$

where l is the thickness of the interfacial layer (Fig. 4a). Similar to eqn (1), the transmembrane flux can be then represented *via* effective surface coverage θ_{eff} and rate constant k_{eff}:

$$F = k_{\text{eff}}\theta_{\text{eff}}n_0 \qquad (4)$$

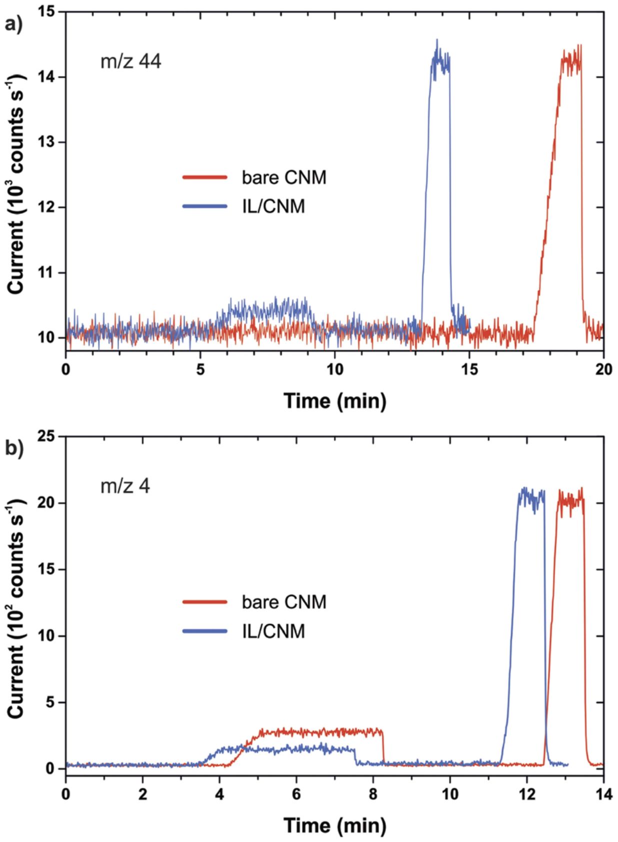

Fig. 3 QMS output for gas permeation measurements with bare and IL-modified CNMs. Red and blue lines are plotted on the same graphs for better comparison. The size of the samples was 15 μm. (a) Experiments with carbon dioxide. Bare CNM was exposed to 200 mbar CO_2 (time period from 4 to 6 min) and 300 mbar CO_2 (time period from 8 to 12 min). IL/CNM was exposed to 200 mbar CO_2 (time period from 6 to 9 min). The calibration signals at 14 and 19 min were obtained with a reference aperture at 2.1 mbar feed pressure. (b) Experiments with helium. Bare CNM was exposed to 200 mbar He (time period from 5 to 8 min). IL/CNM was exposed to 200 mbar He (time period from 4 to 7 min). The calibration signals at 12 and 13 min were obtained with a reference aperture at 2.1 mbar feed pressure.

where $\theta_{\text{eff}} = N/n_0$. In order to utilize the average bulk concentration c, we assume that the near-membrane region consists of at least three molecular layers of IL. Given the molar volume of [bmim][Tf_2N],[58] this approximation gives rise to 2.4 nm for l. In other words, all dissolved D_2O molecules located within that distance from CNMs are supposed to be "trapped" by the surface. This assumption is consistent with the diffusion coefficient of water in the IL (10^{-6}–10^{-7} cm^2 s^{-1}),[65] indicating that translocation in the bulk on such a size scale is faster than permeation through CNMs.

As for the effective constant k_{eff}, there should be a distinct concentration dependence because water molecules in ILs are known to congregate upon increasing their molar fraction.[66] It is clear that in very dilute solutions, absorbed species do not interact with each other and diffuse across the membrane individually, whereas a cooperative mechanism might play a role at higher concentrations. In a first approximation, we express the rate constant *via* the above k_{mono} and k_{multi} as a linear function of c:

$$k_{\text{eff}} = \frac{c}{c_0}(k_{\text{multi}} - k_{\text{mono}}) + k_{\text{mono}} \qquad (5)$$

where c_0 is the critical concentration, and k_{mono} and k_{multi} are determined from boundary conditions with bare CNMs.[51] The physical meaning of the parameter c_0 is a concentration at which absorbed water entirely percolates the IL as a liquid phase. One can see that $k_{\text{eff}} \approx k_{\text{mono}}$ when $c \ll c_0$, and $k_{\text{eff}} = k_{\text{multi}}$ if $c = c_0$. Combining eqn (2)–(5), we calculated the flux of D_2O molecules in CNM/IL membranes *versus* the feed pressure for different values of c_0 (Fig. 4b).

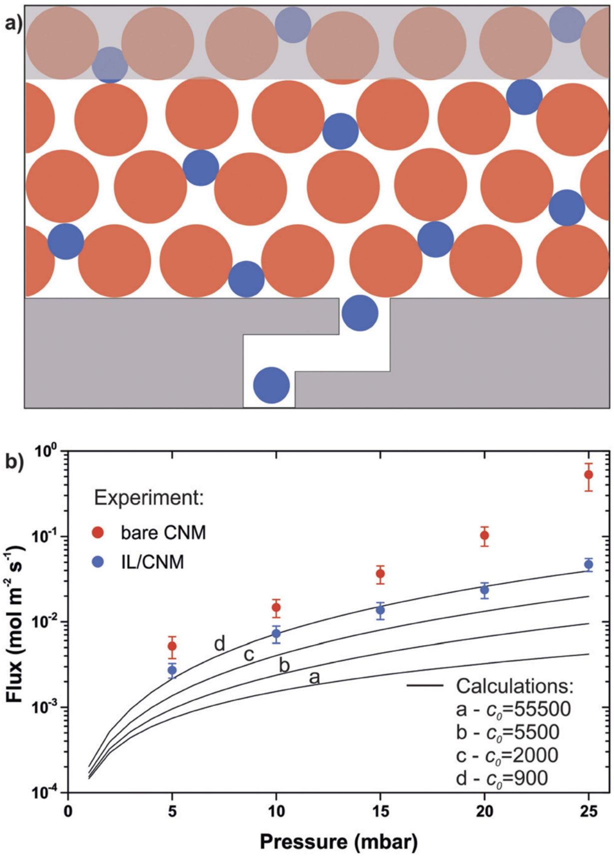

Fig. 4 (a) Phenomenological model for molecular permeation in CNM/IL hybrid membranes. Large circles designate IL ion pairs, while small circles designate absorbed water molecules. (b) Transmembrane flux of D_2O molecules. Data points represent experimental results obtained with bare and IL-modified samples. Solid lines demonstrate kinetic simulations with the rate constant at various c_0 (the values are in mol m^{-3}).

As compared to bare CNMs, the pressure dependence for the hybrids is less steep, but it still deviates from linearity, which would be expected if k_{eff} was constant. Furthermore, the simulations with $c_0 = 5.5 \times 10^4$ mol m^{-3} (molar concentration of water in pure water) yielded a far lower permeation rate than observed in the experiment. This indicates that water molecules absorbed in the IL are involved in hydrogen bonding to form clusters occupying free space between ion pairs. In turn, the agglomerates trigger the single-file transport channel, facilitating the overall permeation rate. This process depends on the uptake of water vapor and is more pronounced at higher humidity. Please note that the effective surface coverage in our calculations reaches only 9% at most. At $c_0 = 9.0 \times 10^2$ mol m^{-3}, the calculated curve reproduces the experimental data points fairly well, meaning a significant contribution of the cooperative mechanism. Thus, the effective rate constant amounts to nearly 85% k_{multi} upon saturation, and under these conditions, most of the D_2O molecules absorbed in [bmim][Tf_2N] are likely to take part in intermolecular interactions. In contrast, permeation rates of carbon dioxide and other gases through the IL-modified membranes are believed to strictly obey Henry's law, albeit its verification is complicated because of the small absolute numbers. As the modifier species are unlikely to impregnate sub-nanometer CNMs conduits, their tortuous nature seems to be the key in preventing the transport of inert particles. To fully benefit from the chemical affinity of ILs towards CO_2, one would need a supporting nanomembrane with straight pores such as those in perforated graphene. However, adhesion of the modifying layer on the membrane surface remains a serious issue.

Conclusions

For the first time, an IL was used to tailor gas separation performance in nanoscale membranes. In contrast to laminar structures incorporating IL inside the nanochannels,[67–71] only the outer side of 1 nm-thick CNMs was modified to promote surface diffusion. [bmim][Tf_2N]-covered free-standing CNMs were shown to preferentially pass carbon dioxide over nitrogen with a ten-fold enhancement in permeation rate compared to bare membranes. At the same time, the permeance of helium in the hybrid membranes was found to be twice lower, correlating with the relative Henry's constants of the gases. Similarly, permeation of water vapor was substantially inhibited in agreement with the kinetic model developed. Additionally, our simulations suggest that absorbed water forms a percolating network of hydrogen-bonded molecules inside an IL matrix.

This study demonstrates that combining ILs and nanomembranes is an intriguing yet challenging route towards advanced separation. Making nanometer-thin active layers by standard methods was proven to fail as the IL deposits tend to coalesce into micrometer-sized droplets. Moreover, mass transfer at IL–nanomembrane interfaces seems to be pivotal for efficient functioning and thus deserves better fundamental understanding. Ultimately, we propose that the development of high-performing membranes requires not only thorough knowledge on the physicochemical properties of individual constituents, but also their interplay should be taken into account.

Conflicts of interest

There are no conflicts to declare.

Acknowledgements

The authors acknowledge financial support from the "Fonds der Chemischen Industrie" (Liebig Fellowship) and thank Prof. Dr Armin Gölzhäuser for access to laboratory infrastructure.

References

1 United Nations Framework Convention on Climate Change. https://unfccc.int/, accessed January 2020.
2 A. Kertik, L. H. Wee, M. Pfannmöller, S. Bals, J. A. Martens and I. F. J. Vankelecom, *Energy Environ. Sci.*, 2017, **10**, 2342.
3 C. Zhang and W. J. Koros, *Adv. Mater.*, 2017, **29**, 1701631.
4 T. Rodenas, I. Luz, G. Prieto, B. Seoane, H. Miro, A. Corma, F. Kapteijn, F. X. Llabrés i Xamena and J. Gascon, *Nat. Mater.*, 2015, **14**, 48.
5 S. M. Meckler, J. E. Bachman, B. P. Robertson, C. Zhu, J. R. Long and B. A. Helms, *Angew. Chem., Int. Ed.*, 2018, **57**, 4912.
6 T. C. Merkel, H. Lin, X. Wei and R. Baker, *J. Membr. Sci.*, 2010, **359**, 126.
7 J. Shen, G. Liu, K. Huang, W. Jin, K.-R. Lee and N. Xu, *Angew. Chem., Int. Ed.*, 2015, **54**, 578.
8 C. H. Park, J. H. Lee, J. P. Jung, W. Lee, D. Y. Ryu and J. H. Kim, *Angew. Chem., Int. Ed.*, 2019, **58**, 1143.
9 Z. Wang, A. Knebel, S. Grosjean, D. Wagner, S. Bräse, C. Wöll, J. Caro and L. Heinke, *Nat. Commun.*, 2016, **7**, 13872.
10 R. W. Baker and B. T. Low, *Macromolecules*, 2014, **47**, 6999.
11 H. B. Park, J. Kamcev, L. M. Robeson, M. Elimelech and B. D. Freeman, *Science*, 2017, **356**, eaab0530.
12 L. Prozorovska and P. R. Kidambi, *Adv. Mater.*, 2018, **30**, 1801179.
13 F. Moghadam and H. B. Park, *2D Mater.*, 2019, **6**, 042002.
14 J. Schrier, *ACS Appl. Mater. Interfaces*, 2011, **3**, 4451.
15 J. Schrier, *ACS Appl. Mater. Interfaces*, 2012, **4**, 3745.
16 L. W. Drahushuk and M. S. Strano, *Langmuir*, 2012, **28**, 16671.
17 C. Huang, H. Wu, K. Deng, W. Tang and E. Kan, *Phys. Chem. Chem. Phys.*, 2014, **16**, 25755.
18 C. Sun, M. S. H. Boutilier, H. Au, P. Poesio, B. Bai, R. Karnik and N. G. Hadjiconstantinou, *Langmuir*, 2014, **30**, 675.
19 B. Wen, C. Sun and B. Bai, *Phys. Chem. Chem. Phys.*, 2015, **17**, 23619.
20 Y. Wang, Q. Yang, J. Li, J. Yang and C. Zhong, *Phys. Chem. Chem. Phys.*, 2016, **18**, 8352.
21 C. Sun and B. Bai, *J. Phys. Chem. C*, 2018, **122**, 6178.
22 L. A. Cunha, L. F. A. Ferrão, F. B. C. Machado and M. Pinheiro Jr, *Phys. Chem. Chem. Phys.*, 2018, **20**, 20124.
23 Z. Tian, S. M. Mahurin, S. Dai and D. Jiang, *Nano Lett.*, 2017, **17**, 1802.
24 G. He, S. Huang, L. F. Villalobos, J. Zhao, M. Mensi, E. Oveisi, M. Rezaei and K. V. Agrawal, *Energy Environ. Sci.*, 2019, **12**, 3305.
25 T. Welton, *Chem. Rev.*, 1999, **99**, 2071.
26 K. N. Marsh, J. A. Boxall and R. Lichtenthaler, *Fluid Phase Equilib.*, 2004, **219**, 93.

27 O. Aschenbrenner, S. Supasitmongkol, M. Taylor and P. Styring, *Green Chem.*, 2009, **11**, 1217.

28 M. Ahrenberg, M. Beck, C. Neise, O. Keßler, U. Kragl, S. P. Verevkin and C. Schick, *Phys. Chem. Chem. Phys.*, 2016, **18**, 21381.

29 Y. U. Paulechka, D. H. Zaitsau, G. J. Kabo and A. A. Strechan, *Thermochim. Acta*, 2005, **439**, 158.

30 D. Yalcin, C. J. Drummond and T. L. Greaves, *Phys. Chem. Chem. Phys.*, 2020, **22**, 114.

31 P. A. Hunt, I. R. Gould and B. Kirchner, *Aust. J. Chem.*, 2007, **60**, 9.

32 C. Schröder, A. Lyons and S. W. Rick, *Phys. Chem. Chem. Phys.*, 2020, **22**, 467.

33 L. C. Tomé and I. M. Marrucho, *Chem. Soc. Rev.*, 2016, **45**, 2785.

34 S. Zeng, X. Zhang, L. Bai, X. Zhang, H. Wang, J. Wang, D. Bao, M. Li, X. Liu and S. Zhang, *Chem. Rev.*, 2017, **117**, 9625.

35 J. Wang, J. Luo, S. Feng, H. Li, Y. Wan and X. Zhang, *Green Energy Environ.*, 2016, **1**, 43.

36 E. Rynkowska, K. Fatyeyeva and W. Kujawski, *Rev. Chem. Eng.*, 2018, **34**, 341.

37 M. J. Muldoon, S. N. Aki, J. L. Anderson, J. K. Dixon and J. F. Brennecke, *J. Phys. Chem. B*, 2007, **111**, 9001.

38 Y.-Y. Jiang, Z. Zhou, Z. Jiao, L. Li, Y.-T. Wu and Z.-B. Zhang, *J. Phys. Chem. B*, 2007, **111**, 5058.

39 J. Ilconich, C. Myers, H. Pennline and D. Luebke, *J. Membr. Sci.*, 2007, **298**, 41.

40 J. J. Close, K. Farmer, S. S. Moganty and R. E. Baltus, *J. Membr. Sci.*, 2012, **390–391**, 201.

41 M. T. Mota-Martinez, M. Althuluth, M. C. Kroon and C. J. Peters, *Fluid Phase Equilib.*, 2012, **332**, 35.

42 P. Jindaratsamee, A. Ito, S. Komuro and Y. Shimoyama, *J. Membr. Sci.*, 2012, **423–424**, 27.

43 Y. Hou and R. E. Baltus, *Ind. Eng. Chem. Res.*, 2007, **46**, 8166.

44 M. B. Shiflett and A. Yokozeki, *Ind. Eng. Chem. Res.*, 2005, **44**, 4453.

45 A. Ahosseini and A. M. Scurto, *Int. J. Thermophys.*, 2008, **29**, 1222.

46 J. L. Anthony, E. J. Maginn and J. F. Brennecke, *J. Phys. Chem. B*, 2002, **106**, 7315.

47 J. Jacquemin, P. Husson, A. A. H. Padua and V. Majer, *Green Chem.*, 2006, **8**, 172.

48 J. Safarov, R. Hamidova, M. Stephan, I. Kul, A. Shahverdiyev and E. Hassel, *J. Phys. Chem. B*, 2014, **118**, 6829.

49 O. Höfft, S. Bahr and V. Kempter, *Langmuir*, 2008, **24**, 11562.

50 Y. Yang, P. Dementyev, N. Biere, D. Emmrich, P. Stohmann, R. Korzetz, X. Zhang, A. Beyer, S. Koch, D. Anselmetti and A. Gölzhäuser, *ACS Nano*, 2018, **12**, 4695.

51 P. Dementyev, T. Wilke, D. Naberezhnyi, D. Emmrich and A. Gölzhäuser, *Phys. Chem. Chem. Phys.*, 2019, **21**, 15471.

52 D. Naberezhnyi, A. Gölzhäuser and P. Dementyev, *J. Phys. Chem. Lett.*, 2019, **10**, 5598.

53 P. Dementyev, Y. Yang, M. Rezvova and A. Gölzhäuser, *J. Phys. Chem. Lett.*, 2020, **11**, 238.

54 P. Dementyev, D. Naberezhnyi, M. Westphal, M. Buck and A. Gölzhäuser, *ChemPhysChem*, 2020, **21**, 1–7.

55 H. Aitchison, H. Lu, S. W. L. Hogan, H. Früchtl, I. Cebula, M. Zharnikov and M. Buck, *Langmuir*, 2016, **32**, 9397.

56 I. Leden, *Acta Chem. Scand.*, 1956, **10**, 812.

57 M. Geppert-Rybczyńska, A. Heintz, J. K. Lehmann and A. Golus, *J. Chem. Eng. Data*, 2010, **55**, 4114.

58 H. Jin, B. O'Hare, J. Dong, S. Arzhantsev, G. A. Baker, J. F. Wishart, A. J. Benesi and M. Maroncelli, *J. Phys. Chem. B*, 2008, **112**, 81.

59 T. Buffeteau, B. Desbat and J. M. Turlet, *Appl. Spectrosc.*, 1991, **45**, 380.

60 A. V. Blokhin, Y. U. Paulechka, A. A. Strechan and G. J. Kabo, *J. Phys. Chem. B*, 2008, **112**, 4357.

61 J. G. Huddleston, A. E. Visser, W. M. Reichert, H. D. Willauer, G. A. Broker and R. D. Rogers, *Green Chem.*, 2001, **3**, 156.

62 P. Scovazzo, *J. Membr. Sci.*, 2009, **343**, 199.

63 L. Cammarata, S. G. Kazarian, P. A. Salter and T. Welton, *Phys. Chem. Chem. Phys.*, 2001, **3**, 5192.

64 F. Di Francesco, N. Calisi, M. Creatini, B. Melai, P. Salvo and C. Chiappe, *Green Chem.*, 2011, **13**, 1712.

65 N. Sieffert and G. Wipff, *J. Phys. Chem. B*, 2006, **110**, 13076.

66 T. Takamuku, Y. Kyoshoin, T. Shimomura, S. Kittaka and T. Yamaguchi, *J. Phys. Chem. B*, 2009, **113**, 10817.

67 D. Chen, W. Ying, Y. Guo, Y. Ying and X. Peng, *ACS Appl. Mater. Interfaces*, 2017, **9**, 44251.

68 W. Ying, J. Cai, K. Zhou, D. Chen, Y. Ying, Y. Cuo, X. Kong, Z. Xu and X. Peng, *ACS Nano*, 2018, **12**, 5385.

69 D. Chen, W. Wang, W. Ying, Y. Guo, D. Meng, Y. Yan, R. Yan and X. Peng, *J. Mater. Chem. A*, 2018, **6**, 16566.

70 H. Dou, B. Jiang, M. Xu, Z. Zhang, G. Wen, F. Peng, A. Yu, Z. Bai, Y. Sun, L. Zhang, Z. Jiang and Z. Chen, *Angew. Chem., Int. Ed.*, 2019, **58**, 13969.

71 W. Ying, K. Zhou, Q. Hou, D. Chen, Y. Guo, J. Zhang, Y. Yan, Z. Xu and X. Peng, *J. Mater. Chem. A*, 2019, 7, 15062.

Electronic Supplementary Material (ESI) for Physical Chemistry Chemical Physics.

Supplementary information

Molecular transport in ionic liquid/nanomembrane hybrids

Daniil Naberezhnyi, Petr Dementyev*

Physics of Supramolecular Systems and Surfaces,
Faculty of Physics, Bielefeld University,
Bielefeld 33615, Germany.

Corresponding author
*E-mail: dementyev@physik.uni-bielefeld.de

XPS spectra

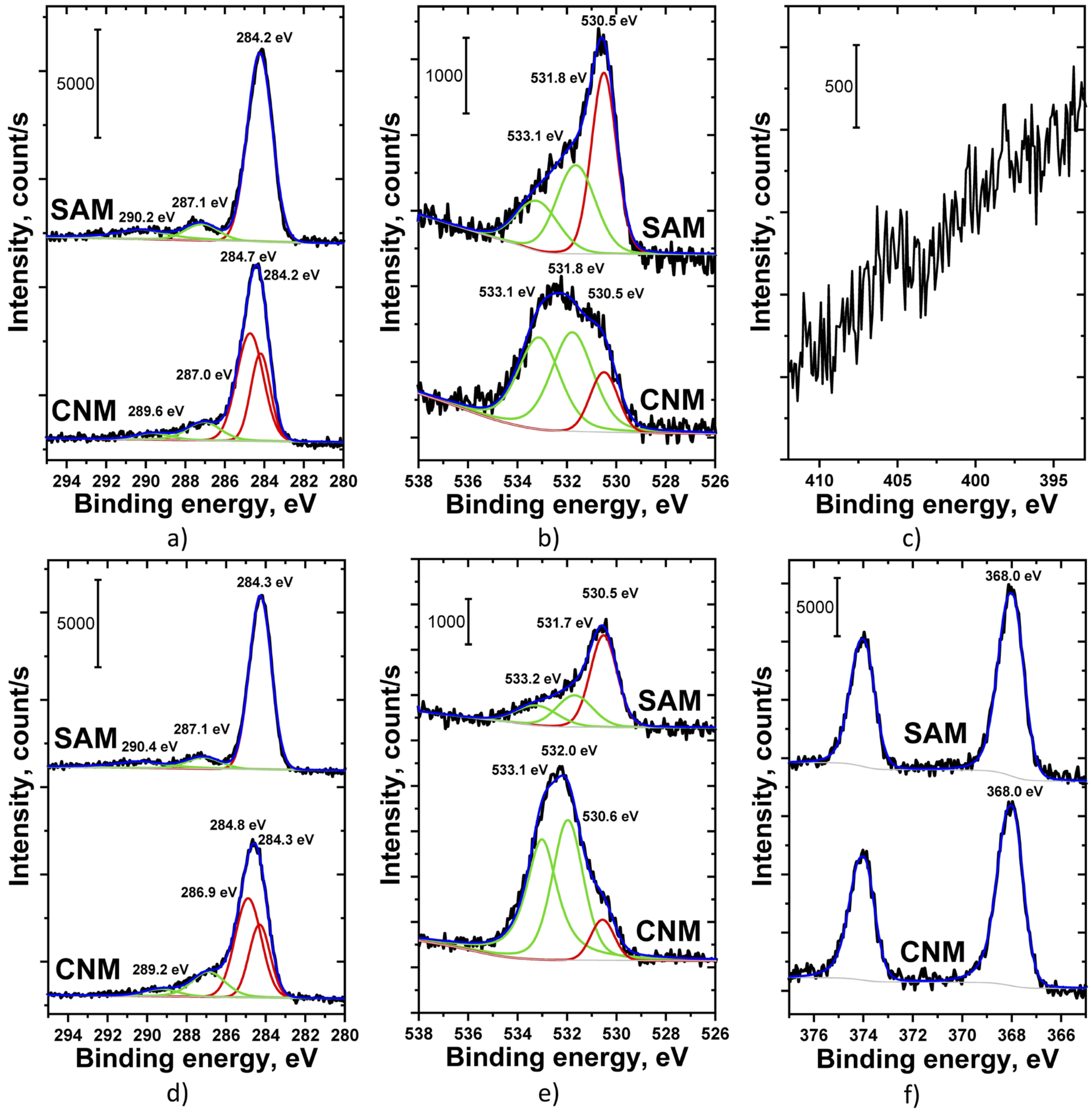

Figure S1. XP spectra. a) C1s for SAM and CNM prepared from biphenyl-4-carboxylic acid; b) O1s for SAM and CNM prepared from biphenyl-4-carboxylic acid; c) N1s for bare silver surface without molecules; d) C1s for SAM and CNM prepared from p-(terphenyl)-4-carboxylic acid; e) O1s for SAM and CNM prepared from p-(terphenyl)-4-carboxylic acid; f) Ag3d for SAM and CNM prepared from p-(terphenyl)-4-carboxylic acid.

Transformation of aromatic carbon (284.2–284.3 eV) with π-π* satellite (290.2-290.4 eV) in self-assembled monolayers to sp^3 carbon (284.7–284.8 eV) and oxidized carbon (286.9–287.0 eV, 289.2–289.6 eV) can be seen after electron irradiation of both BPC and TPC SAMs (Fig. S1a, Fig. S1d).[1] Carbon component 287.1 eV in SAMs corresponds to carbon atoms in the carboxylate groups. Cross-linking of SAM leads to destruction of the carboxylate moiety as evidenced by reduced content of oxygen bonded to silver surface (530.5–530.6 eV) and increase of signals from C=O (531.7–532.0 eV) and C-O (533.1–533.2 eV) functionalities (Fig. S1b, Fig. S1e). XP spectrum in Fig. S1c demonstrates absence of nitrate species in the silver bilayer substrates upon electrodeposition. The chemical state of silver (368.0 eV) remains stable after electron irradiation (Fig. S1f).

PM-IRRAS spectra

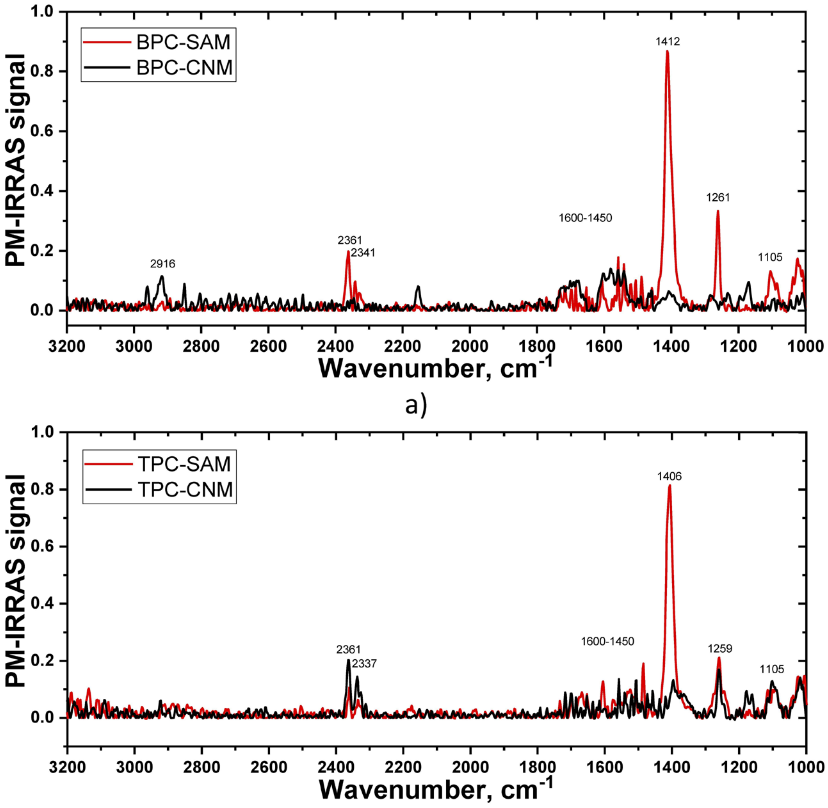

a)

b)

Figure S2. PM-IRRAS spectra. a) SAM and CNM prepared from biphenyl-4-carboxylic acid; b) SAM and CNM prepared from from p-(terphenyl)-4-carboxylic acid.

Surface-bound carboxylate groups are known to be IR active (1412 cm^{-1} for BPC-SAM and 1406 cm^{-1} for TPC-SAM).[2-4] Their decomposition upon irradiation is confirmed by IR-spectra (Fig. S2). Degradation of aromatic structure is also observed in 1600-1450 cm^{-1} region.

5 Gas and vapor permeation in 2D covalent organic framework

5.1 Introduction

While the production of monodisperse pores in graphene, boron nitride, molybdenum disulfide, etc. remains challenging, chemical synthesis allows to create inherently porous 2D covalent organic frameworks (COFs). The sizes of regular monodisperse pores with a record density are designed through a choice of building blocks that constitute COFs potential in membrane separation. However, COF crystals are usually hundreds of nanometers in size which complicates a fundamental transport study in them. Recently, the surfactant-monolayer-assisted interfacial synthesis (SMAIS) allowed to produce the centimeter-sized film with the crystalline domains of AA-stacked boronate ester COF up to several microns in size. These 11-nm thick films were prepared and transferred onto the Si_3N_4/Si chips with single 2 µm-sized orifices in the working group “Molecular Functional Materials” of Prof. Xinliang Feng at the Technische Universität Dresden. The COF/Si_3N_4/Si samples were glued onto copper discs and inserted into the membrane cell of the permeation apparatus at the Bielefeld University as previously described. The gas and vapor permeation across the free-standing 2D COF single crystals was investigated for the first time.

5.2 Results

Although the areal fraction of crystal in the boronate ester COF films was about 50 %, the elongated shapes of the crystalline domains resulted in a lower chance to capture a free-standing crystal than an amorphous region. In this way, six out of ten samples were found to be impermeable for helium and p-xylene because dense amorphous regions without the COF crystals covered the orifices in the Si_3N_4/Si chips. The amorphous and crystal phases were distinguished using helium ion microscopy (HIM) in the transmission mode. The amorphous regions looked darker than the ordered AA-stacked structure of the COF in the HIM images, and the domain boundaries were clearly seen due to the contrast. Since the amorphous regions were more compact, gaseous substances could only pass through the crystalline domains.

The areas of the free-standing crystals were assessed in the four samples from their HIM images. The effective porosity of the crystalline domains was calculated from the helium permeation and amounted to ~ 40 % regardless of the sample. The pore size was estimated as 1.7×1.7 nm^2 resulting in the areal pore density of $(1.4 \pm 0.1) \times 10^{13}$ cm^{-2} that is in excellent agreement with the pore density of 1.5×10^{13} cm^{-2} estimated from the electron microscopy data for this material. Thus, the length of the straight channels and their interior did not affect much the chance of a gas molecule to cross the structure.

The separation performance of the 2D COF was studied with of He, Ne, N_2, Ar, CO_2, Kr, and Xe at 5 mbar. The gas molecules are smaller than the pores and their mean free paths are significantly larger than the pore dimensions. In this way, the membrane selectivity $\alpha_{i,j}$ for free molecular flows complied well with Graham's law of diffusion:

$$\alpha_{i,j} = \sqrt{M_j/M_i}\,, \tag{5.1}$$

where M_i and M_j are the molar mass of gases (kg·mol^{-1}). The permeation rates inversely proportional to the square root of the mass corresponded to the effusion mechanism: the lighter molecules moved faster than heavier species.

However, the permeances of acetone, benzene, toluene and p-xylene deviated positively from Graham's law the more the larger the molecule is. To exclude any artefact, the permeation experiments were performed with a single 180 nm-sized orifice in the fully amorphous film drilled by HIM. An area of the hole was comparable in size to the effective open areas in the free-standing COF crystals, and all vapors passed through this sample similar to atmospheric gases in accordance with Graham's law. Such difference in vapor behavior for 2D COF and the single orifice was explained in terms of surface diffusion. The framework structure exhibits little space between the pores providing about 60 % of the closed area for COF which is a barrier for inert gas particles. The porphyrin-based network can attract the organic molecules through Van der Waals interactions leading to surface transport. In turn, the surface is presented only at the hole edges for the drilled amorphous film, which does not lead to a deviation from the effusion mechanism for vapors.

The adsorption-mediated transport in the 2D COF was more pronounced for more condensable substances in the pressure interval of 1 – 5 mbar. The smallest change in the permeance was noted for acetone ($P_{sat.}$ ~ 250 mbar) the considered vapors of organic solvents. While carbon dioxide ($P_{sat.}$ ~ 5.75×10^4 mbar) exhibited the constant permeance at 1 mbar and at 5 mbar, an increase in the permeation rate depending on pressure was the most pronounced for p-xylene ($P_{sat.}$ ~ 9 mbar).

Since p-xylene has the lowest saturation point, its permeation was studied in the entire range of the relative pressure. At low relative pressures, a detectable flux in the 2D COF crystals was close to a theoretical flux of an ideal gas with a mass of xylene. The discrepancy between the total flux observed and the theoretical flux was increasing with a rise in the relative pressure. Thus, the total flux was at least two times higher than the theoretical one at saturation point. It was assumed that most molecules of p-xylene tended to stick on the narrow COF backbones and diffuse to the downstream side followed by desorption.

5.3 Conclusion

The high pore density in the COF resulted in the superior effective porosity of 40 % that was evaluated from gas permeation experiments. Since square-like pores are larger than gaseous species, the transport in an effusion regime was observed for the atmospheric gases. The free molecular flows were characterized by high permeation rates and low selectivity in accordance with Graham’s law of diffusion.

In counter, larger molecules of organic solvents tended to adsorb on the framework, and the surface diffusion gained the total permeation rate. Thus, the thermodynamic properties of substances play an important role: more condensable species permeate faster through the AA-stacked 2D COF than inert gases. Adsorption-mediated transport leads to at least a double increase in transmembrane flux in the saturated vapor.

5.4 Publication: Mass Transfer in Boronate Ester 2D COF Single Crystals

This article is reprinted with permission from John Wiley and Sons. The original paper appeared as:

D. Naberezhnyi, S. Park, W. Li, M. Westphal, X. Feng, R. Dong and P. Dementyev, *Mass Transfer in Boronate Ester 2D COF Single Crystals*. ***Small***, 2021, 2104392.

Contribution:

Assessment of the crystal area from the HIM images, permeation experiments and data evaluation were performed by the author.

RESEARCH ARTICLE

NANO · MICRO small
www.small-journal.com

Mass Transfer in Boronate Ester 2D COF Single Crystals

Daniil Naberezhnyi, SangWook Park, Wei Li, Michael Westphal, Xinliang Feng, Renhao Dong,* and Petr Dementyev**

Unlike graphene and similar structures, 2D covalent organic frameworks (2D COFs) exhibit intrinsic porosity with a high areal density of well-defined and uniform openings. Given the pore size adjustability, 2D COFs are likely to outperform artificially perforated inorganic layers with respect to their prospects in membrane separation. Yet, exploring the mass transport in 2D COFs is hidden by the lack of laterally extended free-standing membranes. This work reports on direct molecular permeation measurements with single crystals of an interfacially synthesized boronate ester 2D COF. In accordance with the material topography, the atmospheric and noble gases readily pass the suspended nanosheets while their areal porosity is quantified to be almost 40% exceeding that in any 2D membranes known. However, bulkier aromatic hydrocarbons are found to deviate substantially from Graham's law of diffusion. Counterintuitively, the permeation rate is demonstrated to rise from benzene to toluene and further to xylene despite the increase in the molecular mass and dimensions. The results are interpreted in terms of adsorption-mediated flow that appears to be an important transport mechanism for microporous planar nanomaterials.

1. Introduction

Following the isolation of graphene, 2D materials have been pursued as the thinnest separation membranes promising high throughput and selectivity combined.[1] However, graphene, boron nitride, molybdenum disulfide, etc., are impermeable to most molecules and ions, and their usage requires the pores to be produced by harsh physical means, such as focused ion beam (FIB) drilling,[2] plasma treatment,[3] electron irradiation,[4] and ion bombardment.[5] This not only makes it highly challenging to control the pore size distribution, but also jeopardizes the materials integrity. In fact, breaking the chemical bonds and removing atoms from the crystal lattice, i.e., introducing structural defects, would inevitably limit the permeability attainable as the more pores are created, the less stable the membrane becomes. Indeed, perforated single-layer materials are featured by pore densities of less than 10^{13} cm^{-2} whereas their areal porosity, i.e., the integral open area relative to the overall membrane area, rarely exceeds a few percent.[6–8] On the other hand, there exist inherently porous planar nanomaterials, including 2D covalent organic frameworks (COFs) and 2D polymers (2D COFs in monolayer form), that represent ordered fishing net-like structures with monodisperse openings located next to one another.[9] The pore dimensions in the 2D COFs can be easily tailored via changing their building blocks as well as by adopting different packing configurations. Hence, chemical synthesis offers an intriguing opportunity to construct ultimately thin membranes instead of destructing ones.

Although 2D COFs could be exfoliated from polymerized monomer crystals, the size of the flakes obtained was typically limited to a few hundreds of nanometers.[10,11] The bottom-up polymerization on solid surfaces also yielded too small crystallites of the same scale,[12] while reactions at gas–liquid and liquid–liquid interfaces gave rise to macroscopic films with a low degree of long-range order.[13] Only recently, Feng and co-workers developed surfactant-monolayer-assisted interfacial synthesis (SMAIS) of centimeter-sized single- and few-layer 2D polymers with crystalline domains as large as several micrometers.[14,15] Despite the progress in functional characterization of polycrystalline membranes composed of 2D COFs nanosheets,[16–22] no mass transfer experiments with individual single crystals have been accessible thus far.

In this study, we employed a custom-designed permeation apparatus to get insights into the basics of molecular transport across free-standing 2D COFs single crystals.[23] The SMAIS approach was utilized to prepare a boronate ester 2D COF thin-film membrane consisting of porphyrin macrocycles and phenyl linkers with distinct square periodicity.[24] The few-layer 2D COF consisting of 50% single crystals was suspended over separate apertures, followed by securing the nanomembranes in a leak-tight cell to enable gas flow measurements. The size of the crystalline domains in each membrane sample tested was determined via helium ion microscopy (HIM), and the areal porosity

---

D. Naberezhnyi, M. Westphal, P. Dementyev
Physics of Supramolecular Systems and Surfaces
Faculty of Physics
Bielefeld University
33615 Bielefeld, Germany
E-mail: dementyev@physik.uni-bielefeld.de

S. Park, W. Li, X. Feng, R. Dong
Center for Advancing Electronics Dresden
Faculty of Chemistry and Food Chemistry
Technische Universität Dresden
01062 Dresden, Germany
E-mail: xinliang.feng@tu-dresden.de; renhao.dong@tu-dresden.de

The ORCID identification number(s) for the author(s) of this article can be found under https://doi.org/10.1002/smll.202104392.

DOI: 10.1002/smll.202104392

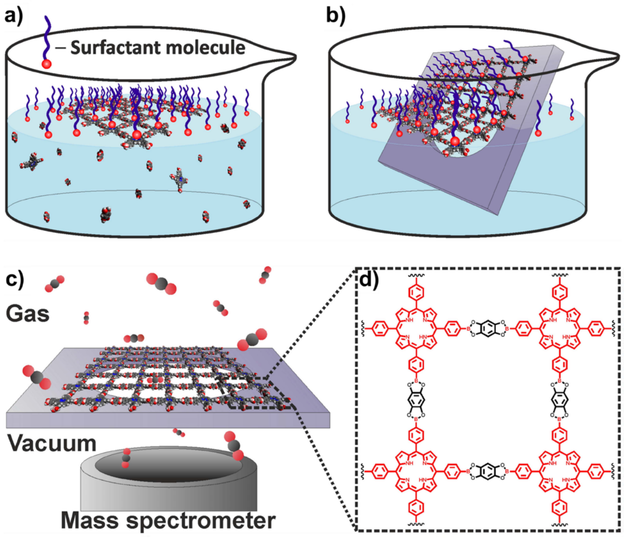

Figure 1. Schematic of the experimental procedures: a) 2D COF via SMAIS. b) Film transfer and cleaning. c) Gas permeation measurements with free-standing nanomembranes. d) Chemical structure of the boronate ester 2D COF.

in the 2D COF was measured to be as high as 40%. We further quantified the permeation rates for a wide range of gaseous and vaporous substances and observed two pathways contributing to the transmembrane diffusion. While atmospheric and noble gases were found to pass the 2D COF membrane with the effusion selectivity, surface flow was shown to play a significant role for homologous arenes leading to a reverse selectivity order. This work highlights the uttermost openness of 2D COFs and reveals mass transfer peculiarities in highly porous nanomembranes.

2. Results and Discussion

The boronate ester 2D COF was synthesized via SMAIS according to the previous report, and the protocol proved to be well reproducible.[24] The anionic surfactant monolayer (typically, sodium oleyl sulfate, SOS) was prepared on water surface to guide the preorganization of 5,10,15,20-(tetra-4-dihydroxyborylphenyl)porphyrin along the 2D directions. Subsequent polycondensation reaction between the porphyrin monomer and 1,2,4,5-tetrahydroxybenzene underneath the monolayer yielded cm^2-sized floating boronate ester 2D COF membranes (**Figure 1**). The chemical composition of the films was verified with Fourier transform infrared (FTIR) spectroscopy (Figure S1, Supporting Information). The resultant 2D COF membrane was transferred onto micromachined Si_3N_4/Si substrates with individual apertures of around 2 µm in diameter. After rinsing with ethanol and drying in air, the suspended membranes were mounted into the vacuum system as described elsewhere.[23] The room-temperature permeation measurements were conducted with a quadrupole mass-spectrometer upon exposing the free-standing 2D COF to gases and vapors of interest at a given feed pressure. To characterize the membrane morphology, the membranes were also transferred onto SiO_2/Si substrates and studied with atomic force microscopy (AFM) and optical microscopy confirming the early evaluation.[24]

The 2D COF membrane exhibits an average thickness of around 11 nm and comprises ribbon-like crystalline domains with the size up to 10 µm (**Figure 2**a). Notably, the areal ratio of the crystalline region is over 50% of the film, but most of the crystals are merged with each other.[24] We measured He permeability in multiple randomly isolated thin-film membranes, and at the micrometer scale, the crystalline domains turned out to be difficult to capture. Due to the shape anisotropy, the crystallites appear to be narrower than the amorphous regions between them (Figure 2b). Following the permeation experiments, the free-standing samples were imaged with bright-field HIM revealing the coexistence of the two phases (Figure 2c). The amorphous region appears darker than the crystalline one, and convex edges that are characteristic to the 2D COF crystallites can be distinguished clearly. As a result, the properties of the final membranes spread out widely that reflects the likelihood of the ordered 2D COF structure to emerge over the aperture (**Table 1**). For convenience, the permeance obtained is converted into the effective open area that would correspond to a circular hole of the same throughput.[25] Surprisingly, many of the membranes were found to completely block the gas flow displaying no open area at all (Samples 3–5, 7–9). This can only be explained by the fact that the related samples contain solely the amorphous material rather than the 2D COF crystals with aligned porous arrays. The observation is consistent with HIM micrographs (Figure S2, Supporting Information) that suggest the impermeable membranes to vary in resistance toward the ion beam

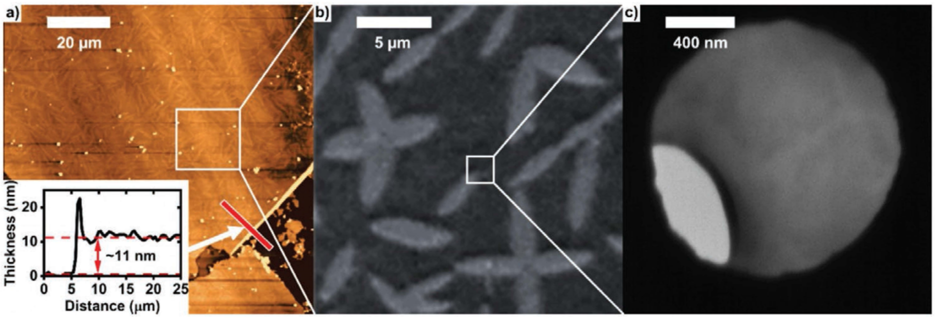

Figure 2. Morphology of the 2D COF membranes: a) AFM image of the film transferred onto silicon. Inset shows the height profile. b) Polarized microscopy image of the film transferred onto silicon. c) Bright-field HIM image of a free-standing sample. The light area corresponds to the crystalline 2D COF.

Table 1. Overview of the transport properties in 2D COF nanomembranes.

Sample[a]	Nanomembrane size [µm][b]	Permeation rate [mol s^{-1} m^{-2} Pa^{-1}][c]	Effective hole size [nm][d]
1	1.55	$(5.9 \pm 0.1) \times 10^{-3}$	≈330
2	1.57	$(7.1 \pm 0.1) \times 10^{-4}$	≈120
3	1.92	$<5.0 \times 10^{-8}$	0
4	1.42	$<5.0 \times 10^{-8}$	0
5	2.07	$<5.0 \times 10^{-8}$	0
6	2.10	$(3.0 \pm 0.1) \times 10^{-3}$	≈320
7	1.51	$<5.0 \times 10^{-8}$	0
8	1.88	$<5.0 \times 10^{-8}$	0
9	1.95	$<5.0 \times 10^{-8}$	0
10	3.07	$(5.8 \pm 0.1) \times 10^{-3}$	≈660

[a] The samples are presented in chronological order. Two other nanomembranes were found ruptured and are not considered here; [b] The diameter of apertures in Si_3N_4/Si substrates; [c] He permeance measured at 5 mbar feed pressure. The detection limit of 5.0×10^{-8} mol s^{-1} m^{-2} Pa^{-1} is determined for 2 µm large samples at 200 mbar applied pressure difference; [d] The effective open area is calculated according to the kinetic theory and shown in the form of the respective diameter (see the Experimental Section).

so that some of the suspended films were even opaque. The permeation results along with the pronounced difference in thickness and the sharp contrast seen in HIM suggest the two phases to differ significantly in density. In other words, the structure of the amorphous regions is likely to be highly compacted making them impermeable even for the smallest molecules.

Although the permeation rates measured in Samples 1, 2, 6, and 10 scatter over an order of magnitude, the gas transport is expected to take place only through the porous framework structure. Given the tightness of the amorphous material, we evaluated the area of the crystalline regions in each nanomembrane and compared it with the effective open area measured (**Table 2**). The areal porosity of the 2D COF membrane can now be calculated as a ratio of the effective open area to the crystal area yielding ≈40 % regardless of the sample. This result implies remarkable regularity of the 2D COF and also points to its extreme openness. For comparison, the areal porosity in the state-of-the-art graphene membranes amounts to 18.5% at most (Table 2).

High-resolution transmission electron microscopy (HR-TEM) was used before to characterize the tetragonal lattice of the material under investigation revealing an eclipsed AA stacking order.[24] This means that every pore confined by the porphyrin moieties represents a straight channel for He atoms to pass through, and according to the HR-TEM analysis, there are as many pores as 1.5×10^{13} cm^{-2}. While the size of the square unit cell was determined to be 2.46×2.46 nm^2,[24] the pore dimensions excluding the backbones can be estimated as 1.7×1.7 nm^2. The latter translate our porosity measurements into the areal pore density of $(1.4 \pm 0.1) \times 10^{13}$ cm^{-2} that is in excellent agreement with the structural definition. It appears that neither the length of the pores nor their interior affects much the chance of the gas particles to cross the membrane.

Table 2. Characteristics of the isolated individual 2D COF crystals and comparison with perforated 2D materials.

Sample[a]	Effective open area [nm^2][b]	Crystal area[nm^2][c]	Areal porosity [%][d]
1	87 900 ± 800	205 000 ± 2000	43.0 ± 1.0
2	10 700 ± 100	28 000 ± 2000	38.0 ± 2.0
6	82 000 ± 500	204 000 ± 2000	40.0 ± 1.0
10	338 000 ± 3000	780 000 ± 20 000	43.0 ± 1.0

2D membrane[e]	Areal porosity [%]	Source
2D COF via SMAIS	41± 2	This work
Graphene perforated with He FIB	3–4	[2]
Graphene perforated with Ga ions and O_2 plasma	0.001	[3b]
WS_2 perforated with Ga FIB	0.01–0.1	[6]
Graphene perforated with Ga ions and O_2 etching	1.6 ± 0.6	[5b]
Graphene perforated with O_2 plasma	18.5	[26]

[a] The samples numbering matches that in Table 1; [b] See the Experimental Section for details; [c] The crystal area was determined from two HIM images for each sample (Figure S3, Supporting Information); [d] The areal porosity refers to the effective open area divided by the crystal area; [e] Overview of reported high-flux 2D membranes.

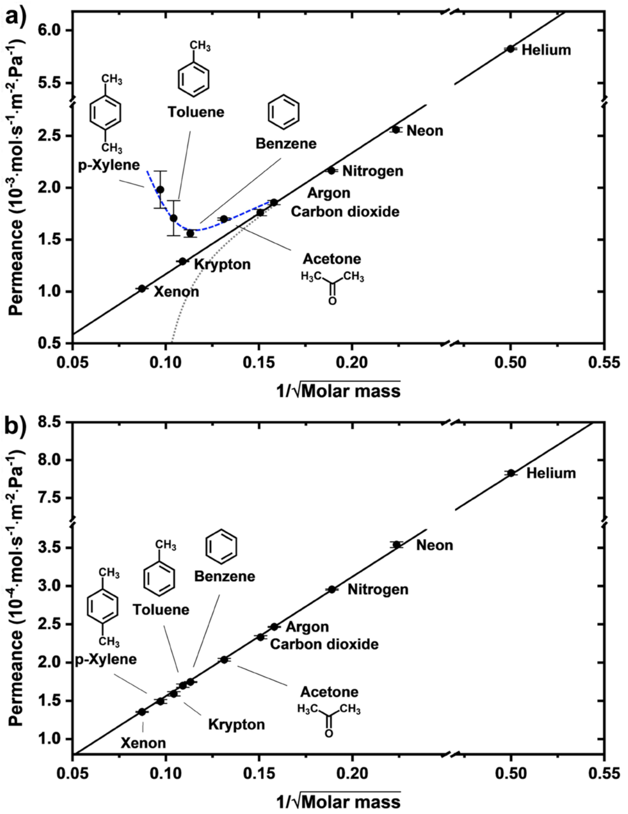

Figure 3. a) Permeation rates in a 2D COF membrane (Sample 10, see Figure S6 in the Supporting Information for other samples). The data points are averaged over three measurements at room temperature and 5 mbar feed pressure. The solid line is the best linear fit; the dashed line is for guiding the eye; the dotted line sketches the size exclusion performance. b) Permeation rates in an artificial orifice of ≈180 nm in size that was created in Sample 8 (see Supporting Information for details). The measurements were also done at room temperature and 5 mbar feed pressure.

Thus, the 2D COF proves to behave as a 2D membrane where its external appearance defines the transport characteristics.

To explore the separation performance of the 2D COF membranes, we investigated a number of gaseous species, including nitrogen and carbon dioxide. In addition, homologous aromatic hydrocarbons were chosen as a model system to enable systematic variations of both the molecular weight and the particle size. **Figure 3a** demonstrates the permeance measured as a function of the molar mass. It is evident that all the gases from He to Xe comply well with Graham's law of diffusion[27]

$$\alpha_{i,j} = \sqrt{M_j/M_i} \tag{1}$$

where α is the membrane selectivity for two species, and M is their molar mass. This dependence describes that lighter molecules move faster than heavier ones, and it is in line with the effusion mechanism.[2] Under our experimental conditions, the 2D COF single crystals allow for the free molecular flow to occur because the gas particles are smaller than the pores.[28] However, one can also see that the vaporous compounds depart from the parabolic law, and the larger the molecules, the greater the deviation relative to the straight line plotted. The disc-shaped aromatic molecules can exceed 0.5 nm in at least two dimensions,[28] but the observed effect is reverse to what would be expected for molecular sieving, i.e., there is selectivity to xylene over benzene rather than the other way around. Note that the purely amorphous membranes (Samples 3–5, 7–9) were also proven to be impermeable to the vapors, and the inverse selectivity order does not emerge for a large orifice drilled in the amorphous film (Figure 3b) to imitate the effective open area (Figure S4, Supporting Information). This contrast experiment shows that the behavior is related to the membrane rather than to any artifact, such as accumulation of the permeating molecules in the detection chamber. Most importantly, the permeation rate for the vaporous substances increases beyond the limit set by the membrane porosity, and this enhancement seems to associate with the microstructure of the 2D COF. In fact, the high pore density means nothing less than very little space between the pores which is represented only by the molecular skeleton (Figure 1). While the porphyrin network acts as a barrier for the inert gases, it can also attract the organic molecules through Van der Waals forces. Consequently, we attribute the enhanced permeance in the 2D COF membranes to adsorption-mediated transport of condensable species. The phenomenon has already been reported for sponge-like carbon nanomembranes suggesting that the vapor molecules stick at the rims of the pores and thereby have a greater likelihood to pass them.[23,29] It appears that both the membrane thickness of a few nanometers and the densely packed openings are prerequisites for the surface diffusion to come into play.

The impact of adsorption on permeation was then established in experiments with varied vapor pressure. **Figure 4**a illustrates the change in the permeation rate of the solvents depending on the applied feed pressure. The behavior contrasts with the permeance of carbon dioxide that appears to be constant in accordance with molecular effusion.[2] It is worth noting that the increase in the permeance correlates negatively with the saturation vapor pressure of the compounds, namely, the lower the saturation point, the more pronounced the pressure dependence. This directly links to the relative pressure that plays a crucial role in adsorption isotherms such as Brunauer–Emmett–Teller theory.[30] Xylene has the lowest saturation vapor pressure at room temperature, and we studied its permeation in the entire range of the relative pressure. Figure 4b shows the transmembrane flux normalized to the surface area of the 2D COF crystals in comparison with the ideal gas flux given by the membrane porosity. The surface flow turns out to contribute substantially to the vapor transport, and eventually, the total flux gets twice as much as the gas-phase pathway. It follows that xylene molecules reaching the 2D framework adsorb, and as the vapor saturates, most of them fall through the pores. In a sense, condensation makes the 2D COF membrane analogous to a fine mesh strainer, although the sieving effect for gaseous species is difficult to demonstrate as larger molecules are not volatile enough under ambient conditions. There are though far more massive particles available in liquid-phase experiments,[31] and the 2D COF film is likely to display outstanding size-exclusion properties.

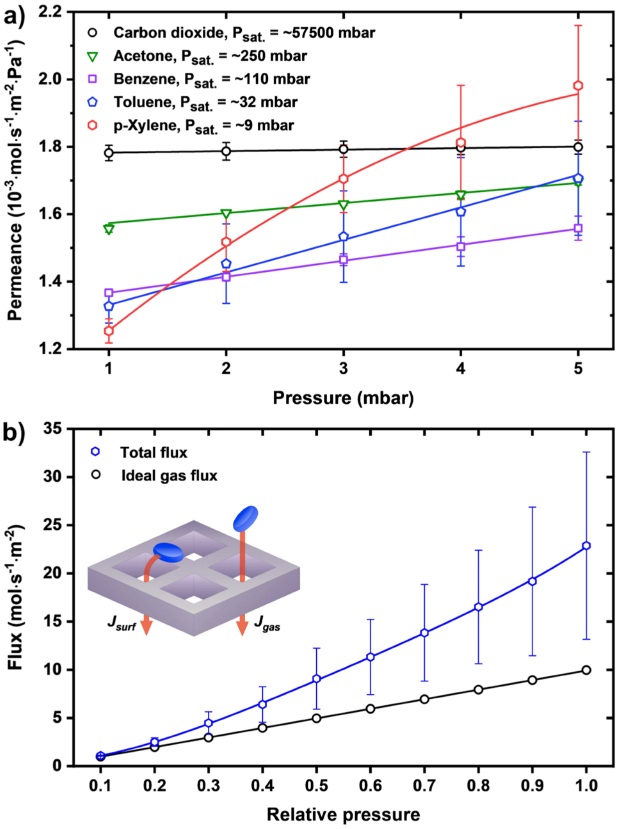

Figure 4. a) Permeation rates in a 2D COF membrane (Sample 10, see Figure S7, Supporting Information for other samples). The data points are averaged over three to six measurements at room temperature. The lines are for guiding the eye. b) Transmembrane flux of *p*-xylene in the 2D COF crystals. The data points are averaged over Samples 2, 6, 10. Inset is a schematic for the surface and gas-phase permeation pathways.

3. Conclusion

For the first time, free-standing single crystals of 2D COF were studied with regard to molecular permeation. The boronate ester 2D COF was demonstrated to enable facile flow of gaseous species exhibiting the areal porosity as high as 40%. The results agree well with the molecular structure of the material and reveal the areal pore density over 1.0×10^{13} cm^{-2}. As expected from the effusion mechanism, the membrane selectivity toward He, Ne, Ar, Kr, Xe, N_2, and CO_2 was shown to obey Graham's law. However, the transport of acetone, benzene, toluene, and *p*-xylene in the 2D membranes was found to be affected by adsorption and surface diffusion resulting in enhanced permeation rates.

In addition, we found the amorphous phase accompanying the 2D COF crystals to be impermeable whereas no grain boundaries were witnessed to be open. Providing the equal proportions, the findings indicate that macroscopic films could be used directly as separation membranes with the effective porosity of around 20% which is still superior to the perforated 2D materials. At the moment, high-flux nanofiltration gains momentum as an important process across diverse industries, e.g., in the pharmaceutical production.[31,32] The liquid transport measurements with nanomembranes are complicated, but we anticipate more fundamental studies on the mass transfer in 2D COFs to come, especially coupled with rational design of the pore geometry.

4. Experimental Section

COF Synthesis: The SMAIS of the boronate ester 2D COF followed the reported protocol.[24] The surfactant solution was prepared by dissolving 1 mg of SOS in 1 mL of chloroform. The precursors 5,10,15,20-(tetra-4-dihydroxyborylphenyl)porphyrin (monomer 1) and 1,2,4,5-tetrahydroxybenzene (monomer 2) were dissolved separately in 1 м HCl. The concentration obtained was 1×10^{-3} and 4×10^{-3} м for the monomers 1 and 2, respectively. First, 20 µL of the surfactant solution was spread onto the surface of 40 mL Milli-Q water, and chloroform was let evaporate. Then, the monomer 1 (1 mL) was injected into water, and the monomer 2 (1 mL) was added in 30 min. The polymerization took place at 50 °C for 7 days. FTIR spectra were taken with Tensor II (Bruker) in the attenuated total reflection mode. The prepared film was directly transferred onto Si_3N_4/Si substrates with micrometer-scale apertures (Silson Ltd.). The samples were rinsed with ethanol to remove the surfactant molecules and dried in air.

Permeation Measurements: The gas and vapor permeation measurements were conducted in the original system described before (see Supporting Information for details).[23] First, the Si_3N_4/Si substrates carrying the 2D COF were fixed with epoxy glue on UHV-compatible copper disks. Each sample was then separately mounted in the membrane cell between the feed compartment and the high-vacuum detection chamber with a quadrupole mass-spectrometer (Hiden Analytical). The transmembrane flow rates were measured upon exposing the sample to species of interest at certain feed pressure as determined with a capacitance manometer (MKS Instruments). The effective open area *A* was calculated from the flow rate measured *J* as following

$$A = \frac{J\sqrt{2\pi mkT}}{p} \tag{2}$$

where *m* is the molecular mass (in kg), *k* is the Boltzmann constant, *T* is the temperature, and *p* is the applied gas pressure. The effective hole size was taken as $\sqrt{4A/\pi}$.

Helium (≥99.996%), neon (≥99.995%), nitrogen (≥99.8%), carbon dioxide (≥99.5%), argon (≥99.998%), krypton (≥99.99%), xenon (≥99.99%) were supplied by Linde. Acetone (≥99.8%, analytical reagent grade, Fisher Scientific), benzene (≥99.5%, for analysis, ROTH), toluene (≥99.8%, analytical reagent grade, Fisher Scientific), *p*-xylene (≥99.0%, analytical standard, Sigma-Aldrich) were repeatedly degassed prior to use.

Microscopy: The 2D COF film transferred onto silicon wafer was imaged in reflection mode with a polarized optical microscope (AxioScope A1, Carl Zeiss). AFM measurement was performed in air on NT-MDT with a SMENA head in semicontact mode. The probes with a typical curvature radius of 6 nm, a resonant frequency of 47–50 kHz, and a force constant of 0.35–6.10 N m^{-1} were used. Height determination and calculation was performed with the software Nova Px 3.2.5 from NT-MDT. The suspended 2D COF samples on Si_3N_4/Si substrates were imaged in a helium ion microscope (Zeiss Orion Plus). The micrographs were scanned in bright-field transmission mode with charge compensation at dwell time of 0.5–1 µs and beam energy of 33.6–35.3 keV. The FIB in the HIM microscope was also applied for milling a 180 nm sized orifice in Sample 8 (Figure S4, Supporting Information).

Supporting Information

Supporting Information is available from the Wiley Online Library or from the author.

Acknowledgements

P.D. acknowledges the financial support from the "Fonds der Chemischen Industrie" (Liebig Fellowship) and cordially thanks Prof. Dr. Armin Gölzhäuser for access to laboratory infrastructure. This work was in part funded by the German Federal Ministry for Education and Research (BMBF, project Caerus 03XP0155 A). R.D. and X.F. acknowledge the financial support from EU Graphene Flagship (Core3, No. 881603), ERC starting grant (FC2DMOF, No. 852909), ERC Consolidator Grant (T2DCP), DFG projects (SFB-1415, No. 417590517, SPP 1928, COORNET), as well as the German Science Council and Center of Advancing Electronics Dresden (cfaed).

Open access funding enabled and organized by Projekt DEAL.

Conflict of Interest

The authors declare no conflict of interest.

Data Availability Statement

Data available on request from the authors.

Keywords

2D covalent organic frameworks, 2D membranes, chemical separation, gas permeation

Received: July 25, 2021
Revised: September 5, 2021

---

[1] a) F. Moghadam, H. B. Park, *2D Mater.* **2019**, *6*, 042002; b) X. Sui, Z. Yuan, Y. Yu, K. Goh, Y. Chen, *Small* **2020**, *16*, 2003400.
[2] K. Celebi, J. Buchheim, R. M. Wyss, A. Droudian, P. Gasser, I. Shorubalko, J.-I. Kye, C. Lee, H. G. Park, *Science* **2014**, *344*, 289.
[3] a) S. P. Surwade, S. N. Smirnov, I. V. Vlassiouk, R. R. Unocic, G. M. Veith, S. Dai, S. M. Mahurin, *Nat. Nanotechnol.* **2015**, *10*, 459; b) M. S. H. Boutilier, D. Jang, J. C. Idrobo, P. R. Kidambi, N. G. Hadjiconstantinou, R. Karnik, *ACS Nano* **2017**, *11*, 5726.
[4] S. M. Gilbert, G. Dunn, A. Azizi, T. Pham, B. Shevitski, E. Dimitrov, S. Liu, S. Aloni, A. Zettl, *Sci. Rep.* **2017**, *7*, 15096.
[5] a) J. P. Thiruraman, K. Fujisawa, G. Danda, P. M. Das, T. Zhang, A. Bolotsky, N. Perea-López, A. Nicolaï, P. Senet, M. Terrones, M. Drndić, *Nano Lett.* **2018**, *18*, 1651; b) K. P. Schlichting, D. Poulikakos, *ACS Appl. Mater. Interfaces* **2020**, *12*, 36468.
[6] J. P. Thiruraman, S. A. Dar, P. M. Das, N. Hassani, M. Neek-Amal, A. Keerthi, M. Drndić, B. Radha, *Sci. Adv.* **2020**, *6*, eabc7927.
[7] P. Cheng, M. M. Kelly, N. K. Moehring, W. Ko, A.-P. Li, J. C. Idrobo, M. S. H. Boutilier, P. R. Kidambi, *Nano Lett.* **2020**, *20*, 5951.
[8] D. Hou, S. Zhang, X. Chen, R. Song, D. Zhang, A. Yao, J. Sun, W. Wang, L. Sun, B. Chen, Z. Liu, L. Wang, *ACS Appl. Mater. Interfaces* **2021**, *13*, 10328.
[9] A. Schneemann, R. Dong, F. Schwotzer, H. Zhong, I. Senkovska, X. Feng, S. Kaskel, *Chem. Sci.* **2021**, *12*, 1600.
[10] W. Wang, A. D. Schlüter, *Macromol. Rapid Commun.* **2019**, *40*, 1800719.
[11] D. Rodríguez-San-Miguel, C. Montoro, F. Zamora, *Chem. Soc. Rev.* **2020**, *49*, 2291.
[12] N. Bilbao, C. Martín, G. Zhan, M. Martínez-Abadía, A. Sanz-Matías, A. Mateo-Alonso, J. N. Harvey, M. Van der Auweraer, K. S. Mali, S. D. Feyter, *ACS Nano* **2020**, *14*, 2354.
[13] R. Dong, T. Zhang, X. Feng, *Chem. Rev.* **2018**, *118*, 6189.
[14] K. Liu, H. Qi, R. Dong, R. Shivhare, M. Addicoat, T. Zhang, H. Sahabudeen, T. Heine, S. Mannsfeld, U. Kaiser, Z. Zheng, X. Feng, *Nat. Chem.* **2019**, *11*, 994.
[15] H. Sahabudeen, H. Qi, M. Ballabio, M. Položij, S. Olthof, R. Shivhare, Y. Jing, S. Park, K. Liu, T. Zhang, J. Ma, B. Rellinghaus, S. Mannsfeld, T. Heine, M. Bonn, E. Cánovas, Z. Zheng, U. Kaiser, R. Dong, X. Feng, *Angew. Chem., Int. Ed.* **2020**, *59*, 6028.
[16] G. Li, K. Zhang, T. Tsuru, *ACS Appl. Mater. Interfaces* **2017**, *9*, 8433.
[17] K. Dey, M. Pal, K. C. Rout, S. Kunjattu H, A. Das, R. Mukherjee, U. K. Kharul, R. Banerjee, *J. Am. Chem. Soc.* **2017**, *139*, 13083.
[18] X. Wang, C. Chi, K. Zhang, Y. Qian, K. M. Gupta, Z. Kang, J. Jiang, D. Zhao, *Nat. Commun.* **2017**, *8*, 14460.
[19] D. B. Shinde, G. Sheng, X. Li, M. Ostwal, A.-H. Emwas, K.-W. Huang, Z. Lai, *J. Am. Chem. Soc.* **2018**, *140*, 14342.
[20] H. Yang, H. Wu, Y. Zhao, M. Wang, Y. Song, X. Cheng, H. Wang, X. Cao, F. Pan, Z. Jiang, *J. Mater. Chem. A* **2020**, *8*, 19328.
[21] Y. Ying, M. Tong, S. Ning, S. K. Ravi, S. B. Peh, S. C. Tan, S. J. Pennycook, D. Zhao, *J. Am. Chem. Soc.* **2020**, *142*, 4472.
[22] Y. Li, Q. Wu, X. Guo, M. Zhang, B. Chen, G. Wei, X. Li, X. Li, S. Li, L. Ma, *Nat. Commun.* **2020**, *11*, 599.
[23] P. Dementyev, T. Wilke, D. Naberezhnyi, D. Emmrich, A. Gölzhäuser, *Phys. Chem. Chem. Phys.* **2019**, *21*, 15471.
[24] S. W. Park, Z. Liao, B. Ibarlucea, H. Qi, H.-H. Lin, D. Becker, J. Melidonie, T. Zhang, H. Sahabudeen, L. Baraban, C.-K. Baek, Z. Zheng, E. Zschech, A. Fery, T. Heine, U. Kaiser, G. Cuniberti, R. Dong, X. Feng, *Angew. Chem., Int. Ed.* **2020**, *59*, 8218.
[25] Z. Yuan, J. D. Benck, Y. Eatmon, D. Blankschtein, M. S. Strano, *Nano Lett.* **2018**, *18*, 5057.
[26] G. He, S. Huang, L. F. Villalobos, J. Zhao, M. Mensi, E. Oveisi, M. Rezaei, K. V. Agrawal, *Energy Environ. Sci.* **2019**, *12*, 3305.
[27] A. S. Kirsch, *Am. J. Phys.* **1981**, *49*, 1076.
[28] Y. Marcus, *J. Phys. Org. Chem.* **2003**, *16*, 398.
[29] a) P. Dementyev, D. Naberezhnyi, M. Westphal, M. Buck, A. Gölzhäuser, *ChemPhysChem* **2020**, *21*, 1006; b) M. Rezvova, A. Gölzhäuser, P. Dementyev, *Adv. Mater. Interfaces* **2020**, *7*, 2000121.
[30] S. Brunauer, P. H. Emmett, E. Teller, *J. Am. Chem. Soc.* **1938**, *60*, 309.
[31] C. Cheng, S. A. Iyengar, R. Karnik, *Nat. Nanotechnol.* **2021**, *16*, 989.
[32] J. R. Werber, C. O. Osuji, M. Elimelech, *Nat. Rev. Mater.* **2016**, *1*, 16018.

NANO MICRO
small

Supporting Information

for *Small,* DOI: 10.1002/smll.202104392

Mass Transfer in Boronate Ester 2D COF Single Crystals

Daniil Naberezhnyi, SangWook Park, Wei Li, Michael Westphal, Xinliang Feng, Renhao Dong,* and Petr Dementyev**

WILEY-VCH

Supporting Information

Mass Transfer in Boronate Ester 2D COF Single Crystals

Daniil Naberezhnyi, SangWook Park, Wei Li, Michael Westphal, Xinliang Feng, Renhao Dong* and Petr Dementyev**

FTIR spectra

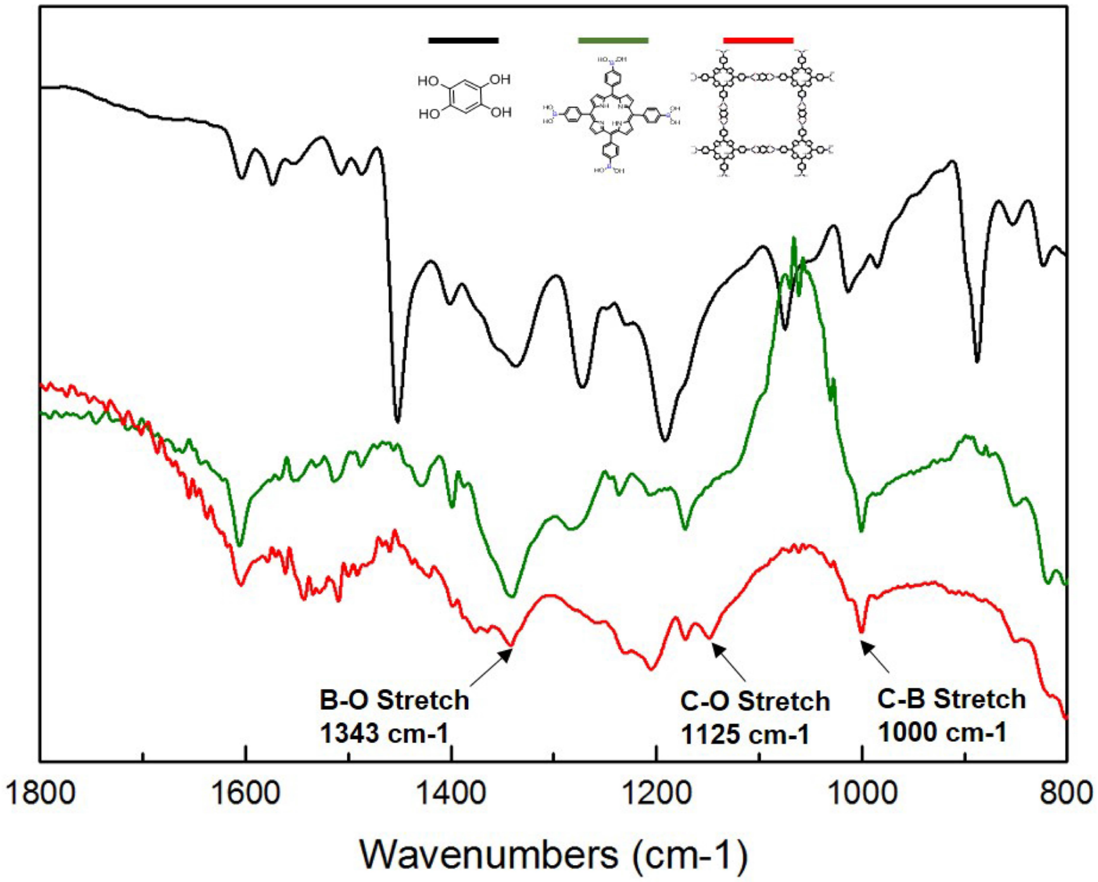

Figure S1. FTIR spectra of 5,10,15,20-(tetra-4-dihydroxyborylphenyl)porphyrin (monomer 1) and 1,2,4,5-tetrahydroxybenzene (monomer 2) as well as of the resulting 2D COF.

HIM images

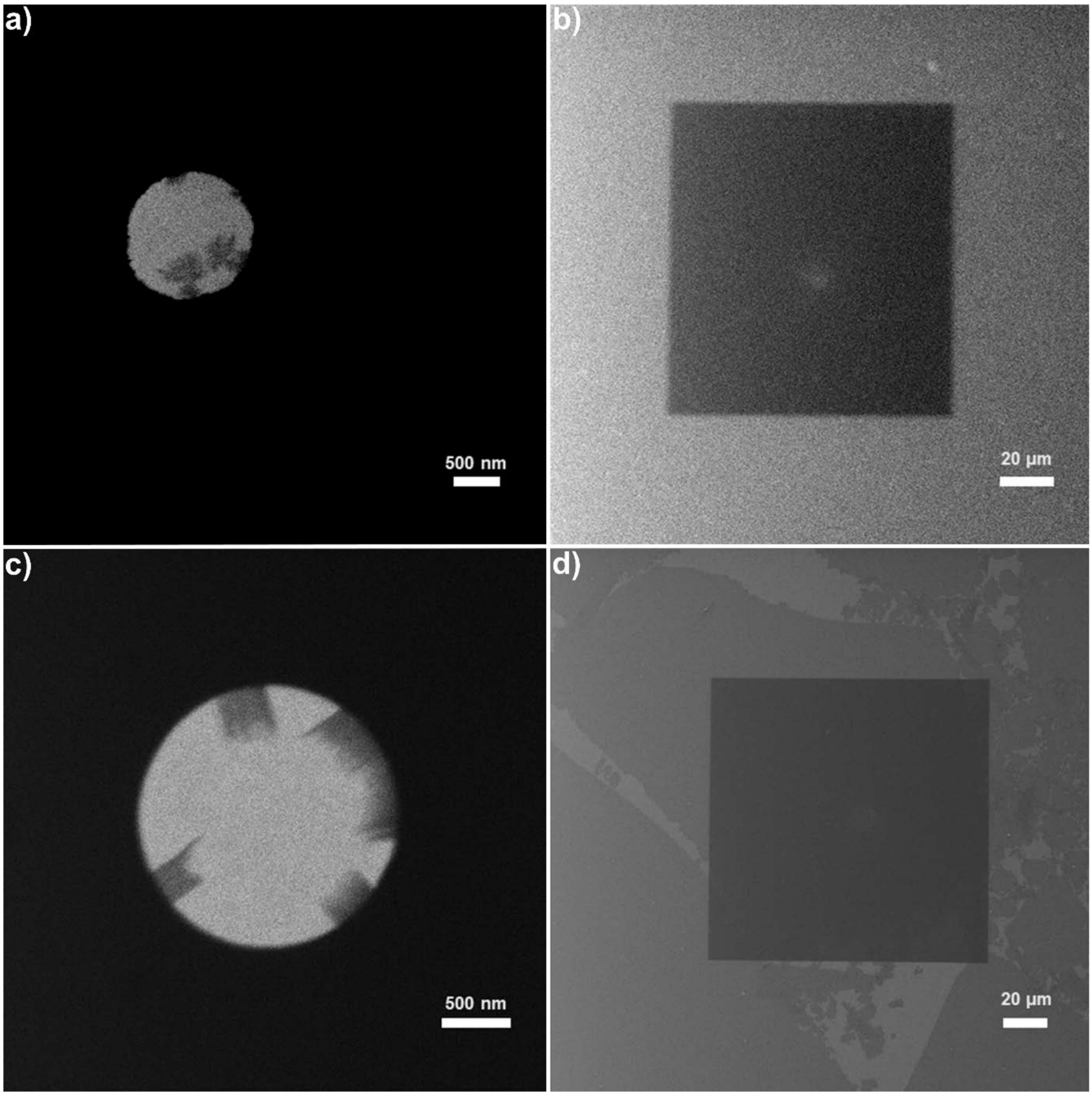

Figure S2. HIM images of the impermeable 2D COF membranes obtained with charge compensation at dwell time 0.5 s and acceleration voltage 35.8 kV. a) Sample 4 (blanker current 0.7 pA, bright-field transmission mode). b) Sample 7 (blanker current 0.7 pA, secondary electron mode). c) Sample 8 (blanker current 2.0 pA, bright-field transmission mode). d) Sample 9 (blanker current 0.7 pA, secondary electron mode).

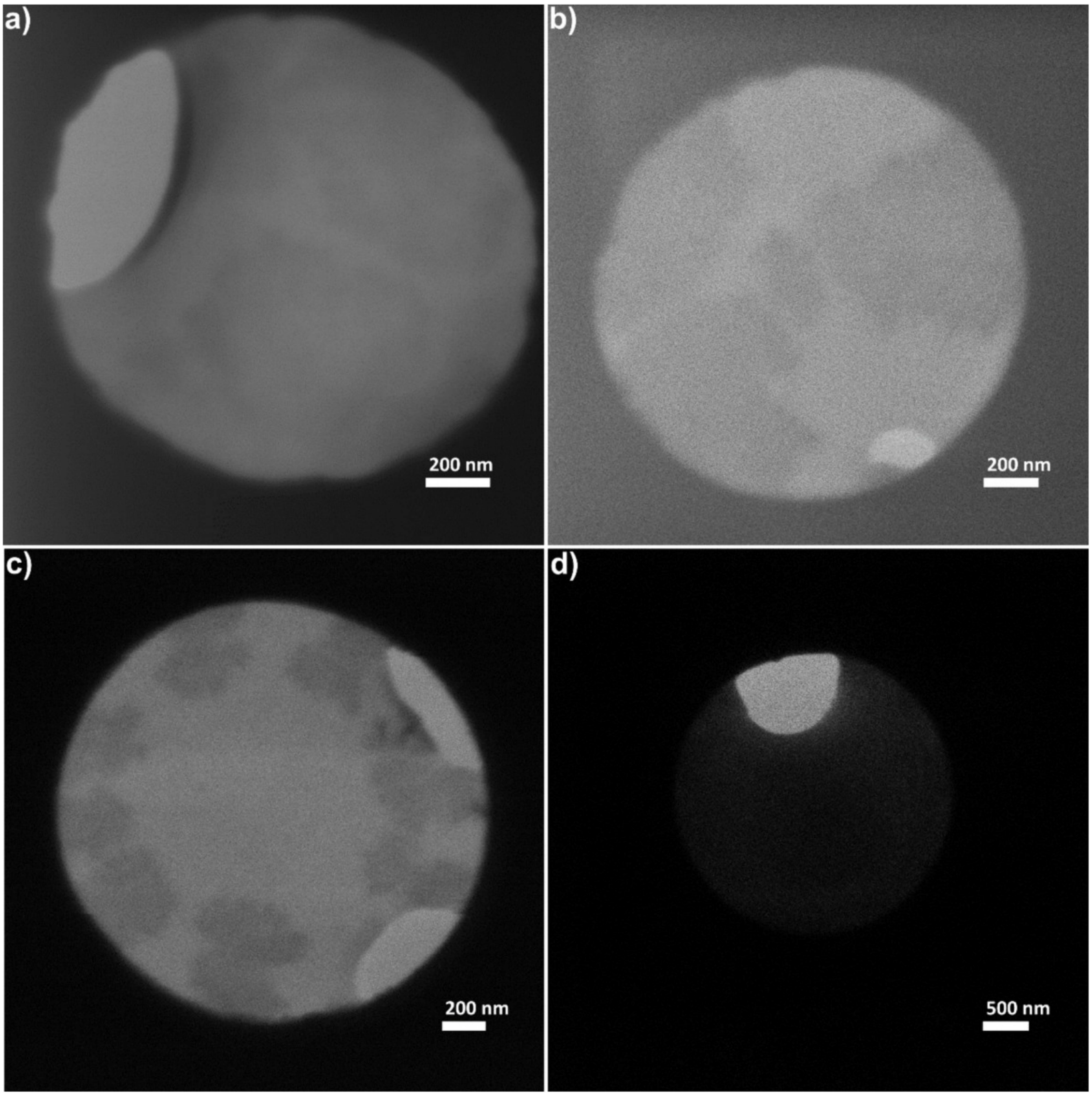

Figure S3. Bright-field HIM images of the 2D COF membranes obtained. a) Sample 1 (dwell time 1.0 µs, blanker current 0.5 pA, acceleration voltage 33.9 kV). b) Sample 2 (dwell time 0.5 µs, blanker current 0.5 pA, acceleration voltage 33.9 kV). c) Sample 6 (dwell time 1.0 µs, blanker current 0.5 pA, acceleration voltage 35.3 kV). d) Sample 10 (dwell time 0.5 µs, blanker current 0.6 pA, acceleration voltage 34.5 kV).

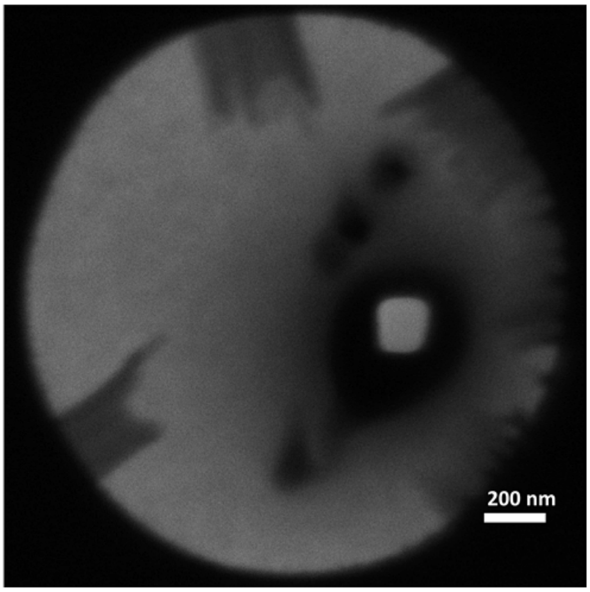

Figure S4. Bright-field HIM image of Sample 8 with an artificial orifice (bright area) of 180 nm in effective diameter. Darker region around the hole is due to sample charging. The orifice was milled with a He$^+$ focused ion beam. The image was scanned without charge compensation at dwell time of 30.0 µs, blanker current of 1.7 pA, acceleration voltage of 35.8 kV.

Permeation measurements

Figure S5 depicts schematically the permeation system in use. The 2D COF films transferred onto micromachined Si_3N_4/Si chips are glued onto UHV-compatible Cu discs. The Cu disc with the membrane is then mounted into the membrane cell representing two conflat flanges that ensure leak-tight connection. The membrane cell is positioned between the high-vacuum detection chamber and the mixing chamber. The mixing chamber is connected to pressurized gas cylinders as well as to stainless-steel containers with liquid substances. The liquid containers are outgassed so as the vaporous compounds can be directly let to the membrane through the mixing chamber. The detection chamber is equipped with the quadrupole mass-spectrometer, and the permeation process is monitored in real time. To calibrate the detector, the system has the reference cell with a nanoscopic aperture. The reference signal is recorded upon introducing the species in question to the reference cell, whereas the membrane cell is evacuated (the pumping lines are not shown for simplicity). The membrane can be successively fed with different gases and vapors via dosing needle valves, and the feed pressure is measured with the capacitance manometer.

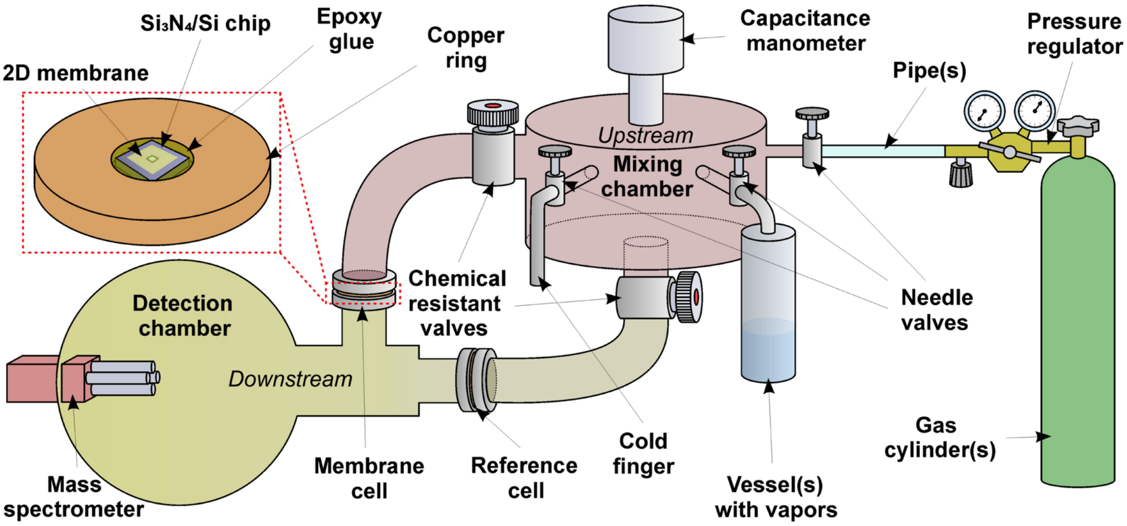

Figure S5. Schematic diagram of the permeation apparatus employed.

Permeation rates

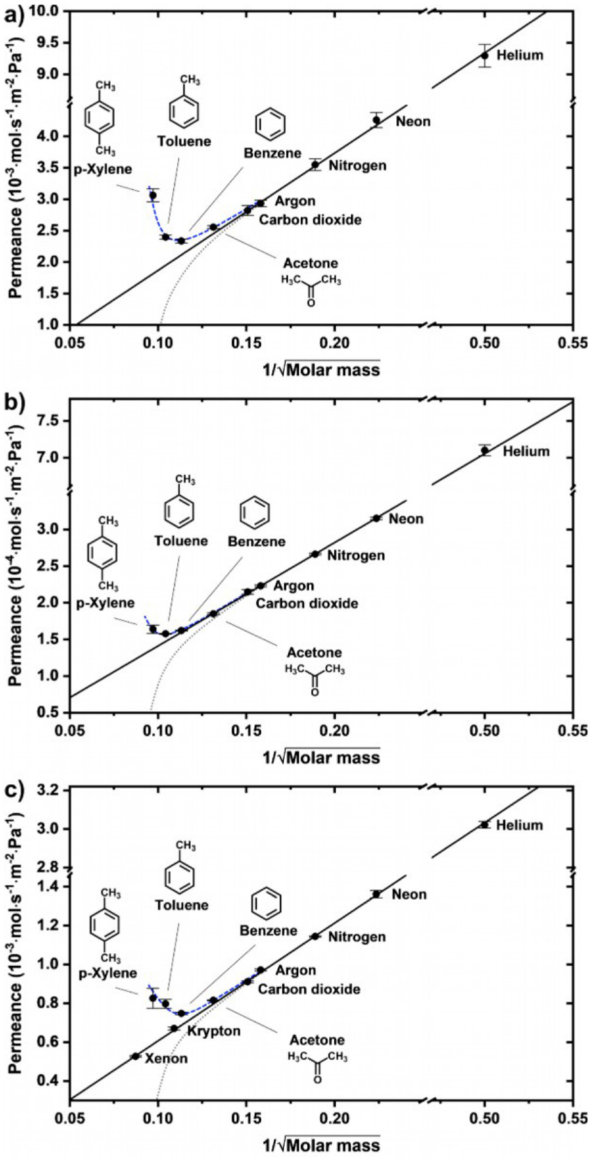

Figure S6. Permeation rates in the 2D COF membranes. a) Sample 1 (see comments below); b) Sample 2; c) Sample 6. The solid lines are best linear fits; the dashed lines are for guiding the eye; the dotted lines are to mimic a molecular sieving effect. The measurements were done at least three times at room temperature and feed pressure of 5 mbar. The error bars are standard deviation.

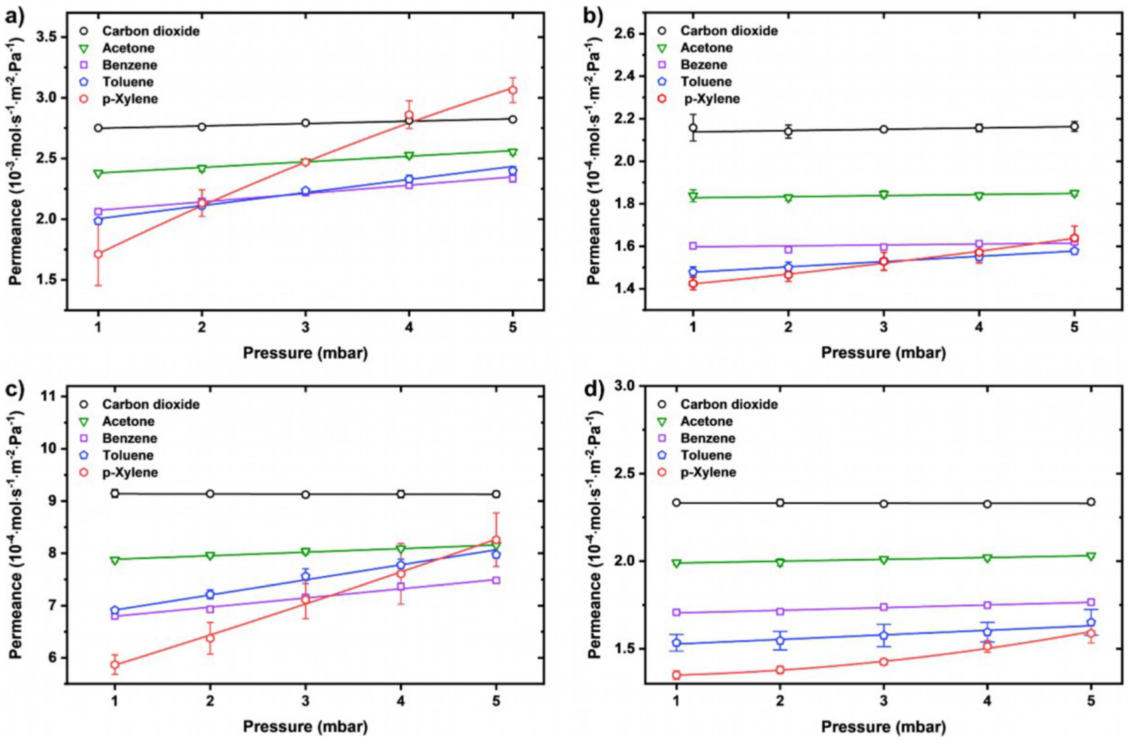

Figure S7. Permeation rates in the 2D COF membranes. a) Sample 1 (see comments below); b) Sample 2; c) Sample 6; d) Sample 8 with an artificial orifice shown in Figure S4. The measurements were repeated three times at room temperature. The error bars are standard deviation. The lines are for guiding the eye.

Comments

The permeation results for Sample 1 shown in Figure S6 and Figure S7 are different from the data presented in Table 1 and Table 2 of the main text. This sample was the first one in the series and experienced many experiments before we came up with the measurements given in this study. In particular, the membrane was exposed to benzene, iso-propanol, n-propanol, D_2O, n-hexane, n-heptane, triethylamine, cyclohexane, p-xylene, toluene, acetone. The point is that there was an irreversible change observed during the experiments with saturated p-xylene vapor. Figure S8a illustrates the row data revealing a sudden drop in the permeance at higher pressure. As a result, the effective open area of the membrane decreased by around 35 %, but the performance remained similar (Figure S8b). Back then we had no idea on the properties of other samples and attributed the change to some chemical transformations. However, the HIM data obtained at the end of the study in conjunction with the permeation measurements with the other membranes suggest that there was bad adhesion between the 2D COF crystal and the Si_3N_4/Si substrate. One can see rough edges of the aperture in Figure S3a that may also mean roughness on the top surface. When we increased the pressure of xylene vapor to over 10 mbar, the crystal was pushed to the surface, and the interface was likely tightened. As the crystal area in Figure S3a fits well to the final permeance (Table 2), we believe this interpretation is correct, but the initial results were not included into Figure 4b. It is also worth noting that the permeation measurements with vaporous compounds are highly sensitive to temperature variations which explains the large scattering in Figure 4b.

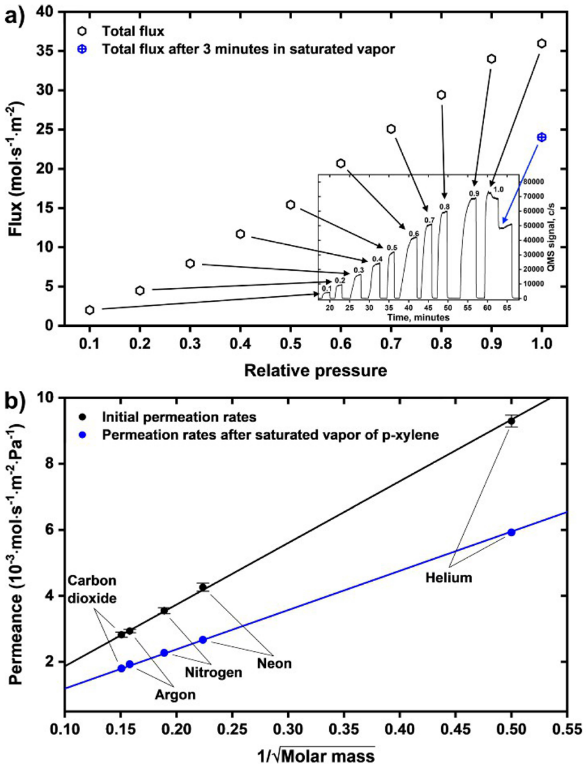

Figure S8. a) The transmembrane flux of p-xylene in Sample 1 as a function of the relative pressure. The inset shows the evolution of the mass-spectrometer signal in time. b) Permeation rates in Sample 1 before and after the change.

6 Gas and vapor permeation in bilayer silica

6.1 Introduction

Bilayer silica (BS) is an intrinsically porous material that has a potential for membrane separation. DFT calculations predicted a great selectivity for the crystalline phase as well as facile gas permeation for vitreous BS. However, it was not previously reported about permeation measurements in the free-standing material. The SiO_2 film on Au/mica substrates were grown by plasma enhanced atomic layer deposition (PEALD) in the working group “Inorganic Materials Chemistry” of Prof. Anjana Devi at the Ruhr-University Bochum. As reference samples, 2 ML of oxidized silicon were deposited on Au/mica substrates by molecular beam epitaxy (MBE) in the working group of Prof. Eric I. Altman at the Yale University. Annealing of the deposited films was performed at 950 – 100 K in air to obtain bilayer silica at the Bielefeld University. The quality of the BS coverage was checked with the PM-IRRAS and XPS methods, and the optimal conditions were found for the preparation of bilayer silicon dioxide via PEALD approach. The BS films were transferred by the PMMA-assisted protocol onto the Si_3N_4/Si chips to study the molecular transport through the thinnest silica membrane.

6.2 Results

After the deposition of SiO_2 and annealing, the characteristic peak at 1290 cm^{-1} in the PM-IRRAS spectra was considered as evidence of the presence of bilayer silica on gold. The samples from the first series were prepared at 60 °C in the PEALD reactor, and the maximally intense vibration was found after 6 ALD cycles. The signal from the bilayer structure was reduced with an increase in the number of ALD cycles and it disappeared at 14 ALD cycles, while the new feature from 3D SiO_2 at 1250 cm^{-1} began rising after 9 ALD cycles. The XPS confirmed a rise in the photoelectron signals of Si2p and O1s with increasing deposition cycles, while the Au4f intensity decreased exponentially. No free-standing material was obtained at 6 ALD cycles due to a low coverage because the deposition temperature of 60 °C resulted in the coexistence of bilayer and multilayer structures.

The samples from the second series were deposited at 150 °C. Again, the most intense vibration was observed after 6 ALD cycles that was close to the signal from the MBE grown crystalline BS. The 2D SiO_2 films were successfully transferred onto TEM grids. As a result, transmission electron microscopy revealed multiple holes in the vitreous bilayer silica after 6 ALD cycles due to incomplete coverage. Notably, the coexistence of holes (10 – 30 nm) and 3D islands with dimensions below 5 nm was observed for the free-standing 2D SiO_2 after 7 ALD cycles at 150 °C.

In order to suppress a multilayer growth, the PEALD was performed at 240 °C. The most intense characteristic peak for bilayer SiO_2 was found for the sample after 6 ALD cycles. It was experimentally confirmed that the higher the substrate temperature during PEALD, the higher the vibration intensity. According to XPS, more silicon dioxide was deposited on gold using PEALD at 240 °C than after deposition at 60 °C. TEM analysis confirmed the presence of a high-quality vitreous BS without holes for the sample after 6 PEALD cycles at 240 °C.

The BS films were transferred onto the Si_3N_4/Si chips with orifices of ~ 2 μm in diameter, glued onto the copper rings and inserted into the permeation apparatus as previously described. The passage of such gases as Ne, N_2, O_2, Ar, CO_2, Kr, Xe and SF_6 was not detected despite the pressure difference of 400 mbar. Only helium permeation with the rate of ~ 1.5×10^{-8} $mol \cdot s^{-1} \cdot m^{-2} \cdot Pa^{-1}$ was revealed. Notably, the pores in vitreous bilayer silica are not too small because even bulky molecules of methyl isobutyl ketone (MIBK) were able to cross them. It seems the probability for an inert gas particle to be in the middle of the pore at the normal incidence angle is very low.

In contrast, great permeances were found for heavy water (HW), 1-propanol (PA) and MIBK in their saturated vapors: 4.5×10^{-5}, 1.7×10^{-5} and 1.9×10^{-4} $mol \cdot s^{-1} \cdot m^{-2} \cdot Pa^{-1}$ respectively. The elongated molecules of 1-octene could not pass through vitreous BS. The permeation rates of HW, PA and MIBK were not detected at the relative pressures below 0.5, but their permeances were steeply rising with an increase in their relative pressures that are typical of adsorption-mediated transport for condensable substances. While inert particles face steric hindrances, the adsorbed molecule from a vapor has enough residence time to change its configuration and cross the micropore.

The vapors of HW ($P_{sat.}$ = 22.4 ± 0.4 mbar), PA ($P_{sat.}$ = 22.6 ± 0.4 mbar), MIBK ($P_{sat.}$ = 23.1 ± 0.3 mbar) and 1-octene ($P_{sat.}$ = 19.8 ± 0.4 mbar) were considered due to their similar saturation pressure under experimental conditions that enabled direct comparison of their permeation rates with nearly the same pressure difference. The fact that small D_2O particles permeates ~ 4 times slower than larger MIBK molecules was explained by the poor affinity of water for bilayer silica. Indeed, the contact angle of pure water on BS/Au amounts to 62.6 ± 2.6°, while organic solvents wet the surface completely. The PM-IRRAS revealed adsorption of PA and MIBK in their vapors on the BS/Au, but the signal from adsorbed water was not detected.

According to DFT calculations, the adsorption energy on the bilayer silica is decreasing in a row MIBK – PA – HW. The adsorbates of HW and PA are supposed to form clusters on the hydrophobic BS due to hydrogen bonding. More common six-membered rings could be permeable to D_2O species, but the PA and MIBK molecules were supposed to permeate only through seven-, eight- and nine-membered rings. The measured vapor permeances were the result of a trade-off between the number of adsorbates on the BS surface and the transmission probability determined by the molecular size. In turn, the spreading of a monolayer seems to be more favorable for MIBK providing the highest permeance among the substances under consideration.

6.3 Conclusion

The bilayer silica films were obtained on Au/mica substrates after PEALD at 240 °C followed by annealing at ~ 1000 K in air. The samples were transferred onto Si3N4/Si chips with ~ 2 µm orifices, and the molecular permeation was studied in vitreous BS *in situ*. Contrary to predictions, the poorly condensable gases did not pass through vitreous bilayer silica with detectable rates due to steric hindrances, and only the helium passage was observed despite the presence of relatively large nine-membered rings in the structure. The molecular sieving effect with a high performance seems to be an illusive permeation regime for inert gases if the pore dimensions are close to the sizes of gas particles.

The gain in a vapor permeance when approaching the saturation point is consistent with the adsorption and surface diffusion of ad-molecules over the BS surface. The size exclusion was revealed for long molecules of 1-octene, while HW, PA and MIBK species passed the 2D SiO_2 with the high rates. Counterintuitively, the highest permeance was found for bulky MIBK particles because of its spreading over the BS surface. The smallest D_2O species can pass through almost any pore, but water permeated more slowly than ketone due to the poor affinity towards SiO_2 and the supposed multilayer adsorption. In turn, the 1-propanol species were assumed to form multilayers in the saturated vapor and experience steric hindrance when passing through the available pores. The adsorption-mediated transport of vapors is unambiguously superior to effusion transport in the 2D membrane with straight sub-nanometer pores. Vapor permeation and selectivity in bilayer silica were determined by the molecular size and affinity of the substance towards the membrane material.

6.4 Publication: Molecular Permeation in Freestanding Bilayer Silica

This submitted article is reprinted from the manuscript. The original paper will appear as:

D. Naberezhnyi, L. Mai, N. Doudin, I. Ennen, A. Hütten, E.I. Altman, A. Devi and P. Dementyev, *Molecular Permeation in Freestanding Bilayer Silica*. ***Nano Lett***, 2021.

Contribution:

Annealing of deposited SiO_2, transfer of bilayer silica, characterization of bilayer silica by XPS and IRRAS, contact angle measurements, vapor adsorption measurements by the IRRAS, permeation experiments and data evaluation were performed by the author.

Molecular Permeation in Freestanding Bilayer Silica

Daniil Naberezhnyi,[†] *Lukas Mai,*[‡] *Nassar Doudin,*[§] *Inga Ennen,*[†] *Andreas Hütten,*[†]
Eric I. Altman,[*,§] *Anjana Devi,*[*,‡] *Petr Dementyev*[*,†]

[†]Faculty of Physics, Bielefeld University, 33615 Bielefeld, Germany

[‡]Inorganic Materials Chemistry, Ruhr University Bochum, 44801 Bochum, Germany

[§]Department of Chemical and Environmental Engineering, Yale University, New Haven, Connecticut 06520, United States

KEYWORDS: bilayer silica, two-dimensional membranes, atomic layer deposition, gas permeation, adsorption

ABSTRACT: Graphene and other single-layer structures are pursued as high-flux separation membranes, although imparting porosity endangers their crystalline integrity. In contrast, bilayer silica composed of corner-sharing [SiO_4] units is foreseen to be permeable for small molecules due to its intrinsic lattice openings. This study sheds light on the mass transport properties of freestanding 2D SiO_2 upon using atomic layer deposition (ALD) to grow large-area films on Au/mica substrates followed by the transfer onto Si_3N_4 windows. The permeation experiments with gaseous and vaporous substances reveal the suspended material to be porous, but the membrane selectivity appears to diverge from the size exclusion principle. While the passage of inert gas molecules is hindered with the permeance below 100 GPU, condensable species like water are found to cross vitreous bilayer silica thousandfold faster in accordance with their superficial affinity. The work paves the way for bilayer oxides to be addressed as inherent 2D membranes.

Soon after its first isolation, pristine graphene was shown to be impermeable for molecular species, including the smallest He atoms.[1] This sparked intense research on defect engineering in 2D materials for separation and other nanofluidics applications.[2-10] While the mass transfer in artificial pores has drawn much attention, there is a promising membrane structure needing no perforation, namely 2D silicon dioxide, that has been largely overlooked.[11] 2D SiO_2 or bilayer silica represents a planar network of [SiO_4] tetrahedra with shared oxygen atoms (Figure 1a) which was discovered back in 2010.[12-14] The building blocks of the material are arranged either into a well-ordered honeycomb lattice or as a vitreous phase with four- to nine-membered rings featuring densely packed subnanometer pinholes.[15] Computations predicted the intrinsic pores in bilayer silica to allow for facile permeation of small gas molecules with the calculated selectivity and throughput suitable for industrial separation.[16] However, no transport measurements with the freestanding membrane have been reported to date.

Molecular beam epitaxy (MBE) can be used to prepare 2D silicon dioxide on a number of single-crystalline metals, such as Ru(0001), Pt(111), Pd(100), Pd(111), and the supported material has been extensively characterized by means of surface-sensitive techniques.[17] Earlier adsorption studies suggested that both CO and D_2 are unlikely to penetrate the pores smaller than seven-membered rings,[18] whereas there was a clear size effect observed in the diffusion of Pd and Au atoms through the two structural polymorphs.[19] The hexagonal pores were later found to trap ionized Ar, Kr, and Xe indicating that smaller He and Ne are able to leave the bilayer film freely.[20] Studying 2D SiO_2 as a membrane though requires more cost-effective fabrication on appropriate sacrificial substrates to yield suspended sheets similar to graphene grown with chemical vapor deposition (CVD).[21] As epitaxial metal films have been advanced instead of expensive single crystals,[22] bilayer silica has recently been obtained with both MBE and atomic layer deposition

(ALD) on Au(111) making the freestanding 2D material attainable.[23] ALD is a variant of CVD consisting of self-limiting reactions of a precursor with a substrate surface and subsequent reactions with a co-reactant which results in materials deposition on a large scale with atomic precision.[24-26]

Herein, we employ plasma-enhanced (PE) ALD to grow 2D SiO_2 on commercially available Au/mica substrates in order to enable direct membrane studies with unsupported layers (Figure 1b). Following the silicon oxide deposition from bis(diethylamino)silane (BDEAS) and oxygen plasma as precursors in a PEALD reactor,[27] the material is annealed in a tube furnace at 950-1000 K under ambient atmosphere. Infrared reflection absorption spectroscopy (IRAS), X-ray photoelectron spectroscopy (XPS) and transmission electron microscopy (TEM) are used to explore the efficacy of the ALD process as a function of the deposition temperature and to optimize the amount of the material needed for forming the 2D SiO_2 structure. We identify that six ALD cycles at 240 °C result in good-quality vitreous bilayer silica and transfer the 2D film onto Si_3N_4/Si chips with micrometer-sized apertures. The suspended nanomembranes are undergone to room-temperature permeation measurements with gaseous and vaporous substances in a custom-made facility.[28] While no transmembrane flux is detected for atmospheric and noble gases (except He), saturated vapors of heavy water (HW), 1-propanol (PA) and methyl isobutyl ketone (MIBK) are found to readily pass 2D SiO_2. The results obtained are rationalized with the help of DFT calculations and adsorption experiments.

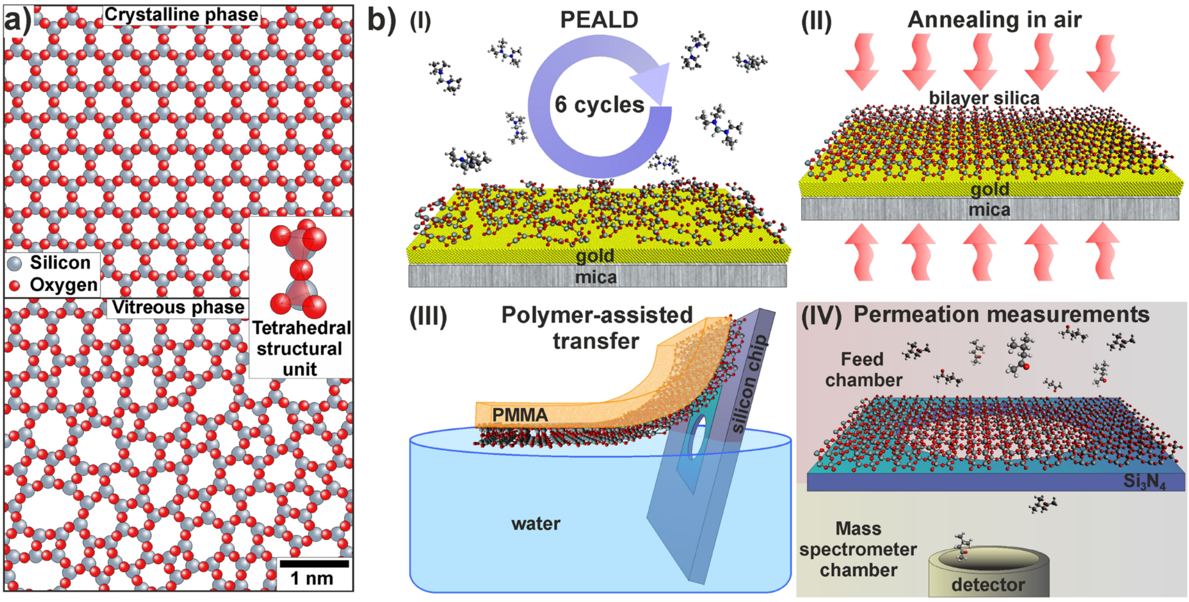

Figure 1. a) Atomic structure of bilayer silica. b) Schematic of experimental procedures: (I) SiO_2 PEALD onto Au/mica; (II) Annealing in a tube furnace at 950-1000 for 30 min; (III) Gold etching and film transfer onto micromachined Si_3N_4/Si chips; (IV) Permeation measurements with freestanding bilayer silica.

Bilayer silica is described by the 2D density of 158 and 167 ng cm^{-2} for the crystalline and the vitreous phase respectively.[13] Given the growth rate of ~40 ng cm^{-2} cycle^{-1} in the PEALD reactor used,[27] at least four ALD cycles would be required to complete a 2D layer providing the same deposition efficacy as on the silicon dioxide. Figure 2a illustrates IRAS spectra for a series of SiO_2 films grown with ALD on Au/mica at 60 °C and subsequently annealed in air. There are two characteristic absorption bands seen that mark the deposition process into three regimes. Initially, only the peak at 1290 cm^{-1} evolves and reaches its maximum intensity at six ALD cycles. This spectral fingerprint corresponds to the out-of-plane Si-O-Si vibrational mode in the bilayer structure and manifests the presence of the 2D phase.[29] The signal then decreases with more ALD cycles accompanied by the emergence of the new feature at 1250 cm^{-1} that is attributed to 3D

SiO_2.[29] The two bands appear to coexist from nine to thirteen cycles, and afterwards solely the bulk-like oxide is observed. The IRAS data indicate that the deposition rate on Au is lower than that on SiO_2 which means a nucleation delay during the initial cycles due to the chemical inertness of the gold surface. Despite the strong peak at six cycles, no freestanding 2D layers could be obtained with ALD at 60 °C as the low substrate temperature seems to favor the formation of multilayer patches before Au is fully covered with bilayer silica.

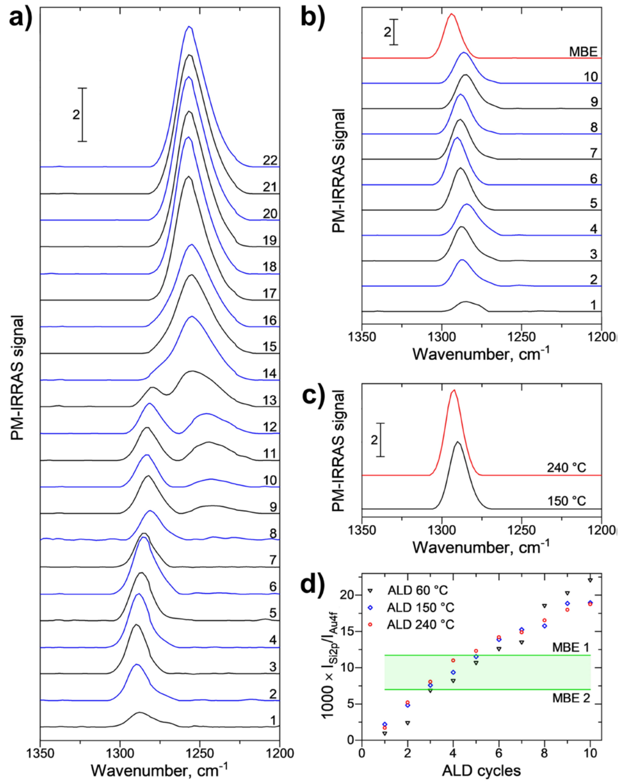

Figure 2. a) Polarization-modulated (PM) IRAS of SiO_2 grown on Au/mica at 60 °C with 1-22 ALD cycles. b) PM IRAS of SiO_2 grown on Au/mica at 150 °C with 1-10 ALD cycles and PM IRAS of MBE-grown bilayer silica. c) PM IRAS of 2D SiO_2 grown with six ALD cycles at 150 and 240 °C. d) Integral XPS of ALD SiO_2 on Au/mica at different deposition temperature. The Si 2p signal is rationed to the Au 4f signal of the underlying substrate. The green area is for MBE-grown bilayer silica (two preparations).

In order to facilitate more uniform 2D growth, we increased the deposition temperature to 150 °C. As shown in Figure 2b, the most intense IRAS band is again produced by six ALD cycles, but in this case, the peak intensity is well comparable with MBE-grown crystalline bilayer silica.[23] Although the two allotropes are not distinguishable in IRAS, the spectral intensity suggests the ALD-grown 2D SiO_2 to have high surface coverage. Similar to the previous report,[23] the films deposited at 150 °C were successfully transferred onto grids and imaged with TEM displaying mostly vitreous bilayer silica (Figure 3a-c). It is worth noting that the morphology of seven-cycle films exhibits 3D particles confirming the buildup of the bulk-like oxide. The particles appear to be firmly integrated into the freestanding layer with a rather narrow size distribution of less than 5 nm in diameter. Besides the small 3D objects, the micrographs also reveal abundance of irregular holes with the size ranging from 10 to 30 nm. As similar defects are also present in the six-cycle samples, they are likely to stem from incomplete film coverage.

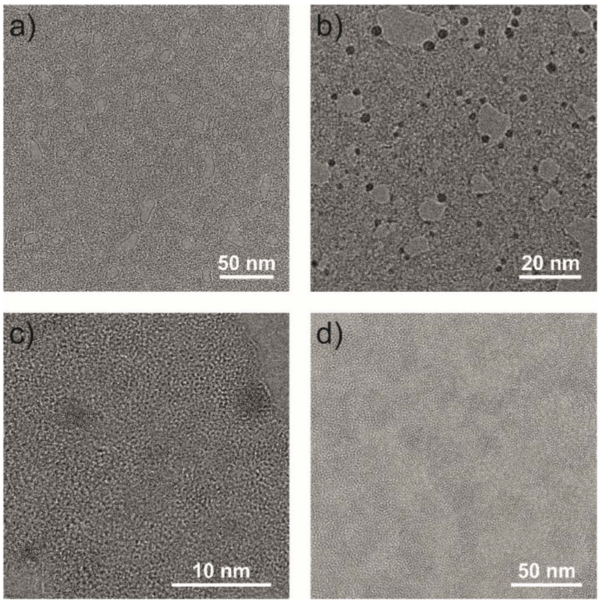

Figure 3. TEM images of freestanding SiO_2 grown on Au/mica: a) Six ALD cycles at 150 °C; b,c) Seven ALD cycles at 150 °C; d) Six ALD cycles at 240 °C.

Because the permeation in 2D membranes is disturbed much by defects, the ALD growth was further improved by elevating the substrate temperature to 240 °C. This gave rise to a closed bilayer film after six cycles (Fig. 3d), and the enhancement achieved is also traceable by IRAS (Fig. 2c). To explore the deposition efficacy in more detail, we performed XPS analysis of the ALD-grown films (**Figures S4-S7**). Figure 2d shows the intensity of the Si signal referenced to the Au signal underneath in comparison with MBE-grown silica. Despite the sample-to-sample deviations, there is a pronounced temperature effect on the amount of the deposited material. While from one to seven ALD cycles more SiO_2 is deposited at 240 °C than at 60 °C, the reverse order is found for eight and following cycles. As the surface reaction of BDEAS on SiO_2 is known to be inhibited at higher temperatures,[30] the observed deflection is likely to occur when the substrate exposes no bare gold anymore which is in line with XPS of MBE-grown bilayer silica.

Vitreous 2D SiO_2 prepared with six ALD cycles at 240 °C was suspended over individual apertures of 2-2.5 μm in diameter and probed with respect to permeation of gaseous molecules. The bilayer silica membranes fixed in a leak-tight cell were exposed to pure feed gases while the downstream side was under high-vacuum pressure of 1.0×10^{-9} mbar (see Supporting Information for details).[28] The steady-state flow rates through the membranes were measured with a quadrupole mass-spectrometer, and the permeation rates obtained are summarized in Figure 4a. By applying a pressure differential of up to 400 mbar, we found that Ne, Ar, Kr, Xe, N_2, O_2, CO_2 and SF_6 virtually do not pass intact bilayer silica, while the detection limit for the membrane permeance can be quantified as low as 1.0×10^{-9} mol s^{-1} m^{-2} Pa^{-1}. Only He demonstrated a measurable flow rate with the permeance of 1.5×10^{-8} mol s^{-1} m^{-2} Pa^{-1} meaning that merely one in ten million atoms arriving to the 2D membrane can cross it. However, this does not imply the pores to be too small as far greater transmembrane fluxes were witnessed when bilayer silica was exposed to saturated vapors of HW, PA and MIBK. The behavior reminds the properties of carbon nanomembranes (CNMs) and 2D covalent organic frameworks (COFs) and can be explained by the permeation of adsorbed molecules as opposed to the backscatter of inert particles.[28,31] The surface-mediated diffusion is also evident from the steep pressure dependence of the permeation rates measured (Figure 4b) which reflects a non-linear increase in the number of adsorbed molecules. Thus, the probability of gas-phase molecules to get right to the middle of the pores at the normal incidence angle seems to be extremely low, while the adsorbates possess enough residence time to adjust their configuration. Note that neither steric nor orientation effects were taken into account in the previous computations of the gas transmission probability in bilayer silica.[16]

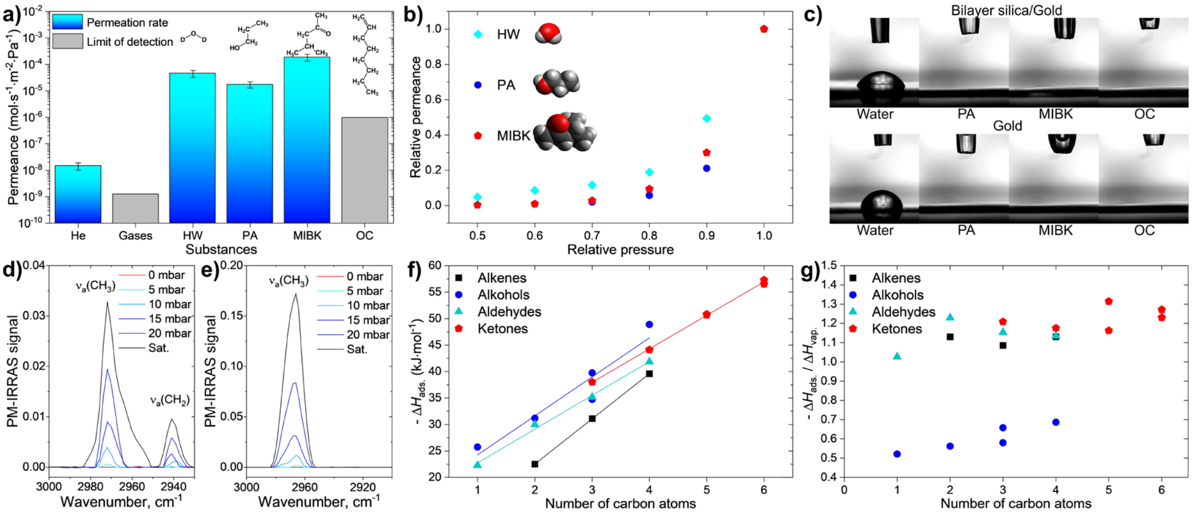

Figure 4. a) Permeation rates in vitreous bilayer silica measured at room temperature. The values are averaged over three intact samples, and the error bars are standard deviation. The limit of detection is determined according to [28]. b) Permeation rates for vaporous substances as a function of relative pressure. The values are normalized to the respective permeance at saturation pressure. c) Contact angle measurements on 2D SiO_2 in comparison with gold surface. d) IRAS of PA adsorbed on bilayer silica as a function of vapor pressure. e) IRAS of MIBK adsorbed on bilayer silica as a function of vapor pressure. f) Adsorption energy of organic compounds on

crystalline 2D SiO_2 from DFT calculations. g) Calculated adsorption energy referenced to evaporation enthalpy of the substances.

HW, PA, MIBK and 1-octene (OC) were picked due to their very similar saturation pressure at room temperature of around 23 mbar (~20 mbar for OC). This enables direct comparison of the permeance values at the identical driving force and addressing how they depend on both the molecular dimensions and the strength of gas-surface interactions. Given the pore architecture limited by nine-membered rings, one would expect the permeation rate in 2D SiO_2 to exhibit a size cutoff that is indeed the case for long OC molecules. On the other hand, the fact that under the same pressure gradient, small HW molecules permeate four times slower than larger MIBK molecules can be understood in terms of their poorer affinity towards the membrane surface. Indeed, bilayer silica was found to be quite hydrophobic with the contact angle of 62.6±2.6 ° as opposed to complete wetting with the organic solvents (Figure 4c). We also carried out IRAS measurements under vaporous environments (see Supporting Information) and observed facile adsorption of PA and MIBK on ALD-grown silica (Figure 4d,e). Even though adsorption of HW vapor is hardly seen in IRAS, it is difficult to convert the spectral data into the absolute surface coverage, and hence, to explain the one-order of magnitude difference in the permeance of PA and MIBK.

DFT calculations were then performed to account for the adsorption energy of organic species on 2D SiO_2 (for simplicity, crystalline phase was considered). As shown in Figure 4f, there is a gradual increase in the adsorption strength depending on the molecular length, and for the same number of C atoms, alcohols appear to bind more strongly compared to alkenes and aldehydes/ketones. However, for highly branched MIBK molecules, the heat of adsorption was found to be 57.3 kJ mol^{-1} as opposed to 39.7 kJ mol^{-1} for smaller PA. The two values are much greater than the adsorption energy of water molecules that was previously calculated to be only 16.6 kJ mol^{-1}.[32] We further looked at the heat of evaporation and compared it with the adsorption energy on 2D SiO_2 (Figure 4g). One can see that due to hydrogen bonding, intermolecular interactions in alcohols are much stronger than their affinity towards the oxide surface. This means that both PA and HW molecules adsorbing on bilayer silica would prefer to form a multilayer over a monolayer whereas MIBK would tend to fill up the first layer. Our interpretation is that the surface coverage produced on the membrane upon vapor condensation obeys the following sequence: MIBK >> PA >> HW. Bearing in mind the dominance of six-membered rings in vitreous 2D SiO_2 followed by five- and seven-membered rings with a minority of eight-, four- and nine-membered rings,[13] we assume that the substances permeate through different pores. It is likely that small HW molecules are able to pass six-membered and larger rings, so that their low surface coverage is compensated by the high density of accessible pores. In contrast, bulkier PA and MIBK molecules would probably fit only to seven-, eight- and nine-membered rings, and as a result, their chance to find a suitable pore is reduced. Therefore, the permeation rates in Figure 4a seem to be an interplay between the number of adsorbed molecules that is governed by adsorption energetics and the transmission probability given by molecular dimensions. To test this hypothesis, permeation measurements with crystalline bilayer silica would be valuable because of its monodisperse pore geometry, but this goes far beyond the scope of the present study. Given the versatility of ALD, we expect the phase control to be achievable upon varying the precursor chemistry and the process parameters.

In conclusion, we elaborated on the ALD growth of vitreous bilayer silica upon Au/mica and accomplished first-ever permeation measurements with the freestanding membrane. It was demonstrated that the deposition efficacy changes with the substrate temperature, and the continuous 2D material could be obtained at 240 °C. The films suspended over microscopic apertures were found to prevent the transport of regular gases, but vaporous substances were shown to easily cross bilayer silica upon condensation. The permeation rates were quantified to be 1.5×10^{-8}, 4.5×10^{-5}, 1.7×10^{-5}, 1.9×10^{-4} mol s^{-1} m^{-2} Pa^{-1} for He, D_2O, C_3H_7OH and $C_4H_9C(O)CH_3$ respectively. Our results indicate that chemical affinity towards the membrane surface plays a significant role in the permeation process, whereas molecular effusion takes no place when the pores are as small as the gas particles. Further mass transfer studies in liquid and solid-state media can help understand the impact of the pore size distribution, especially the contribution of six-membered rings. We anticipate bilayer silica and related tetrahedral structures to reshape the field of 2D membranes as challenging perforation procedures can now be bypassed.

ASSOCIATED CONTENT

Supporting Information. The following files are available free of charge.

Materials preparation and characterization, permeation measurements, contact angle measurements, adsorption measurements, DFT calculations (PDF).

AUTHOR INFORMATION

Corresponding Author

* dementyev@physik.uni-bielefeld.de

* anjana.devi@ruhr-uni-bochum.de

* eric.altman@yale.edu

Author Contributions

The manuscript was written through contributions of all authors. All authors have given approval to the final version of the manuscript.

Notes

The authors declare no competing financial interest.

ACKNOWLEDGMENT

P. D. acknowledges financial support from the 'Fonds der Chemischen Industrie' (Liebig Fellowship) and thanks Prof. Armin Gölzhäuser for access to laboratory infrastructure.

ABBREVIATIONS

2D, two dimensional; ALD, atomic layer deposition; MBE, molecular beam epitaxy; CVD, chemical vapor deposition; IRAS, infrared reflection absorption spectroscopy; XPS, X-ray photoelectron spectroscopy; TEM, transmission electron microscopy; HW, heavy water; PA, propyl alcohol; MIBK, methyl isobutyl ketone; OC, 1-octene; BDEAS bis(diethylamino)silane;

REFERENCES

(1) Bunch, J. S.; Verbridge, S. S.; Alden, J. S.; van der Zande, A. M.; Parpia, J. M.; Craighead, H. G.; McEuen, P. L. Impermeable Atomic Membranes from Graphene Sheets. *Nano Lett.* **2008**, *8*, 2458-2462.

(2) Koenig, S. P.; Wang, L.; Pellegrino, J.; Bunch, J. S. Selective Molecular Sieving through Porous Graphene. *Nature Nanotech.* **2012**, *7*, 728-732.

(3) Celebi, K.; Buchheim, J.; Wyss, R. M.; Droudian, A.; Gasser, P.; Shorubalko, I.; Kye, J.-I.; Lee, C.; Park, H. G. Ultimate Permeation across Atomically Thin Porous Graphene. *Science* **2014***,* *344*, 289-292.

(4) O'Hern, S. C.; Boutilier, M. S. H.; Idrobo, J.-C.; Song, Y.; Kong, J.; Laoui, T.; Atieh, M.; Karnik, R. Selective Ionic Transport through Tunable Subnanometer Pores in Single-Layer Graphene Membranes. *Nano Lett.* **2014**, *14*, 1234-1241.

(5) Surwade, S. P.; Smirnov, S. N.; Vlassiouk, I. V.; Unocic, R. R.; Veith, G. M.; Dai, S.; Mahurin, S. M. Water Desalination Using Nanoporous Single-Layer Graphene. *Nature Nanotech.* **2015**, *10*, 459-464.

(6) Gilbert, S. M.; Dunn, G.; Azizi, A.; Pham, T.; Shevitski, B.; Dimitrov, E.; Liu, S.; Aloni, S.; Zettl, A. Fabrication of Subnanometer-Precision Nanopores in Hexagonal Boron Nitride. *Sci. Rep.* **2017**, *7*, 15096.

(7) Thiruraman, J. P.; Fujisawa, K.; Danda, G.; Das, P. M.; Zhang, T.; Bolotsky, A.; Perea-López, N.; Nicolaï, A.; Senet, P.; Terrones, M.; Drndić, M. Angstrom-Size Defect Creation and Ionic Transport through Pores in Single-Layer MoS_2. *Nano Lett.* **2018**, *18*, 1651-1659.

(8) Zhao, J.; He, G.; Huang, S.; Villalobos, L. F.; Dakhchoune, M.; Bassas, H.; Agrawal, K. V. Etching Gas-Sieving Nanopores in Single-Layer Graphene with an Angstrom Precision for High-Performance Gas Mixture Separation. *Sci. Adv.* **2019**, *5*, eaav1851.

(9) Cheng, P.; Kelly, M. M.; Moehring, N. K.; Ko, W.; Li, A.-P.; Idrobo, J. C.; Boutilier, M S. H.; Kidambi, P. R. Facile Size-Selective Defect Sealing in Large-Area Atomically Thin Graphene Membranes for Sub-Nanometer Scale Separation. *Nano Lett.* **2020**, *20*, 5951-5959.

(10) Liu, J.; Jin, L.; Allen, F. I.; Gao, Y.; Ci, P.; Kang, F.; Wu, J. Selective Gas Permeation in Defect-Engineered Bilayer Graphene. *Nano Lett.* **2021**, *21*, 2183-2190.

(11) Büchner, C.; Wang, Z.-J.; Burson, K. M.; Willinger, M.-G.; Heyde, M.; Schlögl, R.; Freund, H.-J. A Large-Area Transferable Wide Band Gap 2D Silicon Dioxide layer. *ACS Nano* **2016**, *10*, 7982-7989.

(12) Löffler, D.; Uhlrich, J. J.; Baron, M.; Yang, B.; Yu, X.; Lichtenstein, L.; Heinke, L.; Büchner, C.; Heyde, M.; Shaikhutdinov, S.; Freund, H.-J.; Włodarczyk, R.; Sierka, M.; Sauer, J. Growth and Structure of Crystalline Silica Sheet on Ru(0001). *Phys. Rev. Lett*. **2010**, *105*, 146104.

(13) Lichtenstein, L.; Büchner, C.; Yang, B.; Shaikhutdinov, S.; Heyde, M.; Sierka, M.; Włodarczyk, R.; Sauer, J.; Freund, H.-J. The Atomic Structure of a Metal-Supported Vitreous Thin Silica Film. *Angew. Chem. Int. Ed.* **2012**, *51*, 404-407.

(14) Huang, P. Y.; Kurasch, S.; Srivastava, A.; Skakalova, V.; Kotakoski, J.; Krasheninnikov, A. V.; Hovden, R.; Mao, Q.; Meyer, J. C.; Smet, J.; Muller, D. A.; Kaiser, U. Direct Imaging of a Two-Dimensional Silica Glass on Graphene. *Nano Lett.* **2012**, *12*, 1081-1086.

(15) Lichtenstein, L.; Heyde, M.; Freund, H.-J. Crystalline-Vitreous Interface in Two Dimensional Silica. *Phys. Rev. Lett*. **2012**, *109*, 106101.

(16) Yao, B.; Mandrà, S.; Curry, J. O.; Shaikhutdinov, S.; Freund, H.-J.; Schrier, J. Gas Separation Through Bilayer Silica, the Thinnest Possible Silica Membrane. *ACS Appl. Mater. Interfaces* **2017**, *9*, 43061-43071.

(17) Büchner, C.; Heyde, M. Two-Dimensional Silica Opens New Perspectives. *Prog. Sur. Sci.* **2017**, *92*, 341-374.

(18) Emmez. E.; Yang, B.; Shaikhutdinov, S.; Freund, H.-J. Permeation of a Single-Layer SiO_2 Membrane and Chemistry in Confined Space. *J. Phys. Chem. C* **2014**, *118*, 29034−29042.

(19) Büchner, C.; Lichtenstein, L.; Stuckenholz, S.; Heyde, M.; Ringleb, F.; Sterrer, M.; Kaden, W. E.; Giordano, L.; Pacchioni, G.; Freund, H.-J. Adsorption of Au and Pd on Ruthenium-Supported Bilayer Silica. *J. Phys. Chem. C* **2014**, *118*, 20959−20969.

(20) Zhong, J.-Q.; Wang, M.; Akter, N.; Kestell, J. D.; Niu, T.; Boscoboinik, A. M.; Kim, T.; Stacchiola, D. J.; Wu, Q.; Lu, D.; Boscoboinik, J. A. Ionization-Facilitated Formation of 2D (Alumino)Silicate-Noble Gas Clathrate Compounds. *Adv. Funct. Mater*. **2019**, *29*, 1806583.

(21) Zhang, Y.; Zhang, L.; Zhou, C. Review of Chemical Vapor Deposition of Graphene and Related Applications. *Acc. Chem. Res.* **2013**, *46*, 2329–2339.

(22) Jhang, J.-H.; Zhou, C.; Dagdeviren, O. E.; Hutchings, G. S.; Schwarz, U. D.; Altman, E. I. Growth of Two Dimensional Silica and Aluminosilicate Bilayers on Pd(111): from Incommensurate to Commensurate Crystalline. *Phys. Chem. Chem. Phys.* **2017**, *19*, 14001-14011.

(23) Hutchings, G. S.; Shen, X.; Zhou, C.; Dementyev, P.; Naberezhnyi, D.; Ennen, I.; Hütten, A.; Doudin, N.; Hsu, J.; Fishman, Z. S.; Schwarz, U. D.; Hu, S.; Altman, E. I. Scalable Production of Single 2D van der Waals Layers through Atomic Layer Deposition: Bilayer Silica on Metal Foils and Films. *Submitted to 2D Materials* **2021**.

(24) George, S. M. Atomic Layer Deposition: An Overview. *Chem. Rev.* **2010**, *110*, 111-131.

(25) Ahvenniemi, E.; Akbashev, A. R.; Ali, S.; Bechelany, M.; Berdova, M.; Boyadjiev, S.; Cameron, D. C.; Chen, R.; Chubarov, M.; Cremers, V.; Devi, A.; Drozd, V.; Elnikova, L.; Gottardi, G.; Grigoras, K.; Hausmann, D. M.; Hwang, C. S.; Jen, S.-H.; Kallio, T.; Kanervo, J.; Khmelnitskiy, I.; Kim, D. H.; Klibanov, L.; Koshtyal, Y.; Krause, A. O. I.; Kuhs, J.; Kärkkänen, I.; Kääriäinen, M.-L.; Kääriäinen, T.; Lamagna, L.; Łapicki, A. A.; Leskelä, M.; Lipsanen, H.; Lyytinen, J.; Malkov, A.; Malygin, A.; Mennad, A.; Militzer, C.; Molarius, J.; Norek, M.; Özgit-Akgün, C.; Panov, M.; Pedersen, H.; Piallat, F.; Popov, G.; Puurunen, R. L.; Rampelberg, G.; Ras, R. H. A.; Rauwel, E.; Roozeboom, F.; Sajavaara, T.; Salami, H.; Savin, H.; Schneider, N.; Seidel, T. E.; Sundqvist, J.; Suyatin, D. B.; Törndahl, T.; van Ommen, J. R.; Wiemer, C.; Ylivaara, O. M. E.; Yurkevich, O. Review Article: Recommended Reading List of Early Publications on Atomic Layer Deposition—Outcome of the “Virtual Project on the History of ALD”. *J. Vac. Sci. Technol. A* **2017,** *35*, 010801.

(26) Cremers, V.; Puurunen, R. L.; Dendooven, J. Conformality in Atomic Layer Deposition: Current Status Overview of Analysis and Modelling. *Appl. Phys. Rev.* **2019**, *6*, 021302.

(27) Gebhard, M.; Mai, L.; Banko, L.; Mitschker, F.; Hoppe, C.; Jaritz, M.; Kirchheim, D.; Zekorn, C.; de los Arcos, T.; Grochla, D.; Dahlmann, R.; Grundmeier, G.; Awakowicz, P.; Ludwig, A.; Devi, A. PEALD of SiO_2 and Al_2O_3 Thin Films on Polypropylene: Investigations of the Film Growth at the Interface, Stress, and Gas Barrier Properties of Dyads. *ACS Appl. Mater. Interfaces* **2018**, *10*, 7422−7434

(28) Dementyev, P.; Wilke, T.; Naberezhnyi, D.; Emmrich, D.; Gölzhäuser, A. Vapour Permeation Measurements with Free-standing Nanomembranes. *Phys. Chem. Chem. Phys.* **2019**, *21*, 15471-15477.

(29) Yang, B.; Kaden, W. E.; Yu, X.; Boskoboinik, J. A.; Martynova, Y.; Lichtenstein, L.; Heyde, M.; Sterrer, M.; Włodarczyk, R.; Sierka, M.; Sauer, J.; Shaikhutdinov, S.; Freund, H.-J. Thin Silica Films on Ru(0001): Monolayer, Bilayer, and Three-Dimensional Networks of [SiO_4] Tetrahedra. *Phys. Chem. Chem. Phys.* **2012**, *14*, 11344–11351.

(30) Dingemans, G.; van Helvoirt, C. A. A.; van de Sanden, M. C. M.; Kessels, W. M. M. Plasma-Assisted Atomic Layer Deposition of Low Temperature SiO_2. *ECS Transactions* **2011**, *35*, 191-204.

(31) Naberezhnyi, D.; Park, S. W.; Li, W.; Westphal, M.; Feng. X.; Dong. R.; Dementyev, P. Mass Transfer in Boronate Ester 2D COF Single Crystals. *Small* **2021**, 2104392.

(32) Jhang, J.-H.; Altman, E. I. Water Chemistry on Two-Dimensional Silicates Studied by Density Functional Theory and Temperature-Programmed Desorption. *Surf. Sci.* **2019**, *679*, 99-109.

Supporting Information

Molecular Permeation in Freestanding Bilayer Silica

Daniil Naberezhnyi,[†] Lukas Mai,[‡] Nassar Doudin,[§] Inga Ennen,[†] Andreas Hütten,[†] Eric I. Altman,*[,§] Anjana Devi,*[,‡] Petr Dementyev*[,†]

[†]*Faculty of Physics, Bielefeld University, 33615 Bielefeld, Germany*

[‡]*Inorganic Materials Chemistry, Ruhr University Bochum, 44801 Bochum, Germany*

[§]*Department of Chemical and Environmental Engineering, Yale University, New Haven, Connecticut 06520, United States*

Corresponding Authors

*** dementyev@physik.uni-bielefeld.de**

*** anjana.devi@ruhr-uni-bochum.de**

*** eric.altman@yale.edu**

KEYWORDS: bilayer silica, two-dimensional membranes, atomic layer deposition, gas permeation, adsorption

Contents

I. Materials preparation

ALD

300-nm gold films on mica (Georg Albert PVD) were used for both ALD and MBE growth. PEALD of SiO_2 was performed in a custom-built shower head PEALD reactor (modular flow) using a direct 13.56 MHz electron cyclotron wave resonance (ECWR) oxygen plasma. The substrate was placed on a grounded substrate holder between two antennas for the ignition of the plasma and was heated to 60, 150 or 240 °C, depending on the experiment. The bis(diethylamino)silane (BDEAS) precursor was filled in a stainless-steel cartridge heated to 45 °C and was pulsed without carrier gas. Argon (AirLiquide, 99.999%) with a flow of 25 sccm was used for purging, and oxygen (AirLiquide, 99.995%) with a flow of 25 sccm was used during the plasma pulse. All depositions were performed with a plasma power of 200 W. The base pressure of the reactor was 5×10^{-4} mbar. Prior to the deposition the Au/mica substrates were exposed to 10 oxygen plasma pulses of 150 ms with a gap of 850 ms vacuum in between the plasma pulses. Afterwards, the ALD process for deposition was performed. The exact ALD cycle pulse/purge times can be found elsewhere.[1] The applied amount of ALD cycles in the experiments was varied between 1 and 22.

MBE

MBE growth of 2D SiO_2 was conducted in an ultrahigh vacuum (UHV) chamber described elsewhere.[2,3] An effusion cell containing SiO as a silica source (DCA Instruments) was used to sublime SiO onto Au/mica held at room temperature. The deposition was done in 2.7×10^{-6} mbar O_2. The deposition rate was determined with a quartz crystal microbalance (QCM, Leybold Inficon, XTC). The deposition time was set to reach the 1.64×10^{15} SiO/cm^2 coverage needed to completely cover the surface in a crystalline silica bilayer with a 5.3 Å lattice constant.[3,4] Prior to SiO deposition, the Au surface was cleaned by cycles of 1 keV Ar ion sputtering and annealing in UHV at 850 K until no impurities could be detected by Auger electron spectroscopy (AES, Perkin-Elmer 20-810). Following deposition, the surface was annealed in 2×10^{-6} torr O_2 at 575 K to insure complete oxidation to SiO_2 before removal from the system for final annealing at ambient pressure as described below. AES confirmed the complete oxidation to SiO_2.[3]

Annealing and transfer

The Au/mica substrates with SiO_2 deposits were placed onto a preheated quartz crucible and annealed in a tube furnace (Carbolite Gero GmbH, Germany) in air for 30 min. The annealing temperature was varied between 950 and 1000 K in order to obtain most intense IRAS signals in the range 1250-1290 cm^{-1}. The annealed SiO_2 films on Au/mica substrates were sequentially spin-coated with 50K and 950K poly(methyl methacrylate) (PMMA) dissolved in ethyl acetate using a spinner WS-400B (Laurell Technologies). The PMMA-covered samples were cut into smaller pieces and let floating onto the surface of I_2/KI aqueous solution (mass ratio I_2 : KI : H_2O = 1 : 4 : 40) for two days. Once the underlying gold layers were fully etched away, the PMMA/SiO_2 films were detached from mica and carried over to Milli-Q water for rinsing. The clean PMMA/SiO_2 films were transferred either onto TEM grids (Quantifoil) for imaging or onto Si_3N_4/Si chips with single orifices of around 2 µm in diameter (Silson Ltd) for permeation measurements. Afterwards, the TEM grids and Si_3N_4/Si chips were immersed in acetone (Fisher Chemicals, 99.8 %, analytical reagent grade) for 1 hour to remove the PMMA layers.

II. Materials characterization

IRAS

IRAS spectra of SiO_2 on native Au/mica substrates were recorded in a FTIR spectrometer VERTEX 70 (Bruker) coupled with a polarization-modulation accessory PMA50 (Bruker). The spectrometer was constantly purged with dry nitrogen at 3 L min^{-1}. The MCT detector was cooled down with liquid nitrogen. The beam polarization was modulated by a ZnSe photoelastic modulator PEM-90 (Hinds Instruments) in conjunction with a lock-in amplifier SR830 (Stanford Research Systems) to determine reflected signals from the substrate. The spectra for each sample were averaged over 250 scans at resolution of 4 cm^{-1}. Background correction was performed in OPUS software from Bruker.

XPS

XPS spectra were taken in a Multiprobe system (Omicron) with a monochromatic X-ray source (Al K_α, 1486.7 eV) and a hemispherical electron analyzer (SPHERA) in a constant-analyser-energy (CAE) mode. The scan parameters were as follows: pass energy of 25 eV, scanning step of 0.05 eV, dwell time of 0.2 s. The number of scans was taken depending on the noise level: 20 scans for Si2p, 5 scans for O1s, 1 scan for Au4f.

The data were evaluated with CasaXPS software. The binding energy scale was calibrated relative to $Au4f_{7/2}$ peak at 84.0 eV. The spectra were fitted by a sum of Gaussian/Lorentzian functions using linear backgrounds for Si2p, O1s, C1 lines. Asymmetric sum of Gaussian/Lorentzian functions and Shirley background were applied to fit Au4f lines.

TEM

The 2D silica films transferred onto Quantifoil TEM grids were investigated in a JEM 2200FS microscope from JEOL operated at 200kV. Special care was taken to reduce the electron dose in order to prevent beam damage of the silica films. The images were recorded with the CMOS camera “OneView” from GATAN.

III. Permeation measurements

The permeation measurements were carried out in a custom-made setup as detailed elsewhere.[5] The experimental apparatus is illustrated schematically in **Figure S1**. The Si_3N_4/Si chips with suspended bilayer silica were glued with epoxy glue onto UHV-compatible Cu discs. The sample assembly was then mounted into conflat flanges ensuring a leak-tight fixture (membrane cell). Thereby, freestanding bilayer silica was positioned between the high-vacuum detection chamber (base pressure of $2\cdot10^{-9}$ mbar) and the mixing chamber (base pressure $< 1\cdot10^{-3}$ mbar). The mixing chamber was used to feed the 2D membrane with gases and vapors of interest as controlled by the capacitance manometer (MKS Instruments). The permeating molecules were detected with a quadrupole mass-spectrometer (Hiden Analytical). Helium (≥ 99.996 %), neon (≥ 99.995 %), nitrogen (≥ 99.8 %), carbon dioxide (≥ 99.5 %), argon (≥ 99.998 %), krypton (≥ 99.99 %), xenon (≥ 99.99 %), sulfur hexafluoride (≥ 99.9 %) were supplied by Linde. Heavy water (Sigma-Aldrich, 99.9% atom D), 1-propanol (CHEMOSOLUTE, 99.5 %, for analysis), methyl isobutyl ketone (Merck, 99%, for extraction analysis), 1-octene (Acros Organics, 99 %) were repeatedly degassed before use. Their saturation vapor pressure in the mixing chamber at room temperature (22.3 ± 0.5 °C) was determined to be as follows: 22.4 ± 0.4 mbar for heavy water, 22.6 ± 0.4 mbar for 1-propanol, 23.1 ± 0.3 mbar for methyl isobutyl ketone, 19.8 ± 0.4 mbar for 1-octene. Calibration signals were recorded in each experiment upon supplying the gas or vapor concerned to the reference cell while the membrane cell was evacuated with a turbomolecular pump (the pumping lines are not shown for simplicity). The reference was a 110 nm-sized aperture in a Si_3N_4/Si chip fixed on a copper disc similar to the membrane sample.

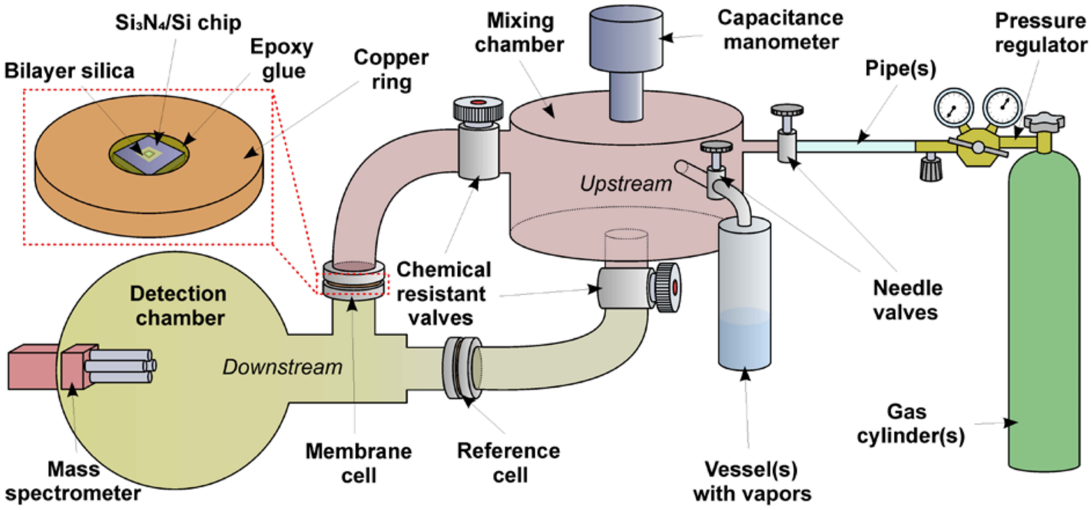

Figure S1. Schematic of the permeation apparatus.

IV. Contact angle measurements

Static contact angle measurements on 2D SiO_2 grown on Au/mica and on clean Au/mica for comparison were done with a handmade construction consisting of a steel substrate, tracing paper, lantern, and a CCD image sensor with a zoom lens (OPTEM ZOOM 70XL). Milli-Q water, 1-propanol (CHEMOSOLUTE, 99.5 %, for analysis), methyl isobutyl ketone (Merck, 99%, for extraction analysis), 1-octene (Acros Organics, 99 %) were probed upon dropping 3 µL of the liquid onto the sample using a micropipette (Gilson) fixed by a clamp stand. Photographs were taken 1 minute after placing the drop on the surface. The organic solvents spread instantly over both bilayer silica and gold surfaces meaning a zero contact angle. Dropping of water was carried out at least 5 times. Each droplet was washed away with Milli-Q water and dried with nitrogen flow. ImageJ software was used to estimate the contact angle from the photographs.

V. Adsorption measurements

Vapor adsorption measurements were performed in a reaction chamber Refractor™ from Harrick Scientific Products as described elsewhere.[6] Briefly, the reaction chamber carrying a 2D SiO_2/Au/mica substrate was positioned into the PM-IRAS spectrometer (Bruker) and coupled to a vacuum system as shown in **Figure S2**. The reaction chamber was evacuated down to ~$1\cdot10^{-3}$ mbar and filled with the vapors of interest up to a certain pressure as determined with a Baratron capacitance manometer (MKS Instruments). Heavy water (Sigma-Aldrich, 99.9% atom D), 1-propanol (CHEMOSOLUTE, 99.5 %, for analysis), methyl isobutyl ketone (Merck, 99%, for extraction analysis) held in stainless steel containers were thoroughly outgassed before use. IRAS spectra of the adsorbates were taken as a function of the vapor pressure. Each measurement consisted of 500 scans acquired with resolution of 4 cm^{-1}.

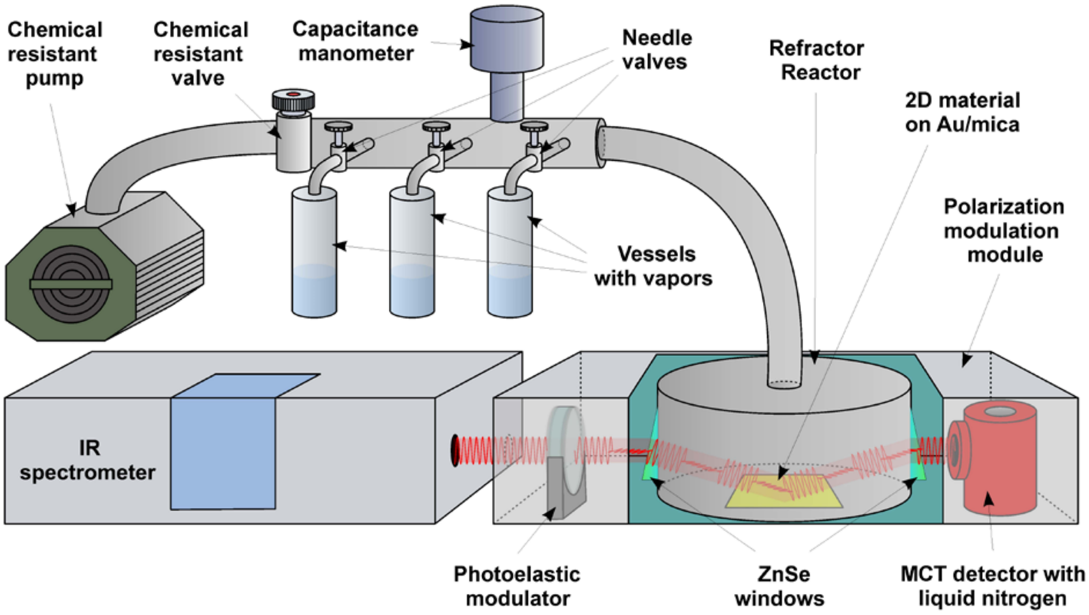

Figure S2. Schematic of the adsorption apparatus.

VI. IRAS spectra

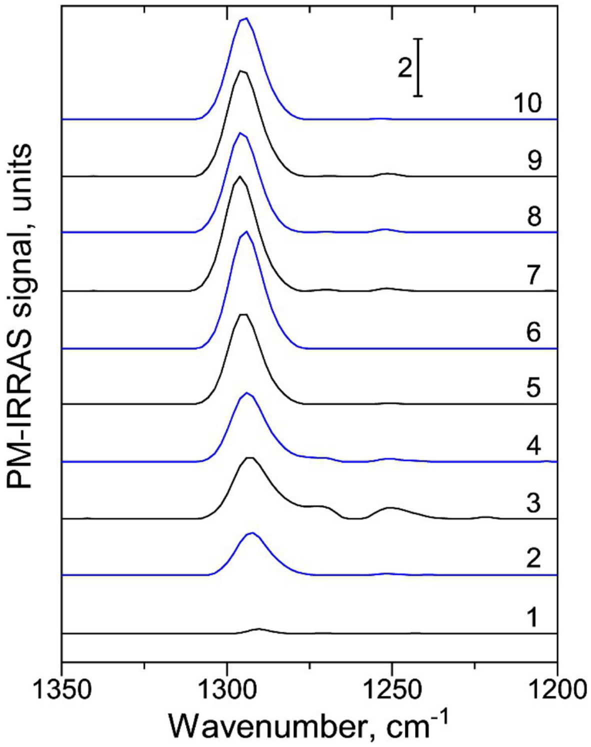

Figure S3. PM IRAS of SiO_2 grown with ALD on Au/mica at 240 °C substrate temperature depending on the number of cycles applied.

VII. XPS spectra

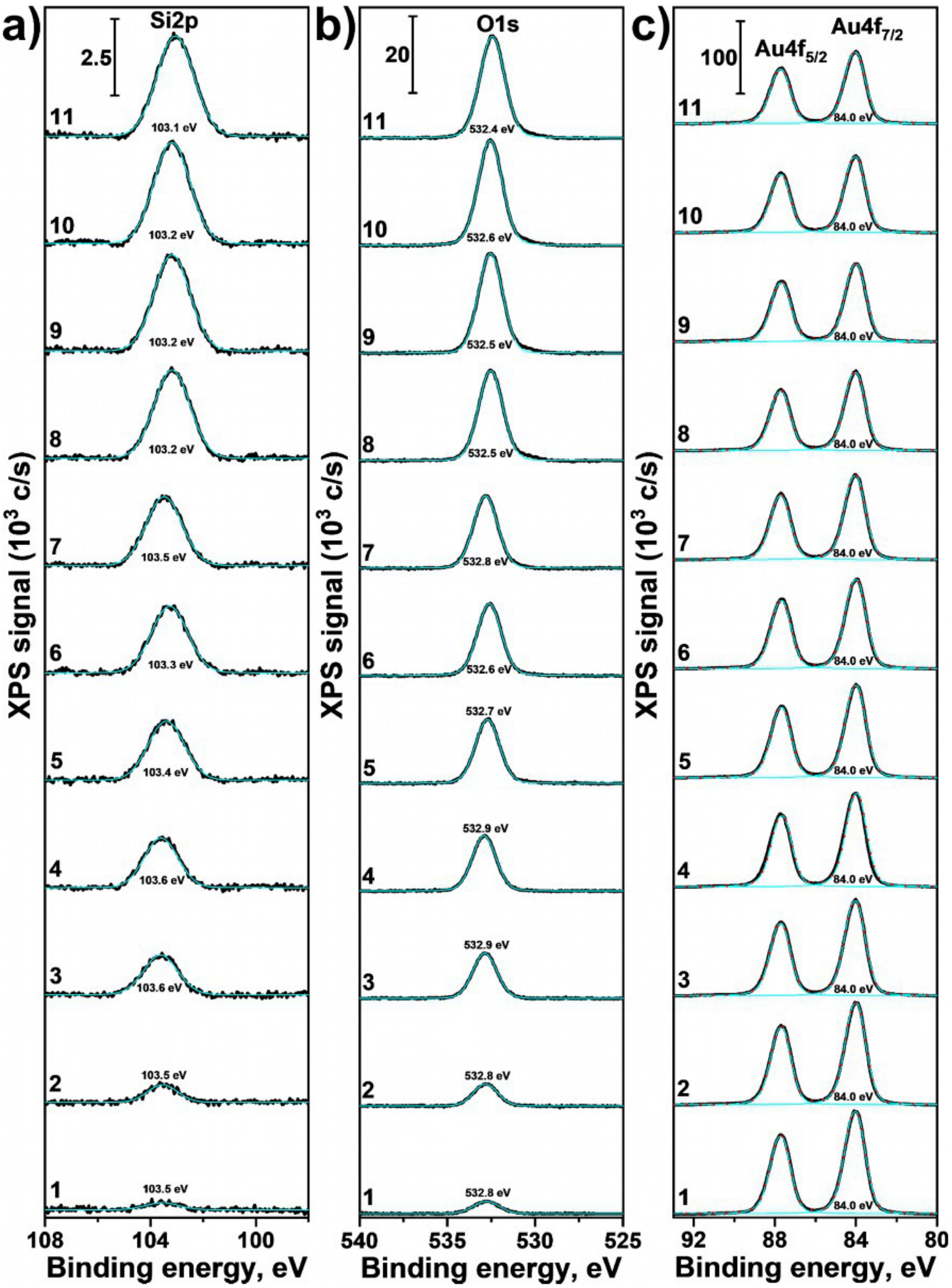

Figure S4. XPS spectra of SiO_2 grown with ALD on Au/mica at 60 °C substrate temperature depending on the number of cycles applied (1-11): a) silicon; b) oxygen; c) gold. The black lines are the raw spectra, the cyan lines are the fitted peaks, the red dot lines are the envelopes.

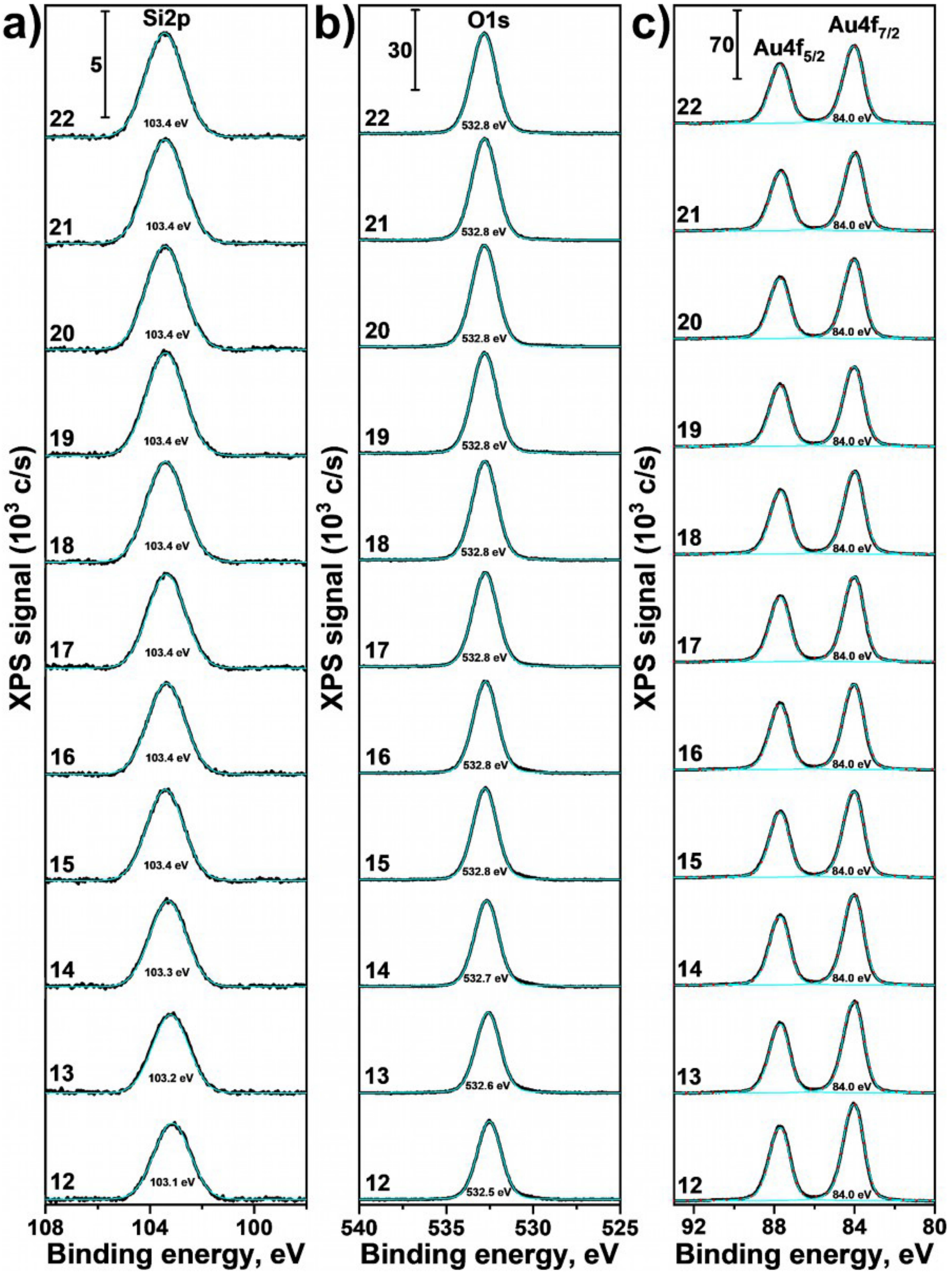

Figure S5. XPS spectra of SiO_2 grown with ALD on Au/mica at 60 °C substrate temperature depending on the number of cycles applied (12-22): a) silicon; b) oxygen; c) gold. The black lines are the raw spectra, the cyan lines are the fitted peaks, the red dot lines are the envelopes.

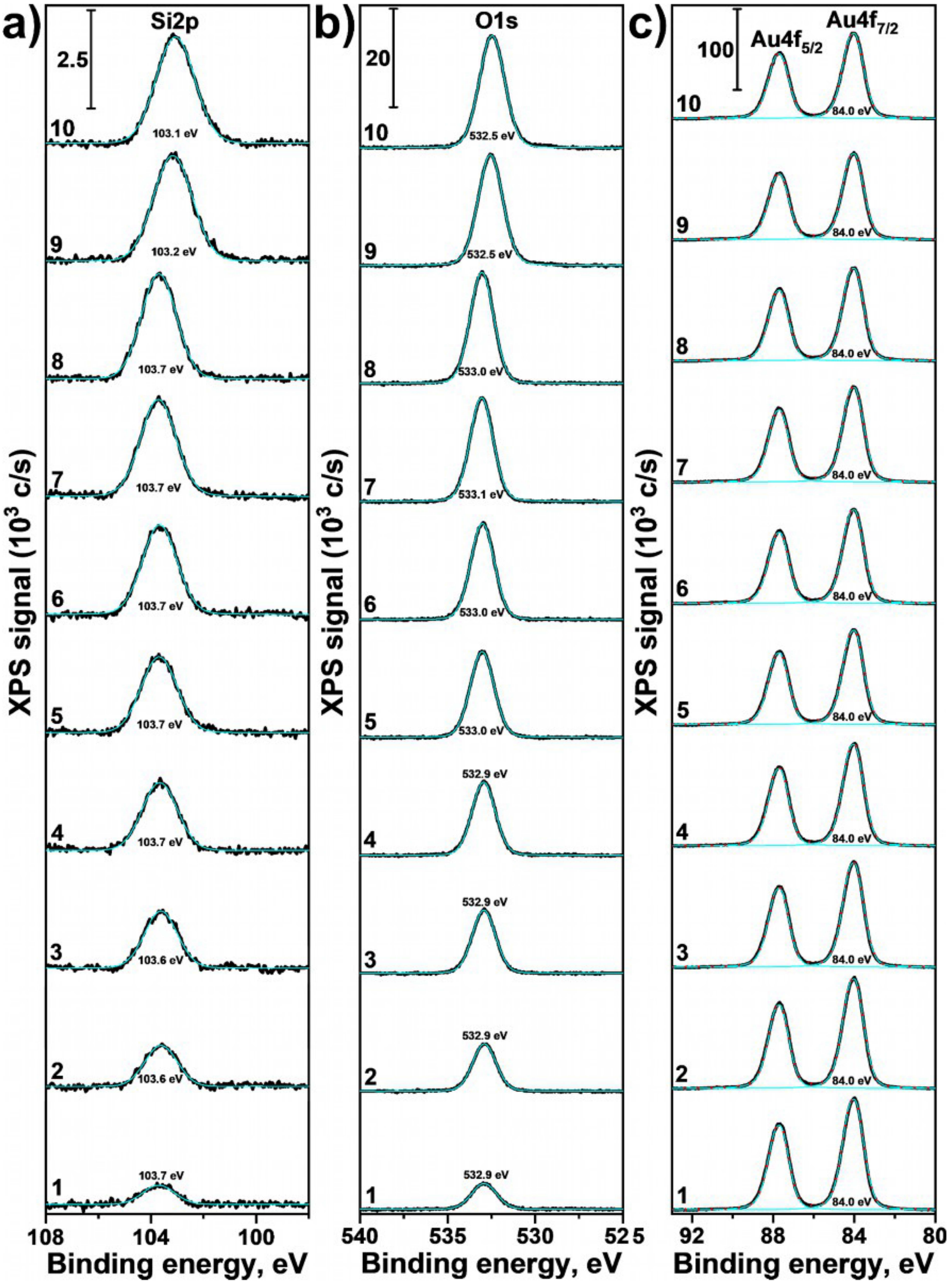

Figure S6. XPS spectra of SiO_2 grown with ALD on Au/mica at 150 °C substrate temperature depending on the number of cycles applied (1-10): a) silicon; b) oxygen; c) gold. The black lines are the raw spectra, the cyan lines are the fitted peaks, the red dot lines are the envelopes.

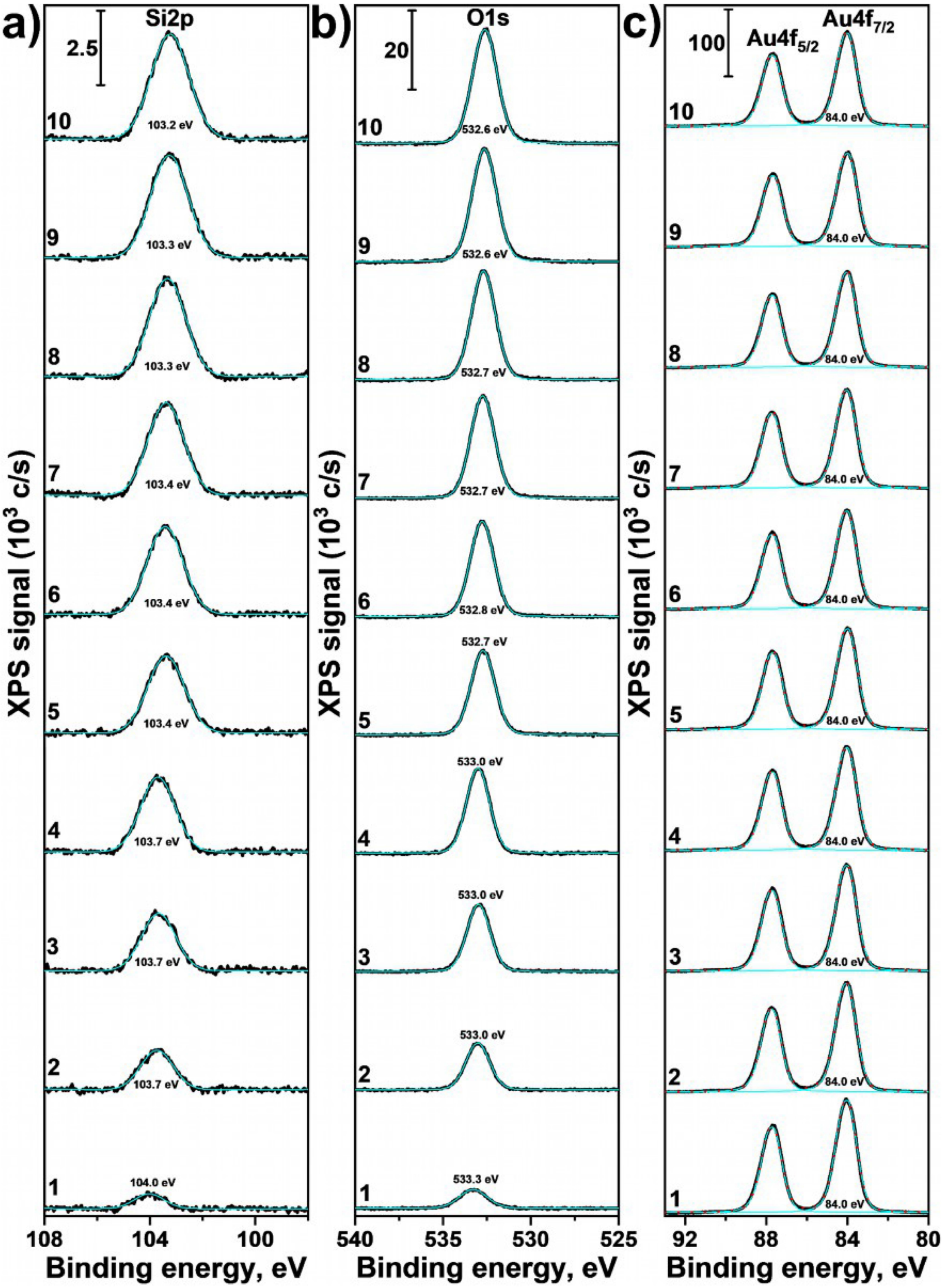

Figure S7. XPS spectra of SiO_2 grown with ALD on Au/mica at 240 °C substrate temperature depending on the number of cycles applied (1-10): a) silicon; b) oxygen; c) gold. The black lines are the raw spectra, the cyan lines are the fitted peaks, the red dot lines are the envelopes.

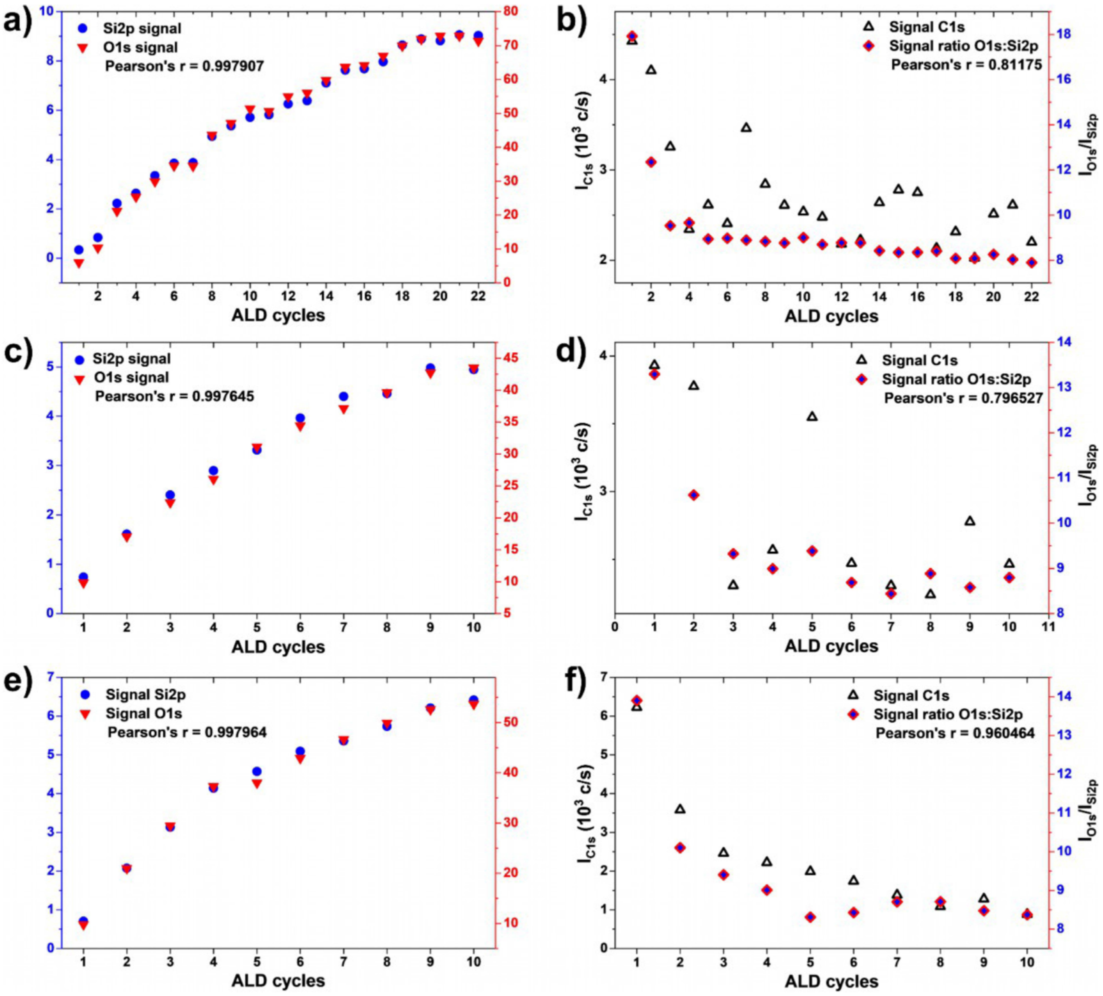

Figure S8. Integral XPS of SiO_2 grown with ALD on Au/mica at different deposition temperatures: a) 60 °C, Si2p and O1s signals; b) 60 °C, C1s signal and O1s:Si2p ratio; c) 150 °C, Si2p and O1s signals; d) 150 °C, C1s signal and O1s:Si2p ratio; e) 240 °C, Si2p and O1s signals; f) 240 °C, C1s signal and O1s:Si2p ratio.

The Si2p doublets ($Si2p_{3/2}$ and $Si2p_{1/2}$) were not resolved that is typical for fully oxidized silicon.[7] The Si2p and O1s spectra were fitted by a single peak. The Au4f doublets (section c in **Figures S4-7**) were exponentially attenuated as the number of cycles increased regardless of the deposition temperature. Differential charging and peak shifts were not revealed even after 22 ALD cycles. Judging by the IRAS spectra of silica grown at 60 °C (Figure 2a), a bulk phase was formed after 14 ALD cycles (**Figure S5**). Binding energies of 103.4 eV for Si2p and 532.8 eV for O1s correspond to Si^{4+} in the lattice of SiO_2.[8] The bilayer phase was receding from 8 to 13 ALD cycles according to the IRAS data. A slight decrease in the oxidation state of silicon (103.1 – 103.2 eV for Si2p) at these stages might be explained by the presence of multiple edge atoms on the particles of bulk silica before they coalesce into a continuous film. It is evident from **Figures S8a, S8c, S8e** that the XPS signals of silicon and oxygen strongly correlate as the number of ALD cycles increases that is in agreement with SiO_2 stoichiometry. However, for first few cycles the O1s:Si2p ratio (**Figures S8b, S8d, S8f)** was found to change which is explained by the presence of oxygen-containing carbonaceous species as carbon contamination is known to be typical for ALD processes.

References

1. Gebhard, M.; Mai, L.; Banko, L.; Mitschker, F.; Hoppe, C.; Jaritz, M.; Kirchheim, D.; Zekorn, C.; de los Arcos, T.; Grochla, D.; Dahlmann, R.; Grundmeier, G.; Awakowicz, P.; Ludwig, A.; Devi, A. PEALD of SiO_2 and Al_2O_3 Thin Films on Polypropylene: Investigations of the Film Growth at the Interface, Stress, and Gas Barrier Properties of Dyads. *ACS Appl. Mater. Interfaces* **2018**, *10*, 7422−7434.

2. Nakakura, C. Y.; Phanse, V. M.; Zheng, G.; Bannon, G.; Altman, E. I.; Lee, K. P. A High-Speed Variable-Temperature Ultrahigh Vacuum Scanning Tunneling Microscope. *Rev. Sci. Instrum*. **1998**, *69*, 3251-3258.

3. Jhang, J.-H.; Zhou, C.; Dagdeviren, O.E.; Schwarz, U.D.; Altman, E. I. Growth of Two-Dimensional Silica and Aluminosilicate Bilayers on Pd(111): From Incommensurate to Commensurate Crystalline. *Phys. Chem. Chem. Phys.* **2017**, *19*, 14001-14011.

4. Huang, P. Y.; Kurasch, S.; Srivastava, A.; Skakalova, V.; Kotakoski, J.; Krasheninnikov, A. V.; Hovden, R.; Mao, Q.; Meyer, J. C.; Smet, J.; Muller, D. A.; Kaiser, U. Direct Imaging of a Two-Dimensional Silica Glass on Graphene. *Nano Lett.* **2012**, *12*, 1081-1086.

5. Dementyev, P.; Wilke, T.; Naberezhnyi, D.; Emmrich, D.; Gölzhäuser, A. Vapour Permeation Measurements with Free-standing Nanomembranes. *Phys. Chem. Chem. Phys.* **2019**, *21*, 15471-15477.

6. Dementyev, P.; Khayya, N.; Kreie, J.; Gölzhäuser, A. Vapor Adsorption Measurements with Two-Dimensional Membranes. *Submitted to ChemPhysChem* **2021**.

7. Mitchell, D. F.; Clark, K. B.; Bardwell, J. A.; Lennard, W. N.; Massoumi, G. R.; Mitchell, I. V. Film thickness measurements of SiO_2 by XPS. *Surf. Interface Anal.* **1994**, *21*, 44-50.

8. Wang, T.-H.; Gole, J. L.; White, M. G.; Watkins, C.; Street, S. C.; Fang, Z.; Dixon, D. A. The surprising oxidation state of fumed silica and the nature of water binding to silicon oxides and hydroxides. *Chem. Phys. Lett.* **2011**, *501*, 159-165.

7 Summary and conclusions

As two-dimensional membranes are believed to ensure high permeation rates and molecular sieving selectivity, this thesis explored the transport of gaseous species in three types of intrinsically microporous planar nanomaterials with various pore morphologies. Carbon nanomembranes (CNMs) with an areal pore density of 6 × 10^{13} cm^{-2} were prepared from self-assembled aromatic precursors via electron-induced cross-linking. While the pore geometry in CNMs is tortuous exhibiting the size distribution from 0.4 to 1.1 nm, 2D covalent-organic frameworks (COFs) feature straight uniform pores of less than 2 nm in lateral dimensions. The boronate ester COF crystallites were synthesized from monomers at the air-water interface resulting in the areal pore density of 1.5 × 10^{13} cm^{-2}. In turn atomic layer deposition was used to obtain bilayer silica (BS) displaying a vitreous crystal structure with the areal pore density of 4 × 10^{14} cm^{-2}. The pore size in BS ranges from 0.06 to 0.46 nm whereas the most frequent hexagonal pores correspond to 0.19 nm.

The 2D membranes were suspended over individual apertures of few micrometers in diameter and inserted into a cutting-edge permeation facility. The high pore densities in the free-standing layers allowed for direct permeation measurements with a wide range of molecular species, including vaporous substances. The pioneering experiments with organic vapors enabled systematic variation of the size as well as the surface affinity of the permeating particles which is inaccessible with ordinary gases under ambient conditions. In particular, exposing the membranes to saturated vapors was used to populate their surface with physisorbed molecules and to probe the effect of adsorption-mediated diffusion. Comparative analysis of the absolute permeation rates determined in well-controlled environments provided mechanistic insights into the performance of the 2D membranes.

The atmospheric and noble gases from helium to xenon were found to readily pass the 2D COF showing the permeance in the range of 10^{-3} $mol \cdot s^{-1} \cdot m^{-2} \cdot Pa^{-1}$. The free molecular flow observed yielded the record membrane porosity of 40 % and was consistent with the pore morphology as the openings in the framework material were many times larger than the gaseous molecules. In contrast, the sub-nanometer pores in BS were demonstrated to be hardly permeable for the inert gases translating into flow rates below the limits of detection. Only the smallest helium atoms revealed the permeance around 2 × 10^{-8} $mol{\cdot}s^{-1}{\cdot}m^{-2}{\cdot}Pa^{-1}$ which contradicted early computational predictions on the molecular transport in 2D SiO_2. Despite the different pore configuration, very similar behavior was seen for CNMs that essentially blocked the permeation of gases except helium. While the CNMs performance could be explained by their tortuous pore morphology posing steric hindrance for gas molecules, the entrance probability in the smaller BS pores was speculated to depend on the incidence angle and appeared extremely low. It followed that the gas particles encountering both BS and CNMs were mostly bouncing back from the membrane without having a chance to cross it. In order to increase the residence time in the near-surface area, 2D membranes were for the first time covered with a layer of an ionic liquid. Thus, CNMs modified with a CO_2-philic ionic liquid were illustrated to enhance the permeation rate of dissolved carbon dioxide up to 2 × 10^{-9} $mol{\cdot}s^{-1}{\cdot}m^{-2}{\cdot}Pa^{-1}$.

Unlike inert gases, all three types of 2D membranes were shown to favor the permeation of vaporous substances, especially upon saturation. Water vapor was found to maintain its high permeance in CNMs of 1 × 10^{-4} $mol{\cdot}s^{-1}{\cdot}m^{-2}{\cdot}Pa^{-1}$ even in mixtures with other species giving rise to the membrane selectivity of more than 100. The permeation rates for other vapors revealed size dependence in agreement with the CNM's morphology. For example, the permeance of acetonitrile around 1 × 10^{-7} $mol{\cdot}s^{-1}{\cdot}m^{-2}{\cdot}Pa^{-1}$ was higher than that for larger molecules of toluene, chloroform, and tetrahydrofuran amounting to ~ 10^{-8} $mol{\cdot}s^{-1}{\cdot}m^{-2}{\cdot}Pa^{-1}$. Eventually complete rejection of elongated n-hexane molecules was achieved with CNMs highlighting sieving-like properties. A similar size exclusion effect was observed in vitreous 2D SiO_2 that did not transmit long 1-octene molecules. However, the simple geometric model failed at describing the transport of water, 1-propanol, and methyl isobutyl ketone with the permeation rates measured to be 5 × 10^{-5}, 2 × 10^{-5}, and 2 × 10^{-4} $mol{\cdot}s^{-1}{\cdot}m^{-2}{\cdot}Pa^{-1}$ respectively. Given the same driving force applied, the results were rationalized in terms of the adsorption energetics on BS that appeared to be the strongest for the bulkiest methyl isobutyl ketone molecules. The impact of the gas-surface interactions was also evident in vapor permeation experiments with the 2D COF membranes that displayed an increase in the transmembrane flux of homologous arene molecules compared to the ideal gas flow. The contribution of the adsorption-mediated transport led to the reverse selectivity order for benzene, toluene, and p-xylene which was correlated with their saturation points.

While the field of 2D membranes is dominated by artificially perforated graphene with poorly defined pore morphology, this work made use of the inherently porous structures and shed light on some of the basic aspects of the gas transport in 2D membranes. Molecular effusion was proved to take place in the pores larger than 1 nm, but the gas permeation in smaller pores appeared to be suppressed. When the pore dimensions are comparable to the size of molecules, the permeation of inert gases is no longer described by the kinetic theory. As regular gas molecules are very close in size, their efficient separation is unlikely feasible with pristine 2D membranes. On the other hand, the surface-mediated diffusion was always found to be pronounced for condensable species which is in line with the escape problem of statistical physics. It suggests that adsorbates have a higher probability to find a pore compared to gas-phase particles. Therefore, chemical functionalization towards specific gases seems to be a promising route in adjusting the membrane selectivity.

Bibliography

1 WHO Coronavirus (COVID-19) Dashboard | WHO Coronavirus (COVID-19) Dashboard With Vaccination Data, https://covid19.who.int/, (accessed May 4, 2021).

2 A. D. Usher, *Medical oxygen crisis: a belated COVID-19 response*, NLM (Medline), 2021, vol. 397.

3 COVID-19 Oxygen Needs Tracker | Market Dynamics | PATH, https://www.path.org/programs/market-dynamics/covid-19-oxygen-needs-tracker/, (accessed May 3, 2021).

4 J. A. Kent, in *Riegel's Handbook of Industrial Chemistry*, Springer US, Boston, MA, 2003, pp. 463–480.

5 S. Tesch, T. Morosuk and G. Tsatsaronis, in *Low-temperature Technologies*, IntechOpen, 2019, pp. 1–20.

6 Eurostat - Data Explorer, https://ec.europa.eu/eurostat/data/database, (accessed May 4, 2021).

7 F. G. Kerry, *Industrial gas handbook: Gas separation and purification*, 2007.

8 T. Banaszkiewicz and M. Chorowski, *Entropy*, 2018, **20**, 232.

9 Y. Ding, *Ind. Eng. Chem. Res.*, 2020, **59**, 556–568.

10 R. Sidhikku Kandath Valappil, N. Ghasem and M. Al-Marzouqi, *J. Ind. Eng. Chem.*, 2021, **98**, 103–129.

11 K. V. Agrawal, *Chimia (Aarau).*, 2018, **72**, 313–321.

12 L. Wang, M. S. H. Boutilier, P. R. Kidambi, D. Jang, N. G. Hadjiconstantinou and R. Karnik, *Nat. Nanotechnol.*, 2017, **12**, 509–522.

13 S. P. Koenig, L. Wang, J. Pellegrino and J. S. Bunch, *Nat. Nanotechnol.*, 2012, **7**, 728–732.

14 K. Celebi, J. Buchheim, R. M. Wyss, A. Droudian, P. Gasser, I. Shorubalko, J. Il Kye, C. Lee and H. G. Park, *Science*, 2014, **344**, 289–292.

15 K. P. Schlichting and D. Poulikakos, *ACS Appl. Mater. Interfaces*, 2020, **12**, 36468–36477.

16 J. P. Thiruraman, S. A. Dar, P. M. Das, N. Hassani, M. Neek-Amal, A. Keerthi, M. Drndić and B. Radha, *Sci. Adv.*, 2020, **6**, 7927–7945.

17 J. Liu, L. Jin, F. I. Allen, Y. Gao, P. Ci, F. Kang and J. Wu, *Nano Lett.*, 2021, **21**, 2183–2190.

18 P. Z. Sun, M. Yagmurcukardes, R. Zhang, W. J. Kuang and F. C. Wang, *arXiv:2104.02560*, 2021, 1–14.

19 M. S. H. Boutilier, D. Jang, J. C. Idrobo, P. R. Kidambi, N. G. Hadjiconstantinou and R. Karnik, *ACS Nano*, 2017, **11**, 5726–5736.

20 K. Choi, A. Droudian, R. M. Wyss, K.-P. Schlichting and H. G. Park, *Sci. Adv.*, 2018, **4**, eaau0476.

21 S. Huang, M. Dakhchoune, W. Luo, E. Oveisi, G. He, M. Rezaei, J. Zhao, D. T. L. Alexander, A. Züttel, M. S. Strano and K. V. Agrawal, *Nat. Commun.*, 2018, **9**, 2632.

22 J. Zhao, G. He, S. Huang, L. F. Villalobos, M. Dakhchoune, H. Bassas and K. V Agrawal, *Sci. Adv.*, 2019, **5**, eaav1851.

23 W.-C. Lee, L. Bondaz, S. Huang, G. He, M. Dakhchoune and K. V. Agrawal, *J. Memb. Sci.*, 2021, **618**, 118745.

24 A. Ebrahimi, M. Meratizaman, H. Akbarpour Reyhani, O. Pourali and M. Amidpour, *Energy*, 2015, **90**, 1298–1316.

25 A. Ebrahimi and M. Ziabasharhagh, *Energy*, 2017, **126**, 868–885.

26 S.-C. Hwang, R. D. Lein and D. A. Morgan, in *Kirk-Othmer Encyclopedia of Chemical Technology*, John Wiley & Sons, Inc., Hoboken, NJ, USA, 2005, vol.

85, pp. 523–527.

27 C. M. Yon and J. D. Sherman, in *Kirk-Othmer Encyclopedia of Chemical Technology*, Wiley, 2003, vol. 1.

28 R. W. Baker, *Membrane Technology and Applications*, John Wiley & Sons, Ltd, Chichester, UK, 2004.

29 T. Matsuura, *Synthetic Membranes and Membrane Separation Processes*, CRC Press, 1994.

30 M. Liu, P. A. Gurr, Q. Fu, P. A. Webley and G. G. Qiao, *J. Mater. Chem. A*, 2018, **6**, 23169–23196.

31 Robert Mortimer, *Physical Chemistry*, Academic Press, Third Edit., 2008.

32 L. M. Robeson, *J. Memb. Sci.*, 1991, **62**, 165–185.

33 L. M. Robeson, *J. Memb. Sci.*, 2008, **320**, 390–400.

34 D. S. Sholl and R. P. Lively, *Nature*, 2016, **532**, 435–437.

35 Z. Petrusová, K. Machanová, P. Stanovský and P. Izák, *Sep. Purif. Technol.*, 2019, **217**, 95–107.

36 P. Bernardo, E. Drioli and G. Golemme, *Ind. Eng. Chem. Res.*, 2009, **48**, 4638–4663.

37 Y. Zhao, Y. Xie, Z. Liu, X. Wang, Y. Chai and F. Yan, *Small*, 2014, **10**, 4521–4542.

38 E. Yang, A. B. Alayande, K. Goh, C. M. Kim, K. H. Chu, M. H. Hwang, J. H. Ahn and K. J. Chae, *Int. J. Hydrogen Energy*, 2021, **46**, 11389–11410.

39 H. B. Park, J. Kamcev, L. M. Robeson, M. Elimelech and B. D. Freeman, *Science*, 2017, **356**, 1138–1148.

40 K. S. Novoselov, A. K. Geim, S. V. Morozov, D. Jiang, Y. Zhang, S. V. Dubonos, I. V. Grigorieva and A. A. Firsov, *Science*, 2004, **306**, 666–669.

41 J. P. O. Bruce E. Poling, John M. Prausnitz, *THE PROPERTIES OF GASES AND LIQUIDS*, The McGraw-Hill Companies, New York, Fifth Edit., 2001.

42 P. Z. Sun, Q. Yang, W. J. Kuang, Y. V Stebunov, W. Q. Xiong, J. Yu, R. R. Nair, M. I. Katsnelson, S. J. Yuan, I. V Grigorieva, M. Lozada-Hidalgo, F. C. Wang and A. K. Geim, *Nature*, 2020, **579**, 229–232.

43 D. E. Jiang, V. R. Cooper and S. Dai, *Nano Lett.*, 2009, **9**, 4019–4024.

44 S. Blankenburg, M. Bieri, R. Fasel, K. Müllen, C. A. Pignedoli and D. Passerone, *Small*, 2010, **6**, 2266–2271.

45 J. Feng, M. Graf, K. Liu, D. Ovchinnikov, D. Dumcenco, M. Heiranian, V. Nandigana, N. R. Aluru, A. Kis and A. Radenovic, *Nature*, 2016, **536**, 197–200.

46 S. M. Gilbert, G. Dunn, A. Azizi, T. Pham, B. Shevitski, E. Dimitrov, S. Liu, S. Aloni and A. Zettl, *Sci. Rep.*, , DOI:10.1038/s41598-017-12684-x.

47 P. Masih Das, J. P. Thiruraman, Y. C. Chou, G. Danda and M. Drndić, *Nano Lett.*, 2019, **19**, 392–399.

48 M. Caglar, I. Silkina, B. T. Brown, A. L. Thorneywork, O. J. Burton, V. Babenko, S. M. Gilbert, A. Zettl, S. Hofmann and U. F. Keyser, *ACS Nano*, 2020, **14**, 2729–2738.

49 P. Cheng, M. M. Kelly, N. K. Moehring, W. Ko, A. P. Li, J. C. Idrobo, M. S. H. Boutilier and P. R. Kidambi, *Nano Lett.*, 2020, **20**, 5951–5959.

50 A. Turchanin and A. Gölzhäuser, *Adv. Mater.*, 2016, **28**, 6075–6103.

51 G. M. . Whitesides and B. Grzybowski, *Science*, 2002, **295**, 2418–2421.

52 J. C. Love, L. A. Estroff, J. K. Kriebel, R. G. Nuzzo and G. M. Whitesides, *Chem. Rev.*, 2005, **105**, 1103–1170.

53 A. J. Muscat, in *Encyclopedia of Interfacial Chemistry*, Elsevier, 2018, pp. 810–816.

54 A. Shaheen, J. M. Sturm, R. Ricciardi, J. Huskens, C. J. Lee and F. Bijkerk, *Langmuir*, 2017, **33**, 6419–6426.

55 L. Kankate, A. Turchanin and A. Gölzhäuser, *Langmuir*, 2009, **25**, 10435–10438.

56 S. Frey, V. Stadler, K. Heister, W. Eck, M. Zharnikov, M. Grunze, B. Zeysing and A. Terfort, *Langmuir*, 2001, **17**, 2408–2415.

57 C. Vericat, M. E. Vela, G. Benitez, P. Carro and R. C. Salvarezza, *Chem. Soc. Rev.*, 2010, **39**, 1805–1834.

58 D. G. Matei, H. Muzik, A. Gölzhäuser and A. Turchanin, *Langmuir*, 2012, **28**, 13905–13911.

59 P. Angelova, H. Vieker, N. E. Weber, D. Matei, O. Reimer, I. Meier, S. Kurasch, J. Biskupek, D. Lorbach, K. Wunderlich, L. Chen, A. Terfort, M. Klapper, K. Müllen, U. Kaiser, A. Gölzhäuser and A. Turchanin, *ACS Nano*, 2013, **7**, 6489–6497.

60 W. Geyer, V. Stadler, W. Eck, M. Zharnikov, A. Gölzhäuser and M. Grunze, *Appl. Phys. Lett.*, 1999, **75**, 2401–2403.

61 W. Eck, V. Stadler, W. Geyer, M. Zharnikov, A. Gölzhäuser and M. Grunze, *Adv. Mater.*, 2000, **12**, 805–808.

62 W. Geyer, V. Stadler, W. Eck, A. Gölzhäuser, M. Grunze, M. Sauer, T. Weimann and P. Hinze, *J. Vac. Sci. Technol. B Microelectron. Nanom. Struct.*, 2001, **19**, 2732.

63 A. Gölzhäuser, W. Eck, W. Geyer, V. Stadler, T. Weimann, P. Hinze and M. Grunze, *Adv. Mater.*, 2001, **13**, 803–806.

64 Y. Tai, A. Shaporenko, W. Eck, M. Grunze and M. Zharnikov, *Langmuir*, 2004, **20**, 7166–7170.

65 M. Zharnikov, W. Geyer, A. Gölzhäuser, S. Frey and M. Grunze, *Phys. Chem. Chem. Phys.*, 1999, **1**, 3163–3171.

66 R. Dalpke, Universität Bielefeld, 2020.

67 W. Eck, A. Küller, M. Grunze, B. Völkel and A. Gölzhäuser, *Adv. Mater.*, 2005, **17**, 2583–2587.

68 A. Turchanin, A. Beyer, C. T. Nottbohm, X. Zhang, R. Stosch, A. Sologubenko, J. Mayer, P. Hinze, T. Weimann and A. Gölzhäuser, *Adv. Mater.*, 2009, **21**, 1233–1237.

69 P. M. G. Van Deursen, Z. Tang, A. Winter, M. J. Mohn, U. Kaiser, A. A. Turchanin and G. F. Schneider, *Nanoscale*, 2019, **11**, 20785–20791.

70 D. Rhinow, J. Vonck, M. Schranz, A. Beyer, A. Gölzhäuser and N. Hampp, *Phys. Chem. Chem. Phys.*, 2010, **12**, 4345.

71 A. Turchanin, D. Käfer, M. El-Desawy, C. Wöll, G. Witte and A. Gölzhäuser, *Langmuir*, 2009, **25**, 7342–7352.

72 A. Turchanin, D. Weber, M. Büenfeld, C. Kisielowski, M. V. Fistul, K. B. Efetov, T. Weimann, R. Stosch, J. Mayer and A. Gölzhäuser, *ACS Nano*, 2011, **5**, 3896–3904.

73 D. Rhinow, N. E. Weber and A. Turchanin, *J. Phys. Chem. C*, 2012, **116**, 12295–12303.

74 T. Kyotani, N. Sonobe and A. Tomita, *Nature*, 1988, **331**, 331–333.

75 D. G. Matei, N. E. Weber, S. Kurasch, S. Wundrack, M. Woszczyna, M. Grothe, T. Weimann, F. Ahlers, R. Stosch, U. Kaiser and A. Turchanin, *Adv. Mater.*, 2013, **25**, 4146–4151.

76 A. Turchanin, M. El-Desawy and A. Gölzhäuser, *Appl. Phys. Lett.*, 2007, **90**, 1–4.

77 J. J. Munro, S. Harrison, M. M. Fujimoto and J. Tennyson, *J. Phys. Conf. Ser.*, 2012, **388**, 012013.

78 M. Schnietz, A. Turchanin, C. T. Nottbohm, A. Beyer, H. H. Solak, P. Hinze, T.

Weimann and A. GOlzhauser, *Small*, 2009, **5**, 2651–2655.

79 A. Turchanin and A. Gölzhäuser, *Prog. Surf. Sci.*, 2012, **87**, 108–162.

80 X. Zhang, H. Vieker, A. Beyer and A. Gölzhäuser, *Beilstein J. Nanotechnol.*, 2014, **5**, 188–194.

81 X. Zhang, M. Mainka, F. Paneff, H. Hachmeister, A. Beyer, A. Gölzhäuser and T. Huser, *Langmuir*, 2018, **34**, 2692–2698.

82 P. Cabrera-Sanfelix, A. Arnau and D. Sánchez-Portal, *Phys. Chem. Chem. Phys.*, 2010, **12**, 1578–1584.

83 A. Mrugalla and J. Schnack, *Beilstein J. Nanotechnol.*, 2014, **5**, 865–871.

84 C. T. Toh, H. Zhang, J. Lin, A. S. Mayorov, Y. P. Wang, C. M. Orofeo, D. B. Ferry, H. Andersen, N. Kakenov, Z. Guo, I. H. Abidi, H. Sims, K. Suenaga, S. T. Pantelides and B. Özyilmaz, *Nature*, 2020, **577**, 199–203.

85 Y. Yang, P. Dementyev, N. Biere, D. Emmrich, P. Stohmann, R. Korzetz, X. Zhang, A. Beyer, S. Koch, D. Anselmetti and A. Gölzhäuser, *ACS Nano*, 2018, **12**, 4695–4701.

86 C. Neumann, M. Szwed, M. Frey, Z. Tang, K. Kozieł, P. Cyganik and A. Turchanin, *ACS Appl. Mater. Interfaces*, 2019, **11**, 31176–31181.

87 X. Zhang, A. Beyer and A. Gölzhäuser, *Beilstein J. Nanotechnol.*, 2011, **2**, 826–833.

88 X. Zhang, C. Neumann, P. Angelova, A. Beyer and A. Gölzhäuser, *Langmuir*, 2014, **30**, 8221–8227.

89 M. Ai, S. Shishatskiy, J. Wind, X. Zhang, C. T. Nottbohm, N. Mellech, A. Winter, H. Vieker, J. Qiu, K. J. Dietz, A. Gölzhäuser and A. Beyer, *Adv. Mater.*, 2014, **26**, 3421–3426.

90 Y. Yang, R. Hillmann, Y. Qi, R. Korzetz, N. Biere, D. Emmrich, M. Westphal, B. Büker, A. Hütten, A. Beyer, D. Anselmetti and A. Gölzhäuser, *Adv. Mater.*, ,

DOI:10.1002/adma.201907850.

91 R. Dalpke, A. Dreyer, R. Korzetz, K. J. Dietz and A. Beyer, *J. Phys. Chem. Lett.*, 2020, **11**, 6737–6741.

92 E. Griffin, L. Mogg, G. P. Hao, G. P. Hao, G. Kalon, G. Kalon, C. Bacaksiz, G. Lopez-Polin, G. Lopez-Polin, T. Y. Zhou, V. Guarochico, J. Cai, C. Neumann, A. Winter, M. Mohn, J. H. Lee, J. Lin, J. Lin, U. Kaiser, I. V. Grigorieva, K. Suenaga, B. Özyilmaz, H. M. Cheng, H. M. Cheng, W. Ren, A. Turchanin, F. M. Peeters, A. K. Geim and M. Lozada-Hidalgo, *ACS Nano*, 2020, **14**, 7280–7286.

93 S. Rajendran, Z. Tang, A. George, A. Cannon, C. Neumann, A. Sawas, E. Ryan, A. Turchanin and L. M. R. Arava, *Adv. Energy Mater.*, 2021, **11**, 2100666.

94 K. Geng, T. He, R. Liu, S. Dalapati, K. T. Tan, Z. Li, S. Tao, Y. Gong, Q. Jiang and D. Jiang, *Chem. Rev.*, 2020, **120**, 8814–8933.

95 A. Schneemann, R. Dong, F. Schwotzer, H. Zhong, I. Senkovska, X. Feng and S. Kaskel, *Chem. Sci.*, 2021, **12**, 1600–1619.

96 M. S. Lohse and T. Bein, *Adv. Funct. Mater.*, 2018, **28**, 1705553.

97 Y. Tian, S. Q. Xu, C. Qian, Z. F. Pang, G. F. Jiang and X. Zhao, *Chem. Commun.*, 2016, **52**, 11704–11707.

98 A. M. Pütz, M. W. Terban, S. Bette, F. Haase, R. E. Dinnebier and B. V. Lotsch, *Chem. Sci.*, 2020, **11**, 12647–12654.

99 H. Sahabudeen, H. Qi, B. A. Glatz, D. Tranca, R. Dong, Y. Hou, T. Zhang, C. Kuttner, T. Lehnert, G. Seifert, U. Kaiser, A. Fery, Z. Zheng and X. Feng, *Nat. Commun.*, 2016, **7**, 1–8.

100 A. P. Côté, A. I. Benin, N. W. Ockwig, M. O. O'Keeffe, A. J. Matzger and O. M. Yaghi, *Science*, 2005, **310**, 1166–1170.

101 L. Grill, M. Dyer, L. Lafferentz, M. Persson, M. V. Peters and S. Hecht, *Nat. Nanotechnol.*, 2007, **2**, 687–691.

102 M. In't Veld, P. Iavicoli, S. Haq, D. B. Amabilino and R. Raval, *Chem. Commun.*, 2008, 1536.

103 N. A. A. Zwaneveld, R. Pawlak, M. Abel, D. Catalin, D. Gigmes, D. Bertin and L. Porte, *J. Am. Chem. Soc.*, 2008, **130**, 6678–6679.

104 J. W. Colson, A. R. Woll, A. Mukherjee, M. P. Levendorf, E. L. Spitler, V. B. Shields, M. G. Spencer, J. Park and W. R. Dichtel, *Science*, 2011, **332**, 228–231.

105 R. Dong, T. Zhang and X. Feng, *Chem. Rev.*, 2018, **118**, 6189–6325.

106 X. Shi, D. Ma, F. Xu, Z. Zhang and Y. Wang, *Chem. Sci.*, 2020, **11**, 989–996.

107 I. Berlanga, M. L. Ruiz-González, J. M. González-Calbet, J. L. G. Fierro, R. Mas-Ballesté and F. Zamora, *Small*, 2011, **7**, 1207–1211.

108 A. P. Côté, H. M. El-Kaderi, H. Furukawa, J. R. Hunt and O. M. Yaghi, *J. Am. Chem. Soc.*, 2007, **129**, 12914–12915.

109 G. Das, F. Benyettou, S. K. Sharama, T. Prakasam, F. Gándara, V. A. De La Peña-O'Shea, N. Saleh, R. Pasricha, R. Jagannathan, M. A. Olson and A. Trabolsi, *Chem. Sci.*, 2018, **9**, 8382–8387.

110 B. P. Biswal, S. Chandra, S. Kandambeth, B. Lukose, T. Heine and R. Banerjee, *J. Am. Chem. Soc.*, 2013, **135**, 5328–5331.

111 S. Chandra, S. Kandambeth, B. P. Biswal, B. Lukose, S. M. Kunjir, M. Chaudhary, R. Babarao, T. Heine and R. Banerjee, *J. Am. Chem. Soc.*, 2013, **135**, 17853–17861.

112 Y. Zhu, X. Chen, Y. Cao, W. Peng, Y. Li, G. Zhang, F. Zhang and X. Fan, *Chem. Commun.*, 2019, **55**, 1434–1437.

113 M. A. Khayum, S. Kandambeth, S. Mitra, S. B. Nair, A. Das, S. S. Nagane, R. Mukherjee and R. Banerjee, *Angew. Chemie - Int. Ed.*, 2016, **55**, 15604–15608.

114 D. N. Bunck and W. R. Dichtel, *J. Am. Chem. Soc.*, 2013, **135**, 14952–14955.

115 S. Wang, Q. Wang, P. Shao, Y. Han, X. Gao, L. Ma, S. Yuan, X. Ma, J. Zhou, X. Feng and B. Wang, *J. Am. Chem. Soc.*, 2017, **139**, 4258–4261.

116 Z. Lei, X. Chen, W. Sun, Y. Zhang and Y. Wang, *Adv. Energy Mater.*, 2019, **9**, 1–13.

117 H. Zhang, W. Sun, X. Chen and Y. Wang, *ACS Nano*, 2019, **13**, 14252–14261.

118 S. Haldar, K. Roy, R. Kushwaha, S. Ogale and R. Vaidhyanathan, *Adv. Energy Mater.*, 2019, **9**, 1–10.

119 Y. Zhu, M. Qiao, W. Peng, Y. Li, Y. Li, G. Zhang, F. Zhang and X. Fan, *J. Mater. Chem. A*, 2017, **5**, 9272–9278.

120 A. Mal, R. K. Mishra, V. K. Praveen, M. A. Khayum, R. Banerjee and A. Ajayaghosh, *Angew. Chemie - Int. Ed.*, 2018, **57**, 8443–8447.

121 A. Mal, S. Vijayakumar, R. K. Mishra, J. Jacob, R. S. Pillai, B. S. Dileep Kumar and A. Ajayaghosh, *Angew. Chemie - Int. Ed.*, 2020, **59**, 8713–8719.

122 G. Li, K. Zhang and T. Tsuru, *ACS Appl. Mater. Interfaces*, 2017, **9**, 8433–8436.

123 P. Wang, Y. Peng, C. Zhu, R. Yao, H. Song, L. Kun and W. Yang, *Angew. Chemie - Int. Ed.*, 2021, **60**, 19047–19052.

124 F. Haase and B. V. Lotsch, *Chem. Soc. Rev.*, 2020, **49**, 8469–8500.

125 L. Wang, H. Sahabudeen, T. Zhang and R. Dong, *npj 2D Mater. Appl.*, 2018, **2**, 1–7.

126 W. Dai, F. Shao, J. Szczerbiński, R. McCaffrey, R. Zenobi, Y. Jin, A. D. Schlüter and W. Zhang, *Angew. Chemie - Int. Ed.*, 2016, **55**, 213–217.

127 D. B. Shinde, G. Sheng, X. Li, M. Ostwal, A. H. Emwas, K. W. Huang and Z. Lai, *J. Am. Chem. Soc.*, 2018, **140**, 14342–14349.

128 K. Liu, H. Qi, R. Dong, R. Shivhare, M. Addicoat, T. Zhang, H. Sahabudeen, T. Heine, S. Mannsfeld, U. Kaiser, Z. Zheng and X. Feng, *Nat. Chem.*, 2019, **11**,

994–1000.

129 K. Dey, M. Pal, K. C. Rout, S. S. Kunjattu, A. Das, R. Mukherjee, U. K. Kharul and R. Banerjee, *J. Am. Chem. Soc.*, 2017, **139**, 13083–13091.

130 M. Matsumoto, L. Valentino, G. M. Stiehl, H. B. Balch, A. R. Corcos, F. Wang, D. C. Ralph, B. J. Mariñas and W. R. Dichtel, *Chem*, 2018, **4**, 308–317.

131 J. Liu, G. Han, D. Zhao, K. Lu, J. Gao and T. S. Chung, *Sci. Adv.*, 2020, **6**, 1–9.

132 Y. Li, M. Zhang, X. Guo, R. Wen, X. Li, X. Li, S. Li and L. Ma, *Nanoscale Horizons*, 2018, **3**, 205–212.

133 S. W. Park, Z. Liao, B. Ibarlucea, H. Qi, H. H. Lin, D. Becker, J. Melidonie, T. Zhang, H. Sahabudeen, L. Baraban, C. K. Baek, Z. Zheng, E. Zschech, A. Fery, T. Heine, U. Kaiser, G. Cuniberti, R. Dong and X. Feng, *Angew. Chemie - Int. Ed.*, 2020, **59**, 8218–8224.

134 H. Qi, H. Sahabudeen, B. Liang, M. Položij, M. A. Addicoat, T. E. Gorelik, M. Hambsch, M. Mundszinger, S. W. Park, B. V. Lotsch, S. C. B. Mannsfeld, Z. Zheng, R. Dong, T. Heine, X. Feng and U. Kaiser, *Sci. Adv.*, 2020, **6**, 1–9.

135 Y. Ying, M. Tong, S. Ning, S. K. Ravi, S. B. Peh, S. C. Tan, S. J. Pennycook and D. Zhao, *J. Am. Chem. Soc.*, 2020, **142**, 4472–4480.

136 H. Wang, M. Wang, X. Liang, J. Yuan, H. Yang, S. Wang, Y. Ren, H. Wu, F. Pan and Z. Jiang, *Chem. Soc. Rev.*, 2021, **50**, 5468–5516.

137 A. M. Boscoboinik, S. J. Manzi, V. D. Pereyra, W. L. Mas and J. A. Boscoboinik, *Nanoscale*, 2021, **13**, 2408–2419.

138 J. A. Boscoboinik, *J. Phys. Condens. Matter*, 2019, **31**, 063001.

139 C. Büchner and M. Heyde, *Prog. Surf. Sci.*, 2017, **92**, 341–374.

140 C. N. Eads, J. A. Boscoboinik, A. R. Head, A. Hunt, I. Waluyo, D. J. Stacchiola and S. A. Tenney, *Angew. Chemie - Int. Ed.*, 2021, **60**, 10888–10894.

141 S. Shaikhutdinov and H. J. Freund, *Adv. Mater.*, 2013, **25**, 49–67.

142 T. SCHROEDER, M. ADELT, B. RICHTER, M. NASCHITZKI, M. BÄUMER and H.-J. FREUND, *Surf. Rev. Lett.*, 2000, **07**, 7–14.

143 J. Weissenrieder, S. Kaya, J.-L. Lu, H.-J. Gao, S. Shaikhutdinov, H.-J. Freund, M. Sierka, T. K. Todorova and J. Sauer, *Phys. Rev. Lett.*, 2005, **95**, 076103.

144 L. Giordano, D. Ricci, G. Pacchioni and P. Ugliengo, *Surf. Sci.*, 2005, **584**, 225–236.

145 S. Shaikhutdinov and H. J. Freund, *J. Phys. Condens. Matter*, 2015, **27**, 443001.

146 D. Stacchiola, S. Kaya, J. Weissenrieder, H. Kuhlenbeck, S. Shaikhutdinov, H. J. Freund, M. Sierka, T. K. Todorova and J. Sauer, *Angew. Chemie - Int. Ed.*, 2006, **45**, 7636–7639.

147 D. Löffler, J. J. Uhlrich, M. Baron, B. Yang, X. Yu, L. Lichtenstein, L. Heinke, C. Büchner, M. Heyde, S. Shaikhutdinov, H. J. Freund, R. Włodarczyk, M. Sierka and J. Sauer, *Phys. Rev. Lett.*, 2010, **105**, 2–5.

148 B. Yang, W. E. Kaden, X. Yu, J. A. Boscoboinik, Y. Martynova, L. Lichtenstein, M. Heyde, M. Sterrer, R. Włodarczyk, M. Sierka, J. Sauer, S. Shaikhutdinov and H. J. Freund, *Phys. Chem. Chem. Phys.*, 2012, **14**, 11344–11351.

149 D. Kuhness, H. J. Yang, H. W. Klemm, M. Prieto, G. Peschel, A. Fuhrich, D. Menzel, T. Schmidt, X. Yu, S. Shaikhutdinov, A. Lewandowski, M. Heyde, A. Kelemen, R. Włodarczyk, D. Usvyat, M. Schütz, J. Sauer and H. J. Freund, *J. Am. Chem. Soc.*, 2018, **140**, 6164–6168.

150 A. L. Lewandowski, S. Tosoni, L. Gura, P. Schlexer, P. Marschalik, W. D. Schneider, M. Heyde, G. Pacchioni and H. J. Freund, *Angew. Chemie - Int. Ed.*, 2019, **58**, 10903–10908.

151 P. Y. Huang, S. Kurasch, A. Srivastava, V. Skakalova, J. Kotakoski, A. V. Krasheninnikov, R. Hovden, Q. Mao, J. C. Meyer, J. Smet, D. A. Muller and U. Kaiser, *Nano Lett.*, 2012, **12**, 1081–1086.

152 L. Lichtenstein, C. Büchner, B. Yang, S. Shaikhutdinov, M. Heyde, M. Sierka, R. Wåodarczyk, J. Sauer and H. J. Freund, *Angew. Chemie - Int. Ed.*, 2012, **51**, 404–407.

153 L. Lichtenstein, M. Heyde and H.-J. Freund, *Phys. Rev. Lett.*, 2012, **109**, 106101.

154 L. Lichtenstein, M. Heyde and H. J. Freund, *J. Phys. Chem. C*, 2012, **116**, 20426–20432.

155 C. Büchner, L. Lichtenstein, X. Yu, J. A. Boscoboinik, B. Yang, W. E. Kaden, M. Heyde, S. K. Shaikhutdinov, R. Włodarczyk, M. Sierka, J. Sauer and H. J. Freund, *Chem. - A Eur. J.*, 2014, **20**, 9176–9183.

156 T. Björkman, S. Kurasch, O. Lehtinen, J. Kotakoski, O. V. Yazyev, A. Srivastava, V. Skakalova, J. H. Smet, U. Kaiser and A. V. Krasheninnikov, *Sci. Rep.*, 2013, **3**, 1–8.

157 K. M. Burson, C. Büchner, M. Heyde and H. J. Freund, *J. Phys. Condens. Matter*, , DOI:10.1088/0953-8984/29/3/035002.

158 H. W. Klemm, M. J. Prieto, F. Xiong, G. B. Hassine, M. Heyde, D. Menzel, M. Sierka, T. Schmidt and H. J. Freund, *Angew. Chemie - Int. Ed.*, 2020, **59**, 10587–10593.

159 J. A. Boscoboinik, X. Yu, B. Yang, F. D. Fischer, R. Wodarczyk, M. Sierka, S. Shaikhutdinov, J. Sauer and H. J. Freund, *Angew. Chemie - Int. Ed.*, 2012, **51**, 6005–6008.

160 J. A. Boscoboinik, X. Yu, B. Yang, S. Shaikhutdinov and H. J. Freund, *Microporous Mesoporous Mater.*, 2013, **165**, 158–162.

161 X. Yu, B. Yang, J. Anibal Boscoboinik, S. Shaikhutdinov and H. J. Freund, *Appl. Phys. Lett.*, 2012, **100**, 1–5.

162 U. Martinez, L. Giordano and G. Pacchioni, *J. Phys. Chem. B*, 2006, **110**, 17015–17023.

163 E. I. Altman, J. Götzen, N. Samudrala and U. D. Schwarz, *J. Phys. Chem. C*,

2013, **117**, 26144–26155.

164 J. H. Jhang, C. Zhou, O. E. Dagdeviren, G. S. Hutchings, U. D. Schwarz and E. I. Altman, *Phys. Chem. Chem. Phys.*, 2017, **19**, 14001–14011.

165 G. S. Hutchings, J. H. Jhang, C. Zhou, D. Hynek, U. D. Schwarz and E. I. Altman, *ACS Appl. Mater. Interfaces*, 2017, **9**, 11266–11271.

166 C. Zhou, X. Liang, G. S. Hutchings, J. H. Jhang, Z. S. Fishman, R. Wu, A. Gozar, U. D. Schwarz, S. Ismail-Beigi and E. I. Altman, *Nanoscale*, 2019, **11**, 21340–21353.

167 C. Zhou, X. Liang, G. S. Hutchings, Z. S. Fishman, J. H. Jhang, M. Li, U. D. Schwarz, S. Ismail-Beigi and E. I. Altman, *Chem. Mater.*, 2019, **31**, 851–861.

168 F. Ben Romdhane, T. Björkman, J. A. Rodríguez-Manzo, O. Cretu, A. V. Krasheninnikov and F. Banhart, *ACS Nano*, 2013, **7**, 5175–5180.

169 F. Ben Romdhane, T. Björkman, A. V. Krasheninnikov and F. Banhart, *J. Phys. Chem. C*, 2014, **118**, 21001–21005.

170 A. L. Lewandowski, S. Tosoni, L. Gura, Z. Yang, A. Fuhrich, M. J. Prieto, T. Schmidt, D. Usvyat, W. D. Schneider, M. Heyde, G. Pacchioni and H. J. Freund, *Chem. - A Eur. J.*, 2021, **27**, 1870–1885.

171 A. L. Lewandowski, P. Schlexer, C. Büchner, E. M. Davis, H. Burrall, K. M. Burson, W. D. Schneider, M. Heyde, G. Pacchioni and H. J. Freund, *Phys. Rev. B*, 2018, **97**, 3–8.

172 A. L. Lewandowski, P. Schlexer, S. Tosoni, L. Gura, P. Marschalik, C. Büchner, H. Burrall, K. M. Burson, W. D. Schneider, G. Pacchioni and M. Heyde, *J. Phys. Chem. C*, 2019, **123**, 7889–7897.

173 A. L. Lewandowski, F. Stavale, S. Tosoni, W. D. Schneider, M. Heyde, G. Pacchioni and H. J. Freund, *Phys. Rev. B*, 2019, **100**, 1–6.

174 E. Gao, B. Xie and Z. Xu, *J. Appl. Phys.*, , DOI:10.1063/1.4939279.

175 J. Zhang, *Comput. Mater. Sci.*, 2018, **142**, 7–13.

176 C. Büchner, Z. J. Wang, K. M. Burson, M. G. Willinger, M. Heyde, R. Schlögl and H. J. Freund, *ACS Nano*, 2016, **10**, 7982–7989.

177 S. Wendt, M. Frerichs, T. Wei, M. S. Chen, V. Kempter and D. W. Goodman, *Surf. Sci.*, 2004, **565**, 107–120.

178 C. Büchner, L. Lichtenstein, S. Stuckenholz, M. Heyde, F. Ringleb, M. Sterrer, W. E. Kaden, L. Giordano, G. Pacchioni and H. J. Freund, *J. Phys. Chem. C*, 2014, **118**, 20959–20969.

179 N. Akter, J. T. Sadowski, C. Zhou, J. Q. Zhong, M. van Spronsen, Y. Xu, X. Tong, T. Kim, S. Tenney, A. R. Head, D. J. Stacchiola and J. A. Boscoboinik, *Top. Catal.*, 2019, **62**, 1067–1075.

180 E. Emmez, B. Yang, S. Shaikhutdinov and H. J. Freund, *J. Phys. Chem. C*, 2014, **118**, 29034–29042.

181 H. Tissot, X. Weng, P. Schlexer, G. Pacchioni, S. Shaikhutdinov and H. J. Freund, *Surf. Sci.*, 2018, **678**, 118–123.

182 P. Schlexer, G. Pacchioni, R. Włodarczyk and J. Sauer, *Surf. Sci.*, 2016, **648**, 2–9.

183 E. Emmez, J. Anibal Boscoboinik, S. Tenney, P. Sutter, S. Shaikhutdinov and H. J. Freund, *Surf. Sci.*, 2016, **646**, 19–25.

184 J. H. Jhang and E. I. Altman, *Surf. Sci.*, 2019, **679**, 99–109.

185 J. H. Jhang, J. A. Boscoboinik and E. I. Altman, *J. Chem. Phys.*, , DOI:10.1063/1.5142621.

186 B. Yao, S. Mandrà, J. O. Curry, S. Shaikhutdinov, H. J. Freund and J. Schrier, *ACS Appl. Mater. Interfaces*, 2017, **9**, 43061–43071.

187 J. Q. Zhong, M. Wang, N. Akter, D. J. Stacchiola, D. Lu and J. A. Boscoboinik, *J. Phys. Chem. C*, 2019, **123**, 13578–13585.

188 J. Q. Zhong, M. Wang, N. Akter, J. D. Kestell, T. Niu, A. M. Boscoboinik, T. Kim, D. J. Stacchiola, Q. Wu, D. Lu and J. A. Boscoboinik, *Adv. Funct. Mater.*, 2019, **29**, 1–10.

189 J.-Q. Zhong, M. Wang, N. Akter, J. D. Kestell, A. M. Boscoboinik, T. Kim, D. J. Stacchiola, D. Lu and J. A. Boscoboinik, *Nat. Commun.*, 2017, **8**, 16118.

190 D. Naberezhnyi, S. Park, W. Li, M. Westphal, X. Feng, R. Dong and P. Dementyev, *Small*, 2021, 2104392.

191 D. Naberezhnyi, A. Gölzhäuser and P. Dementyev, *J. Phys. Chem. Lett.*, 2019, **10**, 5598–5601.

Declaration of autorship

Hereby, I declare that this thesis is my original work. No resources were used other than mentioned literature.

Bielefeld, November 2021

Daniil Naberezhnyi

Scientific publications and contributions of the author

As a result of the doctoral study, the following articles have been published.

1) P. Dementyev, T. Wilke, D. Naberezhnyi, D. Emmrich and A. Gölzhäuser, *Vapour Permeation Measurements with Free-Standing Nanomembranes*. ***Phys. Chem. Chem. Phys.*** 2019, **21**, 15471–15477. https://doi.org/10.1039/c9cp03038g.

2) D. Naberezhnyi, A. Gölzhäuser and P. Dementyev, *Water-Assisted Permeation of Gases in Carbon Nanomembranes*. ***J. Phys. Chem. Lett**.* 2019, **10**, 5598–5601. https://doi.org/10.1021/acs.jpclett.9b02321.

3) P. Dementyev, D. Naberezhnyi, M. Westphal, M. Buck and A. Gölzhäuser, *Carbon Nanomembranes from Aromatic Carboxylate Precursors*. ***ChemPhysChem*** 2020, **21**, 1006–1011. https://doi.org/10.1002/cphc.202000150.

4) D. Naberezhnyi and P. Dementyev, *Molecular Transport in Ionic Liquid/Nanomembrane Hybrids*. ***Phys. Chem. Chem. Phys**.* 2020, **22**, 9808–9814. https://doi.org/10.1039/d0cp01233e.

5) D. Naberezhnyi, S. Park, W. Li, M. Westphal, X. Feng, R. Dong and P. Dementyev, *Mass Transfer in Boronate Ester 2D COF Single Crystals*. ***Small*** 2021, 2104392. https://doi.org/10.1002/smll.202104392.

6) D. Naberezhnyi, L. Mai, N. Doudin, I. Ennen, A. Hütten, E. I. Altman, A. Devi and P. Dementyev, *Molecular Permeation in Freestanding Bilayer Silica*. ***Nano Lett.*** 2021. (summbitted manuscript)

Acknowledgements

I express my deep gratitude to Dr. Petr Dementyev, my mentor in a new scientific field. I thank him for valuable advices and motivation to finish my thesis in three years.

I would like to thank my first reviewer, Prof. Dr. Armin Gölzhäuser, for the opportunity to do research in his working group at the Bielefeld University.

I cordially thank Prof. Dr. Dario Anselmetti for agreeing to be my second reviewer.

Many thanks to Dr. Raphael Dahlpke who taught me how to synthesize CNM and transfer 2D membranes. I also thank him and Dr. Yang Yang for proofreading my thesis.

I want to thank Dr. Berthold Völkel for the technical support and keeping the equipment in order. I appreciate help with laboratory setups from Dr. Nikolaus Meyerbröker, Dr. Xianghui Zhang, Dr. Patrick Stohmann and Hoang Linh Le. I thank Michael Westphal for the HIM imaging of my samples. I am grateful to Riko Korzetz for consultations. I would like to thank Karin Lacey, Dr. Natalie Freese and Dr. Udo Werner for assistance with the documents.

In the end, I thank my family and everyone who supported me during the doctoral study in Bielefeld.